

Long-term hydrological response and physical transport dynamics in response to climatic variability

Insights from the Neckar basin

Wang, S.

DOI

[10.4233/uuid:4c7277e8-6f5c-4024-bedf-20e20d9012a2](https://doi.org/10.4233/uuid:4c7277e8-6f5c-4024-bedf-20e20d9012a2)

Publication date

2025

Document Version

Final published version

Citation (APA)

Wang, S. (2025). *Long-term hydrological response and physical transport dynamics in response to climatic variability: Insights from the Neckar basin*. [Dissertation (TU Delft), Delft University of Technology]. <https://doi.org/10.4233/uuid:4c7277e8-6f5c-4024-bedf-20e20d9012a2>

Important note

To cite this publication, please use the final published version (if applicable).
Please check the document version above.

Copyright

Other than for strictly personal use, it is not permitted to download, forward or distribute the text or part of it, without the consent of the author(s) and/or copyright holder(s), unless the work is under an open content license such as Creative Commons.

Takedown policy

Please contact us and provide details if you believe this document breaches copyrights.
We will remove access to the work immediately and investigate your claim.

**LONG-TERM HYDROLOGICAL RESPONSE AND
PHYSICAL TRANSPORT DYNAMICS IN RESPONSE
TO CLIMATIC VARIABILITY**

INSIGHTS FROM THE NECKAR BASIN

Siyuan WANG
Delft University of Technology

LONG-TERM HYDROLOGICAL RESPONSE AND PHYSICAL TRANSPORT DYNAMICS IN RESPONSE TO CLIMATIC VARIABILITY

INSIGHTS FROM THE NECKAR BASIN

Dissertation

for the purpose of obtaining the degree of doctor
at Delft University of Technology
by the authority of the Rector Magnificus, prof. dr. ir. T.H.J.J. van der Hagen,
chair of the Board for Doctorates
to be defended publicly on Wednesday 15 January 2025 at 12:30 hours

by

Siyuan WANG

Master in Physical Geography
Nanjing University, China
born in Henan, China

This dissertation has been approved by the promotor.

Composition of the doctoral committee:

Rector Magnificus,	chairperson
Dr. M. Hrachowitz,	Delft University of Technology, <i>promotor</i>
Dr.ir G.H.W. Schoups,	Delft University of Technology, <i>copromotor</i>

Independent members:

Prof. dr. T.A. Bogaard,	Delft University of Technology
Dr. ir. Y. van der Velde,	Vrije Universiteit Amsterdam
Prof. dr. S.C. Steele-Dunne,	Delft University of Technology
Univ.Prof. Dr. C. Stumpp,	University of Natural Resources and Life Sciences



<i>Keywords:</i>	hydrological modeling, Neckar basin, root zone storage capacity, water age distributions, climate variability
<i>Printed by:</i>	Ipskamp Printing
<i>Cover by:</i>	Siyuan Wang and Our Friday Goldfish

Copyright © 2025 by Siyuan Wang

ISBN 978-94-6366-983-2

An electronic copy of this dissertation is available at
<https://repository.tudelft.nl/>.

CONTENTS

Summary	vii
Samenvatting	xi
1 Introduction	1
1.1 Hydrological system under climatic change	2
1.2 Research concepts and methodology	5
1.3 Research objective	8
1.4 Research outline	8
2 Development of a hydrological model for the Neckar basin	11
2.1 The Neckar basin.	12
2.2 Hydrological model	14
3 Vegetation adaptation to climatic variability: Testing the effects of temporal evolution of root zone storage capacity on long-term hydrological response	21
3.1 Introduction	23
3.2 Study area	25
3.3 Data sets	26
3.4 Methods	28
3.5 Results	35
3.6 Discussion	44
3.7 Conclusions	48
4 Transport model and tracers: No evidence for underestimation of catchment transit times inferred by water stable isotopes in SAS function models	51
4.1 Introduction	53
4.2 Data	58
4.3 Methods	64
4.4 Results	74
4.5 Implications, limitations and unresolved questions	101
4.6 Conclusions	105
5 Long-term transport dynamics in response to climatic variability based on multi-time scale analysis	107
5.1 Introduction	109
5.2 Data	112
5.3 Methods	114
5.4 Results and discussion	115

5.5	Conclusions	132
6	Conclusions and outlooks	133
6.1	Novel contributions	134
6.2	Implications	135
6.3	Outlook	137
A	Appendix	141
B	Appendix	145
C	Appendix	159
	References	163
	Acknowledgements	185
	Curriculum Vitae	187
	List of Publications	189

SUMMARY

Over recent decades, climatic changes and significant variations in all key components of the hydrological cycle have been observed in many regions worldwide, profoundly altering water availability, river flow regimes, and the concentration of nutrients and pollutants. Ecosystem is a key component of the terrestrial hydrological cycle as it shapes the hydrological functioning of catchments by regulating the long-term average partitioning of water into drainage and evaporative fluxes (i.e. latent heat). In response to a changing environment, ecosystems continuously adapt to allow the most efficient use of available energy and resources. However, direct quantification of how ecosystems adapts to climatic variability over long time periods and the mechanistic drivers thereof at the catchment-scale is missing so far. As a consequence, it remains unclear how climatic variability, such as precipitation regime or canopy water demand, influences the partitioning of water fluxes, the hydrological response, and hydrological processes and transport mechanisms at the catchment-scale. Therefore, the overarching objective of this thesis is to address the following main research question: How does climatic variability affect the hydrological response and transport mechanisms in a temperate-humid basin over multiple decades?

All analysis in this thesis is carried out in a large river basin, the Neckar basin, Germany. A unique long-term dataset is used for this basin, consisting of 70 years of hydrometeorological and tracer data. Hydrological and transport processes in the basin are quantified using a state-of-the-art semi-distributed hydrological model that (i) includes spatial heterogeneity in topography, vegetation and precipitation, (ii) accounts for ecosystem adaptation to climate variability via a time-varying root zone water storage capacity, and (iii) uses StorAge Selection (SAS) functions to account for mixing of tracers and to estimate time-varying water age distributions at catchment scale. Multi-objective calibration of the hydrological model using the long-term hydrometeorological and tracer dataset provides the basis for investigating how climatic variability affects hydrological and physical transport processes in the Neckar basin.

The first research question focuses on ecosystem adaptation to climate variability via changes in root zone storage capacity. The root zone storage capacity is a critical factor regulating latent heat fluxes and thus the moisture exchange between land and atmosphere as well as the hydrological response and biogeochemical processes in terrestrial hydrological systems. To be survive, root systems of vegetation and the associated vegetation-accessible water storage capacity respond to the ever-changing conditions of its environment. However, as these changes occur at landscape scale and are mostly reflected by changes in the composition of plant species present in a specific spatial domain, fluctuations in root zone storage capacity occur largely at time-scales that reflect the life-cycles of individual plants. However, it remains unclear whether root zone storage capacity adapts to climatic variability and evolves over time, thereby reflecting ecosystem adaptation to changing conditions. The thesis investigates this for the Neckar basin by quantifying long-term changes in root zone storage capacity using two different methods, i.e. hydrological model

calibration and an independent water balance estimation method. The analysis provides quantitative mechanistic evidence that root zone storage capacity significantly changes over multiple decades reflecting ecosystem adaptation to climatic variability. However, the analysis also suggests that accounting for temporal evolution of root zone storage capacity with a time-variable formulation of that parameter in a hydrological model does not significantly improve its ability to reproduce the hydrological response and may therefore be of minor importance to predict the effects of a changing climate on the hydrological response.

The second research question investigates the use of different isotopic tracers to estimate water age distributions, i.e. age distributions of water fluxes ("transit time distributions", TTD) and water stored in catchments ("residence time distributions", RTD) as fundamental descriptors of hydrological functioning and catchment storage. These distributions provide a way to quantitatively describe the physical link between the hydrological response of catchments and physical transport processes of conservative solutes. However, water age distributions cannot be directly observed, and instead have to be estimated with tracer-aided models. Stable isotopes ($\delta^{18}\text{O}$) and tritium (^3H) are frequently used as tracers in environmental sciences to estimate age distributions of water. It has previously been argued that seasonally variable tracers, such as $\delta^{18}\text{O}$, generally and systematically fail to detect the tails of water age distributions and therefore substantially underestimate water ages as compared to radioactive tracers, such as ^3H . Early approaches often relied on simple lumped sine-wave or lumped parameter convolution integral models under the assumption that water storage in catchments is at steady state. Here, these methods are compared with the more realistic StorAge Selection (SAS) functions embedded in the dynamic hydrological model used in this thesis. By comparing water age distributions inferred from $\delta^{18}\text{O}$ and ^3H with several different transport model implementations, this thesis demonstrates that previously reported underestimations of water ages are most likely not a result of the use of $\delta^{18}\text{O}$ or other seasonally variable tracers. Instead, these underestimations can be largely attributed to choices of model approaches and complexity. It is therefore strongly advocated to avoid the use of steady-state model types in combination with seasonally variable tracers and to instead adopt SAS-based or other time-variant model formulations that allow for the representation of transient conditions.

The third and final research question investigates the effects of temporal variability of the hydrological response on physical transport processes over a spectrum of time-scales from daily to multiple decades. Due to limited availability of tracer records over longer durations in many catchments, most previous studies focused on daily time scales to analyse temporal variability of water ages as metric of physical transport and the underlying drivers. To improve understanding of long-term transport dynamics, this thesis quantifies the variability in water ages, identifies the associated dominant controls from daily to multi-decadal time scales, and analyses the associated temporal evolution of water ages of streamflow and evaporation. It is shown that there are no major long-term dynamics in water ages, driven by either internal processes or external transport variability. Consequently, the physical transport dynamics in the upper Neckar basin, and potentially in other basins with similar water age characteristics, are inferred to exhibit near-stationarity over multiple decades.

Concluding, this thesis provides sufficient evidence that long-term varying root zone storage capacity significantly reflects ecosystem adaptation to climatic variability. However, the temporal evolution of root zone storage capacity does not control variation in the partitioning of water fluxes and has no significant effects on fundamental hydrological response characteristics of the studied semi-humid river basin in the near future under a changing climatic condition. In addition, the thesis suggests physical transport processes can be assumed to be near-stationary and predictable across multiple decades under either internal (i.e., time-variant root zone storage capacity) or external transport variability (i.e., climatic variability), which contrasts with the frequently reported fractal pattern in stream water solute dynamics. This finding is crucial for management of subsurface water quality and the design of restoration interventions for groundwater affected by legacy contamination such as nitrate.

SAMENVATTING

In de afgelopen decennia zijn klimaatveranderingen en significante variaties in alle belangrijke componenten van de hydrologische cyclus waargenomen in vele regio's wereldwijd. Deze veranderingen hebben een diepgaande invloed op de beschikbaarheid van water, rivierregimes en de concentratie van nutriënten en verontreinigingen. Het ecosysteem is een cruciaal onderdeel van de hydrologische cyclus, omdat het de hydrologische werking van stroomgebieden vormgeeft door de langetermijnverdeling van water in drainage en verdamping (d.w.z. latente warmte) te reguleren. In reactie op een veranderende omgeving passen wortelsystemen van het ecosysteem zich continu aan om zo efficiënt mogelijk gebruik te maken van beschikbare energie en bronnen. Echter, directe kwantificering van hoe het ecosysteem zich aanpast aan klimaatschommelingen over lange perioden en de mechanistische drijfveren daarvan op stroomgebiedschaal ontbreekt tot nu toe. Als gevolg hiervan is het onduidelijk hoe klimaatschommelingen, zoals neerslagregimes of waterbehoefte van het ecosysteem, de verdeling van waterstromen, de hydrologische respons, en hydrologische processen en transportmechanismen op stroomgebiedschaal beïnvloeden. Het overkoepelende doel van dit proefschrift is daarom om de volgende hoofdonderzoeksvraag te beantwoorden: Hoe beïnvloeden klimaatschommelingen de hydrologische respons en transportmechanismen in een gematigd-vochtig stroomgebied over meerdere decennia?

Alle analyses in dit proefschrift zijn uitgevoerd in een groot stroomgebied, het stroomgebied van de Neckar in Duitsland. Voor dit stroomgebied wordt een unieke langetermijndataset gebruikt, bestaande uit 70 jaar aan hydrometeorologische en tracergegevens. Hydrologische- en transportprocessen in het bekken zijn gekwantificeerd met behulp van een modern semi-gedistribueerd hydrologisch model dat (i) ruimtelijke heterogeniteit in topografie, ecosysteem en neerslag in rekening brengt, (ii) rekening houdt met de aanpassing van het ecosysteem aan klimaatschommelingen via een tijdsafhankelijke wateropslagcapaciteit in de wortelzone, en (iii) StorAge Selection (SAS) functies gebruikt om rekening te houden met transport van tracers en om de tijdsafhankelijke leeftijdsdistributie van water op stroomgebiedschaal te schatten. Kalibratie van meerdere parameters van het hydrologische model met behulp van de langetermijns hydrometeorologische en tracer dataset worden vervolgens gebruikt voor het onderzoeken van hoe klimaatschommelingen hydrologische en fysieke transportprocessen in het Neckar-stroomgebied beïnvloeden.

De eerste onderzoeksvraag richt zich op de aanpassing van het ecosysteem aan klimaatschommelingen door middel van veranderingen in de opslagcapaciteit van de wortelzone. De opslagcapaciteit van de wortelzone is een cruciale factor die de latente warmtestromen reguleert en daarmee de vochtuitwisseling tussen land en atmosfeer, evenals de hydrologische respons en biogeochemische processen in terrestrische hydrologische systemen. Om te overleven reageren wortelsystemen van vegetatie en de daarmee samenhangende door vegetatie toegankelijke wateropslagcapaciteit op de voortdurend veranderende omge-

vingscondities. Aangezien deze veranderingen echter op landschapsniveau plaatsvinden en grotendeels worden weerspiegeld in veranderingen in de samenstelling van plantensoorten binnen een specifiek ruimtelijk gebied, vinden schommelingen in de wortelzone-opslagcapaciteit voornamelijk plaats op tijdschalen die de levenscycli van individuele planten weerspiegelen. Het is echter onduidelijk of de opslagcapaciteit van de wortelzone zich aanpast aan klimaatschommelingen en in de loop van de tijd evolueert, en zo de aanpassing van het ecosysteem aan veranderende omstandigheden weerspiegelt. Het proefschrift onderzoekt dit voor het Neckar-stroomgebied door langetermijnsveranderingen in de opslagcapaciteit van de wortelzone te kwantificeren met behulp van twee verschillende methoden, namelijk kalibratie van een hydrologisch model en een onafhankelijke waterbalansschattingsmethode. De analyse levert kwantitatief mechanistisch bewijs dat de opslagcapaciteit van de wortelzone aanzienlijk verandert over meerdere decennia, wat wijst op de aanpassing van het ecosysteem aan klimaatschommelingen. De analyse suggereert echter ook dat het in rekening brengen van de temporele evolutie van de opslagcapaciteit van de wortelzone met een tijdsvariabele formulering van die parameter in een hydrologisch model, de capaciteit om de hydrologische respons te reproduceren niet significant verbetert en daarom mogelijk van ondergeschikt belang is voor het voorspellen van de effecten van een veranderend klimaat op de hydrologische respons.

De tweede onderzoeksvraag onderzoekt het gebruik van verschillende isotopische tracers om waterleeftijdverdelingen te schatten, dat wil zeggen leeftijdsverdelingen van waterstromen ("transitietijdverdelingen", TTD) en water opgeslagen in stroomgebieden ("verblijftijdverdelingen", RTD) als fundamentele beschrijvingen van hydrologische werking en stroomopslag. Deze verdelingen bieden een manier om de fysieke link tussen de hydrologische respons van stroomgebieden en de fysieke transportprocessen van conservatieve opgeloste stoffen kwantitatief te beschrijven. Waterleeftijdverdelingen kunnen echter niet direct worden waargenomen en moeten in plaats daarvan worden geschat met tracer-ondersteunde modellen. Stabiele isotopen ($\delta^{18}\text{O}$) en tritium (^3H) worden vaak gebruikt als tracers in milieuwetenschappen om leeftijdsverdelingen van water te schatten. Eerder is betoogd dat seizoensgebonden variabele tracers, zoals $\delta^{18}\text{O}$, over het algemeen systematisch falen in het detecteren van grotere waterleeftijden en daarom de waterleeftijden aanzienlijk onderschatten in vergelijking met radioactieve tracers, zoals ^3H . Vroege benaderingen vertrouwden vaak op eenvoudige, sinusgolf of parameterconvolutie-integrale modellen, waarbij werd aangenomen dat wateropslag in stroomgebieden in een stationaire toestand verkeert. Hier worden deze methoden vergeleken met de meer realistische Stor-Age Selection (SAS) functies, die geïntegreerd zijn in het dynamische hydrologische model dat in dit proefschrift wordt gebruikt. Door waterleeftijdverdelingen afgeleid van $\delta^{18}\text{O}$ en ^3H te vergelijken met verschillende transportmodelimplementaties, toont dit proefschrift aan dat eerder gerapporteerde onderschattingen van waterleeftijden waarschijnlijk niet het gevolg zijn van het gebruik van $\delta^{18}\text{O}$ of andere seizoensgebonden variabele tracers. Deze onderschattingen kunnen in plaats daarvan grotendeels worden toegeschreven aan de keuzes van modelbenaderingen en complexiteit. Daarom wordt sterk aanbevolen om het gebruik van stationaire modellen in combinatie met seizoensgebonden variabele tracers te vermijden en in plaats daarvan SAS-gebaseerde of andere modelformuleringen aan te nemen die de simulatie van niet-stationaire systemen mogelijk maken.

De derde en laatste onderzoeksvraag richt zich op de effecten van temporele variabiliteit van de hydrologische respons op fysieke transportprocessen over een spectrum van tijdschalen, variërend van dagelijks tot meerdere decennia. Vanwege de beperkte beschikbaarheid van tracergegevens over langere perioden in veel stroomgebieden, richtten eerdere studies zich voornamelijk op dagelijkse tijdschalen om de temporele variabiliteit van waterleeftijden als maatstaf voor fysiek transport en de onderliggende factoren te analyseren. Om het inzicht in de langetermijn-transportdynamiek te verbeteren, kwantificeert dit proefschrift de variabiliteit in waterleeftijden, identificeert het de bijbehorende dominante factoren voor tijdschalen van dagelijks tot meerdere decennia, en analyseert het de bijbehorende temporele evolutie van waterleeftijden in afvoer en verdamping. Er wordt aangetoond dat er geen grote langetermijndynamiek is in waterleeftijden, gedreven door interne processen of externe transportvariabiliteit. Bijgevolg wordt geconcludeerd dat de fysieke transportdynamiek in het Neckar-stroomgebied, en mogelijk in andere stroomgebieden met vergelijkbare waterleeftijdskenmerken, over meerdere decennia een quasi-stationair gedrag vertoont.

Concluderend biedt dit proefschrift voldoende bewijs dat de langetermijnvariatie in de opslagcapaciteit van de wortelzone de aanpassing van het ecosysteem aan klimaat-schommelingen weerspiegelt. Echter, de temporele evolutie van de opslagcapaciteit van de wortelzone bepaalt niet de variatie in de verdeling van waterstromen en heeft geen significante effecten op fundamentele hydrologische responskenmerken in het bestudeerde stroomgebied in de nabije toekomst onder veranderende klimatologische omstandigheden. Daarnaast suggereert het proefschrift dat fysieke transportprocessen als quasi-stationair en voorspelbaar kunnen worden beschouwd over meerdere decennia, zowel onder interne (d.w.z. tijdsvariabele opslagcapaciteit van de wortelzone) als externe transportvariabiliteit (d.w.z. klimaat-schommelingen), wat contrasteert met het vaak gerapporteerde fractale patroon in de dynamiek van opgeloste stoffen in stroomwater. Dit inzicht is cruciaal voor het beheer van de kwaliteit van grondwater dat is aangetast door langetermijn-verontreiniging zoals nitraat.

1

INTRODUCTION

Climate is what we expect, weather is what we get.

Mark Twain

This chapter is partly based on:

Wang, S. et al. “Stable water isotopes and tritium tracers tell the same tale: no evidence for underestimation of catchment transit times inferred by stable isotopes in StorAge Selection (SAS)-function models”. In: *Hydrology and Earth System Sciences* 27.16 (2023), pp. 3083–3114. issn: 1607-7938. doi: [10.5194/hess-27-3083-2023](https://doi.org/10.5194/hess-27-3083-2023).

Wang, S. et al. “Multi-decadal fluctuations in root zone storage capacity through vegetation adaptation to hydro-climatic variability has minor effects on the hydrological response in the Neckar basin, Germany”. In: *Hydrology and Earth System Sciences* 28.17 (2024), pp. 4011–4033. issn: 1812-2116. doi: [10.5194/hess-28-4011-2024](https://doi.org/10.5194/hess-28-4011-2024).

Wang, S. et al. “Multi-decadal stability of water ages and tracer transport in a temperate-humid river basin”. In: *Environmental Research letters* (2024). Under review.

1.1 HYDROLOGICAL SYSTEM UNDER CLIMATIC CHANGE

THE climate is a complex, nonlinear, dissipative, and heterogeneous system that operates outside of thermodynamic equilibrium (Trenberth, 1992; Ghil and Lucarini, 2020; Jones and Ricketts, 2021). It is subject to both internal dynamics, such as the El Niño-Southern Oscillation, and external forcings, including anthropogenic influences (Timmermann et al., 2018; Cai et al., 2021). Climate variability occurs across all temporal scales, from annual fluctuations to changes spanning decades, centuries, and millennia. Extensive research has documented the significant spatial and temporal heterogeneity in impacts of climate variability (Elmendorf et al., 2012; Shrestha et al., 2012; Di Cecco and Gouhier, 2018; Cheng et al., 2021; Jia et al., 2022; Braga and Laurini, 2024). Over the past century, climate variability has notably affected the rate of global average surface temperature increase, with distinct differences observed between land and ocean regions, as well as that between high and low latitudes. Specifically, high-latitude regions have experienced increased precipitation, whereas tropical and subtropical land areas have seen a decline in precipitation (Lee and Romero, 2023). It is broadly predicted that the climatic variability will increase with the ongoing planet warming (Salinger, 2005; Mora et al., 2013; Thornton et al., 2014).

Climate variability exerts extensive and profound impacts on ecosystem functions, particularly on the hydrological cycle (Loaiciga et al., 1996; Bonan, 2008; Wagener et al., 2010; Yang et al., 2014). Climate variability alters global precipitation patterns, with precipitation in high latitudes and equatorial regions generally increasing, while mid-latitude arid and semi-arid regions experience declines (Nicholson, 2000; Dore, 2005; Alizadeh and Babaei, 2022; Huang et al., 2023). This uneven distribution on precipitation patterns affects local available water and ecosystem functions significantly. Then this directly influences stream flow, with some regions experiencing increased runoff and frequent floods due to higher precipitation, whereas others face reduced runoff and frequent droughts due to diminished precipitation. Such changes in the hydrological cycle impact freshwater ecosystems and some terrestrial ecosystems dependent on such water resources. Additionally, the rise in temperatures induced by global warming enhances evaporation and evapotranspiration rates, especially in tropical and subtropical regions (Dai, 2011; Li et al., 2012; Wu et al., 2012; Cook et al., 2014; Thirumalai et al., 2017). This not only accelerates the water cycle but also potentially reduces soil moisture, adversely affecting plant growth and ecosystem productivity (Polley, 2002; Huntington, 2006; Gornall et al., 2010; Pugnaire et al., 2019; Zhou et al., 2021). Following variations in precipitation patterns and evaporation rates, groundwater recharge rates also are influenced. As the critical water resources for many ecosystems, groundwater may experience reduced recharge, leading to the desiccation of wetlands, rivers, and vegetation, thereby compromising ecosystem stability. Moreover, extreme weather events driven by climate variability, such as floods and droughts, significantly affect the physical and chemical properties of river systems (Whitehead et al., 2009; Wetz and Yoskowitz, 2013; Khan et al., 2015; Leigh et al., 2015). Floods can cause soil erosion, increasing turbidity and pollutant levels in rivers, while droughts may lead to the concentration of rivers, elevating harmful substance concentrations and impacting aquatic organism safety and human water use. Hence, researching the long-term impacts of climate change on hydrological systems is imperative.

Vegetation, as a fundamental component of the hydrological cycle and ecosystems, profoundly influences the hydrological functioning of catchments by modulating the long-term partitioning of water into drainage and evaporative fluxes, commonly expressed as runoff ratio and evaporative index, respectively. Vegetation transpiration, despite inherent uncertainties (Coenders-Gerrits et al., 2014), constitutes the largest portion of global evaporative fluxes (Jasechko, 2018). This process is systematically regulated by the dynamic interplay between canopy water demand and subsurface water supply (Donohue et al., 2007; Yang et al., 2016; Jaramillo et al., 2018; Mianabadi et al., 2019). For vegetation to thrive, continuous access to subsurface water that is accessible to roots is critical to meet canopy water demands. Thus, the existing vegetation, particularly its active root system, is indicative of its successful adaptation to prevailing climatic conditions in a region (Laio et al., 2001; Schenk and Jackson, 2002; Rodríguez-Iturbe and Porporato, 2007; Donohue et al., 2007; Gentine et al., 2012; Liancourt et al., 2012). Irrespective of the geometry, distribution, or structure of root systems, the maximum volume of water accessible to vegetation in the unsaturated root zone, referred to as root zone storage capacity, encapsulates the hydrologically relevant attributes of root systems (Rodríguez-Iturbe and Porporato, 2007; Nijzink et al., 2016a; Savenije and Hrachowitz, 2017; Gao et al., 2023). Consequently, root zone storage capacity directly reflects the hydrologically significant properties of root systems at the catchment scale. In response to environmental changes, vegetation root systems continuously adapt to optimize the use of available energy and resources for survival. Therefore, the factors driving changes in root systems also drive changes in root zone storage capacity, as it inherently represents root system adaptations. Nevertheless, a major knowledge gap persists: it remains unclear whether root zone storage capacity adapts to climatic variability and evolves over time, thereby reflecting vegetation adaptation to changing conditions.

In contrast, it is well understood that, due to the importance of vegetation for the hydrological functioning of terrestrial systems, anthropogenic land use management practices, such as de- and afforestation (Brown et al., 2005; Brath et al., 2006; Fenicia et al., 2009; Alila et al., 2009; Jaramillo et al., 2018; Teuling et al., 2019; Stephens et al., 2021; Hoek van Dijke et al., 2022; Ellison et al., 2024) or irrigation (e.g. AghaKouchak et al., 2015; Van Loon et al., 2016; Roodari et al., 2021) can induce major shifts in the partitioning between the major components of the terrestrial water and energy cycles, and thus between evaporative index and runoff coefficient. Two detailed recent studies with well documented information on deforestation in several experimental catchments established explicit mechanistic links between the reduction of root zone storage capacity by $> 50\%$ following deforestation and decreases in evaporative index (and thus increases in runoff coefficient) from $0.4 - 0.5$ to $0.1 - 0.3$, depending on the catchment and the scale of deforestation (Nijzink et al., 2016a; Hrachowitz et al., 2021). Some studies suggest that using a time-variant root zone storage capacity as the parameter in hydrological models can provide more reliable predictions of future hydrological responses in catchments. For example, Bouaziz et al. (2022) demonstrated this in the Meuse basin located at the North-West Europe. Their findings revealed that adjusting the root zone storage capacity in response to projected climatic conditions, as indicated by the aridity index, can induce substantial shifts in seasonal water supply

for hydrological system. Specifically, this adaptation results in an increased root zone storage capacity, thereby enhancing the volume of sub-surface water available to vegetation. This mechanism leads to a potential increase in summer evaporation by up to 15%, consequently reducing groundwater recharge rates. The reduced recharge subsequently causes a decrease in late-summer and autumn groundwater storage by approximately 10%. Moreover, winter flows could be up to 20% lower in comparison to model simulations utilizing constant root zone storage capacity values based on historical hydro-climatic data. These outcomes are qualitatively in agreement with the findings of Van Oorschot et al. (2024) and Tempel et al. (2024) in such a somewhat more humid environment. However, it remains unclear how climatic variability, such as precipitation regime or canopy water demand, affects root zone storage capacity and how fluctuations in root zone storage capacity may influence the partitioning of water fluxes and therefore, also affect the hydrological response at a semi-humid catchment like the Neckar river basin in Germany.

Climate variability not only affects water quantity but also water quality, such as nutrient-induced eutrophication and eutrophication and its related aquatic hypoxia, which pose significant threats to ecosystem stability. Addressing these challenges, it is necessary to develop models for improving scientific understanding of the hydrological system, supported by comprehensive knowledge to precisely characterize how water and solutes move through a river basin.

Water ages and transit time distributions (TTDs) serve as a critical connection between hydrology and water quality at the catchment scale, serving as a fundamental metric of physical transport within a hydrological system (Hrachowitz et al., 2016). Consequently, they play a critical role in elucidating how water, and thereby nutrients and pollutants, are stored within catchments and subsequently released via diverse flow pathways (Birkel and Soulsby, 2015; Rinaldo et al., 2015; Sprenger et al., 2018; Benettin et al., 2022).

While extensive research has explored the temporal variability of celerity-driven hydrological responses across timescales from minutes to decades (Thompson and Katul, 2012; Berghuijs et al., 2014; Sivapalan and Blöschl, 2015; McMillan, 2020; Berghuijs and Slater, 2023), studies focusing on velocity-driven transit times have predominantly examined shorter periods such as daily, monthly, and seasonal scales. These investigations demonstrate significant fluctuations in water ages in fluxes like streamflow and evaporation, primarily influenced by changes in water availability and the magnitude of precipitation inputs (Heidbüchel et al., 2012; Benettin et al., 2015b, Benettin et al., 2017b; Harman, 2015; Hrachowitz et al., 2015; Soulsby et al., 2016; Rodriguez et al., 2018; Kuppel et al., 2020; Wilusz et al., 2020; Kaandorp et al., 2018; Knapp et al., 2019; Stockinger et al., 2019; Birkel et al., 2016; Remondi et al., 2018; Heidbüchel et al., 2013; Birkel et al., 2015; Von Freyberg et al., 2018; Wilusz et al., 2017; Stockinger and Stumpp, 2024). However, due to limited availability of tracer records over longer durations in many catchments, few studies have analyzed water ages over periods exceeding 10 to 20 years (Hrachowitz et al., 2010b; Wang et al., 2023). Consequently, understanding variability over extended timescales and the resulting long-term dynamics of water ages, including potential systematic trends, remains an area requiring further exploration.

The existing gaps in knowledge pose significant challenges for accurately predicting the long-term behavior of legacy solutes such as nitrate (Basu et al., 2010; Howden et al., 2011) and chloride (Hrachowitz et al., 2015) over decadal timescales, as well as the dynamics of solute mobilization at shorter temporal scales, including phosphorus (e.g., Dupas et al., 2018), amidst changing environmental conditions. Compounding these challenges is the observed fractal scaling of solute concentrations in stream water (e.g., Kirchner et al., 2000; Hrachowitz et al., 2009b, Hrachowitz et al., 2015; Godsey et al., 2010; Kirchner and Neal, 2013; Aubert et al., 2014) and their non-self-averaging properties. This phenomenon implies that the variability in daily, monthly, yearly, or decadal averages of solute concentrations does not conform to typical statistical expectations where averages stabilize over time. Instead, these non-self-averaging time series exhibit persistent variability, complicating the interpretation of trends and their reliability in predicting future solute dynamics, as elucidated by Kirchner and Neal, 2013. Therefore, despite advances in understanding solute transport and transformation in river systems, the persistence of non-self-averaging behaviors highlights the need for refined modeling approaches and expanded datasets. Addressing these complexities will be crucial to improve our ability for predicting the impacts of climatic change on solute dynamics in aquatic ecosystems.

1.2 RESEARCH CONCEPTS AND METHODOLOGY

1.2.1 WATER BALANCE

Over the years, numerous hydrological models have been developed to simulate hydrological processes. Notable examples include the HBV model (Bergström et al., 1985), SUPERFLEX (Fenicia et al., 2011), FLEX-Topo (Gao et al., 2014a), SWAT (Arnold et al., 1998), VIC (Liang et al., 1994), and MIKE-SHE (Christian Refsgaard et al., 2010). Although these models vary in their complexity, they all fundamentally rely on the principle of the water balance. Then water balance asserts that the inflows (i.e., precipitation) to any water system or area are equal to its outflows (i.e., streamflow and evaporation) plus the change in storage over a specified time interval. In hydrology, a water balance equation is employed to describe the movement of water into and out of a system. This system can represent various hydrological or water domains, such as a soil column or a drainage basin. And the water balance concept can be used to estimate the root zone storage capacity that is in detail described in previous papers (e.g. Gao et al., 2014b; Nijzink et al., 2016a; De Boer-Euser et al., 2016; Wang-Erlandsson et al., 2016; Bouaziz et al., 2020; Hrachowitz et al., 2021). In addition, based on the assumption of negligible storage change for averaging periods ≥ 10 years for a large majority of catchments worldwide, the Budyko framework is an expression of the long-term average water balance for a catchment (Schreiber, 1904; Ol'Dekop, 1911; Budyko, 1974; Zhang et al., 2004b). According to the Budyko curve, the long-term water partitioning of input water into two fluxes including evaporation and drainage is controlled by the aridity index. Therefore, it is usually used for mapping the relationship between aridity index and the evaporative index.

Within the Budyko framework, it has been observed that land conversions from forest to grass- and rangeland vegetation result in shifts to lower evaporative index as a

function of the aridity index (Schreiber, 1904; Ol'Dekop, 1911; Budyko, 1974). This observation corresponds well with prior studies that suggest catchments dominated by grass consistently exhibit lower evaporative indices at the same aridity index compared to forested environments (e.g., Zhang et al., 2001, Zhang et al., 2004b; Oudin et al., 2008). These variations in long-term average evaporative indices are explained by parametric reformulations of the Budyko framework, such as the Tixeront-Fu equation (Tixeront, 1964; Fu, 1981). The lumped parameters (e.g., ω) in these models delineate long-term average catchment-specific positions within Budyko space, encapsulating vegetation characteristics and other hydro-climatic and physiographic properties unique to each catchment, aside from the aridity index (e.g., Roderick and Farquhar, 2011; Berghuijs and Woods, 2015). A common assumption is that with changes in climatic conditions, represented by the aridity index, individual catchments will shift to new associated positions in evaporative index, following specific trajectories defined by parameter ω (e.g., Zhou et al., 2015; Bouaziz et al., 2022). However, multiple studies have demonstrated that catchments in various regions worldwide often deviate from their expected new evaporative index following changes in the aridity index (e.g., Jaramillo and Destouni, 2014; Van der Velde et al., 2014; Jaramillo et al., 2018; Reaver et al., 2022; Ibrahim et al., 2024; Tempel et al., 2024).

1.2.2 WATER AGE DISTRIBUTIONS

Age distributions of water fluxes (“transit time distributions”, TTD) and water stored in catchments (“residence time distributions”, RTD) are fundamental descriptors of hydrological functioning (Botter et al., 2011; Sprenger et al., 2019) and catchment storage (Birkel et al., 2015). They provide a way to quantitatively describe the physical link between the hydrological response of catchments and physical transport processes of conservative solutes. While the former is largely controlled by the celerities of pressure waves propagating through the system, the latter, in contrast, occur at velocities that can be up to several orders of magnitude lower (McDonnell and Beven, 2014; Hrachowitz et al., 2016).

Water age distributions cannot be directly observed. Instead, they can, in principle, be inferred from observed tracer breakthrough curves. While practically feasible at lysimeter (e.g. Asadollahi et al., 2020; Benettin et al., 2021) and small hillslope scales (e.g. Kim et al., 2022), lack of adequate observation technology together with logistical constraints make this problematic at scales larger than that. At the catchment-scale, estimates of water age distributions are therefore typically inferred from models that describe the relationships between time-series of observed tracer input and output signals.

Two types of environmental tracers have in the past been frequently used to estimate water age distributions with the above models. The first type are tracers that are characterized by distinct differences in their seasonal signals. They include stable isotopes of water (^2H , ^{18}O ; e.g. Małoszewski et al., 1983; Vitvar and Balderer, 1997; Fenicia et al., 2010) or solutes, such as Cl^- (e.g. Kirchner et al., 2001, Kirchner et al., 2010; Shaw et al., 2008; Hrachowitz et al., 2009a, Hrachowitz et al., 2015). With these tracers, water ages and (metrics of) their distributions can be estimated by the degree to which the seasonal amplitudes of the precipitation tracer concentrations are

time-shifted and/or attenuated in the stream flow (McGuire and McDonnell, 2006; Kirchner, 2016). Broadly speaking, the stronger the attenuation of the seasonally variable tracer amplitude in stream flow (A_s) as compared to its amplitude in precipitation (A_p), i.e., the lower the amplitude ratio A_s/A_p , the older stream water is, on average. The second type of commonly used tracers are radioactive isotopes, such as tritium (^3H). Forming the basis for many water dating studies going back to the 1950s (e.g. Begemann and Libby, 1957; Eriksson, 1958; Dinçer et al., 1970; Stewart et al., 2007; Morgenstern et al., 2010; Duvert et al., 2016; Gallart et al., 2016; Rank et al., 2018; Visser et al., 2019), water age can be estimated with radioactive tracers based on the level of radioactive decay experienced by precipitation input signals experience before they reach the stream. Stewart et al. (2010), Stewart et al. (2012) argued that water older than that remains hidden to stable water isotopes and other seasonally variable tracers, which inevitably results in a misleading truncation of water age distributions and further argue that the use of radioactive tracers, such as ^3H , can largely avoid the truncation of the long tails of TTDs. There are only a few studies that have directly and systematically compared estimates of water age derived from both, seasonally variable (^2H , ^{18}O) and radioactive tracers (^3H) at the same study site and based on (at least partly) comparable model approaches (Małoszewski et al., 1983; Uhlenbrook et al., 2002; Stewart et al., 2007; Stewart and Thomas, 2008). However, a recent study by Rodriguez et al. (2021) indicated that their results cast some doubt on “[...] the perception that stable isotopes systematically truncate the tails of TTDs” (Rodriguez et al., 2021). However, their interpretation was questioned by Stewart et al. (2021), who pointed out that simply no older water may be present in their study catchment.

1.2.3 TRANSPORT MODELLING

Over the past decades a wide spectrum of transport models for estimating water age distributions has been developed. Early approaches often relied on simple lumped sine-wave (hereafter: SW) or lumped parameter convolution integral models (hereafter CO; Małoszewski and Zuber, 1982; Małoszewski et al., 1983; McGuire and McDonnell, 2006), originally developed for aquifers. In spite of their wide-spread application, these models feature multiple critical simplifying assumptions. Most importantly, the vast majority of these model implementations work under the assumption that water storage in catchments is at steady state and that, as a consequence, TTDs are time-invariant and can be a priori defined or calibrated. While the role of storage as first order control on water ages was described early in the general definition of mean turnover times (e.g. Eriksson, 1958; Bolin and Rodhe, 1973; Nir, 1973), the steady state assumption, i.e. constant storage, may have limited effect on TTDs in aquifers, as the fraction of transient water volumes in such systems is typically rather low. However, given the temporal variability in the hydro-meteorological system drivers (e.g. precipitation, atmospheric water demand) and the spatial heterogeneity in near-surface hydrological processes, this assumption is violated in most surface water systems world-wide and can lead to misinterpretations of the model results. This triggered the development of a more coherent framework to estimate water age distributions without the need of an a priori definition of time-invariant TTDs. Instead, probability distributions, referred to as StorAge Selection (SAS) functions, are a priori defined or calibrated, and changes in

water storage are explicitly accounted for. Thus, water fluxes within and released from the system are sampled from water volumes of different ages stored in the system according to these SAS functions (Botter et al., 2011; Rinaldo et al., 2015). The general concept is firmly rooted in the development of hydro-chemical routing schemes for the Birkenes, HBV or similar models going back to at least the 1970s (e.g. Lundquist, 1977; Christophersen and Wright, 1981; Christophersen et al., 1982; Seip et al., 1985; De Grosbois et al., 1988b; Hooper et al., 1988; Barnes and Bonell, 1996), as illustrated by Figure 1 in Bergström et al. (1985). Although functionally very similar to CO model implementations that allow for transient, i.e. time-variant TTDs (Nir, 1973; Niemi, 1977), the sampling procedure based on SAS functions has the advantage to explicitly track the history of water (and tracer) input to and output from the system through the water age balance. As such, it does explicitly account for non-steady state conditions, which in turn leads to the emergence of time-variable TTDs and RTDs (see review Benettin et al., 2022).

1.3 RESEARCH OBJECTIVE

To improve our understanding of the long-term hydrological response and transport dynamics in response to climatic variability in the Neckar basin, we benefit from the long-term hydrometeorological data and tracer data, with a tracer-aided semi-distributed hydrological model, to quantify the effects of climatic changing on hydrological response through vegetation adaptations and on transport dynamics through temporal evolution of water ages. Specifically, the following objectives were addressed:

1. to quantify the multi-decadal fluctuation of catchment-scale root zone storage capacity following the notion that vegetation, i.e. individual plants but also the species composition of plant communities, continuously adapts to climatic conditions;
2. to determine the effects of a time-dynamic implementation of root zone storage capacity on the long-term partitioning of drainage and evaporation, and the representation of streamflow in a hydrological model;
3. to explore how different factors contribute to the apparent underestimation of water ages by water stable isotopes compared with tritium using long-term data, including potential effects of uncertainties arising from short data records, spatial aggregation and the use of oversimplified time-invariant, lumped models;
4. to quantify the variability in water ages as well as to identify the associated dominant controls across time-scales from daily to multi-decadal and to analyze the associated temporal evolution of water ages for streamflow and evaporation.

1.4 RESEARCH OUTLINE

Following the introduction, the rest of this thesis is structured as follows:

Chapter 2 presents the data for the case study river basin used in this thesis, i.e. the Neckar river basin in Germany, and details the semi-distributed, process-based

hydrological model for this basin based on the flexible DYNAMITE modular modelling framework.

Chapters 3, 4, and 5 use the data and hydrological model from Chapter 2 to investigate effects of climatic variability from three perspectives.

In Chapter 3, this model is used to quantify multi-decadal fluctuation of catchment-scale root zone storage capacity following vegetation adaptation to climatic conditions. From that, the effects of a time-dynamic implementation of root zone storage capacity on the long-term partitioning of drainage and evaporation, and the representation of streamflow in a hydrological model in the Neckar River basin is analyzed.

In environmental sciences, stable isotopes ($\delta^{18}\text{O}$) and tritium (^3H) are frequently utilized as tracers to estimate the water age distributions. However, it has been argued that seasonally variable tracers, such as $\delta^{18}\text{O}$, generally and systematically fail to detect the tails of water age distributions. Consequently, these kinds of tracers substantially underestimate water ages compared to radioactive tracers like ^3H . In Chapter 4, several unresolved questions of how different factors may or may not contribute to the apparent underestimation of water ages by seasonally variable tracers are explored, including potential effects of uncertainties arising from short data records, spatial aggregation and the use of oversimplified time-invariant, lumped models.

The temporal dynamics of water ages provide crucial insights into hydrological processes and transport mechanisms, yet there remains a significant gap in quantifying water age variability across different temporal scales. In Chapter 5, a comprehensive dataset spanning 70 years of hydrological observations and tritium records with the developed semi-distributed hydrological model with an integrated tracer routing routine based on StorageAge Selection functions, is used to quantify the temporal variability in water ages as well as to identify their dominant controls across time-scales from daily to multi-decadal and to analyze the associated temporal evolution of water ages for streamflow and evaporation.

Finally, Chapter 6 provides a synthesis, including a summary of the main findings, and discusses limitations and opportunities for further research.

2

DEVELOPMENT OF A HYDROLOGICAL MODEL FOR THE NECKAR BASIN

Water is the driving force of all nature.

Leena Arif

This chapter is partly based on:

Wang, S. et al. “Stable water isotopes and tritium tracers tell the same tale: no evidence for underestimation of catchment transit times inferred by stable isotopes in StorAge Selection (SAS)-function models”. In: *Hydrology and Earth System Sciences* 27.16 (2023), pp. 3083–3114. ISSN: 1607-7938. DOI: [10.5194/hess-27-3083-2023](https://doi.org/10.5194/hess-27-3083-2023).

Wang, S. et al. “Multi-decadal fluctuations in root zone storage capacity through vegetation adaptation to hydro-climatic variability has minor effects on the hydrological response in the Neckar basin, Germany”. In: *Hydrology and Earth System Sciences* 28.17 (2024), pp. 4011–4033. ISSN: 1812-2116. DOI: [10.5194/hess-28-4011-2024](https://doi.org/10.5194/hess-28-4011-2024).

Wang, S. et al. “Multi-decadal stability of water ages and tracer transport in a temperate-humid river basin”. In: *Environmental Research letters* (2024). Under review.

2.1 THE NECKAR BASIN

THE Neckar basin, located in South-West Germany, is used as case study in this thesis. Due to its ecological and landscape diversity, the Neckar basin is important in various aspects including freshwater resources, agriculture, hydropower, recreation, industry and urban development. And a unique long-term comprehensive data sets in this basin, including not only hydrometeorological data but also tracer data, provides a potential opportunity to improve our understanding of the effects of climatic changes on hydrological response and physical transport dynamics.

2.1.1 LANDSCAPE

The Neckar River basin covers an area of $\sim 13,000 \text{ km}^2$ in Southwestern Germany, with a varying topography with the elevation ranging from 122 m at the outlet in the north to about 1019 m in the South (Fig. 2.1a; Table 2.1). Following the elevation gradient, the landscape is remarkably diverse with the Black Forest in the western part, the Swabian Jura in the middle regions, and the northern regions (Fig. 2.1c). Specifically, Black Forest is the location where the Neckar river originates, dominated by increasingly steep and narrow dense coniferous forested valleys towards the southern parts, and the soils are coarse-textured and well drained. Swabian Jura is characterized by terrace-like elements and undulating hills with wide valleys used as grass- and croplands in lower regions, mainly with the loamy and loess soils. And there are mainly vineyards, orchards, and croplands in the northern region, with flat grassland in river valley bottoms, dominated by alluvial, loamy and sandy loam soils.

2.1.2 CLIMATE

The Neckar basin is characterized by a temperate-humid climate, with warm, moderately wet summers and cold winters. The streamflow is affected by precipitation patterns, presenting a remarkable seasonal variation with lower flows in summer and high lows in winter. Briefly, the snowmelt from Black Forest and rainfall in spring and early summer causes higher streamflow, however, less rainfall and higher evaporation rate make the streamflow decreased in summer, with short-time increases due to summer storms. Therefore, the streamflow seasonal characteristics reflects the seasonality of potential evaporation. The Neckar basin exhibits an obvious precipitation gradient from the high region Black Forest to lower region in the north part. Annual mean precipitation (P) over the whole river basin has a considerable spatial heterogeneity ranging from $\sim 660 \text{ mm yr}^{-1}$ in the lower parts of the basin to $\sim 1600 \text{ mm yr}^{-1}$ over the Black Forest with catchment average long-term mean precipitation (P) reaching $\sim 909 \text{ mm yr}^{-1}$ (Fig. 2.1b, Table 2.1). Precipitation exhibits some seasonality with $\sim 500 \text{ mm yr}^{-1}$ for summer months (from May to October) and $\sim 380 \text{ mm yr}^{-1}$ for winter months (from November to April), respectively. Although snow is in general not a major component of precipitation in the study region, snowmelt can have a significant influence during individual storm events. The long-term mean temperature is about 8.9°C and potential evaporation (E_p) is around $\sim 870 \text{ mm yr}^{-1}$ with a runoff ratio $C_r = Q/P \sim 0.43$ and an aridity index $I_A = E_p/P \sim 0.98$.

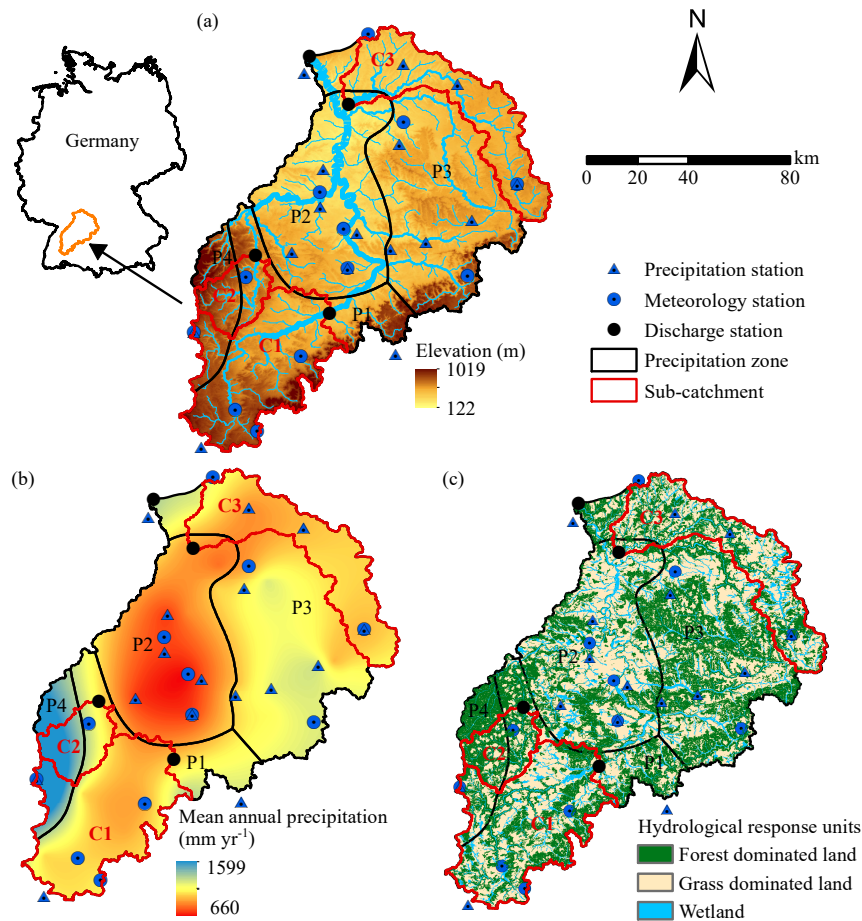


Figure 2.1: (a) Elevation of the Neckar catchment with discharge and hydro-meteorological stations as well as the water sampling locations used in this study, (b) the spatial distribution of long-term mean annual precipitation in the Neckar catchment and the stratification into four distinct precipitation zones P1 – P4 (black line), (c) hydrological response units classified according to their land-cover and topographic characteristics.

Table 2.1: Characteristics of the Neckar catchment in Germany

Characteristics	
latitude (N)	48°2'0" - 49°33'45"
longitude (E)	8°18'45" - 10°18'45"
Area (km ²)	13,041
Average annual precipitation (mm yr ⁻¹)	909
Average annual temperature (°C)	8.9
Aridity index (-)	0.98
Elevation range (m)	122-1019
Mean elevation (m)	569
Slope range (°)	0-53
Mean slope (°)	5.1
Forest dominated land (%)	38.1
Grass dominated land (%)	51.2
Wetland (%)	10.7

2.2 HYDROLOGICAL MODEL

2.2.1 IDENTIFICATION OF PRECIPITATION ZONES

To account in the subsequent model applications, at least to some degree, for spatial heterogeneity in precipitation, the Neckar River basin is stratified into precipitation zones that each are characterized by distinct long-term average annual precipitation totals based on several precipitation stations which is described briefly in the following chapters individually. Goovaerts (2000) and Lloyd (2005) showed that areal precipitation estimates informed by elevation data were often more accurate than those based on precipitation gauge observations alone. Thus, to interpolate and to estimate areal precipitation across the basin we used Co-Kriging, considering elevation, as a preliminary analysis suggested lower errors. Finally, the individual precipitation estimates for each grid cell were used with K-means clustering to establish four clusters, representing the four precipitation zones P1 – P4 (see Fig. 2.1b).

2.2.2 CLASSIFICATION OF LANDSCAPE

To distinguish different hydrological response dynamics associated with different observed landscape units, the height above the nearest drainage (HAND; Gharari et al., 2011), slope and land use datasets (<https://land.copernicus.eu/pan-european/corine-land-cover>) were used for deriving a hydrologically meaningful landscape classification. The landscape units for the Neckar basin have been classified into wetland with HAND ≤ 5 m and slope $\leq 10\%$, forest-dominated land with slope $> 10\%$ and dominated with forest, and grass dominated land for the rest of the landscape elements (Fig. 2.1c). For this purpose, the 90 m \times 90 m digital elevation model of this basin (Fig. 2.1a) was obtained from the HDMA database of the USGS (Verdin, 2017; <https://doi.org/10.5066/F7S180ZP>) and used to derive the local topographic indices including HAND and slope. According to this classification, the wetland areas cover 10.7%, forest-dominated areas cover 38.1% and grass dominated areas cover 51.2% (Fig. 2.1c; Table 2.1).

2.2.3 MODEL STRUCTURE

Loosely based on the flexible DYNAMITE modular modelling framework (e.g. Hrachowitz et al., 2014), we here developed a semi-distributed, process-based model. Similar versions of that model, have previously been successfully implemented and tested for many other contrasting environments world-wide (e.g. Prenner et al., 2018; Hulsman et al., 2021a, Hulsman et al., 2021c; Hanus et al., 2021; Bouaziz et al., 2022). Briefly, this hydrological model consists of a suite of storage components and associated water fluxes between them. The influence of functionally different landscape elements, i.e. forest, grass-/cropland and flat valley bottoms, for brevity hereafter referred to as wetland, is represented by parallel hydrological response units (HRU), linked by a common storage component representing the groundwater system (Fig. 2.2), as previously implemented and successfully tested in many contrasting environments (e.g. Gao et al., 2014a; Gharari et al., 2014; Euser et al., 2015; Nijzink et al., 2016b; Prenner et al., 2018; Hanus et al., 2021). Briefly, precipitation P (mm d^{-1}) falling on days with temperatures below threshold temperature T_t ($^{\circ}\text{C}$), is accumulated as snow P_{snow} (mm d^{-1}) in the snow storage S_{snow} (mm). On days with temperatures higher than that, precipitation enters the system as rainfall P_{rain} (mm d^{-1}) and, based on a simple degree-day approach, water is released from S_{snow} as snow melt M_{snow} (mm d^{-1}), controlled by melt factor C_{melt} ($\text{mm d}^{-1} ^{\circ}\text{C}^{-1}$; e.g. Gao et al., 2017; Giron Lopez et al., 2020). Rain water is then routed through the interception storage S_i (mm). With E_i (mm d^{-1}) as interception evaporation at the potential evaporation rate, effective precipitation P_{re} (mm d^{-1}) generated by overflow once the maximum interception capacity (S_{imax}) is exceeded, together with M_{snow} , enters the unsaturated root-zone S_u (mm). From S_u water can then be released as vapor via a combined soil evaporation and transpiration flux E_a (mm d^{-1}). Drainage of liquid water from S_u can either recharge the groundwater S_s (mm) over a percolation flux R_{perc} (mm d^{-1}) and a faster preferential recharge R_{pref} (mm d^{-1}). Alternatively, it can be routed via R_{uf} (mm d^{-1}) to a faster responding component S_f (mm) from where it is directly released to the stream as Q_f (mm d^{-1}), representing lateral preferential flow. Rain and snow melt entering the wetland HRU directly reach S_u . Soil moisture levels in the wetland S_u are further sustained by a fraction of groundwater R_{cap} (mm d^{-1}) that is upwelling into S_u from S_s (e.g., Hulsman et al., 2021a). The detailed equations of the model are provided as Table 2.2.

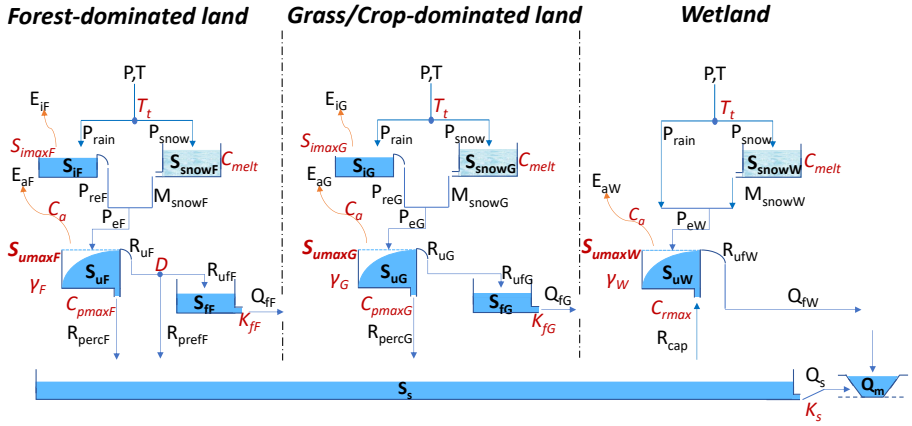


Figure 2.2: Model structure of the integrated model, discretized into three parallel hydrological response units HRU, i.e. forest, grassland and wetland in each precipitation zone P1 – P4. The light blue boxes indicate the hydrologically active individual storage volumes. The arrow lines indicate water fluxes and model parameters are shown in red. All symbols are described in Table 2.3.

Table 2.2: Water balance and constitutive equations of the semi-distributed hydrological model in Chapters 3, 4, and 5

Reservoirs	Water balance	Constitutive equations
Interception	$\frac{ds_i}{dt} = P_{rain} - E_i - P_{re}$ (2.1)	$P_{rain} = P$, when $T > T_i$ (2.2) $E_i = \min(E_p, S_i/dt)$ (2.3) $P_{re} = \max((S_i - S_{imax}/dt, 0))$ (2.4)
Snow	$\frac{ds_{snow}}{dt} = P_{snow} - M_{snow}$ (2.5)	$P_{snow,e} = P$, when $T > T_i$ (2.6) $P_{snow} = \sum P_{snow,e} \cdot W_e$ (2.7) $M_{snow,e} = \min(C_{melt} \cdot (T_e - T_i), S_{snow,e}/dt)$, when $T_e > T_i$ (2.8) $M_{snow} = \sum M_{snow,e} \cdot W_e$ (2.9) $P_e = P_{re} + M_{snow}$ (2.11) $\rho = S_u/S_{umax}$ (2.12) $E_a = (E_p - E_i) \cdot \min(\rho/C_a, 1)$ (2.13) $C_r = 1 - (1 - \rho)^r$ (2.14) $R_u = (1 - C_r) \cdot P_e$ (2.16) $R_{perc} = \min(c_{pmax} \cdot \rho, S_u/dt)$ (2.17) $R_{cap} = \min(c_{pmax} \cdot (1 - \rho), \frac{S_s}{dt} \cdot P_{RHU})$ (2.18) $R_{pref} = (1 - D) \cdot R_u$ (2.19)
Unsaturated reservoir		
	Forest/grass: $\frac{ds_u}{dt} = P_e - E_a - R_u - R_{perc}$ (2.10)	
	Wetland: $\frac{ds_u}{dt} = P_e - E_a - R_u + R_{cap}$ (2.15)	
Fast reservoir	$\frac{ds_f}{dt} = R_f - Q_f$ (2.20)	Forest/grass: $R_f = D * R_u$ (2.21) Wetland: $R_f = D \cdot R_u$ (2.22) $Q_f = K_f \cdot S_f$ (2.23)
Slow reservoir	$\frac{ds_s}{dt} = R_{perc} + R_{pref} - R_{captot} - Q_s$ (2.24)	$R_{perc} = \sum R_{perc} \cdot P_{RHU}$ (2.25) $R_{pref} = \sum R_{pref} \cdot P_{RHU}$ (2.26) $R_{captot} = \sum R_{cap} \cdot P_{RHU}$ (2.27) $Q_s = K_s \cdot S_s$ (2.28)

Table 2.3: The model parameters and their constraints and prior bounds used in the multi-objective calibration method in Chapters 3, 4, and 5.

Parameters	Unit	Description	Constraints	Prior bounds	References
T_l	°C	Threshold temperature to split snowfall and rainfall		-2.5-2.5	(Gao et al., 2014a; Hrachowitz et al., 2013)
Global					
C_{melt}	mm °C ⁻¹ d ⁻¹	Melt factor		1-5	Prenner et al., 2018
C_a	-	Evapotranspiration coefficient		0.1-0.7	Gao et al., 2017
K_s	d ⁻¹	Recession coefficient of slow response reservoir		0.002-0.2	Prenner et al., 2018
S_{sp}	mm	Passive storage Volume		100-20000	Wang et al., 2023
Forest					
S_{maxF}	mm	Interception capacity	$S_{maxF} > S_{maxG}$	0.1-5	Gao et al., 2014a
S_{umaxF}	mm	Root zone storage capacity	$S_{umaxF} > S_{umaxG}$	50-200	Gao et al., 2014a
Y_F	-	Shape parameter		0.1-5	Gao et al., 2014a
D	-	Splitter to fast and slow response reservoirs		0-1	Gao et al., 2014a
Grassland					
c_{pmaxF}	mm d ⁻¹	Percolation capacity		0.1-4	Prenner et al., 2018
K_{FF}	d ⁻¹	Recession coefficient of fast response reservoir	$K_{FF} > K_s$	0.2-5	Hrachowitz et al., 2013
Wetland					
S_{umaxW}	mm	Root zone storage capacity	$S_{umaxW} < S_{umaxG}$	50-200	Gao et al., 2014a
Y_W	-	Shape parameter		0.1-5	Gao et al., 2014a
c_{j-max}	mm d ⁻¹	Percolation capacity		0.1-4	Gao et al., 2014a

To balance the need for spatial detail to some extent with the adverse effects of increased parameter uncertainty (e.g. Beven, 2006) and computational capacity, we here implemented the hydrological model in parallel in the four precipitation zones P1 – P4 and forced it with the corresponding input (e.g. P, tracers) for each precipitation zone as described in section 2.2.1. Each precipitation zone was further discretized (1) into 100 m elevation zones for a stratified representation of the snow storage S_{snow} (e.g. Mostbauer et al., 2018) and (2) into three HRUs, i.e., forest, grassland, wetland as described in section 2.2.2 (Fig. 2.2; e.g. Gharari et al., 2014; Hanus et al., 2021). Rain P_{rain} and melt water M_{snow} from the different elevation zones was aggregated according to their associated spatial weights in each elevation zone. This total liquid water input was then routed through the three parallel HRUs. In total, there are therefore 12 individual, parallel model components, i.e., three HRUs in each of the four precipitation zones, not counting the elevation zones for the snow module. All flux and storage variables of the 12 components are weighted according to their areal fractions. While each of the three HRUs was characterized by individual parameters (e.g. Gao et al., 2016; Prenner et al., 2018), the same parameter values were used in all four precipitation zones in distributed moisture accounting approach (e.g. Ajami et al., 2004; Euser et al., 2015; Hulsman et al., 2021b; Roodari et al., 2021). Overall, the spatially distributed implementation has 19 model parameters, including five global parameters (T_t , C_{melt} , C_a , K_s and $S_{s,p}$) that are identical for each HRU and 14 HRU-specific parameters (Table 2.3; Fig. 2.2).

VEGETATION ADAPTATION TO CLIMATIC VARIABILITY: TESTING THE EFFECTS OF TEMPORAL EVOLUTION OF ROOT ZONE STORAGE CAPACITY ON LONG-TERM HYDROLOGICAL RESPONSE

A tree with strong roots laughs at storms.

Malay Proverb

This chapter is based on:

Wang, S. et al. "Multi-decadal fluctuations in root zone storage capacity through vegetation adaptation to hydro-climatic variability has minor effects on the hydrological response in the Neckar basin, Germany". In: *Hydrology and Earth System Sciences* 28.17 (2024), pp. 4011–4033. ISSN: 1812-2116. DOI: [10.5194/hess-28-4011-2024](https://doi.org/10.5194/hess-28-4011-2024).

SUMMARY

Climatic variability can considerably affect the catchment-scale root zone storage capacity (S_{umax}) which is a critical factor regulating latent heat fluxes and thus the moisture exchange between land and atmosphere as well as the hydrological response and biogeochemical processes in terrestrial hydrological systems. However, direct quantification of changes in S_{umax} over long time periods and the mechanistic drivers thereof at the catchment-scale are missing so far. As a consequence, it remains unclear how climatic variability, such as precipitation regime or canopy water demand, affects S_{umax} and how fluctuations in S_{umax} may influence the partitioning of water fluxes and therefore, also affect the hydrological response at the catchment-scale. Based on long-term daily hydrological records (1953-2022) in the Upper Neckar river basin in Germany, it was found that variability in hydroclimatic conditions, with aridity index I_A (i.e. E_p/P) ranging between ~ 0.9 and 1.1 over multiple consecutive 20-year periods was accompanied by deviations ΔI_E between -0.02 and 0.01 from the expected I_E inferred from the long-term parametric Budyko curve. Similarly, fluctuations in S_{umax} , ranging between ~ 95 and 115 mm or $\sim 20\%$, were observed over the same time period. While uncorrelated with long-term mean precipitation and potential evaporation, it was shown that the magnitude of S_{umax} is controlled by the ratio of winter over summer precipitation ($p < 0.05$). In other words, S_{umax} in this basin does not depend on the overall wetness condition as for example expressed by I_A , but rather on how water supply by precipitation is distributed over the year. However, fluctuations in S_{umax} were found to be uncorrelated with observed changes in ΔI_E . Consequently, replacing a long-term average, time-invariant estimate of S_{umax} with a time-variable, dynamically changing formulation of that parameter in a hydrological model did not result in an improved representation of the long-term partitioning of water fluxes, as expressed by I_E (and fluctuations ΔI_E thereof), nor in an improved representation of the shorter-term response dynamics.

Overall, this chapter provides quantitative mechanistic evidence that S_{umax} significantly changes over multiple decades reflecting vegetation adaptation to climatic variability. However, this temporal evolution of S_{umax} cannot explain long-term fluctuations in the partitioning of water (and thus latent heat) fluxes as expressed by deviations ΔI_E from the parametric Budyko curve over multiple time periods with different climatic conditions. Similarly, it does not have any significant effects on shorter term hydrological response characteristics of the upper Neckar catchment. This further suggests that accounting for temporal evolution of S_{umax} with a time-variable formulation of that parameter in a hydrological model does not improve its ability to reproduce the hydrological response and may therefore be of minor importance to predict the effects of a changing climate on the hydrological response in the study region over the next decades to come.

3.1 INTRODUCTION

VEGETATION is a key component of the terrestrial hydrological cycle as it shapes the hydrological functioning of catchments by regulating the long-term average partitioning of water into drainage and evaporative fluxes (i.e. latent heat), frequently expressed as runoff ratio $C_r = Q/P$ [-] and evaporative index $I_E = 1 - Q/P = E_A/P$ [-], respectively. More specifically, vegetation transpiration, that in spite of uncertainties (Coenders-Gerrits et al., 2014) globally constitutes the largest fraction of all evaporative fluxes (Jasechko, 2018), is systematically controlled by the interplay between canopy water demand and water supply from the subsurface (Donohue et al., 2007; Yang et al., 2016; Jaramillo et al., 2018; Mianabadi et al., 2019). To survive, vegetation needs continuous access to water stored in the subsurface and accessible to roots to satisfy its canopy water demand. As a consequence, the vegetation present at any moment, and in particular its active root system, reflects its successful adaptation to the prevalent climatic conditions in a region (Laio et al., 2001; Schenk and Jackson, 2002; Rodríguez-Iturbe and Porporato, 2007; Donohue et al., 2007; Gentile et al., 2012; Liancourt et al., 2012). Irrespective of geometry, distribution or structure of root systems, the maximum vegetation-accessible water storage volume in the unsaturated root zone of the subsurface, hereafter referred to as root zone storage capacity S_{umax} [mm], represents the hydrologically relevant information of root systems (Rodríguez-Iturbe and Porporato, 2007; Nijzink et al., 2016a; Savenije and Hrachowitz, 2017; Gao et al., 2024). Therefore, the S_{umax} directly reflects the hydrologically relevant information of root-systems at the catchment-scales. In response to a changing environment, these root systems of vegetation continuously adapt to allow the most efficient use of available energy and resources for surviving. The driving factors of changes in root systems are thus also the driving factors for changes in S_{umax} , as S_{umax} inherently represents adaptations of the root system.

As a central part of hydrological systems, S_{umax} is also a critical parameter in hydrological and land-surface models. As such, it can, in principle, be estimated as a function of root depths and the subsurface pore volume between field capacity and permanent wilting point (Scrivner and Ruppert, 1970; Sivandran and Bras, 2012, 2013). However, these data are typically not available at sufficient levels of detail. Alternatively, catchment-scale S_{umax} can be estimated by three broad approaches. Firstly, it can be obtained by calibration as parameter of a hydrological model (Nijzink et al., 2018; Bouaziz et al., 2020; Wang et al., 2023; Sriwongsitanon et al., 2023; Roberts et al., 2021; Bahremand and Hosseinalizadeh, 2022; Sadayappan et al., 2023; Tong et al., 2022). Secondly, based on optimality principles, there are some variables like transpiration, nitrogen uptake or carbon gain that can be maximized to quantify S_{umax} (Guswa, 2008; McMurtrie et al., 2012; Sivandran and Bras, 2012; Yang et al., 2016; Speich et al., 2018). Thirdly, S_{umax} can be robustly estimated at the catchment scale directly from annual water deficits based on observed hydro-climatic data, i.e. precipitation and transpiration (e.g., Donohue et al., 2012; Gentile et al., 2012; Gao et al., 2014a; De Boer-Euser et al., 2016; Nijzink et al., 2016a; Dralle et al., 2021; McCormick et al., 2021; Hrachowitz et al., 2021; Stocker et al., 2023; Van Oorschot et al., 2021; Van Oorschot et al., 2024). For applications of hydrological and land-surface models S_{umax} (or equivalent parameters) has, except for very few exceptions (Wagener et al., 2003; Merz et al., 2011; Bouaziz

et al., 2022; Tempel et al., 2024) been assumed constant over time. As a major knowledge gap, it remains so far unknown if S_{umax} follows climatic variability and evolves over time, thereby reflecting vegetation adaptation to changing conditions.

In contrast, it is well understood that, due to the importance of vegetation for the hydrological functioning of terrestrial systems, anthropogenic land use management practices, such as de- and afforestation (Brown et al., 2005; Brath et al., 2006; Fenicia et al., 2009; Alila et al., 2009; Jaramillo et al., 2018; Teuling et al., 2019; Stephens et al., 2021; Hoek van Dijke et al., 2022; Ellison et al., 2024) or irrigation (e.g. AghaKouchak et al., 2015; Van Loon et al., 2016; Roodari et al., 2021) can induce major shifts in the partitioning between the major components of the terrestrial water and energy cycles, and thus between I_E and C_r . Two detailed recent studies with well documented information on deforestation in several experimental catchments could establish explicit mechanistic links between the reduction of S_{umax} by > 50% following deforestation and decreases in I_E (and thus increases in C_r) from $\sim 0.4 - 0.5$ to $\sim 0.1 - 0.3$, depending on the catchment and the scale of deforestation (Nijzink et al., 2016a; Hrachowitz et al., 2021).

Mapping the shifts to lower I_E that followed these land conversions from forest to grass- and rangeland type vegetation as a function of the aridity index $I_A = E_p/P$ in the Budyko framework (Schreiber, 1904; Ol'Dekop, 1911; Budyko, 1974) corresponds well to the results of previous studies that suggest that, across the world, catchments dominated by grass exhibit consistently lower I_E at the same I_A than forest environments (e.g. Zhang et al., 2001; Zhang et al., 2004a; Oudin et al., 2008). These differences in long-term average I_E are accounted for by parametric reformulations of the Budyko framework, such as the Tixeront-Fu equation (Tixeront, 1964; Fu, 1981). The lumped parameters (here: ω) of these expressions define long-term average catchment-specific positions in the $I_A - I_E$ space. As such, the parameters are typically interpreted to encapsulate vegetation characteristics and all other hydro-climatic and physiographic properties of individual catchments besides I_A (e.g. Roderick and Farquhar, 2011; Berghuijs and Woods, 2015). A frequent assumption is that with changes in climatic conditions, here represented by I_A , individual catchments can be expected to move to the associated new positions I_E , following their specific trajectories defined by ω (e.g. Zhou et al., 2015; Bouaziz et al., 2022). However, several studies have demonstrated that catchments in many regions world-wide experience deviations ΔI_E from their expected new I_E following a change in I_A (e.g. Jaramillo and Destouni, 2014; Van der Velde et al., 2014; Jaramillo et al., 2018; Reaver et al., 2022; Ibrahim et al., 2024; Tempel et al., 2024).

From the above the following questions arise: (1) following the notion that vegetation, i.e. individual plants but also the species composition of plant communities, continuously adapts to climatic conditions, does catchment-scale root zone storage capacity S_{umax} change over multi-decadal time scales? (2) do multi-decadal changes in the vegetation response, expressed by changes in S_{umax} , explain deviations ΔI_E from expected I_E ? (3) does a time-variable representation of S_{umax} as parameter in a hydrological model improve the models' ability to reproduce the hydrological response?

Building on previous studies, the objectives of this chapter are therefore to provide an analysis of multi-decadal changes in S_{umax} as a result of changing climatic conditions

over a 70-year period (1953 – 2022), and how this further affects hydrological dynamics. More specifically, three hypotheses are tested: (1) S_{umax} significantly changes over multiple decades reflecting vegetation adaptation to climatic variability, (2) changes in S_{umax} affect the long-term partitioning of drainage and evaporation and thus control deviations ΔI_E from the catchment-specific trajectory in the Budyko space and (3) a time-dynamic implementation of S_{umax} improves the representation of streamflow in a hydrological model.

3.2 STUDY AREA

The hypotheses are tested in the Upper Neckar basin in South-West Germany (Fig. 3.1), due to availability of the essential long-term hydrometeorological data. Covering an area of $\sim 4000 \text{ km}^2$, this basin is upper part of the entire Neckar basin described in Chapter 2, with the similar landscape composition and similar climatic characteristics (Table 3.1). This basin is characterized by a temperate-humid climate, with warm, wet summers (from May to October) and cold, drier winters (from November to April), more detailed climatic information is described in Table 3.2.

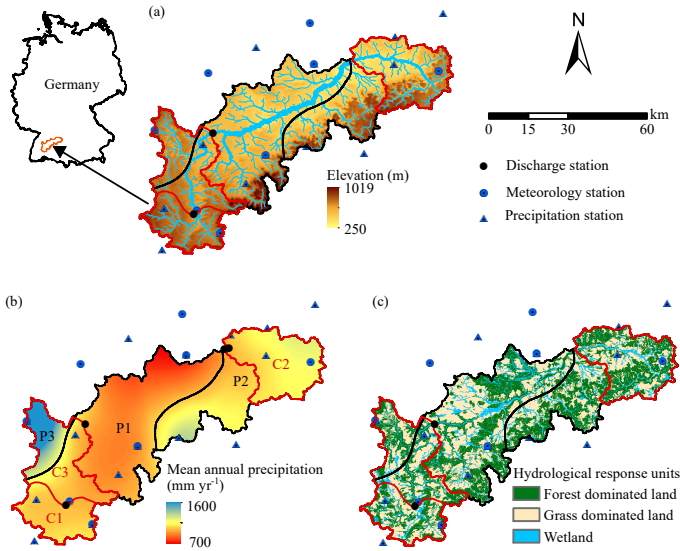


Figure 3.1: (a) Elevation of the Neckar catchment with discharge and hydro-meteorological stations as well as the water sampling locations used in this study, (b) the spatial distribution of long-term mean annual precipitation in the upper Neckar catchment and the stratification into three distinct precipitation zones P1 – P3 (black outline), and the red outlines indicate three sub-catchments (C1: Rottweil, C2: Plochingen at Files river, and C3: Horb) within the upper Neckar basin, (c) hydrological response units classified according to their land-cover and topographic characteristics.

Table 3.1: Characteristics of the Upper Neckar catchment in Germany.

Characteristics	
Latitude (N)	48°2'0'' - 48°46'59''
Longitude (E)	8°18'45'' - 9°56'33''
Area (km ²)	3968
Average annual precipitation (mm yr ⁻¹)	880
Average annual temperature (°C)	8.39
Elevation range (m)	250-1019
Mean elevation (m)	554
Slope range (°)	0-53
Mean slope (°)	5.80
Forest dominated land (%)	39.6
Grass dominated land (%)	49.6
Wetland (%)	10.8

3.3 DATA SETS

Daily hydro-meteorological data were available for the period 01/01/1953 – 31/12/2022 (Fig. 3.2). Daily precipitation and daily mean air temperature were obtained from stations operated by the German Weather Service (DWD). Precipitation was recorded at 15 stations and temperature measurements were available at 8 stations (Fig. 3.1) in or close to the study basin. Daily potential evaporation E_p (mm d⁻¹) was estimated using the Hargreaves equation based on the observed daily maximum and minimum temperature, which has been used in many previous studies and shown to be a suitable method for modelling applications (Oudin et al., 2005). Daily mean discharge data for the period 01/01/1953 – 31/12/2022 at the outlet of the upper Neckar basin at Plochingen station were provided by the German Federal Institute of Hydrology (BfG). In addition, to test the representation ability of the hydrological model on spatial hydrological response differences, data of daily mean discharge for the same time period from three sub-catchments within the upper Neckar basin (Fig. 3.1) at the gauges Rottweil (C1; 422 km²), Plochingen at the Fils river (C2; 706 km²) and Horb (C3; 1111 km²) were available from the Environmental Agency of the Baden-Württemberg region (LUBW).

Based on the CORINE Land Cover data set of the upper Neckar river basin during the period 01/01/1953 – 31/12/2022 (<https://land.copernicus.eu/pan-european/corine-land-cover>), there is only very minor change (< 2%) for all defined land cover classes (Fig. 3.1c). The 90 m × 90 m digital elevation model of the study region (Fig. 3.1a) was obtained from the HDMA database of the USGS (Verdin, 2017; <https://doi.org/10.5066/F7S180ZP>) and used to derive the local topographic indices including height above nearest drainage (HAND) and slope.

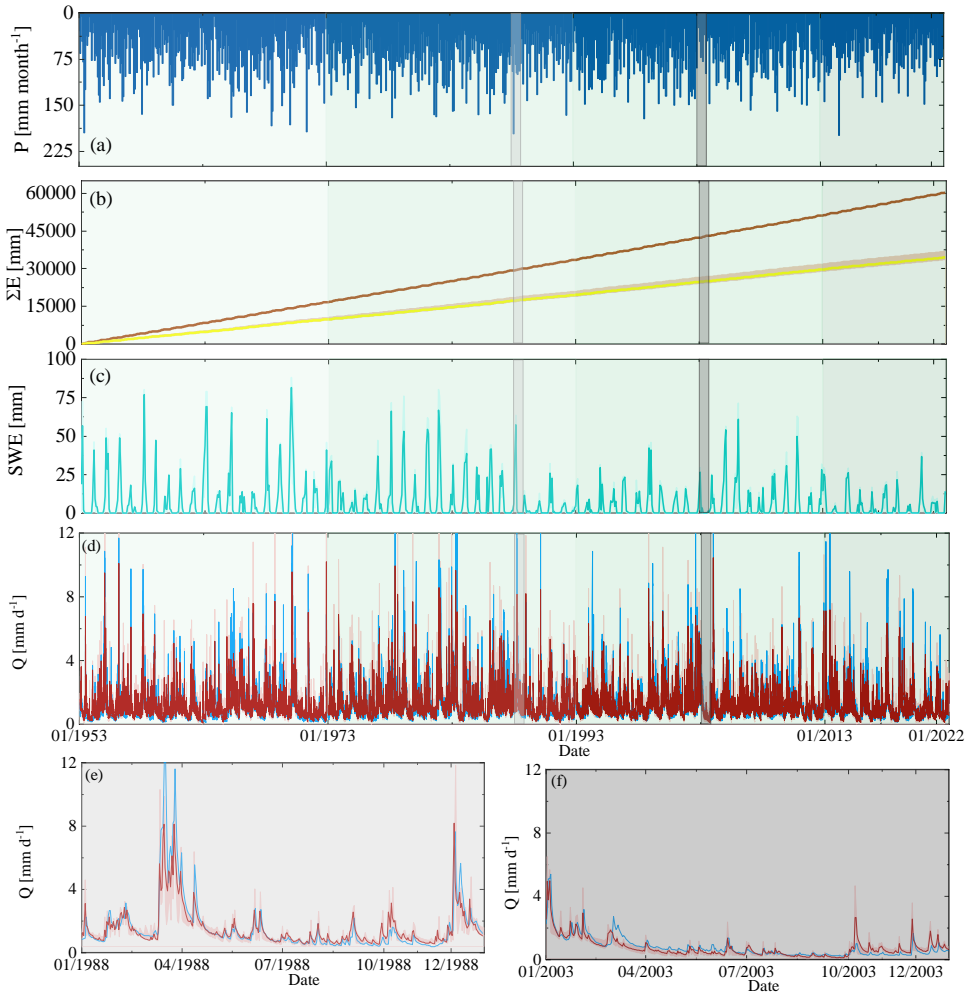


Figure 3.2: (a) Time series of observed monthly precipitation P ; (b) daily cumulative evaporative fluxes for entire time period (1953–2022), where the dark brown line indicates potential evaporation E_P and the yellow lines and the light orange shaded areas show the actual evaporation E_A modelled using the best fit parameter sets and the associated 5th/95th percentiles of all feasible solutions calibrated based on entire time period; (c) monthly maximum values of snow water equivalent (SWE) for 1953–2022 time period where green line indicates the most balanced solution and light green shade indicates the 5th/95th inter-quantile range obtained from all Pareto optimal solutions calibrated based on entire time period; (d) observed (blue line) and modelled daily streamflow Q ; red line indicates the most balanced solution and the shaded area indicates the 5th/95th percentile of all feasible solutions calibrated based on entire time period, respectively; the different green background shades from lighter to darker indicate sub-time periods from t_1 to t_4 ; (e) and (f) zoom-in to the observed and modelled streamflow for the selected wet year (light gray shade, 01/01/1988 – 31/12/1988) and dry year (gray shade, 01/01/2003 – 31/12/2003) respectively.

Table 3.2: Mean annual precipitation P , potential evaporation E_p , temperature T_M , aridity index I_A , evaporative index I_E , parameter ω for parametric Budyko framework, root zone storage capacity $S_{umax,WB}$ and $S_{umax,cal}$ based on respectively water balance data and hydrological model calibration for scenario 1 (entire time period T: 1953-2022) and scenario 2 (four sub-periods t_1 :1953-1972, t_2 :1973-1992, t_3 :1993-2012, and t_4 :2013-2022).

	Scenario 1	Scenario 2			
	T (1953-2022)	t_1 (1953-1972)	t_2 (1973-1992)	t_3 (1993-2012)	t_4 (2013-2022)
P (mm yr ⁻¹)	876	870	907	915	811
E_p (mm yr ⁻¹)	867	836	840	884	906
T_M (°C)	8.4	7.4	7.9	8.7	9.5
I_A (-)	0.97	0.96	0.93	0.97	1.12
I_E (-)	0.57	0.58	0.56	0.56	0.59
ω (-)	1.95	2.01	1.98	1.93	1.89
$S_{umax,WB}$ (mm)	105	95	115	95	100
$S_{umax,cal}$ (mm)	116	98	123	99	107

3.4 METHODS

To explore the climatic variability and the fluctuations of the key vegetation parameter, i.e. the root zone storage capacity S_{umax} over long time scales, the available data record 1953-2022 was divided into four subsequent sub-periods ($t_1 - t_4$ in Table 3.2). To be survive, root systems of vegetation and the associated vegetation-accessible water storage capacity S_{umax} respond to the ever-changing conditions of its environment. However, as these changes occur at landscape scale and are mostly reflected by changes in the composition of plant species present in a specific spatial domain, fluctuations in S_{umax} occur largely at time-scales that reflect the life-cycles of individual plants. Thus, periods of at least 20-years are required to reflect this and to allow for meaningful estimates of S_{umax} , as also demonstrated by many other studies (e.g. Gao et al., 2014c; Wang-Erlandsson et al., 2016; Singh et al., 2020; Stocker et al., 2023). Therefore, it is necessary to strike a balance between the number of independent time periods (here: $t_1 - t_4$) and the robustness of the associated S_{umax} estimates.

This chapter deliberately chose to emphasize fewer but longer time periods and thus rather reliable estimates of S_{umax} . For the main objectives of this chapter, the following stepwise approach is designed: (1) Estimate the *observed* deviations ΔI_E from the long-term average expected I_E for four consecutive periods $t_1 - t_4$ in the study period (Table 3.2), (2) Estimate the root zone storage capacity over the entire study period ($S_{umax,WB,T}$) as well as for the four individual periods $t_1 - t_4$ ($S_{umax,WB,t}$) based on observed water balance data, (3) Estimate the root zone storage capacity over the entire study period ($S_{umax,cal,T}$) and the four individual periods $t_1 - t_4$ ($S_{umax,cal,t}$) by *calibration* of a hydrological model over the respective time periods to evaluate whether the changes in calibrated $S_{umax,cal}$ reflect changes in $S_{umax,WB}$ directly estimated from water balance data from step (2), (4) Estimate the *modelled* deviations ($\Delta I_{E,mT,O}$) from expected I_E using both, a long-term average time-invariant $S_{umax,WB,T}$ and individual $S_{umax,WB,t}$ for the four periods $t_1 - t_4$ as model parameters.

3.4.1 ESTIMATION OF THE TEMPORAL TRAJECTORY IN THE BUDYKO FRAMEWORK

Mapping aridity $I_A = E_P/P$, where E_P is potential evaporation [mm d^{-1}] and P is precipitation [mm d^{-1}], against the evaporative index $I_E = E_A/P = 1 - Q/P$, where E_A is actual evaporation [mm d^{-1}] and Q is stream flow [mm d^{-1}], the Budyko framework is an expression of the long-term average water balance for a catchment. It is based on the assumption of negligible storage change over the averaging time period, i.e. $dS/dt \sim 0$. As demonstrated by Han et al. (2020), this assumption holds for averaging periods ≥ 10 years for a large majority of catchments worldwide. Note, that hereafter the term evaporation is used to refer to all combined evaporative fluxes, including interception and soil evaporation (E_i) as well as transpiration (E_T), following the terminology proposed by Savenije (2004) and Miralles et al. (2020).

The analysis in this paper is based on the parametric Tixeront-Fu formulation of the Budyko framework (Tixeront, 1964; Fu, 1981):

$$I_{E,T} = 1 + I_{A,T} - (1 + I_{A,T}^{\omega_T})^{1-\omega_T} \quad (3.1)$$

where $I_{E,T}$ is the observed evaporative index based over a chosen averaging period T , $I_{A,T}$ is the observed aridity index over the same period and ω_T is the associated catchment-specific parameter that represents all combined catchment properties other than I_A .

In a theoretical catchment that only experiences changes in I_A and no changes in any other hydro-climatic and/or physical catchment characteristics, it can be assumed that ω_T remains constant over time so that $\omega_T = \omega_{t_i} = \omega_{t_{i+1}}$. This implies that following a disturbance ΔI_A in a subsequent time period t_{i+1} the catchment stays on its specific curve defined by ω_T , to a new $I_{E,t_{i+1}}$. In such a case, ω_T can thus be used to predict future hydrological partitioning I_E . Based on this assumption, the complete available hydro-climatic data record is used to estimate the long-term average ω_{OT} as reference over the entire 1953 – 2022 study period. The sub-division into the four time periods $t_1 - t_4$: as shown in Table 3.2, then allowed to estimate the expected I_{E,t'_i} in the individual periods $t_1 - t_4$: depending on the shift in the observed aridity index along the x-axis in t_i ($\Delta I_{A,T,t_i} = I_{A,t_i} - I_{A,T}$), a catchment will move along its parametric Budyko curve defined by ω_{OT} to a new expected position I_{E,t'_i} (Fig. 3.3).

Based on the available data we then estimate the individual observed I_{E,t_i} together with the associated ω_{t_i} for each of the four time periods $t_1 - t_4$ (Fig. 3.4). For each of the four time periods $t_1 - t_4$ the deviation of I_{E,t_i} from the catchment-specific expected I_{E,t'_i} , corresponding to a shift from ω_T to $\omega_{t_i} \neq \omega_T$ was then computed as $\Delta I_{E,t_i,t'_i} = I_{E,t_i} - I_{E,t'_i}$.

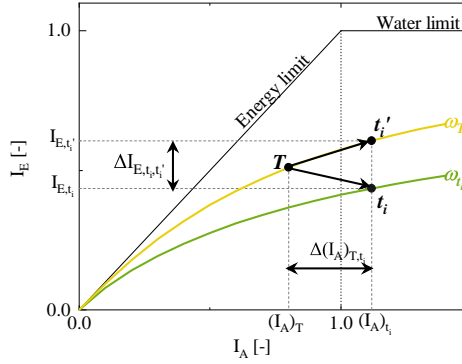


Figure 3.3: Representation of the Budyko space, which shows the evaporative index ($I_E = 1 - Q/P$) as a function of the aridity index ($I_A = E_p/P$) and the water and energy limit. A catchment with the long term mean aridity index $I_{A,T} = E_{p,T}/P_T$ and evaporative index $I_{E,T} = 1 - Q_T/P_T$, which is derived from observed entire-time-period data, plots at location T on the parametric Budyko curve with ω_T (yellow line) as the baseline. Based on observed sub-time-period data, with the aridity index $I_{A,t_i} = E_{p,t_i}/P_{t_i}$ and evaporative index $I_{E,t_i} = 1 - Q_{t_i}/P_{t_i}$, the same catchment plots at location t_i on the parametric Budyko curve with ω_{t_i} (green line). A movement in the Budyko space towards t'_i along the ω_T curve is shown as a result of a change in the aridity index I_{A,t_i} with the assumption that the long-term mean Budyko curve trajectory and the parameter ω is transferable across time for an individual catchment, which results in a significant deviation $\Delta I_{E,t_i,t'_i}$ between the observed evaporative index I_{E,t_i} and the predicted evaporative index I_{E,t'_i} .

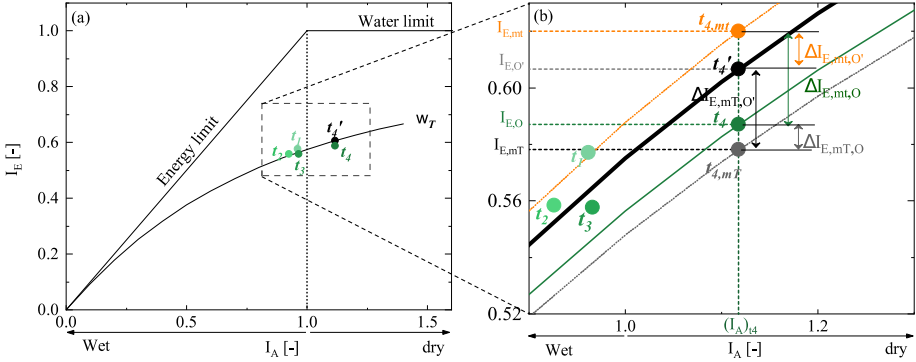


Figure 3.4: (a) Green dots from light "•" to dark "•" indicate the observed positions for four sub-time periods from t_1 to t_4 . The black dot "•" t'_4 indicates the expected location on the parametric Budyko curve with ω_T derived from observed entire time period. We select time period t_4 as an example to present the modelled positions in the zoom-in plot (b). The gray dot "•" $t_{4,mT}$ indicates the modelled position based on scenario 1 which is with S_{umax,WB,t_4} , and the orange dot "•" $t_{4,mt}$ indicates the modelled position based on scenario 2 which is with S_{umax,WB,t_4} . $\Delta I_{E,mT,O'}$ (black arrow) indicates the deviation between modelled $I_{E,mT}$ ("•") based on Scenario 1 and expected $I_{E,O'}$ ("•"). $\Delta I_{E,mT,O'}$ (orange arrow) indicates the deviation between modelled $I_{E,mT}$ ("•") based on Scenario 2 and expected $I_{E,O'}$ ("•"), $\Delta I_{E,mT,O}$ (gray arrow) indicates the deviation between modelled $I_{E,mT}$ ("•") based on Scenario 1 and observed $I_{E,O}$ ("•"), $\Delta I_{E,mT,O}$ (green arrow) indicates the deviation between modelled $I_{E,mT}$ ("•") based on Scenario 2 and observed $I_{E,O}$ ("•").

3.4.2 ESTIMATION OF ROOT ZONE STORAGE CAPACITY DERIVED BY WATER BALANCE METHOD

The root zone storage capacity is the *maximum* volume of water which can be held in soil pores of the unsaturated zone and which is accessible to root systems of vegetation for transpiration. Here the water balance method that is in detail described in previous papers (e.g. Gao et al., 2014a; Nijzink et al., 2016a; De Boer-Euser et al., 2016; Wang-Erlandsson et al., 2016; Bouaziz et al., 2020; Hrachowitz et al., 2021) is used to determine $S_{umax, WB}$. Briefly, $S_{umax, WB}$ is estimated based on daily observations of precipitation (P), potential evaporation (E_p) and stream flow (Q). As a first step, effective precipitation P_e [mm d^{-1}] that enters the subsurface is computed by accounting for interception evaporation by:

$$P_e(t) = P(t) - E_i(t) - dS_i/dt \quad (3.2)$$

where E_i (mm d^{-1}) is daily interception evaporation, S_i (mm) is the interception storage.

For each time step, E_i is determined by:

$$E_i(t) = \begin{cases} E_p(t) & \text{if } E_p dt < S_i \\ \frac{S_i}{dt} & \text{if } E_p dt \geq S_i \end{cases} \quad (3.3)$$

Then further to estimate the effective precipitation P_e (mm d^{-1}) according to:

$$P_e(t) = \begin{cases} 0 & \text{if } S_i < S_{imax} \\ \frac{S_i - S_{imax}}{dt} & \text{if } S_i \geq S_{imax} \end{cases} \quad (3.4)$$

where S_{imax} (mm) is the maximum interception storage. As S_{umax} is not very sensitive to the choice of S_{imax} as previously shown by Hrachowitz et al., 2021 and Bouaziz et al., 2022, we used here a value of $S_{imax} = 2$ mm, which was previously also used by de De Boer-Euser et al. (2016). Hereafter, the long-term mean transpiration (\bar{E}_r) (mm d^{-1}) is estimated from the long-term water balance, with the assumption of no additional gains or losses:

$$\bar{E}_r = \bar{P}_e - \bar{Q}_o \quad (3.5)$$

where \bar{P}_e (mm d^{-1}) is the long-term mean effective precipitation and \bar{Q}_o (mm d^{-1}) is the long-term mean observed streamflow. Considering the seasonal fluctuation of energy input, the daily transpiration E_r (mm d^{-1}) is estimated by subsequently scaling the daily potential evaporation E_p (mm d^{-1}) minus the interception evaporation E_i (mm d^{-1}) (see Eqs 3.2&3.3) by the long-term mean transpiration \bar{E}_r (mm d^{-1}), according to (Bouaziz et al., 2022, Hrachowitz et al., 2021):

$$E_r(t) = \frac{\bar{E}_r}{\bar{E}_p - \bar{E}_i(E_p - E_i)} \quad (3.6)$$

Where \bar{E}_p (mm d⁻¹) is the long-term mean potential evaporation, \bar{E}_i (mm d⁻¹) is the long-term mean interception evaporation. From daily storage deficits $S_{rd,n}(t)$ (mm) during dry periods, estimated as the cumulative sum of daily effective precipitation P_e (mm d⁻¹) minus transpiration E_r (mm d⁻¹), the maximum storage deficit $S_{rd,n}$ of a specific year n is then computed as follows:

$$S_{rd,n} = \begin{cases} \int_{t_{0,w}}^{t_{0,d}} (P_e(t) - E_r(t)) dt, & \text{if } \int_{t_{0,w}}^{t_{0,d}} (P_e(t) - E_r(t)) dt \leq 0 \\ 0 & \text{if } \int_{t_{0,w}}^{t_{0,d}} (P_e(t) - E_r(t)) dt > 0 \end{cases} \quad (3.7)$$

$$S_{rd,n} = \max(|S_{rd,n}(t)|) \quad (3.8)$$

Where t is the time step (d), $t_{0,w}$ is the day at the end of the wet period when the storage deficits are zero but $P_e(t) - E_r(t) < 0$, and $t_{0,d}$ is the day when storage deficits return to zero again after the begin of the next wet period when the water supply exceeds canopy water demand, i.e., $(P_e(t) - E_r(t)) > 0$. Any cumulative precipitation surplus is assumed to be drained from root zone and released from the system either directly as streamflow or via recharge of the groundwater.

The Gumbel extreme value distribution (Gumbel, 1941) was previously used for estimating the root zone storage capacity through the water balance approach by several other studies (Gao et al., 2014c; Nijzink et al., 2016a; De Boer-Euser et al., 2016; Bouaziz et al., 2020; Bouaziz et al., 2022; Hrachowitz et al., 2021). Based on fitting the Gumbel distribution to the maximum annual storage deficits for all n years during one of the four time periods $t_1 - t_4$, the root zone storage capacity $S_{umax,WB}$ can be derived from various return periods of the sequence of n maximum annual storage deficits S_{rd} . Previous studies suggested that vegetation develops root zone storage capacities large enough to survive in dry spells with return periods of $\sim 20 - 40$ years (Gao et al., 2014c; De Boer-Euser et al., 2016; Wang-Erlandsson et al., 2016; Hrachowitz et al., 2021). Therefore, $S_{umax,WB}$ here is defined as the maximum storage deficit in a 40-year period so that $S_{umax,WB} = S_{rd,40yr}$.

Using the above water balance based method, the entire study period 1953 – 2022 ($S_{umax,WB,T}$) as well as individually for the four time periods $t_1 - t_4$ ($S_{umax,WB,t}$) are determined to quantify potential fluctuations of root zone storage capacity reflecting the adaptation to changing climatic conditions.

3.4.3 HYDROLOGICAL MODEL

MODEL ARCHITECTURE

Given that S_{umax} is a critical parameter in hydrological models, the semi-distributed, process-based model, developed in Chapter 2, was also used as the alternative method for estimating S_{umax} . It is noted that the same method as Chapter 2 was used to stratify the Upper Neckar basin into three precipitation zones P1 – P3 by distinct long-term precipitation pattern (hereafter: precipitation zones), represented in Fig. 3.1b. Overall, the model consists of snow (S_{snow}), interception (S_i), unsaturated root zone (S_u), fast responding (S_f) and slow responding storage (S_s) components for each HRU

and precipitation zone (Figure 2.2 in Chapter 2). The maximum storage volume in the unsaturated root zone component in each HRU is defined by the corresponding calibration parameters $S_{umax,F}$, $S_{umax,G}$ and $S_{umax,W}$, respectively. The catchment average $S_{umax,cal}$ is then inferred by aggregating these parameters according to their spatial weights. Water can be released from unsaturated root zones as combined soil evaporation and transpiration flux E_t (mm d⁻¹) which is a frequently applied way to represent vegetation water stress (e.g., Bouaziz et al., 2021, Gharari et al., 2013; Gao et al., 2014a).

MODEL CALIBRATION

The model was run with a daily time step and has 18 calibration parameters. Briefly, the model parameters were calibrated by using the Borg_MOEA algorithm (Borg Multi-objective evolutionary algorithm; Hadka and Reed, 2013) and based on uniform prior distributions (Table 2.3 in Chapter 2). To best reflect different aspects of the hydrograph, including high flows, low flows and the partitioning of precipitation into runoff and evaporation, the parameters are calibrated using a multi-criteria approach that includes 7 objective functions as performance metrics $E_{Q,n}$ (Table 3.3). There are multiple ways to deal with sets of pareto front solutions as in detail described by e.g. (Efstratiadis and Koutsoyiannis, 2010) or (Gharari et al., 2013). We chose to use all solutions on the Pareto front to obtain a conservative estimate of uncertainty. The 7 performance metrics were subsequently also combined into an overall performance metric based on the Euclidian distance (D_E), where $D_E = 1$ indicates a perfect fit. To find a somewhat balanced solution in absence of more detailed information all individual performance metrics were here equally weighted (e.g., Hrachowitz et al., 2021; Hulsman et al., 2021a; Wang et al., 2023):

$$D_E = 1 - \sqrt{\frac{\sum_{n=1}^N (1 - E_{Q,n})^2}{N}} \quad (3.9)$$

where $N = 7$ is the number of performance metrics with respect to stream flow ($E_{Q,n}$). Note that the different units and thus different magnitudes of residuals in the individual performance metrics introduce some subjectivity in finding the most balanced overall solution according to D_E (Eq. 3.9).

However, a preliminary sensitivity analysis with varying weights for the individual performance metrics in D_E suggested limited influence on the overall results and is thus not further reported here. In addition, the model was tested for its ability to represent spatial differences in the hydrological response by evaluating it against streamflow observations in three sub-catchments (C1 – C3) of the upper Neckar catchment without further re-calibration whereby each one of the sub-catchments largely represents the hydrological response from one of the precipitation zones (Fig. 3.1).

The model is calibrated following two distinct calibration scenarios as indicated in Table 3.2. In the first scenario, the model and thus also $S_{umax,F}$, $S_{umax,G}$ and $S_{umax,W}$ are calibrated over the full length of the 70-yr study period from 1953 – 2022. This reflects the common assumption of a system that is stable over time. By extension, this also implies that the role of vegetation and thus S_{umax} does not change and that vegetation

does not adapt to climatic variability. In the second scenario, individual calibration to the four time periods $t_1 - t_4$ allowed to estimate fluctuations in the parameters $S_{umax,F}$, $S_{umax,G}$ and $S_{umax,W}$ between the time periods as indicator of vegetation adaption to changing climatic conditions.

Table 3.3: Signatures of flow and the associated performance metrics used for model calibration and evaluation. The performance metrics include the Nash–Sutcliffe efficiency (NSE) and the relative error (RE).

Signature	Symbol	Performance metric
Time series of stream flow	Q	NSE_Q
Time series of $\log(Q)$	$\log(Q)$	$NSE_{\log(Q)}$
Flow duration curve of $\log(Q)$	$FDC_{\log(Q)}$	$NSE_{FDC_{\log(Q)}}$
Seasonal runoff coefficient	C_r	NSE_{C_r}
Autocorrelation function of flow (AC)	AC	NSE_{AC}
Runoff coefficient in summer	$C_{r,summer}$	$RE_{C_{r,summer}}$
Runoff coefficient in winter	$C_{r,winter}$	$RE_{C_{r,winter}}$

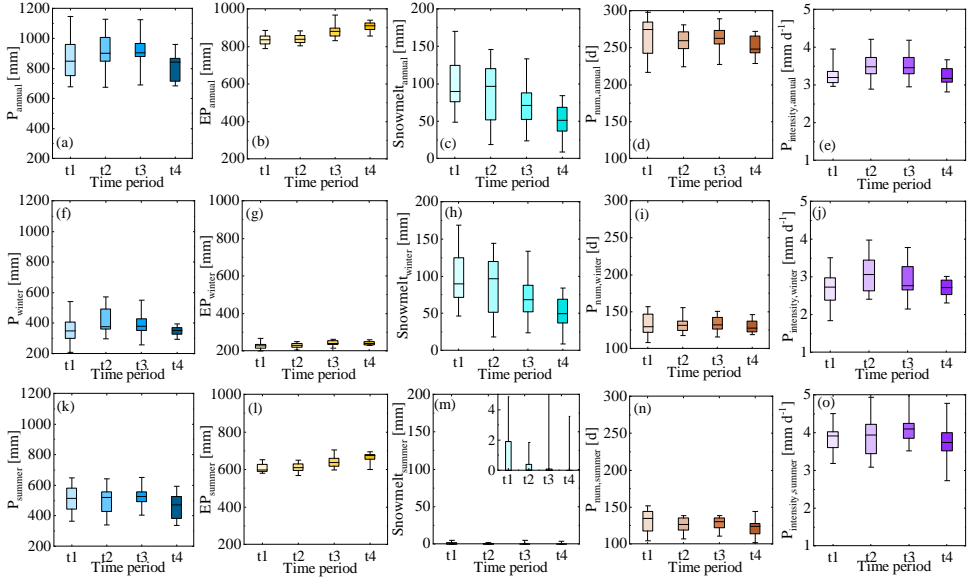


Figure 3.5: The annual and seasonal variability (i.e., winter and summer) of selected climatic indices including annual averages of precipitation (P), potential evaporation (E_p), estimated snow melt water, the number of precipitation days (P_{num}) and precipitation intensity ($P_{intensity}$) for four sub-time periods (t_1 :1953-1972, t_2 :1973-1992, t_3 :1993-2012, and t_4 :2013-2022). (a) – (e) the annual variability of selected climatic indices; (f) – (j) the seasonal variability of selected climatic indices in winter periods; (k) – (o) the seasonal variability of selected climatic indices in summer periods.

3.5 RESULTS

3.5.1 OBSERVED MULTI-DECADAL HYDROCLIMATIC VARIABILITY

Based on the initial analysis of water balance data for four sub-time periods, significant differences were observed in the variability of different hydroclimatic indicators over the 1953 – 2022 study period (Fig. 3.5). While periods t_1 and t_4 were characterized by rather low mean annual precipitation of ~ 870 and 811 mm yr^{-1} , respectively, periods t_2 and t_3 were subject to, on average, higher precipitation with $\sim 911 \text{ mm yr}^{-1}$. While summer precipitation remained rather stable over the study period (Fig. 3.5f), the above was mostly caused by fluctuations in winter precipitation (Fig. 3.5k). In contrast, potential evaporation E_P has gradually increased by 7% from 836 to 906 mm yr^{-1} (Fig. 3.5b). Similarly reflecting increases in temperature (Fig. 3.5b), the annual snowpack and associated snowmelt have continuously decreased from around 98 mm yr^{-1} to around 50 mm yr^{-1} between t_1 and t_4 (Fig. 3.5c). A slight decrease of the number of days with precipitation from ~ 264 to 251 (Fig. 3.5d), on average, mostly due to changes in the summer months (Fig. 3.5n) was accompanied by some rather limited variability in precipitation intensities (Fig. 3.5e), mostly during winter (Fig. 3.5j). Overall, the comparatively humid periods $t_1 - t_3$ that were characterized by I_A fluctuating between $0.93 - 0.97$ were followed by a markedly more arid period t_4 with $I_A = 1.12$ (Table 3.2; Fig. 3.4). In response to the multi-decadal variability in I_A , expressed as movement along the x-axis in the Budyko framework, the catchment experienced I_E to vary between 0.56 and 0.59 (Table 3.2; Fig. 3.4). However, this observed variability was somewhat lower than the variability $I_{E,\omega_T} = 0.55 - 0.61$ that would have been expected based on ω_T . This illustrates that the hydrological response did not consistently follow its long-term trajectory defined by ω_T . Instead, deviations $\Delta I_{E,t_i}$ from the expected positions, and thus values of ω_{t_i} that are different to ω_T , were observed for the individual periods. More specifically, the deviations gradually decreased from $\Delta I_{E,t_1} = 0.01$ in t_1 to $\Delta I_{E,t_4} = -0.02$ in t_4 (Fig. 3.4). This systematic shift towards lower (more negative) $\Delta I_{E,t_i}$ and thus also lower ω_{t_i} indicates that at the same I_A a smaller fraction of precipitation is released as evaporation, i.e. I_E , now than at the start of the 70 year study period. Although the magnitude of deviations remains with $\Delta I_{E,t_i} \leq \pm 0.02$ rather minor, similar to what has been recently reported elsewhere (Ibrahim et al., 2024; Tempel et al., 2024), in particular their systematic shift into one direction implies that changes in the system other than I_A have a visible effect on the hydrological response pattern.

3.5.2 ROOT ZONE STORAGE CAPACITY $S_{umax,WB}$ ESTIMATED FROM WATER BALANCE DATA

As the baseline of our study, the annual maximum storage deficits fluctuate between 97 mm in 2022 and 16 mm in 1970 (Fig. 3.6a). Assuming an adaptation to dry spells with 40-yr return periods the root zone storage capacity over the entire 1953 – 2022 study period (Scenario 1) was estimated to $S_{umax,WB,T} = 105 \text{ mm}$ (Table 3.2; Fig. 3.6b). In the next step, the storage deficits and the associated root zone storage capacity for each period $t_1 - t_4$ was estimated (Scenario 2). S_{umax,WB,t_1} and S_{umax,WB,t_3} for periods t_1 and t_3 , respectively, are estimated at the same value of 95 mm . In contrast, and somewhat counterintuitively, the highest value over the study period is found in the wettest period

(t_2) and reaches $S_{umax,WB,t_2} = 115$ mm, while the driest period (t_4) is characterized by $S_{umax,WB,t_4} = 100$ mm (Table 3.2; Fig. 3.6c-j). These pattern suggest that $S_{umax,WB}$ did vary by ~ 20 mm, equivalent to $\sim 20\%$ throughout the 1953 - 2022 period. In contrast to $\Delta I_{E,t_i}$ that was characterized by a systematic shift towards more negative deviations over time, no evidence was found for a systematic, one-directional shift in $S_{umax,WB}$. Instead, $S_{umax,WB}$ evolved following a somewhat cyclic pattern.

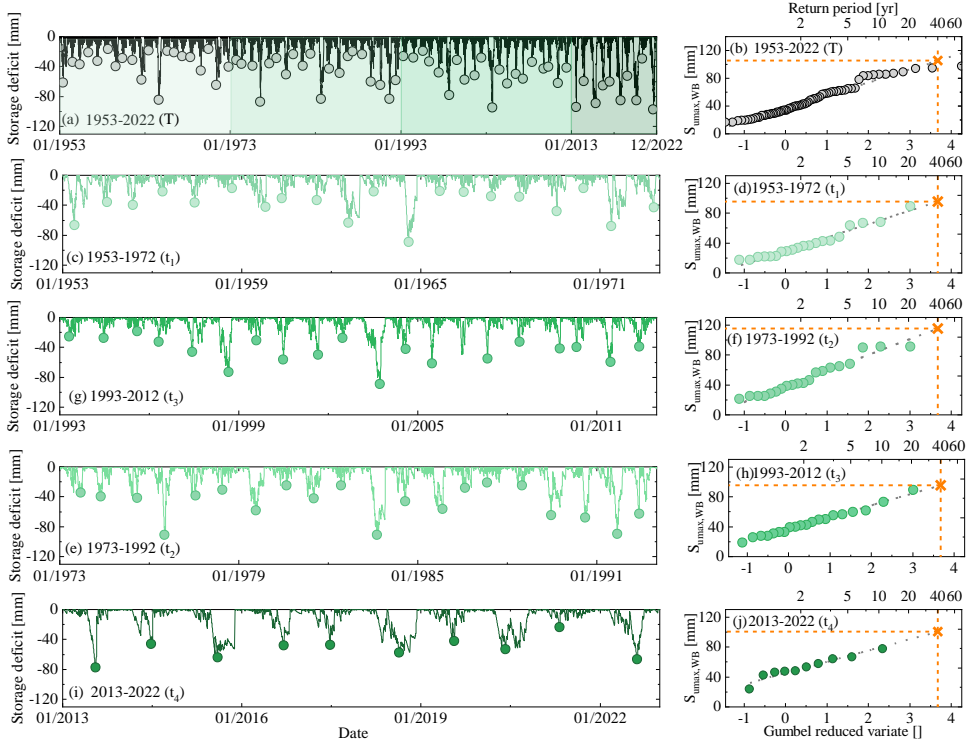


Figure 3.6: (a), (c), (e), (g) and (i) The time series of storage deficits as calculated by Eq. 3.7, for entire time period T (1953-2022) and four sub-time periods (green shades from light to dark for time period from t_1 to t_4). The maximum annual deficits are indicated by the dots. (b), (d), (f), (h) and (j) Estimation of $S_{umax,WB}$ as the storage deficit associated with a 40-year return period using the Gumbel extreme value distribution for different time periods. The orange crosses indicate the values of $S_{umax,WB}$ for different time periods.

3.5.3 ROOT ZONE STORAGE CAPACITY $S_{umax,cal}$ ESTIMATED AS CALIBRATION PARAMETER

MODEL CALIBRATION FOR 1953 – 2022 (SCENARIO 1)

The model parameter sets obtained as feasible after calibration over the entire 1953-2022 study period in Scenario 1 reproduce the main features of the hydrological response (Fig. 3.2d). More specifically, the modelled hydrographs in particular describe well the timing of high flows, albeit somewhat underestimating flow peaks for the best-performing model in terms of the D_E (Eq. 3.9). The low flows and the shapes of recessions are in general well captured ($NSE_{logQ} = 0.67$). Crucially, the model also reproduces well the other observed stream flow signatures such as the flow duration curves ($NSE_{logFDC} = 0.96$), the autocorrelation function ($NSE_{AC} = 0.99$) as well as the long-term and seasonal runoff coefficients ($NSE_{C_r} = 0.90$, $RE_{C_r,summer} = 0.83$ and $RE_{C_r,winter} = 0.91$). The latter further implies that the modelled long-term actual evaporative fluxes E_A (Fig. 3.2b) and thus I_{E,ω_T} are, on average, consistent with the observed ones, which can be seen in Figure 6. The model, calibrated on the overall response of the Upper Neckar basin, also exhibited considerable skill to represent spatial differences in the hydrological response by reproducing observed stream flow in the three sub-catchments (C1 – C3) similarly well (Fig. 3.7) without any further re-calibration. The overall model skill to mimic the hydrological response corresponds well to a similar implementation of the model in the greater study region by Wang et al., 2023. The detailed list of performance metrics is provided in Table 3.4.

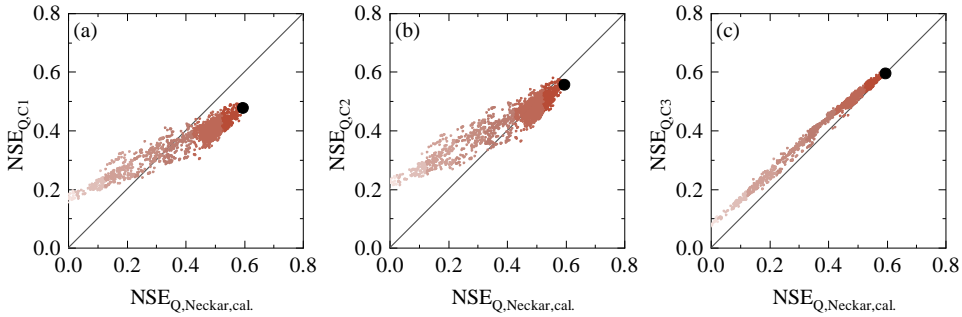


Figure 3.7: Selected model performance metrics in the entire time period 01/01/1953 – 31/12/2022 of the upper Neckar basins against the model performance in uncalibrated sub-catchment C1: Rottweil, C2: Plochingen at files river, and C3: Horb based parameter sets derived from the calibration for entire time period. The dots indicate all pareto optimal solutions in the multi-objective model performance space. The shades from dark to light indicate the overall model performance based on the Euclidean Distance D_E , with the black solutions representing the overall better solutions (i.e. larger D_E).

The model calibration resulted in pronounced differences in the root zone storage capacity parameters for three individual landscape classes. While for forest dominated land it was estimated at $S_{umax,F} = 158$ mm for the best performing model (5th/95th percentile of all feasible solutions: 138–168 mm), it reached $S_{umax,G} = 95$ mm (5th/95th: 71 – 123 mm) for grass/cropland and $S_{umax,W} = 61$ mm for wetland (5th/95th: 49–68 mm), which reflects differences in vegetation type and position in the landscape (cf. Fan et al., 2017). Remarkably, the catchment root zone storage capacity, estimated by aggregating the individual values according to their areal fractions, came with $S_{umax,cal} = 116$ mm (5th/95th : 99 – 130 mm, Fig. 3.8a) very close to the estimate $S_{umax,WB} = 105$ mm that is directly derived from water balance method without any calibration, as described in section 3.5.2.

3.5.4 MODEL CALIBRATION FOR INDIVIDUAL PERIODS $t_1 - t_4$ (SCENARIO 2)

The model parameter sets obtained from the individual calibration for each period $t_1 - t_4$ reproduce the hydrographs of the corresponding periods as well or slightly better than when using the long-term average parameters from Scenario 1 (see detailed performance metrics in Table 3.4). In particular, the runoff coefficients could with $NSE_{C_r} \sim 0.86 - 0.91$, $RE_{C_r,summer} \sim 0.84 - 0.90$ and $RE_{C_r,winter} \sim 0.88 - 0.92$ be rather well mimicked. Similarly, the daily dynamics with $NSE_{log Q} \sim 0.63 - 0.72$ for the best- performing model of each period and most other hydrological signatures, could be reproduced marginally better.

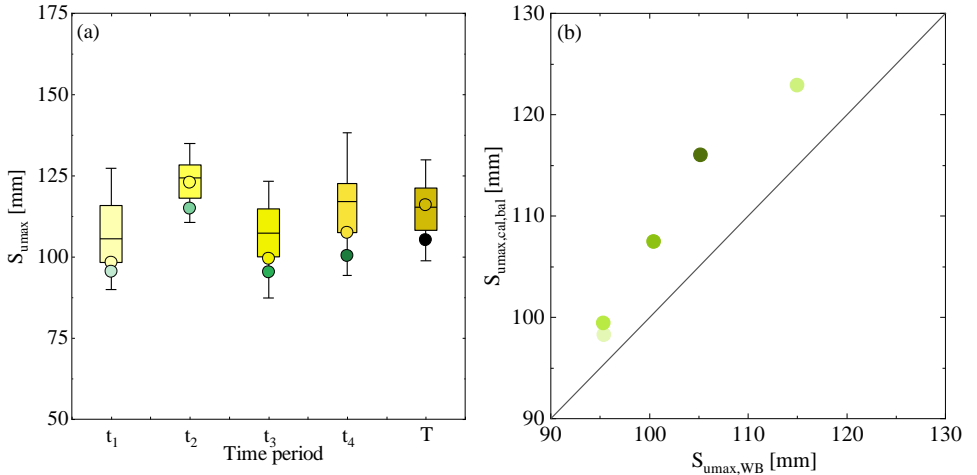


Figure 3.8: (a) S_{umax} values derived from water-balance method and hydrological model for different time periods. The yellow boxes from light to dark indicate the range of $S_{umax,cal}$ for the sub-time period from t_1 to t_4 and entire time period T based on the corresponding parameter sets derived from the model, yellow dots indicate the corresponding $S_{umax,cal,bal}$ based on the most balanced solution, and green dots indicate the corresponding $S_{umax,WB}$ derived from water-balance method. (b) the values of $S_{umax,cal,bal}$ against $S_{umax,WB}$. The yellow-green dots from light to dark indicate the values of S_{umax} for the sub-time period from t_1 to t_4 and entire time period T .

Table 3.4: The performance metrics for the most balanced solution (out of the basket) and the 5th-95th percentile of all performance metrics (inside of the basket) for the full set of pareto optimal solutions for the multi-objective calibration cases (Scenarios 1 – 2) with $S_{umax,cal}$ are shown here.

	Scenario 1					Scenario 2				
	T (1953-2022)	t_1 (1953-1972)	t_2 (1973-1992)	t_3 (1993-2012)	t_4 (2013-2022)	t_1 (1953-1972)	t_2 (1973-1992)	t_3 (1993-2012)	t_4 (2013-2022)	
NSE_Q	0.59 (0.06-0.55)	0.60 (0.09-0.57)	0.58 (0.07-0.55)	0.60 (0.09-0.56)	0.57 (0.11-0.53)	0.60 (-0.16-0.57)	0.57 (0.02-0.54)	0.59 (-0.32-0.52)	0.56 (-0.61-0.50)	
$NSE_{log(Q)}$	0.67 (0.34-0.64)	0.65 (0.36-0.62)	0.68 (0.37-0.65)	0.66 (0.30-0.63)	0.70 (0.32-0.66)	0.69 (0.23-0.62)	0.65 (0.30-0.59)	0.63 (-0.33-0.53)	0.72 (-0.77-0.66)	
$NSE_{FDClog(Q)}$	0.96 (0.92-0.99)	0.93 (0.89-0.98)	0.95 (0.90-0.99)	0.98 (0.93-0.99)	0.97 (0.91-0.98)	0.96 (0.94-0.99)	0.98 (0.88-0.99)	0.98 (0.58-0.99)	0.97 (0.16-0.99)	
NSE_{C_r}	0.90 (0.86-0.91)	0.86 (0.84-0.88)	0.91 (0.89-0.93)	0.90 (0.88-0.92)	0.91 (0.87-0.91)	0.86 (0.84-0.89)	0.91 (0.86-0.93)	0.90 (0.87-0.92)	0.89 (0.63-0.92)	
NSE_{AC}	0.99 (0.56-0.97)	0.94 (0.45-0.96)	0.98 (0.55-0.96)	0.98 (0.62-0.98)	0.82 (0.11-0.91)	0.98 (0.21-0.94)	0.87 (0.47-0.96)	0.95 (0.27-0.94)	0.90 (0.07-0.97)	
$RE_{C_r, summer}$	0.83 (0.82-0.89)	0.80 (0.79-0.90)	0.83 (0.81-0.90)	0.85 (0.83-0.89)	0.85 (0.83-0.87)	0.90 (0.81-0.90)	0.89 (0.79-0.90)	0.87 (0.77-0.89)	0.84 (0.69-0.88)	
$RE_{C_r, winter}$	0.91 (0.89-0.91)	0.89 (0.87-0.89)	0.93 (0.92-0.93)	0.91 (0.89-0.91)	0.92 (0.90-0.92)	0.88 (0.88-0.90)	0.92 (0.92-0.93)	0.90 (0.89-0.91)	0.91 (0.82-0.92)	
D_E	0.78 (0.54-0.76)	0.77 (0.53-0.76)	0.79 (0.56-0.77)	0.79 (0.55-0.77)	0.78 (0.53-0.74)	0.79 (0.39-0.76)	0.78 (0.51-0.73)	0.78 (0.27-0.72)	0.79 (0.01-0.75)	

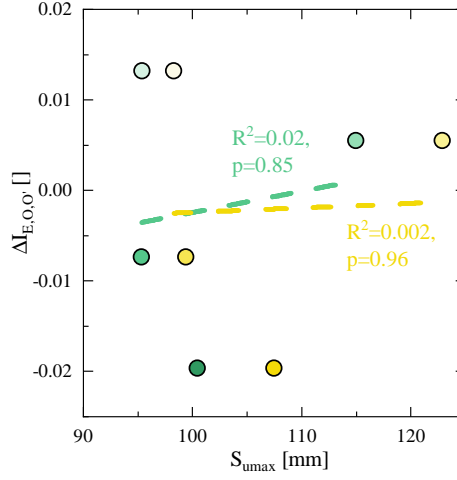


Figure 3.9: Relationships between the deviations $\Delta I_{E,O,O'}$ and the values of $S_{umax,WB}$ and $S_{umax,cal}$ for four sub-time periods (t_1 - t_4) which are respectively derived from the water-balance-method (green circles) and hydrological model calibration (yellow circles).

The individual calibration over each period $t_1 - t_4$ resulted in associated differences in the catchment-scale root-zone storage capacity of each period. Based on the best-performing models, the calibrated values varied between low values for t_1 and t_2 , with $S_{umax,cal,t_1} = 98$ mm and $S_{umax,cal,t_3} = 99$ mm and higher values for the two other periods with $S_{umax,cal,t_2} = 122$ mm and $S_{umax,cal,t_4} = 107$ mm (Table 3.2; Fig. 3.8a). The magnitudes of S_{umax,cal,t_i} obtained by calibration in the individual time periods $t_1 - t_4$ are with a difference of 5 mm ($\sim 5\%$), on average, very close to S_{umax,WB,t_i} estimated on basis of the water balance for the same periods. Perhaps even more notably the temporal evolution of S_{umax,cal,t_i} and S_{umax,WB,t_i} follows the same sequence over time ($R^2 = 0.95$, $p = 0.05$; Fig. 3.8b).

3.5.5 EFFECT OF S_{umax} ON TEMPORAL FLUCTUATION IN THE TRAJECTORIES OF THE BUDYKO CURVE

The deviations $\Delta I_{E,O,O'}$ between expected evaporative index $I_{E,O'}$ and observed evaporative index $I_{E,O}$ for all periods $t_1 - t_4$ become gradually more negative from t_1 ($\Delta I_{E,O,O'} = 0.013$) to t_4 ($\Delta I_{E,O,O'} = -0.020$), which is consistent with decreases of ω_{t_i} and downward shifts of the associated parametric Budyko curves over time as described in section 3.5.1. These systematic reductions of $\Delta I_{E,O,O'}$ over the 70-year study period are not reflected in the fluctuations of root zone storage capacities, irrespective of how they were estimated, i.e. S_{umax,WB,t_i} ($p = 0.85$) or S_{umax,cal,t_i} ($p = 0.96$), as illustrated by Figure 3.9.

The above is further corroborated by comparing the modelled I_E from Scenarios 1 and 2 for each period $t_1 - t_4$. More specifically, in Figure 3.10c it can be seen that Scenario 1, based on a long-term average, time-invariant $S_{umax,WB,T}$ obtained over the entire 1953 – 2022 period, generates deviations $\Delta I_{E,mT,O'}$ from the expected long-term

average $I_{E,O'}$ for each period $t_1 - t_4$. In this case, the modelled I_E does not follow the expected $I_{E,O'}$. However, it also does not follow the sequence of increasingly negative deviations from 0.013 in t_1 to -0.020 in t_4 as observed in reality ($\Delta I_{E,O,O'}$). Instead, $\Delta I_{E,mT,O'}$ remains negative for all time periods and fluctuates between $\Delta I_{E,mT,O'} = -0.005$ and -0.029 (white boxplots in Fig. 3.10c). Replacing the time-invariant $S_{umax,WB,T}$ by individual $S_{umax,WB,ti}$ for each period $t_1 - t_4$ in Scenario 2, accounts for the different effects of vegetation in the individual periods. If S_{umax} controlled the observed deviations from expected $I_{E,O'}$, Scenario 2 would generate estimates of $\Delta I_{E,mti,O'}$ that are closer to the observed ones than those of Scenario 1. However, no evidence was found for that: the deviations $\Delta I_{Emt,O'}$ obtained by Scenario 2 with time-variable S_{umax} for each period $t_1 - t_4$ are largely indistinguishable (orange boxplots in Fig. 3.10c) from those generated by Scenario 1 with time-invariant S_{umax} . As a consequence, the evaporative index I_E modelled with time-variable $S_{umax,WB,ti}$ is not found to be closer to the observed I_E for Scenario 2 than for Scenario 1. On the contrary, the deviations $\Delta I_{Em,O}$ from the observed I_E obtained from the time-invariant Scenario 1 are in most time periods, albeit only slightly, less pronounced (Fig. 3.10d).

3.5.6 EFFECT OF S_{umax} ON STREAM FLOW

Corresponding to the above findings, there is no significant difference in modelled average streamflow between Scenario 1, using long-term average S_{umax} , and Scenario 2, using individual S_{umax} values for each time period (Fig. 3.11d). While the model for both scenarios consistently and similarly underestimates high flows (Q^{5th} , Fig. 3.11a) by $\sim 10\%$, it overestimates median flow by $\sim 15\%$ with both time-invariant and time-variable S_{umax} , for all time periods (Fig. 3.11b). Interestingly, the low flows are over-predicted by $\sim 10 - 20\%$ in the first two periods, while they are under-predicted by up to $\sim 20\%$ in the later periods in both Scenarios (Fig. 3.11c). In addition, it was found that using time variable S_{umax} in Scenario 2 did also not have any discernible effect on seasonal flow pattern. The fact that both scenarios generate similar estimates over different flow percentiles and, in particular, that the time-variable Scenario 2 reflects the same systematic shift in the ability of the model to reproduce low flows as Scenario 1, suggests, together with the very minor effects of time-variable S_{umax} in Scenario 2 on the model performance metrics, that the adaptation of S_{umax} to changing climatic conditions does not significantly affect the average hydrological response pattern in the Neckar basin.

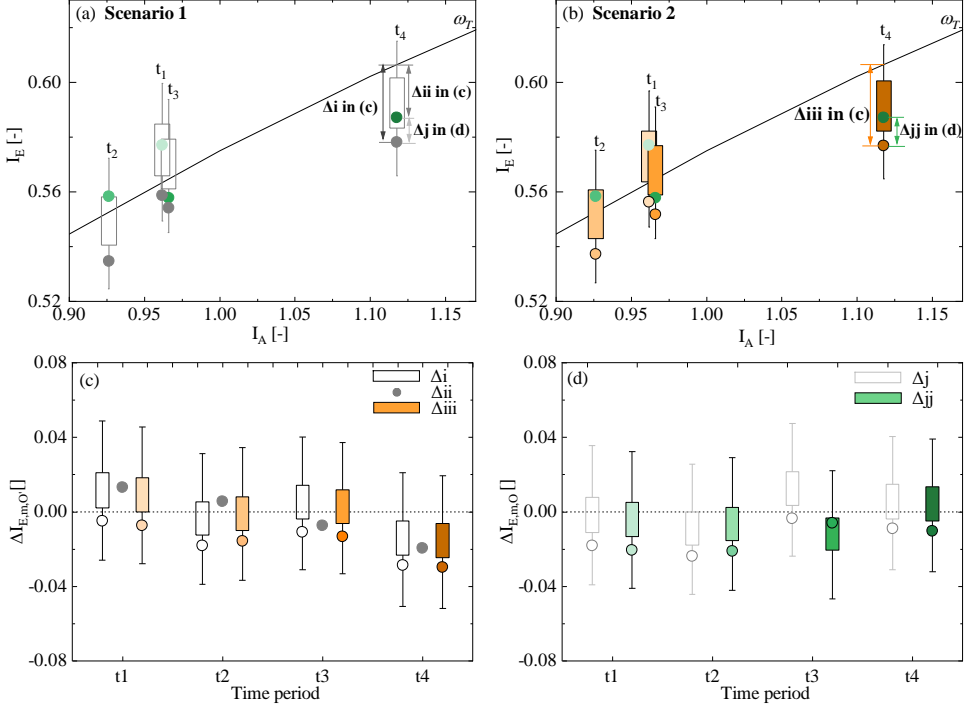


Figure 3.10: (a) The gray boxes ($I_{E,mT}$) indicate the modelled evaporative index based on all Pareto front solutions for four sub-time periods based on Scenario 1 with a stationary $S_{umax,WB,T}$ and gray dots based on the most balanced solution based on Scenario 1. The green circles from light to dark in (a) and (b) indicate the observed evaporative index for four sub-time periods from t_1 to t_4 . (b) The orange circles ($I_{E,mt}$) indicate the modelled evaporative index based on all Pareto front solutions for four sub-time periods (from lighter to darker shades) based on Scenario 2 with time-variant $S_{umax,WB,ti}$ and the orange circles based on the most balanced solution for Scenario 2. Black boxes in (c) indicate the deviations $\Delta I_{E,mT,O'} = I_{E,mT} - I_{E,O'}$ (Δi) based on all Pareto front solutions for four sub-time periods, and the dark gray circles based on the most balanced solution based on Scenario 1. Orange boxes in (c) indicate the deviations $\Delta I_{E,mt,O'} = I_{E,mt} - I_{E,O'}$ (Δiii) based on all Pareto front solutions for four sub-time periods, and the orange circles based on the most balanced solution for Scenario 2. The gray dots indicate the deviation $\Delta I_{E,O,O'}$ (Δii) between observed $I_{E,O}$ for each sub-time period and corresponding expected $I_{E,O'}$. Light gray boxes in (d) indicate the deviations $\Delta I_{E,mT,O} = I_{E,mT} - I_{E,O}$ (Δj) based on all Pareto front solutions for four sub-time periods, and the gray circles based on the most balanced solution. Green boxes in (d) indicate the deviations $\Delta I_{E,mt,O} = I_{E,mt} - I_{E,O}$ (Δjj) based on all Pareto front solutions for four sub-time periods, and the green circles based on the most balanced solution.

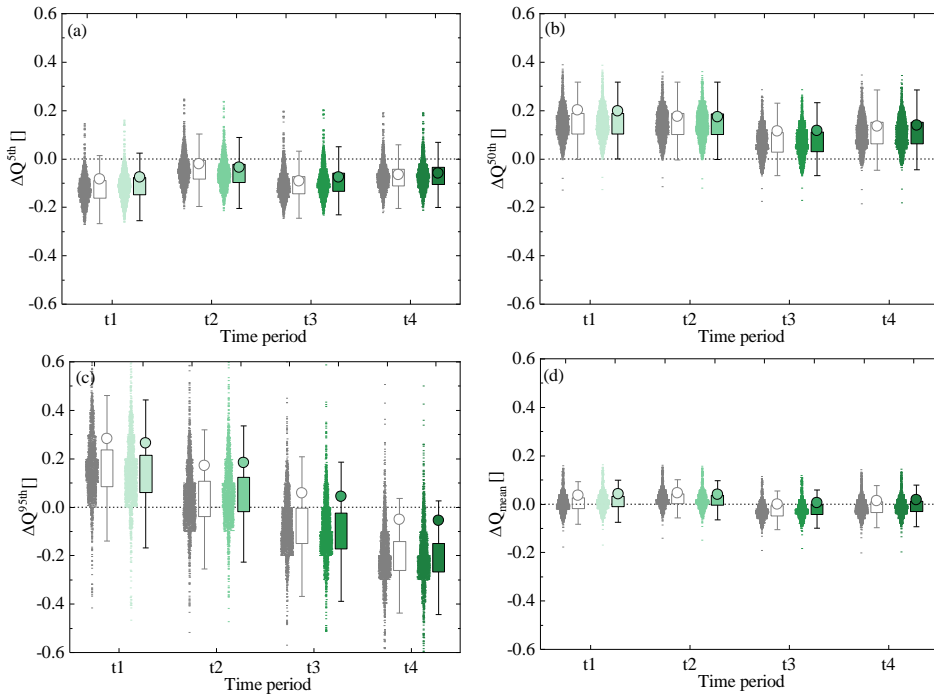


Figure 3.11: The relative errors of observed and modelled high (Q^{5th}), median (Q^{50th}), and low (Q^{95th}) flow quantiles and the mean Q for different time periods based on two scenarios. The gray shades and corresponding dots indicate the relative errors based on scenario 1 with all Pareto front solutions and the gray circles indicate the most balanced solution. The corresponding values for scenario 2 are shown in green.

3.6 DISCUSSION

3.6.1 MULTI-DECADAL CHANGES IN ROOT ZONE STORAGE CAPACITY

As Gao et al. (2023) suggested, considering the terrestrial ecosystem structure can improve our understanding of hydrological processes and how the ecosystem can be survived and developed. It is valuable to explore how ecosystems adapt to climatic variability, reflected by fluctuations in S_{umax} , and how this affects on the long-term partitioning of drainage and evaporation and hydrological response. This study is the first to systematically and explicitly quantify how root zone storage capacity S_{umax} changes with changing climatic conditions over time. The values of root zone storage capacity, estimated from both, water balance data and as model calibration parameter, show indeed significant and corresponding fluctuations over multiple decades, varying by up to $\pm 20\%$. The overall estimated magnitudes fall with $S_{umax} \sim 95 - 115$ mm well within the range of long-term average values reported previously for the greater region (e.g. Bouaziz et al., 2021; Hrachowitz et al., 2021; Tempel et al., 2024) and other temperate, humid environments (e.g. Kleidon and Lorenz, 2004; Gao et al., 2014a; De Boer-Euser et al., 2016; Wang-Erlandsson et al., 2016; Stocker et al., 2023; Van Oorschot et al., 2024).

The values of S_{umax} obtained from both methods are very similar and within an error margin of merely $\sim 5\%$. In addition, they both follow a comparable change over time. Together, this lends support to the underlying assumption that this temporal evolution of S_{umax} may indeed be a fingerprint of vegetation adaptation to changing climatic conditions. More specifically, as $S_{umax, WB}$ is explicitly based on the estimates of transpiration E_r (Eq. 3.9), it could be plausibly argued that during specific years merely more water is used for E_r but that the size of the water storage volume accessible for roots may not necessarily change. In that case, changes in $S_{umax, WB}$ would not reflect actual changes of the active root system but only in how much water was used by them. In contrast, $S_{umax, cal}$ inferred as calibration parameter of a hydrological model does not only regulate transpiration, but, critically, also the generation of streamflow. If therefore the active root system did in reality not change and fluctuations in $S_{umax, WB}$ were a mere artifact of changes in water uptake from a fixed-size volume instead of an actual change in of maximum vegetation-accessible subsurface water volumes, fluctuations in $S_{umax, cal}$ would not mirror those of $S_{umax, WB}$ and the use of $S_{umax, WB}$ in the hydrological model would, due to the non-linear character of the flow generation function in the model (Eq. 2.17), lead to misrepresentations of streamflow dynamics. Yet here, no deteriorations of the model performance with changing S_{umax} were found. Even more, the fact that $S_{umax, WB}$ and $S_{umax, cal}$ are characterized by very similar magnitudes and fluctuations does add further evidence that their evolution over time is a manifestation of vegetation adapting its active root system to changing climatic conditions.

Several previous studies in similar environments found that the root zone storage capacity S_{umax} can decrease by 50% or more after deforestation and that these changes do not only cause reductions in I_E by -0.2 or more, which reflect changes in ω and thus changes of the overall functioning of the system, but also influence hydrological dynamics at short time scales, such as the magnitudes of flow peaks (Nijzink et al., 2016a; Hrachowitz et al., 2021). In contrast to the above studies, the $\pm 20\%$ fluctuations of

S_{umax} here did not lead to similarly marked shifts in I_E or ω . This is further corroborated by an analysis of different variables as potential controls on S_{umax} and ΔI_E as shown in Figure 13. Fluctuations of S_{umax} can to a large part be attributed to the variability in the ratio of winter precipitation over summer precipitation (Fig. 3.12s) as simplified metric for precipitation seasonality. This comes as no surprise, as the computation of $S_{umax, WB}$ is explicitly based on the seasonal water deficit (Eq. 3.7). It merely visualizes that the more precipitation falls in summer, in a time when evaporative demand is highest, the lower S_{umax} needs to be to provide vegetation sufficient and continuous access to water for continuous vegetation transpiration. All other tested variables do not exert any major influence on S_{umax} in the study region. Conversely, it was found that the deviations ΔI_E are largely independent of the seasonality of precipitation (Fig. 3.12g). Instead, increases in summer E_P are correlated with decreases in ΔI_E (Fig. 3.12h) and thus with a reduction of E_T . The observed systematic shift towards more negative ΔI_E which indicates proportionally less evaporation thus coincides with the gradually increasing summer E_P over time. This points towards different controls on ΔI_E than on S_{umax} and the potential role of increased vegetation water stress in summer as main driver of ΔI_E . Thus, while there is compelling evidence for fluctuations in S_{umax} , the above illustrates that these changes cannot explain the observed deviations from the expected long-term Budyko trajectory in the study region.

It is also important to note that the temporal fluctuations of both S_{umax} and ΔI_E can be subject to uncertainties. In spite of the findings reported by Han et al., 2020, that for most river catchments world-wide $dS/dt \sim 0$ holds over averaging periods similar to the ones used here ($t_1 - t_4$), this assumption may not completely hold in the study region. In relation with that, we also did not consider potential effects of unobserved groundwater import or export on the long-term water balance (Bouaziz et al., 2018).

As only $< 2\%$ of the study area experienced documented land use change over the 1953 – 2022 period and no major reservoirs are present upstream of the study basin outlet, we here interpret fluctuations in S_{umax} as a reflection of adaptation of root-systems to changing hydroclimatic conditions. However, some of the fluctuations may be the consequence of land management practices not quantified by available gridded land cover products such as CORINE, including forest thinning (cf. Hrachowitz et al., 2021) or rejuvenation (cf. Teuling and Hoek van Dijke, 2020). In addition, although we here attribute changes in S_{umax} mainly to changes in root systems, these may be complemented by additional effects of changes in vegetation water use due to feedbacks with increases in atmospheric CO_2 (e.g. Berghuijs et al., 2017; Jaramillo et al., 2018).

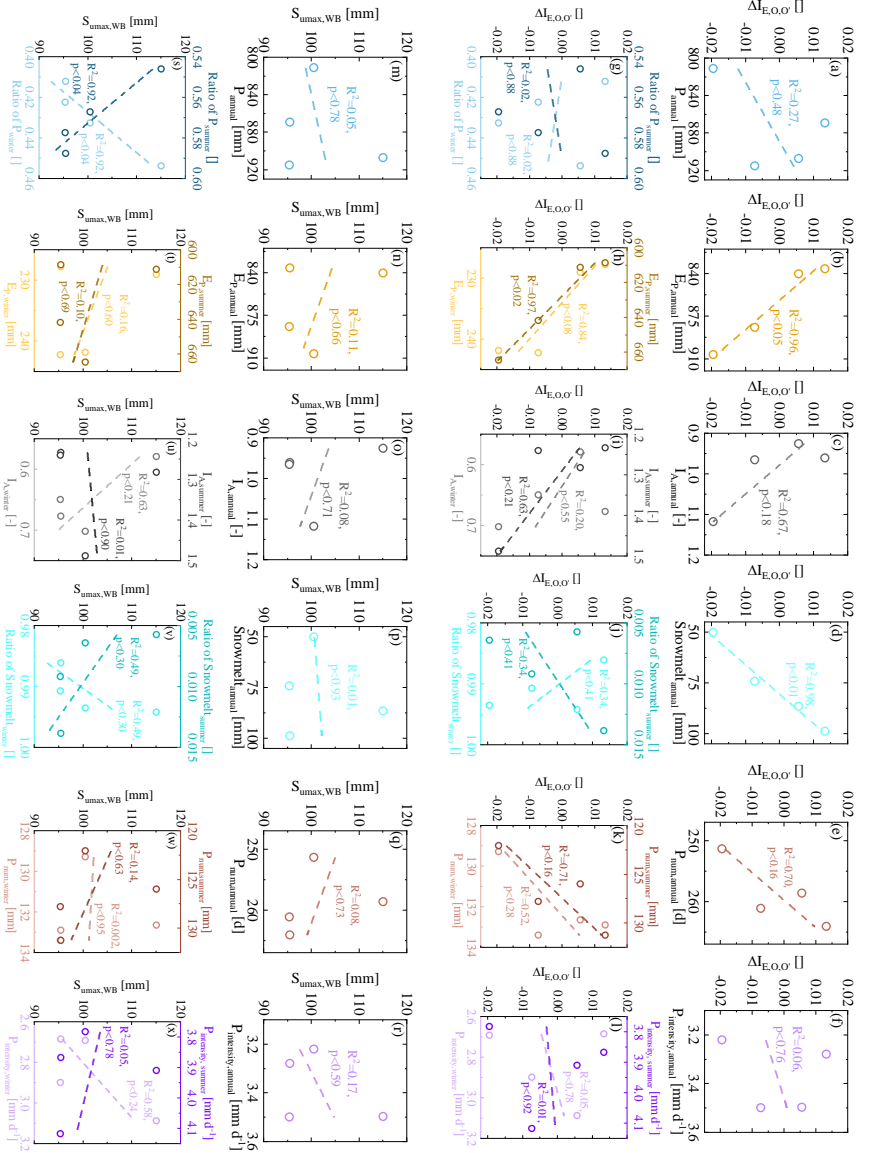


Figure 3.12: Relationships between the temporal fluctuation of the deviations ($\Delta E_{O,0'}$, the black dots in Fig. 10(a), and $S_{max,WB}$ and climate indices including precipitation (P), potential evaporation (E_p), aridity index (I_A), estimated snow melt water (Snowmelt), the number of precipitation days (P_{annual}) and precipitation intensity ($P_{intensity}$) for the four sub-time periods. Relationships between the temporal fluctuation of the deviations ($\Delta E_{O,0'}$, the black dots in Fig. 10(a) and climate indices) for the first two periods are shown in the first two rows (a)-(f) (i.e., (a)-(f) $\Delta E_{O,0'}$ vs. annual climatic indices, (g)-(l) $\Delta E_{O,0'}$ vs. seasonal climatic indices). Relationships between the temporal fluctuation of $S_{max,WB}$ derived from the water-balance method and climate indices for the four sub-time periods are shown in the last two rows (m)-(x) (i.e., (m)-(t) $S_{max,WB}$ vs. annual climatic indices, (s)-(x) $S_{max,WB}$ vs. seasonal climatic indices).

3.6.2 EFFECT OF CHANGING S_{umax} ON THE REPRESENTATION OF STREAM FLOW IN A MODEL

Reflecting its lack of explanatory power for the changes in ΔI_E , our results correspondingly indicate that signatures of both annual flow, such as the average Q^{5th} , Q^{50th} or Q^{95th} but also of seasonal flow are not better reproduced by the hydrological model when replacing a time-invariant, long-term average S_{umax} by a temporally dynamic S_{umax} . Overall, these results are in contrast to previous studies that quantified the effect of a time variable S_{umax} parameter following deforestation. For example, Nijzink et al. (2016a) reported that adjusting parameter S_{umax} to a lower value does improve a model's ability to reproduce streamflow after deforestation. These findings were strongly supported by Hrachowitz et al. (2021), who found that post-deforestation model recalibration resulted in lower S_{umax} and a significantly better performance compared to using parameters from pre-deforestation calibration. However, our results are also different to those reported by Duethmann et al. (2020), who found that accounting for vegetation dynamics in a model in form of changing surface resistances to vegetation improved the long-term performance of the model. Similarly, Bouaziz et al. (2022), who estimated future S_{umax} based on projected future hydro-climatic conditions. In a somewhat more humid environment, they found that an estimated ~25% future increase of S_{umax} from ~170 mm to 226 mm may lead to reductions in mean and maximum annual Q of ~5%. More pronounced effects were reported at the intra-annual time scale, with reductions of autumn and winter Q by up to ~15%. This was accompanied by up ~15% increases in summer evaporation and 10% decreases in winter groundwater levels. Irrespective of the additional uncertainties in their study introduced by future projections, the much less pronounced effects we found in our analysis are most likely a consequence of the lower absolute magnitude of S_{umax} that remains below 115 mm in the study region. These lower S_{umax} values reflect lower storage requirements in summer, due to a precipitation pattern in the Neckar basin that is more evenly spread throughout the year. In other words, the fact that here ~55 – 60 % of the annual precipitation falls in summer (Fig. 3.3f, k) when it is needed most by vegetation due to high E_p , removes the need for larger S_{umax} as water storage buffer to allow vegetation to survive. However, the lower the magnitude of S_{umax} , the more frequently storage deficits can be overcome by even rather small rainstorms and the less water is (or needs to be) stored. Thus even if the relative changes are similar between Bouaziz et al. (2022) and Tempel et al. (2024) in a somewhat more humid environment and our study, abundant summer precipitation causes absolute S_{umax} fluctuations of less than ± 20 mm over time in the Neckar. This in turn limits the influence of the changes on the hydrological response, which has wider implications on the use of models in the Neckar basin and potentially in other temperate regions with similar hydro-climatic characteristics. More specifically, it has been argued that a changing climate will affect the properties of terrestrial hydrological systems (e.g. Stevenson et al., 2021). As these properties are represented by typically time-invariant parameters in hydrological or land surface models, accounting for changing system properties with time-variable formulations of parameters may facilitate more reliable predictions. For many model parameters such a time-variable formulation to estimate their future values is not trivial due to frequently insufficient data and a general lack of

mechanistic understanding of the underlying processes. The estimation of S_{umax} and its temporal evolution based on observed historical or projected future water balance data opens an opportunity to estimate its magnitude under future conditions for use in models. However, in contrast to the findings in other regions (e.g. Merz et al., 2011) and as discussed above, adapting S_{umax} to changing conditions in the Neckar basin does not lead to improved modelled representations of the hydrological response. It is therefore plausible to assume that the use of a time-variable parameter S_{umax} does not substantially improve future predictions and is thus not necessarily required for at least the next few decades to come and that the use of a long-term average S_{umax} , obtained either by calibration or based on the water balance is sufficient in the Neckar basin and in hydro-climatically similar regions. This in itself is already an interesting finding as it gives modelers process-based evidence that the use of time-invariant S_{umax} as model parameter will be also sufficient for meaningful hydrological predictions in the near future in such an environment. However, it can also be expected that in more arid regions with less summer precipitation and generally higher S_{umax} (see e.g. Gao et al., 2014c; Stocker et al., 2023) changes in S_{umax} will play a more prominent role.

3.7 CONCLUSIONS

The catchment-scale root zone storage capacity (S_{umax}) is a critical factor reflecting the moisture exchange between land and atmosphere as well as the hydrological response in terrestrial hydrological systems. However, as a major knowledge gap, it is unclear if S_{umax} at the catchment-scale evolves over time, reflecting vegetation adaptation to changing climatic conditions. As a consequence, it also remains unclear how potential changes in S_{umax} may affect the partitioning of water fluxes and as a consequence, the catchment-scale hydrological response. In this study, for the upper Neckar catchment, based on long-term daily hydrological data (1953 – 2022), we quantify and analyze how S_{umax} dynamically evolves over multiple decades reflecting vegetation adaptation to climate variability and the effects on the hydrological system.

The main findings of this analysis are the following:

1. S_{umax} has fluctuated by ± 20 % between 95 and 115 mm, in response to climatic variability over the 70-year study period.
2. Estimates of S_{umax} obtained from both methods, i.e. based on water balance data and as model calibration parameter, respectively, were with differences of $\sim 5\%$ highly consistent with each other and correlated in time ($R^2 = 0.95$, $p = 0.05$). Findings (1) and (2) support the hypothesis that S_{umax} , even in temperate, humid climates such as in the Neckar basin, significantly changes over multiple decades, reflecting vegetation adaptation to climatic variability.
3. The estimated fluctuations of S_{umax} were inconsistent with the temporal sequence of observed deviations $\Delta I_E \sim \pm 0.02$ from the expected I_E over the study period ($R^2 = 0.02$, $p = 0.85$).
4. As a consequence, replacing a long-term average, time-invariant parameter S_{umax} in a hydrological model with a time variable formulation of S_{umax} does not lead to

a better representation of the observed ΔI_E . Based on (3) and (4), the hypothesis that S_{umax} affects the long-term partitioning of drainage and evaporation and thus controls deviations ΔI_E from the catchment-specific trajectory in the Budyko space therefore needs to be rejected for the Neckar basin.

5. Replacing time-invariant S_{umax} with a time-variable S_{umax} in the hydrological model leads to only very minor improvements of the model to reproduce streamflow dynamics. The hypothesis that a time-dynamic implementation of S_{umax} improves the representation of streamflow in the hydrological therefore also needs to be rejected for the Neckar basin.

Overall, this analysis is the first to systematically document the temporal evolution of S_{umax} , and although limited to the Neckar basin, it provides clear quantitative evidence that S_{umax} can significantly change over multiple decades reflecting vegetation adaptation to climate variability. However, these changes do not cause deviations from the long-term average Budyko curve under changing climatic conditions. This implies that the temporal evolution of S_{umax} does not control variation in the partitioning of water fluxes and has no significant effects on fundamental hydrological response characteristics of the Upper Neckar basin. As the use of time-variable S_{umax} over the 70-year study period does not improve performance of the hydrological model, it can plausibly be assumed that in the study region the use of time-invariant S_{umax} as model parameter will be sufficient for meaningful predictions over at least the next few decades.

TRANSPORT MODEL AND TRACERS: NO EVIDENCE FOR UNDERESTIMATION OF CATCHMENT TRANSIT TIMES INFERRED BY WATER STABLE ISOTOPES IN SAS FUNCTION MODELS

Rivers know this: there is no hurry. We shall get there someday.

A.A. Milne

This chapter is based on:

Wang, S. et al. "Stable water isotopes and tritium tracers tell the same tale: no evidence for underestimation of catchment transit times inferred by stable isotopes in StorAge Selection (SAS)-function models". In: *Hydrology and Earth System Sciences* 27.16 (2023), pp. 3083–3114. ISSN: 1607-7938. DOI: [10.5194/hess-27-3083-2023](https://doi.org/10.5194/hess-27-3083-2023).

SUMMARY

Stable isotopes ($\delta^{18}\text{O}$) and tritium (^3H) are frequently used as tracers in environmental sciences to estimate age distributions of water. However, it has previously been argued that seasonally variable tracers, such as $\delta^{18}\text{O}$, generally and systematically fail to detect the tails of water age distributions and therefore substantially underestimate water ages as compared to radioactive tracers, such as ^3H . In this chapter, based on a >20-year record of hydrological, $\delta^{18}\text{O}$ and ^3H data, the above postulate together with the potential role of spatial aggregation effects to exacerbate the underestimation of water ages were systematically scrutinized. This was done by comparing water age distributions inferred from $\delta^{18}\text{O}$ and ^3H with a total of 21 different model implementations, including time-invariant, lumped parameter sine-wave (SW) and convolution integral models (CO) as well as SAS-function models (P-SAS) and a SAS-function integrated into the hydrological model described in Chapter 2 (IM-SAS).

It was found that, indeed, water ages inferred from $\delta^{18}\text{O}$ with commonly used SW and CO models are with mean transit times (MTT) $\sim 1 - 2$ years substantially lower than those obtained from ^3H with the same models, reaching MTTs ~ 10 years. In contrast, several implementations of P-SAS and IM-SAS models did not only allow simultaneous representations of storage variations and stream flow as well as $\delta^{18}\text{O}$ and ^3H stream signals, but water ages inferred from $\delta^{18}\text{O}$ with these models were with MTTs $\sim 11 - 17$ years much higher and similar to those inferred from ^3H , which suggested MTTs $\sim 11 - 13$ years. Characterized by similar parameter posterior distributions, in particular for parameters that control water age, P-SAS and IM-SAS model implementations individually constrained with $\delta^{18}\text{O}$ or ^3H observations, exhibited only limited differences in the magnitudes of water ages in different parts of the models as well as in the temporal variability of TTDs in response to changing wetness conditions. This suggests that both tracers lead to comparable descriptions of how water is routed through the system. These findings provide evidence that allowed us to reject the hypothesis that $\delta^{18}\text{O}$ as a tracer generally and systematically “cannot see water older than about 4 years” and that it truncates the corresponding tails in water age distributions, leading to underestimations of water ages. Instead, our results provide evidence for a broad equivalence of $\delta^{18}\text{O}$ and ^3H as age tracers for systems characterized by MTTs of at least 15 – 20 years. The question to which degree aggregation of spatial heterogeneity can further adversely affect estimates of water ages remains unresolved as the lumped and distributed implementations of the IM-SAS model provided inconclusive results.

Overall, this study demonstrates that previously reported underestimations of water ages are most likely not a result of the use of $\delta^{18}\text{O}$ or other seasonally variable tracers per se. Rather, these underestimations can be largely attributed to choices of model approaches and complexity not considering transient hydrological conditions next to tracer aspects. Given the additional vulnerability of time-invariant, lumped SW and CO model approaches in combination with $\delta^{18}\text{O}$ to substantially underestimate water ages due to spatial aggregation and potentially other, still unknown effects, we therefore advocate to avoid the use of this model type in combination with seasonally variable tracers if possible, and to instead adopt SAS-based models or time-variant formulations of CO models.

4.1 INTRODUCTION

AGE distributions of water fluxes (“transit time distributions”, TTD) and water stored in catchments (“residence time distributions”, RTD) are fundamental descriptors of hydrological functioning (Botter et al., 2011; Sprenger et al., 2019) and catchment storage (Birkel et al., 2015). They provide a way to quantitatively describe the physical link between the hydrological response of catchments and physical transport processes of conservative solutes. While the former is largely controlled by the celerities of pressure waves propagating through the system, the latter, in contrast, occur at velocities that can be up to several orders of magnitude lower (McDonnell and Beven, 2014; Hrachowitz et al., 2016).

Water age distributions cannot be directly observed. Instead, they can, in principle, be inferred from observed tracer breakthrough curves. While practically feasible at lysimeter (e.g. Asadollahi et al., 2020; Benettin et al., 2021) and small hillslope scales (e.g. Kim et al., 2022), lack of adequate observation technology together with logistical constraints make this problematic at scales larger than that. At the catchment-scale, estimates of water age distributions are therefore typically inferred from models that describe the relationships between time-series of observed tracer input and output signals.

Over the past decades a wide spectrum of such models has been developed. Early approaches often relied on simple lumped sine-wave (hereafter: SW) or lumped parameter convolution integral models (hereafter CO; Małoszewski and Zuber, 1982; Małoszewski et al., 1983; McGuire and McDonnell, 2006), originally developed for aquifers. In spite of their wide-spread application, these models feature multiple critical simplifying assumptions. Most importantly, the vast majority of these model implementations work under the assumption that water storage in catchments is at steady state and that, as a consequence, TTDs are time-invariant and can be *a priori* defined or calibrated. While the role of storage as first order control on water ages was described early in the general definition of mean turnover times (e.g. Eriksson, 1958; Bolin and Rodhe, 1973; Nir, 1973), the steady state assumption, i.e. constant storage, may have limited effect on TTDs in aquifers, as the fraction of transient water volumes in such systems is typically rather low. However, given the temporal variability in the hydro-meteorological system drivers (e.g. precipitation, atmospheric water demand) and the spatial heterogeneity in near-surface hydrological processes, this assumption is violated in most surface water systems world-wide and can lead to misinterpretations of the model results. This triggered the development of a more coherent framework to estimate water age distributions without the need of an *a priori* definition of time-invariant TTDs. Instead, probability distributions, referred to as StorAge Selection (SAS) functions, are *a priori* defined or calibrated, and changes in water storage are explicitly accounted for. Thus, water fluxes within and released from the system are sampled from water volumes of different ages stored in the system according to these SAS functions (Botter et al., 2011; Rinaldo et al., 2015). The general concept is firmly rooted in the development of hydro-chemical routing schemes for the Birkenes, HBV or similar models going back to at least the 1970s (e.g. Lundquist, 1977; Christophersen and Wright, 1981; Christophersen et al., 1982; Seip et al., 1985; De Grosbois et al., 1988a; Hooper et al., 1988; Barnes and Bonell, 1996), as illustrated by Figure 1 in Bergström

et al., 1985). Although functionally very similar to CO model implementations that allow for transient, i.e. time-variant TTDs (Nir, 1973; Niemi, 1977), the sampling procedure based on SAS functions has the advantage to explicitly track the history of water (and tracer) input to and output from the system through the water age balance. As such it does explicitly account for non-steady state conditions, which in turn leads to the emergence of time-variable TTDs and RTDs (see review Benettin et al. (2022)).

Irrespective of the modelling approach, two types of environmental tracers have in the past been frequently used to estimate water age distributions with the above models. The first type are tracers that are characterized by distinct differences in their seasonal signals. They include stable isotopes of water (^2H , $\delta^{18}\text{O}$; e.g. Małoszewski et al., 1983; Vitvar and Balderer, 1997; Fenicia et al., 2010) or solutes, such as Cl^- (e.g. Kirchner et al., 2001; Kirchner et al., 2010; Shaw et al., 2008; Hrachowitz et al., 2009a, Hrachowitz et al., 2015). With these tracers, water ages and (metrics of) their distributions can be estimated by the degree to which the seasonal amplitudes of the precipitation tracer concentrations are time-shifted and/or attenuated in the stream flow (McGuire and McDonnell, 2006; Kirchner, 2016). Broadly speaking, the stronger the attenuation of the seasonally variable tracer amplitude in stream flow (A_s) as compared to its amplitude in precipitation (A_p), i.e., the lower the amplitude ratio A_s/A_p , the older stream water is, on average. The second type of commonly used tracers are radioactive isotopes, such as tritium (^3H). Forming the basis for many water dating studies going back to the 1950s (e.g. Begemann and Libby, 1957; Eriksson, 1958; Dinçer et al., 1970; Stewart et al., 2007; Morgenstern et al., 2010; Duvert et al., 2016; Gallart et al., 2016; Rank et al., 2018; Visser et al., 2019), water age can be estimated with radioactive tracers based on the level of radioactive decay experienced by precipitation input signals experience before they reach the stream.

The relationship between the tracer amplitude ratios A_s/A_p and water age that is exploited by seasonally variable tracers is highly non-linear. With increasing attenuation of the tracer signal in the stream, i.e., a lower A_s/A_p , water therefore does not only become older but the age estimates become more sensitive to changes in the amplitude ratio (Kirchner, 2016). This implies that the older the water, uncertainties in the observed amplitude ratios lead to increased uncertainties in water age estimates. As a consequence, there is an upper limit to the age of water which can be practically and feasibly determined with seasonally variable tracers. A rare attempt to quantify this potential upper detectable age limit was reported by DeWalle et al. (1997). With an observed $\delta^{18}\text{O}$ precipitation amplitude $A_p = 3.41\text{‰}$, an assumed lowest possible $\delta^{18}\text{O}$ stream water amplitude that equaled the observational error $A_s = 0.1\text{‰}$, and the use of a lumped, time-invariant exponential TTD (“complete mixing”) they determined a maximum detectable mean transit time (MTT) of around 5 years at their study site. Several authors subsequently emphasized that estimates of MTT and in particular of maximum detectable MTT such as reported by DeWalle et al. (1997) are specific to A_p at individual study sites (McGuire and McDonnell, 2006) and highly sensitive to choices in the modelling process (Stewart et al., 2010; Seeger and Weiler, 2014; Kirchner, 2016). For example, multiple previous studies demonstrated that the use of gamma distributions with a shape parameter $\alpha \sim 0.5$ as TTD produces model results that are more consistent with observed tracer data than the use of exponential distributions

(i.e. $\alpha = 1$) in a wide range of contrasting environments world-wide (Kirchner et al., 2001; Godsey et al., 2010; Hrachowitz et al., 2010b; Hrachowitz et al., 2010a). Merely replacing the exponential distribution by a gamma distribution with $\alpha = 0.5$ as TTD at the study site of DeWalle et al., 1997 leads, in a quick back-of-the-envelope calculation, to a substantial increase of the maximum MTT from the reported 5 years to ~ 90 years. This is exacerbated by the potential presence of spatial aggregation bias in the lumped implementation of that model, which may cause further considerable underestimation of MTT as demonstrated by Kirchner (2016).

The relevance of the above assumptions is often overlooked and in spite of little additional quantitative evidence, it remains widely assumed that water ages in systems characterized by MTTs $> 4 - 5$ years cannot be meaningfully quantified with seasonally variable tracers. Most notably, Stewart et al., 2010; Stewart, 2012 argued that water older than that remains hidden to stable water isotopes and other seasonally variable tracers, which inevitably results in a misleading truncation of water age distributions. Such a pronounced and systematic underestimation of water ages would have far reaching consequences for estimates of water storage (e.g. Birkel et al., 2015; Pfister et al., 2017) and the associated turnover times of nutrients and contaminants in catchments (e.g. Harman, 2015; Hrachowitz et al., 2015). Stewart (2012), further argue that the use of radioactive tracers, such as ^3H , can largely avoid the truncation of the long tails of TTDs. This is mostly owed to the ^3H half-life of $T_{1/2} = 12.32$ years. Even with the current atmospheric ^3H concentrations that, after peaking in the early 1960s, have been converging back towards pre-nuclear bomb testing levels, precipitation ^3H signals can be detected in the system for several decades, making ^3H an effective tracer now and for the foreseeable future (Michel et al., 2015; Harms et al., 2016; Stewart and Morgenstern, 2016). Indeed, a range of studies, based on ^3H and often in conjunction with lumped parameter convolution integral approaches, suggest that many catchments and larger river basins world-wide are characterized by MTTs that are decadal or higher (e.g. Stewart et al., 2010 and references therein). It is further rather remarkable that such elevated water ages are largely absent in estimates derived from lumped parameter convolution integral studies based on seasonally variable tracers, which often indicate MTTs between 1 – 3 years (e.g. McGuire and McDonnell, 2006 and references therein; Hrachowitz et al., 2009b; Godsey et al., 2010), as correctly and importantly pointed out by Stewart et al. (2010). This in itself could be supporting evidence for the failure of seasonally variable tracers to detect long tails of TTDs, as postulated by Stewart et al. (2012). However, it could just as well be a mere artifact arising from a sample bias due to the different catchments analyzed or from choices in the modelling process. There are only a few studies that have directly and systematically compared estimates of water age derived from both, seasonally variable (^2H , ^{18}O) and radioactive tracers (^3H) at the same study site and based on (at least partly) comparable model approaches (Małoszewski et al., 1983; Uhlenbrook et al., 2002; Stewart et al., 2007; Stewart and Thomas, 2008). The MTT estimates derived from seasonally variable tracers in these comparative studies are consistently, but to varying degrees lower than estimates based on ^3H . However, these studies are nevertheless subject to limitations that may weaken the generality of the conclusion that seasonally variable tracers underestimate catchment water ages. More specifically, tracer data were available for only rather short time periods of about 2 – 3

years, including, for some studies, only a handful of ^3H data points. Many these studies relied on lumped parameter convolution integral approaches with time-invariant TTDs whose pre-defined functional form when applied with seasonally variable tracers was limited to shapes (e.g. exponential) that already a priori precluded the representation of heavy-tails and thus a meaningful representation of old ages. In addition, the models to estimate water ages in these studies were implemented in a spatially lumped way, which further exacerbates the potential for underestimating water ages due to spatial aggregation effects in environments that are likely subject to considerable heterogeneity in hydrological functioning (Kirchner, 2016).

Addressing some of the concerns above, a recent study by Rodriguez et al. (2021) compared catchment water ages inferred from two-year data records of a seasonally variable tracer (^2H ; 1088 data points) and ^3H (24 data points) using a spatially lumped implementation of a previously developed simple tracer circulation model based on the SAS approach, which generates time-variable TTDs (Rodriguez and Klaus, 2019). In spite of consistently higher age estimates obtained from ^3H , the absolute differences to ^2H inferred estimates were very minor. While the difference in mean transit times was estimated at $\Delta\text{MTT} \sim 0.22$ years for MTTs ~ 3 years, the difference in the estimate of the 90th percentile of water ages, as metric for the presence of old ages, was with $\Delta 90^{\text{th}} \sim 0.15$ years even lower. The authors concluded that these results cast some doubt on “[...] the perception that stable isotopes systematically truncate the tails of TTDs” (Rodriguez et al., 2021). However, their interpretation was questioned by Stewart et al. (2021), who pointed out that simply no older water may be present in their study catchment.

Building on the above work of Rodriguez et al. (2021), the objective of this chapter is therefore to further scrutinize the notion that the use of seasonally variable tracers leads to truncated estimates of water age distributions in a systematic comparative experiment. The novel aspects of this analysis for the $\sim 13,000 \text{ km}^2$ Neckar River basin in South-West Germany, described briefly in Chapter 2, include: (1) long-term records, i.e. > 20 years, of hydrological data as well as of seasonally variable (^{18}O) and radioactive tracers (^3H) together with (2) a suite of lumped and spatially semi-distributed implementations of (3) SW, CO and SAS-function based models, including a formulation of an integrated, process-based model to simultaneously reproduce hydrological and tracer response dynamics and to track temporally variable water age distributions in the system. The above points allow to, at least partially, explore several unresolved questions how different factors may or may not contribute to the apparent underestimation of water ages by seasonally variable tracers, including potential effects of uncertainties arising from short data records, spatial aggregation and the use of oversimplified time-invariant, lumped models. More specifically, the hypothesis is tested that ^{18}O as tracer generally and systematically cannot detect tails in water age distributions and that this truncation leads to systematically younger water age estimates than the use of ^3H .

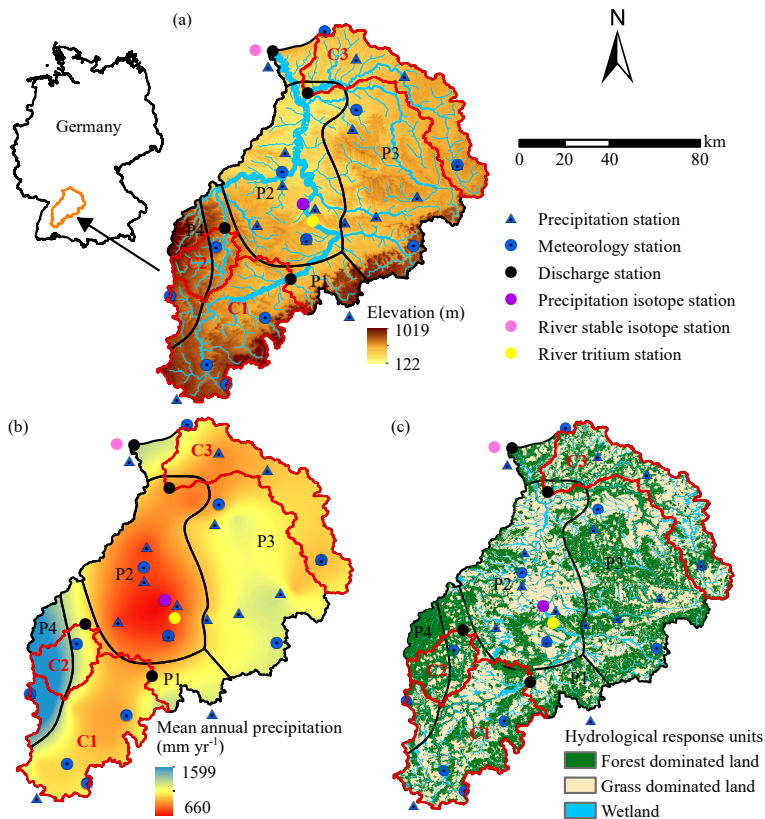


Figure 4.1: (a) Elevation of the Neckar catchment with discharge and hydro-meteorological stations as well as the water sampling locations used in this study, (b) the spatial distribution of long-term mean annual precipitation in the Neckar catchment and the stratification into four distinct precipitation zones P1 – P4 (black line), (c) hydrological response units classified according to their land-cover and topographic characteristics.

4.2 DATA

4.2.1 DATASETS

Daily hydro-meteorological data were available for the period 01/01/1970 – 31/12/2016. As the forcing data of the hydrological models, daily precipitation and daily mean air temperature were obtained from stations operated by the German Weather Service (DWD). Precipitation was recorded at 16 stations and temperature measurements were available at 12 stations (Fig. 4.1) in or close to the study basin. Daily mean discharge data for the period 01/01/1970 – 31/12/2016 at the outlet of the Neckar basin at Rockenau station were provided by the German Federal Institute of Hydrology (BfG). In addition, data of daily mean discharge for the same time period from three sub-catchments within the Neckar basin (Fig. 4.1) at the gauges Kirchentellinsfurt (C1; 2324 km²), Calw (C2; 584 km²) and Untergriesheim (C3; 1827 km²) were available from the Environmental Agency of the Baden-Württemberg region (LUBW).

Long-term volume-weighted monthly $\delta^{18}\text{O}$ data in precipitation was available for the period 01/01/1978 – 31/12/2016 at the Stuttgart station. At the sampling gauge, a monthly accumulation bottle was filled with the collected daily precipitation, and all collected water was mixed together. Therefore, the water samples of precipitation reflect the volume-weighted monthly isotopic composition. Then, a monthly isotope sample bottle for stable isotope (i.e., ^{18}O) was filled with 50 ml precipitation water from the corresponding monthly accumulation bottle. All precipitation samples were tightly sealed and stored in a dark room at $\sim 4^\circ\text{C}$ before analysis. Monthly stream water samples were collected at Schwabenheim, close to the Rockenau discharge station, by the BfG for the period of 01/10/2001 – 31/12/2016 (Schmidt et al., 2020; Königer et al., 2022). Note that the available data do not represent instantaneous grab samples but bulk samples from mixed daily samples. River water was sampled automatically by samplers (SP III-XY-36, Maxx Meb- und Probenahmetechnik GmbH, Germany), which contained 36 bottles (each with a volume of 2.5 L). Every 30 minutes, 50 ml river water was pumped into one bottle (48 subsamples per day). A new bottle was filled every 24 h with the same procedure. All daily river water samples were stored in the sample compartment at $\sim 4^\circ\text{C}$ and were subsequently combined into monthly samples in the laboratory of BfG. This means the stream water samples reflect a non-flow-weighted monthly average isotopic composition. The stable isotopes ratios were analyzed with dual-inlet mass spectrometry and a laser-based cavity ring-down spectrometer (L2120-i/L2130-i, Picarro Inc.) at Helmholtz Zentrum München, Germany. When changing from dual-inlet mass spectrometry to cavity ring-down spectrometry, the long-term precision of the analytical systems ($\pm 0.15\text{‰}$ and $\pm 0.1\text{‰}$, respectively, for $\delta^{18}\text{O}$) was ensured (Stumpp et al., 2014; Reckerth et al., 2017).

Long-term monthly ^3H data in precipitation were obtained for the period 01/01/1978 – 31/12/2016 at Stuttgart station (same station as ^{18}O data in precipitation; Schmidt et al., 2020). For the purpose of establishing robust initial conditions for the model experiment (see section 4.4.2) the tritium record in precipitation was reconstructed for the preceding 1970–1977 period by bias correcting data from the sampling station Vienna, available from the Global Network of Isotopes in Precipitation which is a joint database of the International Atomic Energy Agency (IAEA) and the World

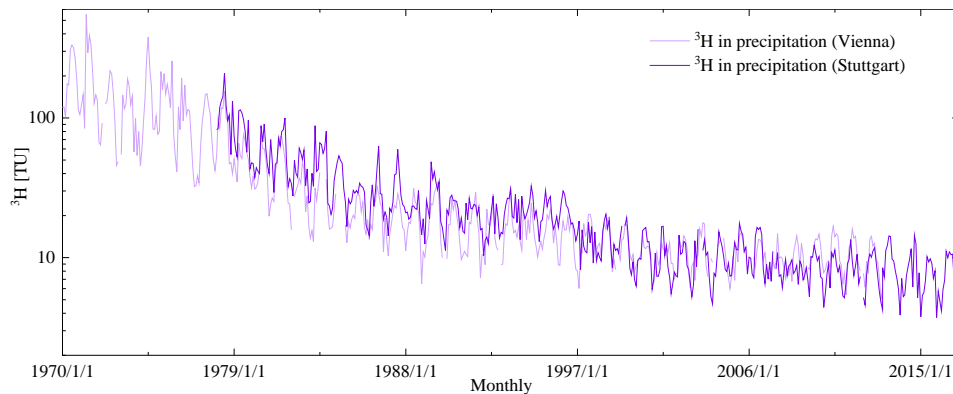


Figure 4.2: Long term ^3H data in precipitation at Vienna station and Stuttgart (thin violet line for Vienna station and dark violet line for Stuttgart station).

Metrological Organization (WMO) (Fig. 4.2). The precipitation for tritium data was sampled based on the same method as that for ^{18}O in precipitation which means that the precipitation samples for tritium also reflect the volume-weighted monthly isotopic composition. Stream water samples for tritium were collected based on the same method as that for ^{18}O in stream. Therefore, tritium stream water samples also reflect non-volume-weighted monthly average isotopic compositions. The tritium stream water samples are not influenced by water release from nuclear power stations. All water samples were analyzed for tritium concentrations by the BfG Environmental Radioactivity Laboratory using liquid scintillation counters (Ultima Gold LLT) with a 2-sigma analytical uncertainty (Schmidt et al., 2020).

Land use types of the catchments are determined using the CORINE Land Cover data set of 2018 (<https://land.copernicus.eu/pan-european/corine-land-cover>). The 90 m \times 90 m digital elevation model of the study region (Fig. 4.1a) was obtained from <https://www.usgs.gov/> and used to derive the local topographic indices including height above nearest drainage (HAND) and slope.

4.2.2 DATA PRE-PROCESSING

For the subsequent model experiment (section 4.4.2), the basin was stratified into four regions P1 – P4 that are characterized by distinct long-term precipitation pattern (hereafter: precipitation zones) as defined in Chapter 2. In the following the procedure to estimate the associated differences in $\delta^{18}\text{O}$ and ^3H input is described.

SPATIAL EXTRAPOLATION OF PRECIPITATION $\delta^{18}\text{O}$ TO PRECIPITATION ZONES

Records of observed precipitation $\delta^{18}\text{O}$ are available at one location close to the center of the Neckar Basin (Fig. 4.1). However, it is well described (e.g. Kendall and McDonnell, 2012) that precipitation $\delta^{18}\text{O}$ input can be subject to considerable spatial heterogeneity, largely controlled by topographic and meteorological influences. Stumpp et al., 2014 specifically identified latitude, elevation and temperature as the key factors controlling $\delta^{18}\text{O}$ input heterogeneity in the greater study region. To at least partially account for

these effects and to locally adjust $\delta^{18}\text{O}$ input signals throughout the study basin, we made use of the sinusoidal isoscapes method (Allen et al., 2018, Allen et al., 2019). Briefly, this method exploits the seasonal pattern in $\delta^{18}\text{O}$ precipitation signal by fitting sine functions to observed $\delta^{18}\text{O}$ input signals for a large sample of locations:

$$\delta^{18}\text{O}_P(t) = a_P \sin(2\pi t - \phi_P) + b_P \quad (4.1)$$

with a_P [‰] the amplitude of the seasonal precipitation signal, b_P [‰] a constant offset and ϕ_P [rad] the phase of the signal. For each of the three fitting parameters, i.e., a_P , b_P and ϕ_P , multiple regression relationships were previously developed (Allen et al., 2018). Depending on the fitting parameter, predictor variables included a selection of latitude, longitude, elevation, range of annual temperature range and mean annual precipitation (Allen et al., 2018). The relationships defined by these predictor variables then allow to estimate a_P , b_P and ϕ_P , and thus the seasonal signal of $\delta^{18}\text{O}_P$ for locations where no precipitation $\delta^{18}\text{O}$ observations are available.

Here, we adopted the method as described in the following. In a first step, we estimated the sine wave parameters for the time series of precipitation $\delta^{18}\text{O}$ observed at the station Stuttgart, using the procedure described by Allen et al., 2018. Subsequently, we estimated the associated sine wave parameters a_P , ϕ_P and b_P in each of the four precipitation zones (P1 – P4; Table 4.2) based on following Eqs. 4.2 – 4.4, using the above-described individual predictor variables, averaged for each precipitation zone (Table 4.2). We then used the estimated sine wave parameters to construct an individual $\delta^{18}\text{O}_P$ sine wave for each precipitation zone (Eq. 4.1). In a last step, we adjusted the observed $\delta^{18}\text{O}$ input for the four precipitation zones by rescaling and bias correcting the observed $\delta^{18}\text{O}$ signal according to the differences between the sine waves at the observation station and sine waves estimated for each precipitation zone, respectively (Fig. 4.3).

$$a_P = (-7.90 \cdot 10^{-6}) \cdot La_P + (-2.62 \cdot 10^{-6}) \cdot Lo_P + 0.0006 \cdot H_P + 0.28 \cdot Tr_P - 0.009 \cdot P_P \quad (4.2)$$

$$\phi_P = (-6.29 \cdot 10^{-7}) \cdot La_P + 1.82 \quad (4.3)$$

$$b_P = (3.45 \cdot 10^{-6}) \cdot La_P + (1.19 \cdot 10^{-6}) \cdot Lo_P - 0.002 \cdot H_P - 0.18 \cdot Tr_P - 5.83 \quad (4.4)$$

with La_P [°] latitude, Lo_P [°] longitude, H_P [m] elevation, Tr_P [°C] mean annual range of monthly temperatures, and P_P [cm] mean annual precipitation. Note that all of the above individual spatial predictor variables, averaged for each precipitation zone (P1 – P4) (Table 4.2).

Table 4.1: The sine parameters' predictor variables in different precipitation zones in the Neckar river basin.

Precipitation zone	L_{ap} [°]	L_{op} [°]	H_p [m]	Tr_p [°C]	P_p [cm]
P1	48.42	8.87	568.04	19.90	93.28
P2	48.92	9.12	322.20	20.05	80.87
P3	49.05	9.71	420.53	20.09	88.97
P4	48.56	8.52	673.21	19.76	105.27
Stuttgart station	48.83	9.20	314.00	20.04	69.08

Table 4.2: The estimates of sine parameters for different precipitation zones and Stuttgart station.

	a_p [‰]	ϕ_p [rad]	b_p [‰]
P1	4.64	1.82	-10.55
P2	4.65	1.82	-10.08
P3	4.65	1.82	-10.29
P4	4.56	1.82	-10.73
Stuttgart	4.75	1.82	-10.06

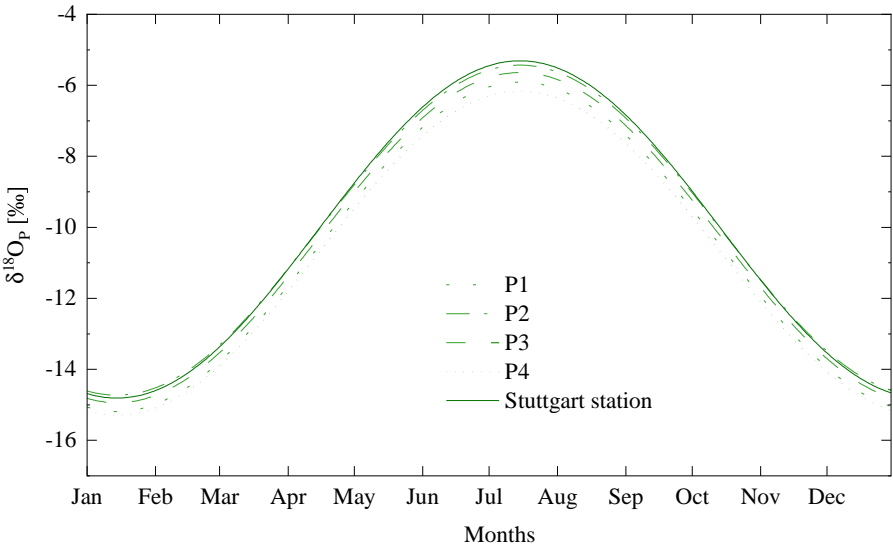


Figure 4.3: The $^{18}\text{O}_p$ sine wave for precipitation zones (P1 – P4) and Stuttgart station.

SPATIAL EXTRAPOLATION OF PRECIPITATION ^3H TO PRECIPITATION ZONES

As for $\delta^{18}\text{O}$, it is well documented that ^3H exhibits spatial heterogeneity that is to some extent controlled by geographical factors. It has been shown that the ^3H concentration in precipitation increases with latitude, with highest concentrations in polar regions (Rozanski et al., 1991). In addition, ^3H concentrations in precipitation increase with elevation due to the ^3H -enriched upper troposphere and isotopic exchange between liquid water and atmospheric moisture, depleting ^3H in lower tropospheric layers (Tadros et al., 2014). Considering the above effects, we established a multiple linear regression relationship between ^3H concentrations in precipitation observed at 15 multiple locations across Germany (Fig. 4.4) as available through the WISER database (IAEA and WMO, 2022; Schmidt et al., 2020), and their corresponding elevation and latitude, respectively (Fig. 4.5). We then used this relationship to adjust the ^3H precipitation input for the four precipitation zones according to their corresponding average latitude and elevation estimate:

$$^3\text{H}_P(t) = -0.75(L_P - L_o) - 0.002(E_P - E_o) + ^3\text{H}_o \quad (4.5)$$

where $^3\text{H}_P$ is the latitude- and elevation-adjusted tritium precipitation concentration for each precipitation zone (P1 – P4), $^3\text{H}_o$ is the tritium precipitation concentration observed at the Stuttgart station, L_P and E_P are the mean latitude and elevation, respectively, of each precipitation zone and L_o and E_o are the latitude and elevation, respectively, of the Stuttgart station.

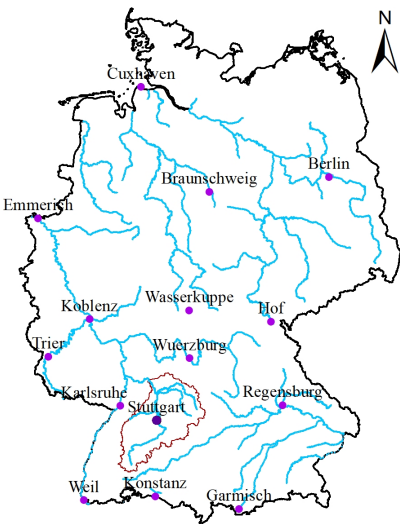


Figure 4.4: ³H concentrations in precipitation observed at 15 multiple locations across Germany.

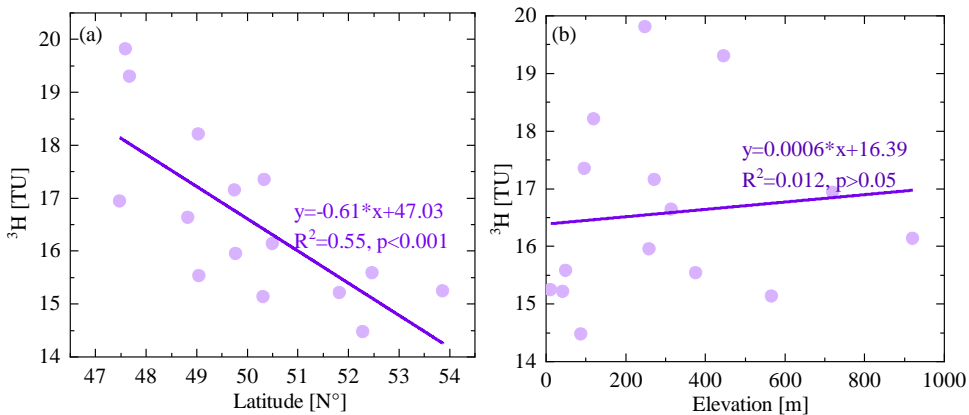


Figure 4.5: The linear regression relationships between ³H concentrations in precipitation observed at 15 locations across Germany with latitude and elevation respectively

4.3 METHODS

The experiment to test the hypothesis that the use of $\delta^{18}\text{O}$ data systematically leads to truncated water age distributions and associated underestimations of water ages is designed and executed in a step-wise approach. 21 different scenarios of model types and spatial implementations thereof are sequentially calibrated and tested to reproduce observed $\delta^{18}\text{O}$ and ^3H signals in stream flow. For each of these models, several metrics of water age distributions resulting from the 2 independent calibration procedures, i.e., for $\delta^{18}\text{O}$ and ^3H , respectively, are then estimated and compared. As a baseline and to ensure comparability with previous studies, water ages are quantified with spatially lumped, time-invariant implementations of twelve commonly used SW/CO model scenarios (Table 4.3): sine-wave models using exponential (SW-EM) and gamma distributions as TTDs (SW-GM; only $\delta^{18}\text{O}$), lumped parameter convolution integral models using exponential (CO-EM) and gamma distributions as TTDs (CO-GM), two parallel reservoirs (CO-2EM), three parallel reservoirs (CO-3EM) as well as an exponential piston flow (CO-EPM) implementation. The above baseline scenarios are complemented by nine additional models on the basis of SAS-functions (Table 4.4). In order of increasing complexity, these include three spatially integrated formulations of a “pure” SAS-function approach with one storage component and based on observed stream flow (P-SAS), three implementations of a spatially integrated hydrological model with tracer routing based on SAS-functions (IM-SAS-L) as well as three spatially distributed implementations of the same integrated hydrological model in combination with SAS-functions (IM-SAS-D).

4.3.1 MODELS

SINE-WAVE MODEL (SW)

As demonstrated by Małoszewski et al. (1983), sine waves fitted to $\delta^{18}\text{O}$ precipitation and stream flow signals can be used to indicatively determine water ages. More specifically, the ratio of the amplitudes of the fitted sine waves, i.e. A_s/A_p , can be used together with the assumption of a shape of the TTD to estimate the associated MTT of a system. In the case of a gamma distribution as TTD, this is done according to (Kirchner, 2016):

$$\bar{\tau} = \alpha\beta, \quad (4.6)$$

with

$$\beta = \frac{1}{2\pi f} \sqrt{(A_s/A_p)^{-2/\alpha} - 1}, \quad (4.7)$$

where τ is the MTT, α is a shape parameter, β is a scale parameter and f here is the frequency for the seasonal $\delta^{18}\text{O}$ signal, i.e., $f = 1 \text{ yr}^{-1}$. Here we analyze the two cases $\alpha = 1$ (SW-EM) and 0.5 (SW-GM). Note that with $\alpha = 1$, the gamma distribution is equivalent to an exponential distribution. The sine wave model is a simplification of a convolution integral model and can be directly derived from that. For a more

detailed description of the method and underlying assumptions we refer to McGuire and McDonnell (2006) and Kirchner (2016).

TIME-INVARIANT, LUMPED PARAMETER CONVOLUTION INTEGRAL MODEL (CO)

While the sine wave approach requires regular cyclic signals of tracer composition, i.e., sine waves fitted to the observations, convolution integral models make direct use of the observed tracer data (e.g. Kreft and Zuber, 1978). Tracer composition in the system output can thus be estimated based on a convolution operation of the tracer composition in the system input together with an *a priori* assumption of a TTD (e.g. Małozewski and Zuber, 1982; Kirchner et al., 2001):

$$C_O(t) = \int_0^\infty g(\tau) C_i(t - \tau) e^{\lambda \tau} d\tau \quad (4.8)$$

where $C_O(t)$ is the tracer composition of the system output (here: stream flow) at time t , $C_i(t - \tau)$ is the tracer composition of the system input (here: precipitation) at any previous time $t - \tau$, λ is the radioactive decay constant ($\lambda = 0.00015 \text{ d}^{-1}$ for ^3H and $\lambda = 0 \text{ d}^{-1}$ for stable isotopes) and $g(\tau)$ is the distribution of transit times τ . Here, we used gamma distributions as basis for a flexible and general formulation of TTDs in the different CO scenarios tested in this study:

$$g(\tau) = \sum_{i=1}^N \eta f_i \frac{\tau^{\alpha-1}}{\beta_i^\alpha \Gamma(\alpha)} e^{\frac{-\tau}{\eta \beta_i} + \frac{1}{\eta} - 1} \text{ for } \tau \geq \tau_m(l - \eta), g(\tau) = 0 \text{ otherwise} \quad (4.9)$$

with the α and β_i being the shape and scale parameters, respectively, f_i the fraction of the contribution of the i^{th} reservoir, so that $\sum f_i = 1$ and η the ratio of the exponential volume to the total volume. For a single exponential TTD (CO-EM) with $\alpha = 1$, $N = 1$, $\eta = 1$ and $f_1 = 1$, β_1 was the only calibration parameter. The two parallel exponential TTD model (CO-2EM) with $\alpha = 1$, $N = 2$, $\eta = 1$ and $f_2 = 1 - f_1$, required β_1 , β_2 and f_1 as calibration parameters, while the three parallel exponential TTD model (CO-3EM) with $\alpha = 1$, $N = 3$, $\eta = 1$ and $f_3 = 1 - f_1 - f_2$, required β_1 , β_2 , β_3 as well as f_1 and f_2 as calibration parameters. The exponential piston flow model (CO-EPM) with $\alpha = 1$, $N = 1$ and $f_1 = 1$ was characterized by the two calibration parameters β_1 and η . In contrast, the Gamma distribution model (CO-GM), with $N = 1$, $\eta = 1$ and $f_1 = 1$, used both, α and β_1 as free calibration parameters.

The MTTs associated with the above parameters in the individual model implementations are then obtained with Eq. 4.10.

$$\bar{\tau} = \sum_{i=1}^N f_i \alpha \beta_i \quad (4.10)$$

For more detailed description of the method and the individual shapes of TTDs considered here, refer to McGuire and McDonnell (2006).

Table 4.3: The 12 time-invariant, lumped SW/CO model scenarios here implemented for the Neckar study basin together with the associated calibration strategies, the individual calibration performance metric, the type of models as well as the prior parameter ranges and the optimal parameter value from calibration. SW indicates sine-wave models, CO indicates time-invariant, lumped parameter convolution integral models. EM represents an exponential TTD and GM indicates a gamma distribution TTD. 2EM indicates a two parallel linear reservoir model, 3EM indicates a three parallel linear reservoir model and EPM indicates an exponential piston flow model. The calibration strategies show which variable a model was calibrated to using the Mean Square Error (MSE) with C_{18O} calibration to the observed stream water $\delta^{18}O$ signal and C^3H calibration to observed stream water 3H . *) Note, that for SW models calibration involves least-square fits of sine waves to both, the precipitation and stream flow signals available. †) fixed to a value of 1.

Scenario		1	2	3	4	5	6	7	8	9	10	11	12
Model		SW-EM	SW-GM	CO-EM	CO-GM	CO-2EM	CO-3EM	CO-EPM					
Signature	Calibration strategy → Performance metric ↓	$C_X^*)$	$C_X^*)$	$C_{\delta^{18}O}$	C^3H	$C_{\delta^{18}O}$	C^3H	$C_{\delta^{18}O}$	C^3H	$C_{\delta^{18}O}$	C^3H	$C_{\delta^{18}O}$	C^3H
Times series $\delta^{18}O$	MSE $_{\delta^{18}O}$	•	•	•	-	•	-	•	-	•	-	•	-
Time series 3H	MSE $_{^3H}$	-	-	-	•	-	•	-	•	-	•	-	•
Parameter		Prior range		Optimal parameter value									
A_p (‰)	-*)	2.69											
A_s (‰)	-*)	0.57											
α (-)	0.1 – 2	-	-	1†)	1†)	0.44	0.58	1†)	1†)	1†)	1†)	1†)	1†)
β_1 (d)	1 – 15000	-	-	513	3795	2048	6086	16	84	11	66	662	3665
β_2 (d)	1 – 15000	-	-	-	-	-	-	832	5388	12	112	-	-
β_3 (d)	1 – 15000	-	-	-	-	-	-	-	-	963	5299	-	-
f (-)	0 – 1	-	-	1†)	1†)	1†)	1†)	0.18	0.36	0.06	0.02	1†)	1†)
β_2 (-)	0 – 1	-	-	-	-	-	-	-	-	0.12	0.34	-	-
η (-)	1 – 3	-	-	1†)	1†)	1†)	1†)	1†)	1†)	1†)	1†)	1.91	1.01

SAS-FUNCTION MODELS (P-SAS, IM-SAS)

The storage-age selection function (SAS) concept as outlined by Rinaldo et al., 2015 requires the explicit tracking of water and tracer storage volumes. The age compositions of water fluxes are then sampled from the age composition in the associated storage volume. Two alternative and frequently used approaches to account for the evolution of water storage volumes were explored here: firstly, a “pure” SAS-function model in which the observed stream flow was used to account for changes in water storage volumes (P-SAS) and secondly, an integrated process-based hydrological model that generates stream flow and other fluxes in the system (IM-SAS). Water ages, their distributions, and the associated moments thereof were then estimated by tracking water and tracer fluxes through the models.

HYDROLOGICAL MODEL

The hydrological component of the “pure” SAS-function model (P-SAS) was implemented as described in Benettin et al., 2017a. This model consists of one single storage volume, which receives observed precipitation P as input and releases observed stream flow as output. Evaporation E_A from that storage is modelled following the simplifying assumption that there is negligible storage change over the entire 47-year study period (01/01/1970 – 31/12/2016), as expressed by:

$$E_A(t) = E_P(t) \left(\frac{\bar{P} - \bar{Q}}{\bar{E}_P} \right) \quad (4.11)$$

With \bar{P} and \bar{Q} being long-term mean daily precipitation P (mm d⁻¹) and discharge Q (mm d⁻¹), respectively, and \bar{E}_P the long-term mean daily potential evaporation E_P (mm d⁻¹).

In contrast, the water storage fluctuations and fluxes in the IM-SAS approach were modelled based on the semi-distributed hydrological model developed in Chapter 2. The detailed equations of the model are provided as Table 2.2 in Chapter 2.

TRACER TRANSPORT MODEL

$\delta^{18}\text{O}$ and ^3H were routed through the above-described storage components of both the P-SAS and the IM-SAS (Fig. 2.2 in Chapter 2) models by sampling the observed (i.e. Q in P-SAS) and modeled outflow volumes (i.e. E_a in P-SAS; all outflows in IM-SAS) that leave the individual components at each time step t (d) (e.g. M_{snow} , R_{perc} , E_a , etc.) from the individual water volumes of different age T (d) that are stored in the associated storage component (e.g. S_{snow} , S_u , etc.) at each time step according to a SAS function. The distribution of water volumes of different ages in each storage component, i.e., the residence time distribution RTD, depends on the past sequence of inflows I (mm d⁻¹) and outflows O (mm d⁻¹) and therefore varies over time. As a consequence of being sampled from RTDs that evolve over time, both, inflows I and outflows O are correspondingly characterized by water age distributions (or transit time distributions TTD) that change over time. A straightforward implementation of this SAS concept is facilitated by the formulation of age-ranked storages $S_T(T, t)$ (mm). As emphasized by Benettin et al. (2017a), $S_T(T, t)$ describes “at any time t the cumulative volumes of water

in a storage component as ranked by their age T^n . Correspondingly, the total inflow (I) into as well as the total outflow volumes (O) from different storages can be expressed in terms of their cumulative, age-ranked volumes $I_T(T, t)$ and $O_T(T, t)$ (mm d^{-1}). At any time, closing the resulting water age balance for each storage component j (e.g. S_{snow} , S_u , etc.) also leads to an updated age-ranked storage $S_{T,j}(T, t)$ for that component, formulated as (Benettin et al., 2015c; Rinaldo et al., 2011; Harman, 2015; Van der Velde et al., 2012):

$$\frac{\partial S_{T,j}(T, t)}{\partial t} + \frac{\partial S_{T,j}(T, t)}{\partial T} = \sum_{n=1}^N I_{T,n,j}(T, t) - \sum_{m=1}^M O_{T,m,j}(T, t), \quad (4.12)$$

where $\frac{\partial S}{\partial T}$ is the aging process of water in storage. Here, the water age balance (Eq. 4.12) was formulated individually for each storage reservoir j , also accounting for different numbers N of storage component inflows I (e.g. P_{rain} , M_{snow} , R_{perc}) and numbers M of outflows O (e.g., R_{perc} , R_{pref} , E_a) (Fig. 2.2 in Chapter 2), similar to previous studies (e.g. Hrachowitz et al., 2021). For a daily modelling time step, it can in the water age balance be assumed that precipitation $P(t)$ that is falling on day t is characterized by an age $T = 0$. This implies for the age ranked inflow $I_{T,p,j}(0, t) = P_T(0, t) = P(t)$. Note, that all other age ranked inflows $I_{T,n,j}(T, t)$ that enter a storage component are equivalent to the corresponding age ranked outflows $O_{T,m,j}(T, t)$ that leave a “higher” storage component.

Depending on the total volume of outflow $O_{m,j}(t)$ and the cumulative distribution of ages $P_{o,m,j}(T, t)$ of that flow, an age-ranked outflow $O_{T,m,j}(T, t)$ for each flux m released from each storage component j can be defined as:

$$O_{T,m,j}(T, t) = O_{m,j}(t) P_{o,m,j}(T, t), \quad (4.13)$$

While the outflow $O_{m,j}(t)$ from any storage component j is computed for each time step t by the hydrological model described above, the associated $P_{o,m,j}$ cannot be assumed to be known as it is controlled by the temporally evolving distribution of water ages present in that storage component $S_{T,j}(T, t)$ at t . However, the temporally variable $P_{o,m,j}$ can be inferred for each time step t by defining for each storage j and for each outflow m released from j a SAS function $\omega_{o,m,j}$ together with its cumulative form $\Omega_{o,m,j}$. These functions then describe how the water volumes of different ages, stored in component j at time t , i.e. $S_{T,j}(T, t)$, are sampled and combined into the corresponding total outflow volume $\Omega_{m,j}$:

$$P_{o,m,j}(T, t) = \Omega_{o,m,j}(S_{T,j}(T, t), t), \quad (4.14)$$

The probability density function $p_{o,m,j}(T, t)$ associated with the cumulative distribution of ages $P_{o,m,j}(T, t)$, then represents the transit time distribution TTD of that outflow and can be written as:

$$p_{o,m,j}(T,t) = \bar{\omega}_{(o,m,j)}(S_{T,j}(T,t),t) \frac{\partial S_{T,j}}{\partial T}, \quad (4.15)$$

Conservation of mass dictates that

$$\Omega_{o,m,j}(S_{T,j}(T,t) \rightarrow S_j(t),t) = 1, \quad (4.16)$$

Where S_j (mm) is the total volume of water stored in component j at time t . The resulting need to rescale $\omega_{o,m,j}$ for each time step was here avoided by instead normalizing and therefore bounding the age ranked storage to the interval $[0,1]$ according to

$$S_{T,norm,j}(T,t) = \frac{S_{T,j}(T,t)}{S_j(t)}, \quad (4.17)$$

Note that $S_{T,norm,j}$ also represents the RTD of storage component j at time t . For the P-SAS model implementation in this study, we used power law distributions with one parameter to sample streamflow (k_Q) and evaporation (k_E), respectively, as described by Benettin et al. (2017a). In contrast, we used uniform distributions in the form of $\omega = \text{const.}$ as SAS function in each storage component in the IM-SAS model implementations as previously shown to be effective in many studies (e.g. Birkel et al., 2011; Van der Velde et al., 2015; Benettin et al., 2015b, Benettin et al., 2017a; Ala-Aho et al., 2017; Kuppel et al., 2018; RRodriguez et al., 2018). The latter implies random sampling and the assumption that each storage component is fully mixed and that there is no preference for sampling younger or older water. However, note that due to distinct storage capacities and time-scales of the individual storage components, the “combined” SAS functions of all storage components will *not* lead to an overall fully mixed system response. Uniform SAS functions were here chosen over other shapes, such as beta-distributions (e.g. Van der Velde et al., 2012; Hrachowitz et al., 2021), as they do not need additional model parameters and avoid the need for explicit calculation of TTDs at each model time step to route tracers through the model (Benettin et al., 2015b), thereby drastically reducing computer memory requirements and computational time (Benettin et al., 2022).

To adequately damp tracer input signals, suitable system storage volumes have to be defined as calibration parameters. In the P-SAS implementation the parameter S_{tot} is used, reflecting the initial total system storage (e.g. Benettin et al., 2017a). In contrast, the IM-SAS implementations made use of additional and hydrologically passive storage volumes (e.g. Christophersen and Wright, 1981; Birkel et al., 2010; Hrachowitz et al., 2015, Hrachowitz et al., 2016), which physically represents groundwater volumes below the river bed, as illustrated by Zuber (1986; Fig.1 therein). Such a passive water storage volume $S_{s,p}$ (mm), characterized by $dS_{s,p}/dt = 0$, was thus added as calibration parameter to the active groundwater storage S_s (Fig. 2.2 in Chapter 2). While the outflow Q_s from the groundwater storage is exclusively regulated by the temporally

varying storage volume in S_s (Eq. ?? in Table 2.2, Chapter 2), the tracer and age composition of that outflow is also randomly sampled from the total groundwater storage volume $S_{s,tot} = S_s + S_{s,p}$.

The $\delta^{18}\text{O}$ and ^3H concentrations were then routed through each individual storage component according to (e.g. Harman, 2015; Benettin et al., 2017a):

$$C_{o,m,j}(t) = \int_0^{S_j} C_{s,j}(S_{T,j}(T, t), t) \omega_{o,m,j}(S_{T,j}(T, t), t) e^{-\lambda T} dS_T, \quad (4.18)$$

Where $C_{o,m,j}$ is the tracer concentration in outflow m from storage component j at time t , $C_{s,j}$ is the tracer concentration of water in storage at time t and λ is the radioactive decay constant ($\lambda = 0 \text{ d}^{-1}$ for $\delta^{18}\text{O}$ and $\lambda = 0.00015 \text{ d}^{-1}$ for ^3H).

4

4.3.2 MODEL IMPLEMENTATION

SPATIALLY LUMPED MODEL IMPLEMENTATION

The original argument that the use of seasonally variable tracers underestimates water ages was exclusively based on lumped, time-invariant implementations of sine-wave and convolution integral models (Stewart et al., 2010). For a baseline comparison and to check whether the above conclusion would also have been reached for our study basin using the same methods, we here similarly implemented the sine-wave (SW-EM, SW-GM) and convolution integral (CO-EM, CO-GM, CO-2EM, CO-3EM, CO-EPM) in a spatially lumped way. For this baseline case the catchment average tracer input was estimated as the spatially weighted mean from the four precipitation zones P1 – P4 as described in section 4.2.2. The calibration parameters of the CO implementations are shown in Table 4.3.

The “pure” SAS-model (P-SAS; Table 4.4) and the spatially lumped implementation of the integrated model (IM-SAS-L) were also forced with the same spatially averaged input. In addition, the spatial fractions of the grassland and wetland HRUs for IM-SAS-L, respectively, were set to 0 and the entire study basin therefore represented by one HRU which is equivalent to the forest HRU described in distributed model, similar to many traditional lumped formulations of process-based conceptual models (Bouaziz et al., 2021; Clark et al., 2008; Fenicia et al., 2006; Fovet et al., 2015; Seibert et al., 2010). This implementation has 11 calibration parameters (Table 4.4).

SPATIALLY DISTRIBUTED MODEL IMPLEMENTATION

To balance the need for spatial detail to some extent with the adverse effects of increased parameter uncertainty (e.g. Beven, 2006) and computational capacity (in particular for the calculation of TTDs), we here implemented the integrated model in parallel (IM-SAS-D) in the four precipitation zones P1 – P4 and forced it with the corresponding input (e.g. P , $\delta^{18}\text{O}$ and ^3H) for each precipitation zone as described in section 4.3.2. Each precipitation zone was further discretized (1) into 100 m elevation zones for a stratified representation of the snow storage S_{snow} (e.g. Mostbauer et al., 2018) and (2) into three HRUs, i.e., forest, grassland, wetland (Fig. 2.2 in Chapter 2; e.g. Gharari et al., 2014; Hanus et al., 2021). Rain P_{rain} and melt water M_{snow} from the different elevation zones was aggregated according to their associated spatial weights

in each elevation zone. This total liquid water input was then routed through the three parallel HRUs. The classification into the three HRUs was based on the metric Height-above-nearest-drainage (HAND; Gharari et al., 2011) and land cover. While landscape elements with $\text{HAND} < 5$ m were classified as wetland, all other parts of the landscape were classified as forest or grassland according to land-use data. In total, there are therefore 12 individual, parallel model components, i.e., three HRUs in each of the four precipitation zones, not counting the elevation zones for the snow module. All flux and storage variables of the 12 components are weighted according to their areal fractions. While each of the three HRUs was characterized by individual parameters (e.g. Gao et al., 2016; Prenner et al., 2018), the same parameter values were used in all four precipitation zones in distributed moisture accounting approach (e.g. Ajami et al., 2004; Euser et al., 2015; Hulsman et al., 2021b; Roodari et al., 2021). Overall, the spatially distributed implementation has 19 model parameters, including five global parameters (T_t , C_{melt} , C_a , K_s and $S_{s,p}$) that are identical for each HRU and 14 HRU-specific parameters (Table 4.4; Fig. 2.2 in Chapter 2).

4.3.3 MODEL CALIBRATION AND POST-CALIBRATION EVALUATION

The models were run at a daily time step, whereby the observed volume-weighted monthly tracer concentration in precipitation was used as model input for each day of that month together with the daily data of precipitation. Model performance was evaluated based on the Mean Square Error (MSE) as error metric. The time-invariant, lumped convolution integral models, using uniform prior parameter distributions as shown in Table 4.3, were individually calibrated to the observed $\delta^{18}\text{O}$ (calibration strategy $C_{\delta^{18}\text{O}}$; Table 4.3) and ^3H stream water concentrations ($C_{^3\text{H}}$), respectively. In contrast, a multi-objective calibration approach was applied for the integrated IM-SAS models to simultaneously reproduce stream flow volumes and tracer concentrations thereof (e.g. ^3H and/or $\delta^{18}\text{O}$). Briefly, the model parameters were calibrated by using Borg_MOEA algorithm (Borg Multi-objective evolutionary algorithm; Hadka and Reed, 2013) and based on uniform prior distributions (Table 4.4). The model performances were evaluated based on the models' ability to simultaneously reproduce multiple signatures of stream flow as well as signatures of tracer dynamics as shown in Table 4.6. The sets of pareto optimal solutions obtained from the calibration procedures were then retained as acceptable solutions for the subsequent analysis. To compare the water age distributions (i.e., TTDs and RTDs) and thus to test the research hypothesis, different calibration strategies, $C_{\delta^{18}\text{O},Q}$, $C_{^3\text{H},Q}$ and $C_{\delta^{18}\text{O},^3\text{H},Q}$, were adopted (Table 4.4). While in strategy $C_{\delta^{18}\text{O},Q}$ the models were calibrated to simultaneously reproduce signatures of stream flow and $\delta^{18}\text{O}$, $C_{^3\text{H},Q}$ combined the stream flow signatures with ^3H . In strategy $C_{\delta^{18}\text{O},^3\text{H},Q}$ the model was finally calibrated to simultaneously reproduce the six stream flow signatures, $\delta^{18}\text{O}$, and ^3H dynamics. For each strategy, all performance metrics were also combined into an overall performance metric based on the Euclidian distance (D_E), where $D_E = 0$ indicates a perfect fit. To find a somewhat balanced solution in absence of more detailed information all individual performance metrics were here equally weighted (e.g., Hrachowitz et al., 2021; Hulsman et al., 2021b):

Table 4.4: The 9 P-SAS and IM-SAS model scenarios here implemented for the Neckar study basin together with the associated calibration strategies, the individual calibration performance metrics and the type of spatial implementation (lumped or distributed) as well as the associated prior parameter ranges and the ranges of the pareto optimal solutions from calibration. P-SAS indicates the model with one compartment as described in Benettin et al., 2017a, and IM-SAS indicates the integrated hydrological model based on SAS-functions. The symbols L and D indicate lumped and distributed model implementations, respectively. The calibration strategies show which variables/signatures a model was simultaneously calibrated to using the Mean Square Error (MSE) with $C_{\delta^{18}\text{O}}$ simultaneous calibration to $\delta^{18}\text{O}$ and six signatures of stream flow Q : $C_{\text{H}_2\text{O}}$ simultaneous calibration to ^3H and the signatures of Q : $C_{\delta^{18}\text{O}, ^3\text{H}}$ the simultaneous calibration to $C_{\delta^{18}\text{O}, ^3\text{H}}$ and the signatures of Q : \dagger fixed to a value of 1.

		Scenario			P-SAS			Lumped			IM-SAS-D			Distributed		
		Model	13	14	15	16	17	18	19	20	21					
Implementation																
Signature																
Times series $\delta^{18}\text{O}$																
Time series ^3H																
Time series of stream flow (Q)																
Time series of $\log(Q)$																
Flow duration curve of $Q(FDC_Q)$																
Flow duration curve $\log(Q)$ ($FDC_{\log(Q)}$)																
Seasonal runoff coefficient (RC)																
Autocorrelation function of $Q(AC_Q)$																
Parameter		Prior range	Optimal parameter value													
k_E		0.1-1.0	1 [†]	1 [†]	1 [†]	-	-	-	-	-	-	-	-	-	-	
k_Q		0.1-1.0	0.34	0.28	0.29-0.33	-	-	-	-	-	-	-	-	-	-	
S_{tot} (mm)		100-20000	15595	16638	7414-18245	-	-	-	-	-	-	-	-	-	-	
T_r ($^{\circ}\text{C}$)		-2.5-2.5	-	-	-	-0.94-2.08	-0.88-1.75	-2.15-1.57	-1.84-1.81	-1.74-0.16	-1.92-1.54	-	-	-	-	
C_{melt} (mm $^{\circ}\text{C}^{-1}\text{d}^{-1}$)		1-5	-	-	-	2.32-4.42	1.67-3.96	1.79-3.77	2.30-4.89	1.56-3.25	1.23-4.10	-	-	-	-	
S_{maxF} (mm)		0.1-5	-	-	-	1.53-3.73	1.35-4.39	0.55-4.10	3.18-4.03	2.94-4.98	2.04-4.39	-	-	-	-	
S_{maxG} (mm)		0.1-5	-	-	-	-	-	-	0.30-0.60	0.46-0.70	0.38-1.39	-	-	-	-	
C_a (-)		0.1-0.7	-	-	-	0.24-0.43	0.35-0.55	0.33-0.62	0.30-0.66	0.38-0.52	0.30-0.56	-	-	-	-	
S_{maxF} (mm)		50-500	-	-	-	314-415	236-355	233-464	355-438	301-441	352-485	-	-	-	-	
S_{maxG} (mm)		50-500	-	-	-	-	-	-	161-199	152-287	173-297	-	-	-	-	
S_{maxW} (mm)		50-500	-	-	-	-	-	-	56-149	89-149	85-148	-	-	-	-	
Y_F (-)		0.1-5	-	-	-	0.93-1.68	0.61-1.01	0.57-2.03	0.99-4.59	2.04-3.98	0.76-4.94	-	-	-	-	
Y_G (-)		0.1-5	-	-	-	-	-	-	0.15-0.26	0.23-0.53	0.11-0.52	-	-	-	-	
Y_W (-)		0.1-5	-	-	-	-	-	-	0.14-3.64	0.12-0.32	0.10-2.88	-	-	-	-	
D (-)		0-1	-	-	-	0.30-0.77	0.41-0.81	0.30-0.69	0.03-0.35	0.06-0.33	0.03-0.33	-	-	-	-	
C_{pmaxF} (mm d^{-1})		0.1-4	-	-	-	1.04-2.03	0.98-1.83	1.05-2.62	0.91-3.19	0.94-3.66	1.37-3.72	-	-	-	-	
C_{pmaxG} (mm d^{-1})		0.1-4	-	-	-	-	-	-	0.74-1.80	0.22-1.17	0.93-2.13	-	-	-	-	
C_{max} (mm d^{-1})		0-4	-	-	-	-	-	-	0.00-0.31	0.02-1.06	0.01-0.98	-	-	-	-	
K_{FF} (d^{-1})		0.2-5	-	-	-	0.27-2.99	0.24-1.52	0.31-3.79	0.21-3.03	0.21-0.70	0.50-4.21	-	-	-	-	
K_{FG} (d^{-1})		0.2-5	-	-	-	-	-	-	0.21-4.04	0.25-0.41	0.25-3.66	-	-	-	-	
K_S (d^{-1})		0.002-0.2	-	-	-	0.04-0.19	0.05-0.18	0.05-0.18	0.05-0.17	0.03-0.14	0.05-0.17	-	-	-	-	
S_{3p} (mm)		100-20000	-	-	-	4107-10029	3924-9339	4078-13676	4278-9011	3270-4622	4150-8568	-	-	-	-	

$$D_E = \sqrt{\frac{1}{2} \left(\frac{\sum_{n=1}^N (E_{MSE,Q,n})^2}{N} + \frac{\sum_{m=1}^M (E_{MSE,tracer,m})^2}{M} \right)}, \quad (4.19)$$

Where $N = 6$ is the number of performance metrics with respect to stream flow ($E_{MSE,Q,n}$) and M is the number of performance metrics for tracers ($E_{MSE,tracer,m}$) in each combination (e.g. $M = 1$ for $C_{\delta^{18}O,Q}$, and $C_{^3H,Q}$, $M = 2$ for $C_{\delta^{18}O,^3H,Q}$). Note that the different units and thus different magnitudes of residuals introduce some subjectivity in finding the most balanced overall solution according to D_E (Eq. 4.19). However, a preliminary sensitivity analysis with varying weights for the individual performance metrics in D_E suggested limited influence on the overall results and is thus not further reported here.

After a warm-up period 01/01/1978 – 30/09/2001 the models were calibrated for the 01/10/2001 – 31/12/2009 period. The calibration period was chosen so that observations of all three calibration variables, i.e., Q , 3H and $\delta^{18}O$, are available for the entire calibration period to allow a consistent comparison. The long model warm-up period was deemed necessary to meaningfully approximate the model initial conditions due to the potential and *a priori* unknown relevance of old water in the study basin, and thus to avoid underestimation of water ages inferred from 3H data. The pareto optimal solutions (parameter sets) of the Neckar basin model were then used to test the model in the post-calibration evaluation period 01/01/2010 – 31/12/2016. In addition, the model was tested for its ability to represent spatial differences in the hydrological response by evaluating it against streamflow observations in three sub-catchments (C1 – C3) of the Neckar without further re-calibration whereby each one of them largely represents the hydrological response from one of the precipitation zones (Fig. 4.1). The water age distributions, i.e., TTDs and RTDs, extracted from the individual models and calibration strategies were then estimated based on the corresponding sets of pareto optimal solutions obtained for each calibration strategy.

4.4 RESULTS

4.4.1 MODEL PERFORMANCE

The stream tracer responses of the lumped baseline models were found to be broadly consistent with the available observations (Table 4.6). For the SW models (scenarios 1, 2) in particular the sine wave fitted to the stream water $\delta^{18}\text{O}$ observations provides a robust characterization of the observed signal with $\text{MSE}_{\delta^{18}\text{O}} = 0.121$ and 0.144 ‰ for calibration and model evaluation periods, respectively (Fig. 4.6). Similarly, the CO models (scenarios 3, 5, 7, 9, 11) reproduced the overall pattern of seasonal fluctuations and the degree of dampening of the $\delta^{18}\text{O}$ response (Fig. 4.7). The best performing model, the CO-3EM model, was characterized by $\text{MSE}_{\delta^{18}\text{O}} = 0.171$ and 0.191 ‰ for the calibration and model evaluation periods, respectively while, in comparison, the CO-EM implementation with exhibited considerably higher errors with $\text{MSE}_{\delta^{18}\text{O}} = 0.327$ and 0.432 ‰ (Table 4.6). When used with ^3H data (scenarios 4, 6, 8, 10, 12), the CO models do capture the general decrease in the magnitude of stream water ^3H concentrations although fluctuations at shorter timescales are not well reproduced (Fig. 4.8). The CO-2EM model gives the best performance with $\text{MSE}_{^3\text{H}} = 5.171$ and 3.964 TU^2 for the calibration and evaluation periods, respectively, while the CO-EPM model resulted in $\text{MSE}_{^3\text{H}} = 5.926$ and 5.115 TU^2 (Table 4.6). It is also noted that the models already mimic the ^3H response well in the 1978 – 2001 pre-calibration model warm-up period.

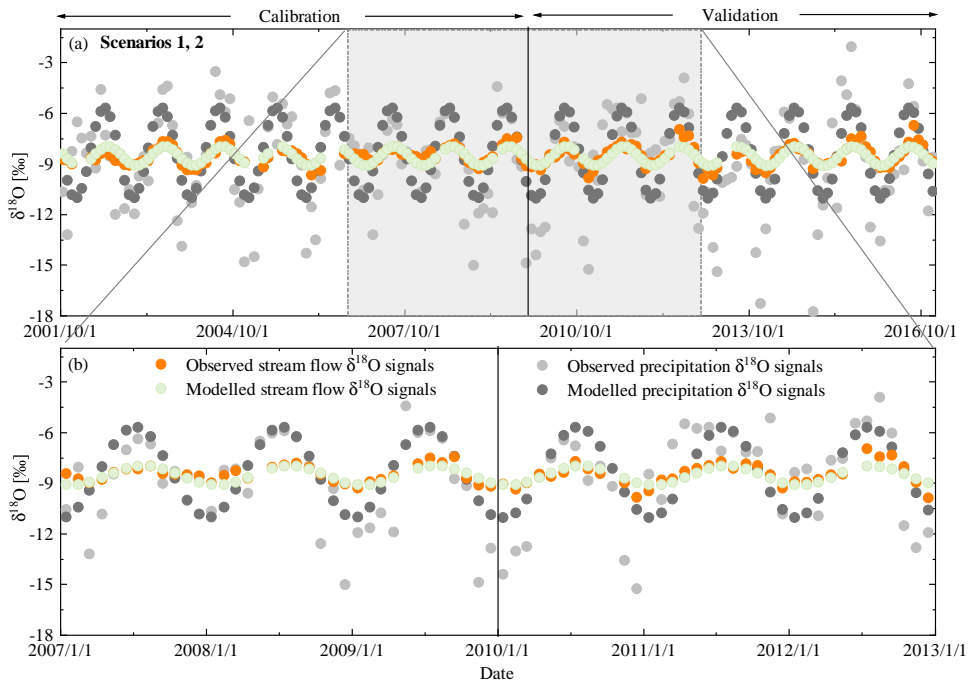


Figure 4.6: The time series of stream $\delta^{18}\text{O}$ reproduced by SW models, i.e., calibration strategy C_x (scenario 1, 2), for the model calibration and evaluation periods. (a) Observed $\delta^{18}\text{O}$ signals in precipitation (light grey dots) and modelled $\delta^{18}\text{O}$ signals in precipitation (dark grey dots), and observed stream $\delta^{18}\text{O}$ signals (orange dots) as well as modelled stream $\delta^{18}\text{O}$ signals (light green dots), (b) zoom-in of observed and modelled $\delta^{18}\text{O}$ signals for the 01/01/2007 – 31/12/2012 period.

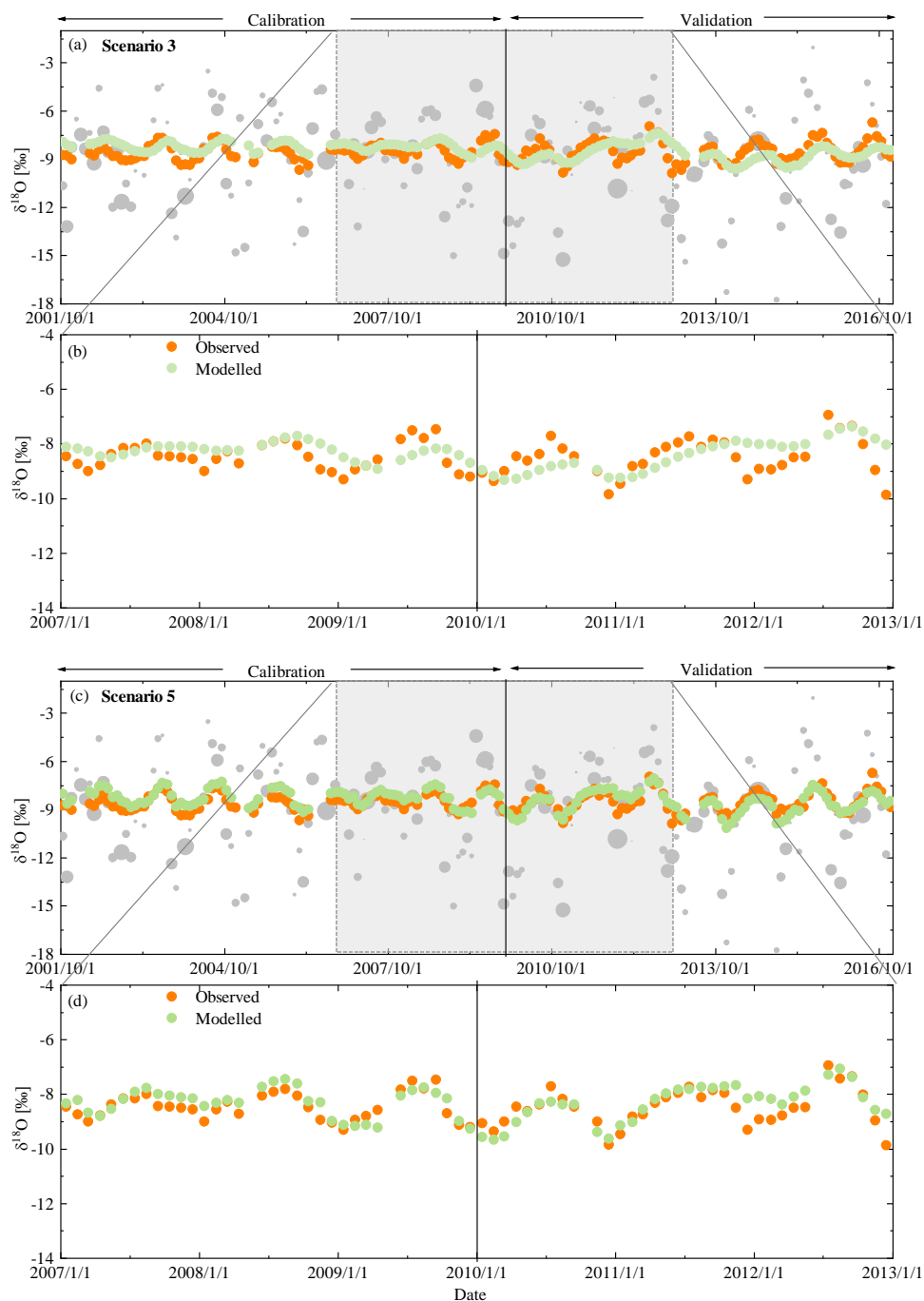


Figure 4.7: The time series of stream $\delta^{18}\text{O}$ reproduced by CO models, i.e., calibration strategy $C_{\delta^{18}\text{O}}$ (scenario3, 5), for the model calibration and evaluation periods. (a) Observed $\delta^{18}\text{O}$ signals in precipitation (light grey dots; size of dots indicates the precipitation volume) and observed stream $\delta^{18}\text{O}$ signals (orange dots) as well as the modelled stream $\delta^{18}\text{O}$ signals (light green dots) for scenarios 3, (b) zoom-in of observed and modelled $\delta^{18}\text{O}$ signals in the stream for the 01/01/2007 – 31/12/2012 period for scenarios 3, (c) Observed $\delta^{18}\text{O}$ signals in precipitation and in stream same as (a), and the modelled stream $\delta^{18}\text{O}$ signals (relatively darker green dots) for scenarios 5, (d) zoom-in of observed and modelled $\delta^{18}\text{O}$ signals in the stream for the 01/01/2007 – 31/12/2012 period for scenarios 5.

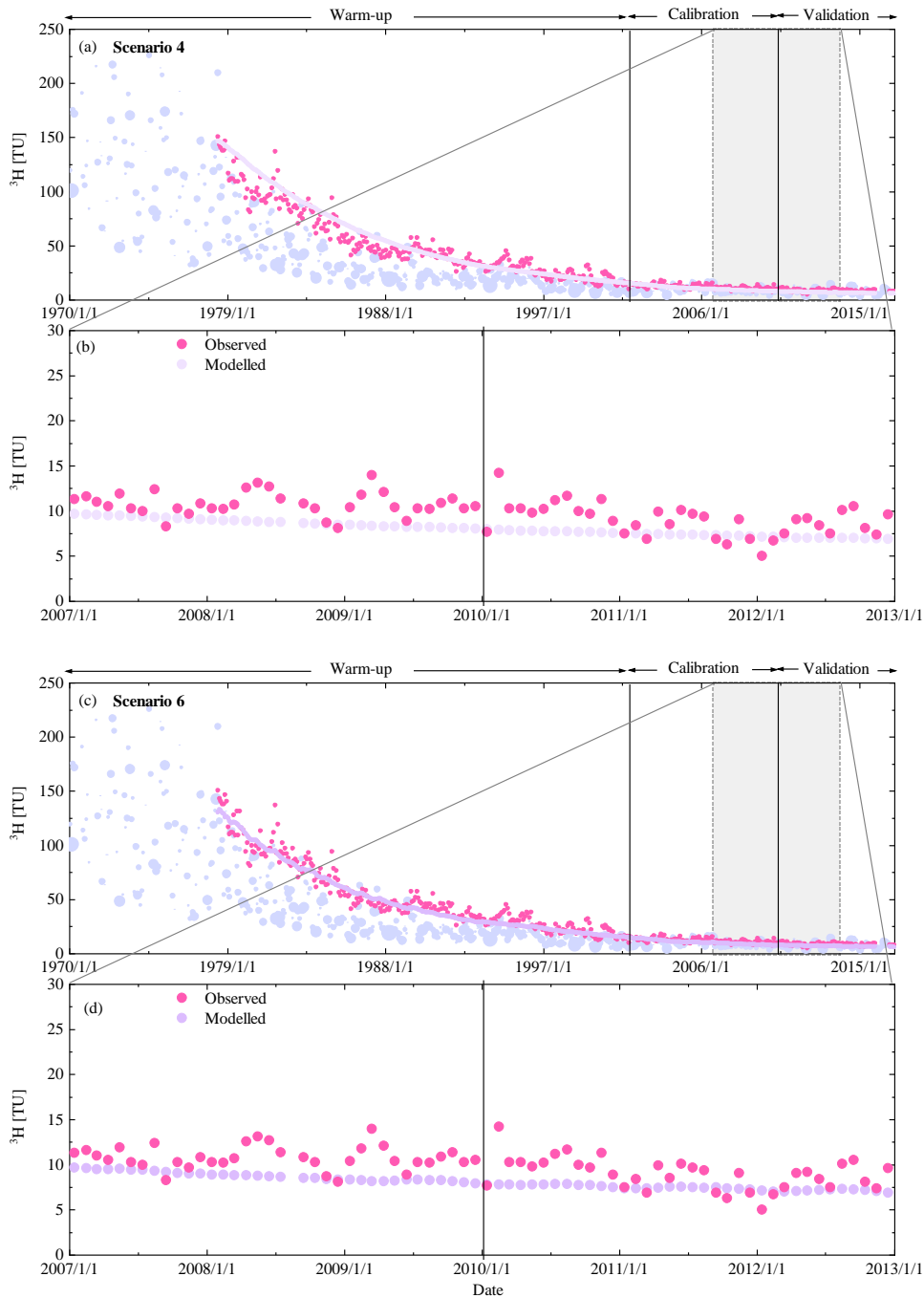


Figure 4.8: Time series of stream ^3H reproduced by CO models, i.e., calibration strategy C_3^H (scenario4, 6), for the model calibration and evaluation periods. (a) Observed ^3H signals in precipitation (light blue-purple dots; size of dots indicates associated precipitation volume) and in streamflow (pink dots) as well as the modelled ^3H stream signal (light purple dots), (b) zoom-in of observed and modelled ^3H signals for the 01/01/2007 – 31/12/2012 period for scenarios 4, (c) Observed ^3H signals in precipitation and in stream same as (a), and the modelled stream ^3H signals (relatively darker purple dots) for scenarios 6, (d) zoom-in of observed and modelled ^3H signals in the stream for the 01/01/2007 – 31/12/2012 period for scenarios 6.

Table 4.6: Performance metrics of the 12 time-invariant, lumped SW/CO model implementations for the 2001 – 2009 calibration period (cal) and the 2010 – 2016 model evaluation period (val.). For brevity only the values for the most balanced solution are shown here. *) The MSE values provided for C_x describe the sine wave fits of both, the precipitation and stream flow $\delta^{18}\text{O}$ signals, respectively.

Scenario	1	2	3	4	5	6	7	8	9	10	11	12
Model	SW-EM	SW-GM	CO-EM		CO-GM		CO-2EM		CO-3EM		CO-EPM	
Calibration strategy → Performance metric ↓	C_x	C_x	$C_{\delta^{18}\text{O}}$	$C_{^3\text{H}}$	$C_{\delta^{18}\text{O}}$	$C_{^3\text{H}}$	$C_{\delta^{18}\text{O}}$	$C_{^3\text{H}}$	$C_{\delta^{18}\text{O}}$	$C_{^3\text{H}}$	$C_{\delta^{18}\text{O}}$	$C_{^3\text{H}}$
MSE $_{\delta^{18}\text{O}}$	cal.	3.850/0.121*)	0.327	-	0.204	-	0.171	-	0.171	-	0.254	-
	val.	5.208/0.144*)	0.432	-	0.192	-	0.192	-	0.191	-	0.683	-
MSE $_{^3\text{H}}$	cal.	-	-	5.903	-	5.791	-	5.171	-	5.170	-	5.926
	val.	-	-	5.155	-	4.597	-	3.964	-	4.000	-	5.115

The P-SAS implementations (scenarios 13 – 15; Table 4.7; Fig. 4.9a – d and Fig. 4.11a – d) show a somewhat higher skill to reproduce the dampening of $\delta^{18}\text{O}$ response with $\text{MSE}_{\delta^{18}\text{O}} = 0.069 - 0.078 \text{ ‰}$ for the calibration and $0.215 - 0.231 \text{ ‰}$ for the evaluation periods, respectively, as well as the general decrease in the magnitude of stream water ^3H with $\text{MSE}_{^3\text{H}} < 3TU^2$. In contrast to the above, the implementations of the integrated model IM-SAS (Table 4.7) aim to not only to reproduce the $\delta^{18}\text{O}$ or ^3H stream signals, but to additionally and simultaneously describe the hydrological response (Table 4.7). Both, the lumped IM-SAS-L (scenario 16; Fig. 4.10a, b) and the distributed IM-SAS-D (scenario 19) reproduce the seasonal fluctuations as well as the degree of dampening of the $\delta^{18}\text{O}$ signals with $\text{MSE}_{\delta^{18}\text{O}} = 0.079 - 0.083 \text{ ‰}$ for the calibration and $0.273 - 0.332 \text{ ‰}$ for the evaluation periods similar to or better than the baseline SW/CO models. The IM-SAS models do also describe the evolution of the ^3H stream signals rather well (scenarios 17 and 20). With $\text{MSE}_{^3\text{H}} < 3TU^2$, IM-SAS-L (Fig. 4.12) and IM-SAS-D (Fig. 4.11e – h) do not only outperform the baseline models with respect to the overall magnitude of ^3H , but do, in spite of somewhat underestimating the magnitude of seasonal amplitudes, also provide a better representation of these intra-annual fluctuations. Similar to the SW/CO baseline models, both the P-SAS and IM-SAS implementations also very well capture the overall decline of the stream water ^3H levels in the 1978 – 2001 pre-calibration model warm-up period. The simultaneous calibration to the hydrological response and the $\delta^{18}\text{O}$ and ^3H stream signals (scenarios 18 and 21) led to a comparable model skill to reproduce the tracer signals. In addition to the tracer concentrations, all IM-SAS implementations do also reproduce the main features of the hydrological response (Table 4.7). More specifically, the modelled hydrographs in particular describe well the timing of peaks as well as the shape of recessions, although in some cases peak flows were underestimated and low flows overestimated as shown for scenario 21 in Figure 4.14 (similar results for scenarios 16 – 20, Fig. 4.13 and Appendix B Figs. B.1 – B.4). The resulting in MSE_Q remains $\leq 0.336 \text{ mm}^2 \text{ d}^{-2}$ across all IM-SAS implementations (scenarios 16 – 21). Crucially, the models also reproduce well the other observed stream flow signatures such as the flow duration curves ($\text{MSE}_{\text{FDCQ}} \leq 0.047 \text{ mm}^2 \text{ d}^{-2}$; Fig. 4.14d), the seasonal runoff coefficients ($\text{MSE}_{\text{RC}} \leq 0.008$; Fig. 4.13e) and the autocorrelation functions ($\text{MSE}_{\text{ACQ}} \leq 0.007$; Fig. 4.14f). The model, calibrated on the overall response of the Neckar basin, also exhibited considerable skill to represent spatial differences in the hydrological response by reproducing observed stream flow in the three sub-catchments (C1 – C3) similarly well (Fig. 4.15) without any further re-calibration.

Table 4.7: Performance metrics of the 9 P-SAS and IM-SAS model scenarios for the 2001 – 2009 calibration period (cal.) and the 2010 – 2016 model evaluation period (val.). For brevity only the values for the most balanced solution, i.e., lowest D_E (Eq. 4.19) are shown here.

Scenario	13	14	15	16	17	18	19	20	21
Model	P-SAS			IM-SAS-L			IM-SAS-D		
Implementation	Lumped			Distributed			Distributed		
Calibration strategy → Performance metric	$C_{\delta^{18}\text{O}}$	$C_{^3\text{H}}$	$C_{\delta^{18}\text{O}, ^3\text{H}}$	$C_{\delta^{18}\text{O}_Q}$	$C_{^3\text{H}_Q}$	$C_{\delta^{18}\text{O}, ^3\text{H}_Q}$	$C_{\delta^{18}\text{O}_Q}$	$C_{^3\text{H}_Q}$	$C_{\delta^{18}\text{O}, ^3\text{H}_Q}$
$\text{MSE}_{\delta^{18}\text{O}}$	cal. 0.069	-	0.078	0.083	-	0.118	0.079	-	0.114
	val. 0.231	-	0.215	0.332	-	0.273	0.273	-	0.475
$\text{MSE}_{^3\text{H}}$	cal. -	2.828	2.847	-	2.972	2.823	-	2.920	2.981
	val. -	1.717	1.710	-	2.389	2.285	-	2.357	2.450
MSE_Q	cal. -	-	-	0.202	0.299	0.308	0.228	0.263	0.317
	val. -	-	-	0.224	0.297	0.329	0.251	0.283	0.336
$\text{MSE}_{\log(\text{Q})}$	cal. -	-	-	0.120	0.158	0.174	0.130	0.171	0.161
	val. -	-	-	0.120	0.148	0.150	0.127	0.201	0.165
$\text{MSE}_{\text{FDC}_Q}$	cal. -	-	-	0.058	0.024	0.073	0.022	0.017	0.025
	val. -	-	-	0.103	0.022	0.142	0.043	0.065	0.059
$\text{MSE}_{\text{FDC}_{\log(\text{Q})}}$	cal. -	-	-	0.011	0.011	0.047	0.006	0.019	0.009
	val. -	-	-	0.015	0.009	0.047	0.009	0.050	0.018
MSE_{FC}	cal. -	-	-	0.004	0.005	0.007	0.003	0.006	0.003
	val. -	-	-	0.004	0.004	0.005	0.003	0.008	0.003
MSE_{AC_Q}	cal. -	-	-	0.003	0.002	0.003	0.002	0.001	0.001
	val. -	-	-	0.008	0.002	0.001	0.005	0.002	0.007

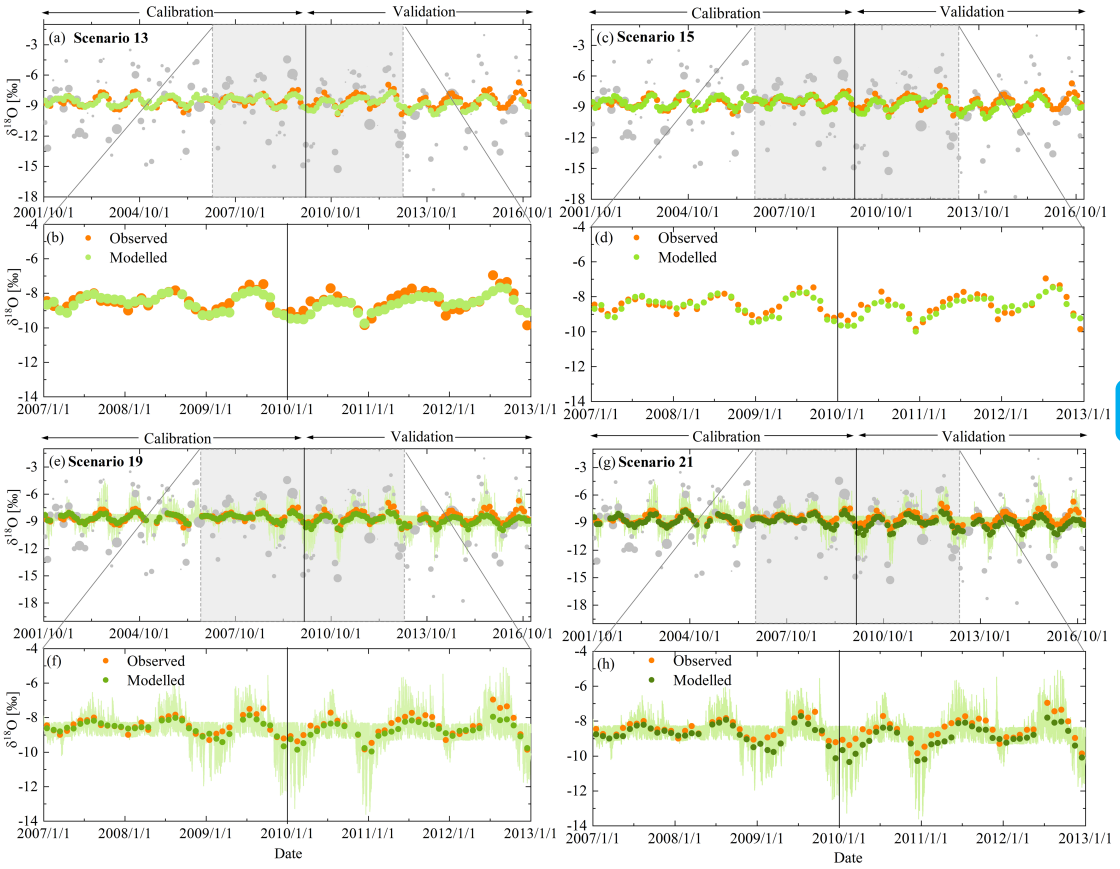


Figure 4.9: The time series of stream $\delta^{18}\text{O}$ reproduced by models P-SAS (scenarios 13 and 15) and IM-SAS-D (scenarios 19 and 21) based on different calibration strategies. IM-SAS-D model based on simultaneous calibration to $\delta^{18}\text{O}$ and the streamflow signatures, i.e. calibration strategy $C_{\delta^{18}\text{O},Q}$ (scenario 19) and $C_{\delta^{18}\text{O},^3\text{H}_Q}$ (scenario 21), for the model calibration and evaluation periods. (a) Observed $\delta^{18}\text{O}$ signals in precipitation (light grey dots; size of dots indicates the precipitation volume) and observed stream $\delta^{18}\text{O}$ signals (orange dots) as well as the most balanced modelled $\delta^{18}\text{O}$ signal in the stream (light green dots) for scenario 13 from calibration strategy $C_{\delta^{18}\text{O}}$, (b) zoom-in of observed and modelled $\delta^{18}\text{O}$ signals in the stream for the 01/01/2007 – 31/12/2012 period for scenario 13, (c) Observed $\delta^{18}\text{O}$ signals in precipitation and in stream same as (a), and the modelled stream $\delta^{18}\text{O}$ signals (relatively darker green dots) for scenario 15 from calibration strategy $C_{\delta^{18}\text{O},^3\text{H}}$, (d) zoom-in of observed and modelled $\delta^{18}\text{O}$ signals in the stream for the 01/01/2007 – 31/12/2012 period for scenario 15. (e) Observed $\delta^{18}\text{O}$ signals in precipitation and in stream same as (a), and the modelled stream $\delta^{18}\text{O}$ signals (relatively darker green dots) for scenario 19 and the 5th/95th percentile of all retained pareto optimal solutions obtained from calibration strategy $C_{\delta^{18}\text{O},Q}$ (light green shaded area), (f) zoom-in of observed and modelled $\delta^{18}\text{O}$ signals in the stream for the 01/01/2007 – 31/12/2012 period for scenario 19, (g) Observed $\delta^{18}\text{O}$ signals in precipitation and in stream same as (a), and the modelled stream $\delta^{18}\text{O}$ signals (relatively darker green dots) for scenario 21 and the 5th/95th percentile of all retained pareto optimal solutions obtained from calibration strategy $C_{\delta^{18}\text{O},^3\text{H}_Q}$ (light green shaded area), (h) zoom-in of observed and modelled $\delta^{18}\text{O}$ signals in the stream for the 01/01/2007 – 31/12/2012 period for scenario 21.

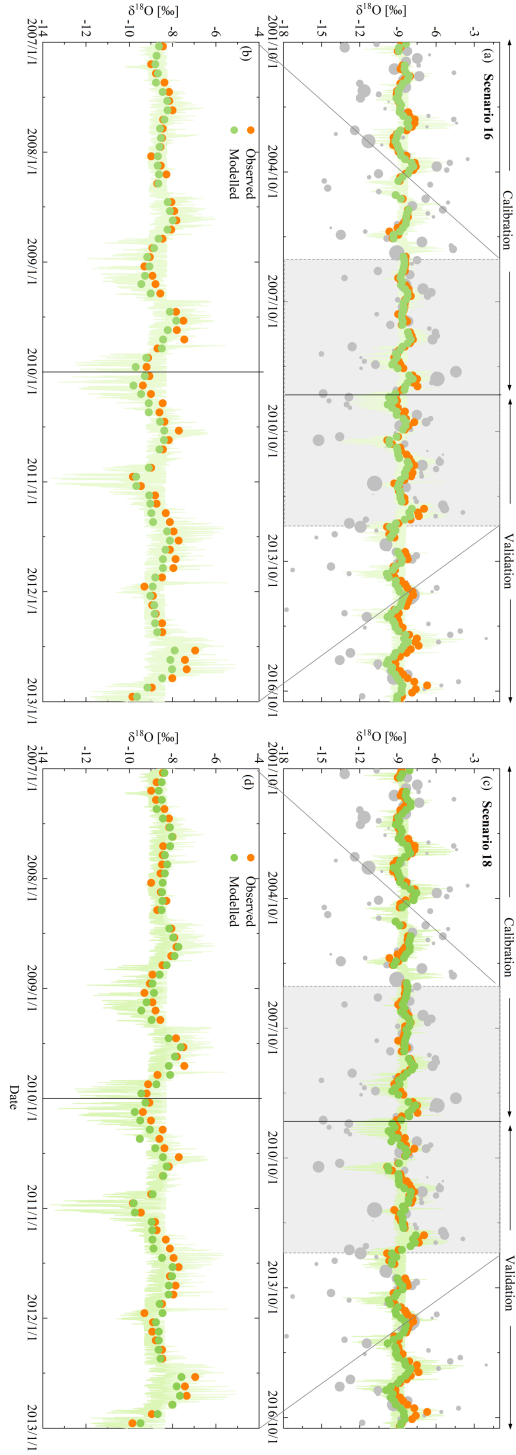


Figure 4.10: The time series of stream $\delta^{18}\text{O}$ reproduced by IM-SAS-L models based on simultaneous calibration to $\delta^{18}\text{O}$ and the streamflow signatures, i.e., calibration strategy $C_{\delta^{18}\text{O},Q}$ (scenario 16) and $C_{\delta^{18}\text{O},^3\text{H}_2\text{O}}$ (scenario 18), for the model calibration and evaluation periods. (a) Observed $\delta^{18}\text{O}$ signals in precipitation (light grey dots; size of dots indicates the precipitation volume) and observed stream $\delta^{18}\text{O}$ signals (orange dots) as well as the modelled stream $\delta^{18}\text{O}$ signals (green dots) and the 5th/95th percentile of all retained Pareto optimal solutions obtained from calibration strategy $C_{\delta^{18}\text{O},Q}$ (light green shaded area) for scenarios 16. (b) Zoom-in of observed and modelled $\delta^{18}\text{O}$ signals in the stream for the 01/01/2007 – 31/12/2012 period for scenarios 16. (c) Observed $\delta^{18}\text{O}$ signals in precipitation and in stream same as (a), and the modelled stream $\delta^{18}\text{O}$ signals (relatively darker green dots) with the 5th/95th percentile of all retained Pareto optimal solutions obtained from calibration strategy $C_{\delta^{18}\text{O},^3\text{H}_2\text{O}}$ (light green shaded area) for scenarios 18. (d) Zoom-in of observed and modelled $\delta^{18}\text{O}$ signals in the stream for the 01/01/2007 – 31/12/2012 period for scenarios 18.

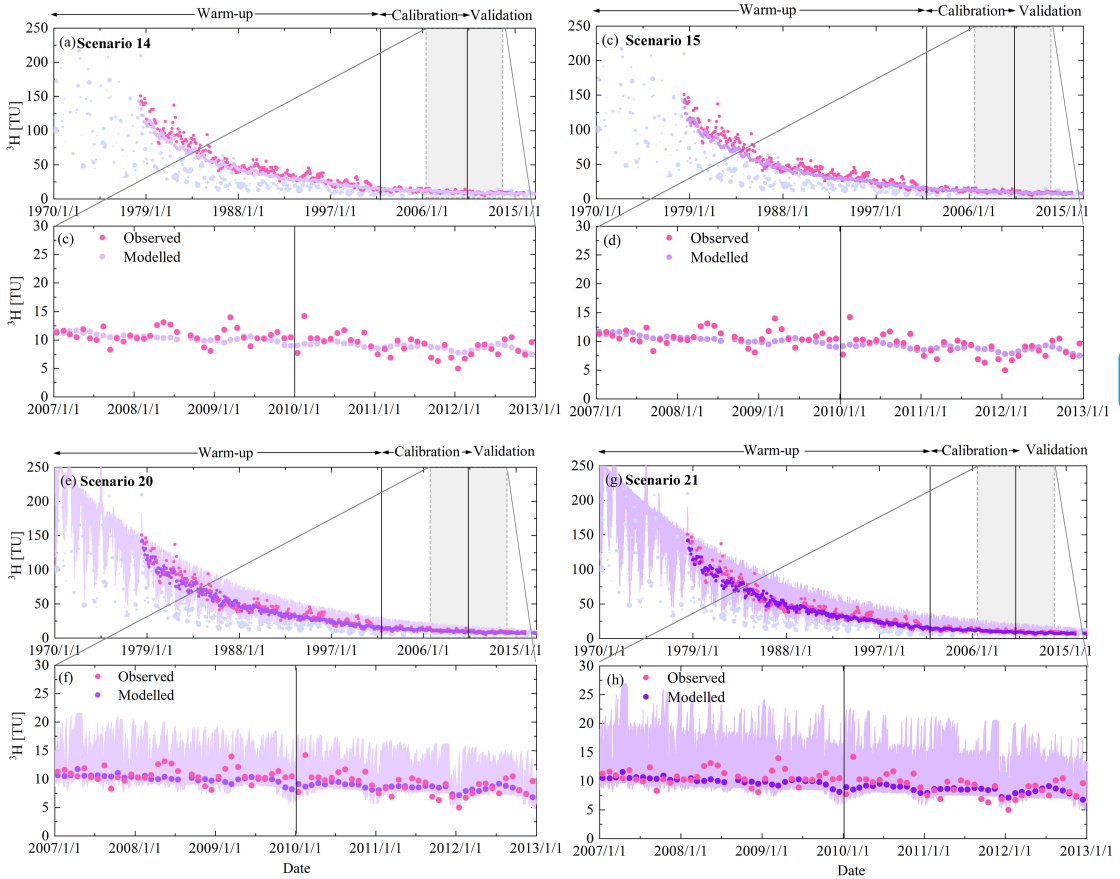


Figure 4.11: The time series of stream ^3H reproduced by models P-SAS (scenarios 14 and 15) and IM-SAS-D (scenarios 20 and 21) based on different calibration strategies. IM-SAS-D model based on simultaneous calibration to ^3H and the streamflow signatures, i.e. calibration strategy $\text{C}_{^3\text{H},\text{Q}}$ (scenario 20) and $\text{C}_{\delta^{18}\text{O},^3\text{H},\text{Q}}$ (scenario 21), for the model calibration and evaluation periods. (a) Observed ^3H signals in precipitation (light blue-purple dots; size of dots indicates the precipitation volume) and observed stream ^3H signals (pink dots) as well as the most balanced modelled ^3H signal in the stream (light purple dots) for scenario 14 from calibration strategy $\text{C}_{^3\text{H}}$, (b) zoom-in of observed and modelled ^3H signals in the stream for the 01/01/2007 – 31/12/2012 period for scenario 14, (c) Observed ^3H signals in precipitation and in stream same as (a), and the modelled stream ^3H signals (relatively darker purple dots) for scenario 15 from calibration strategy $\text{C}_{\delta^{18}\text{O},^3\text{H}}$, (d) zoom-in of observed and modelled ^3H signals in the stream for the 01/01/2007 – 31/12/2012 period for scenario 15. (e) Observed ^3H signals in precipitation and in stream same as (a), and the modelled stream ^3H signals (relatively darker purple dots) for scenario 20 and the 5th/95th percentile of all retained pareto optimal solutions obtained from calibration strategy $\text{C}_{^3\text{H},\text{Q}}$ (light purple shaded area), (f) zoom-in of observed and modelled ^3H signals in the stream for the 01/01/2007 – 31/12/2012 period for scenario 20, (g) Observed ^3H signals in precipitation and in stream same as (a), and the modelled stream ^3H signals (relatively darker green dots) for scenario 21 and the 5th/95th percentile of all retained pareto optimal solutions obtained from calibration strategy $\text{C}_{\delta^{18}\text{O},^3\text{H},\text{Q}}$ (light green shaded area), (h) zoom-in of observed and modelled ^3H signals in the stream for the 01/01/2007 – 31/12/2012 period for scenario 21.

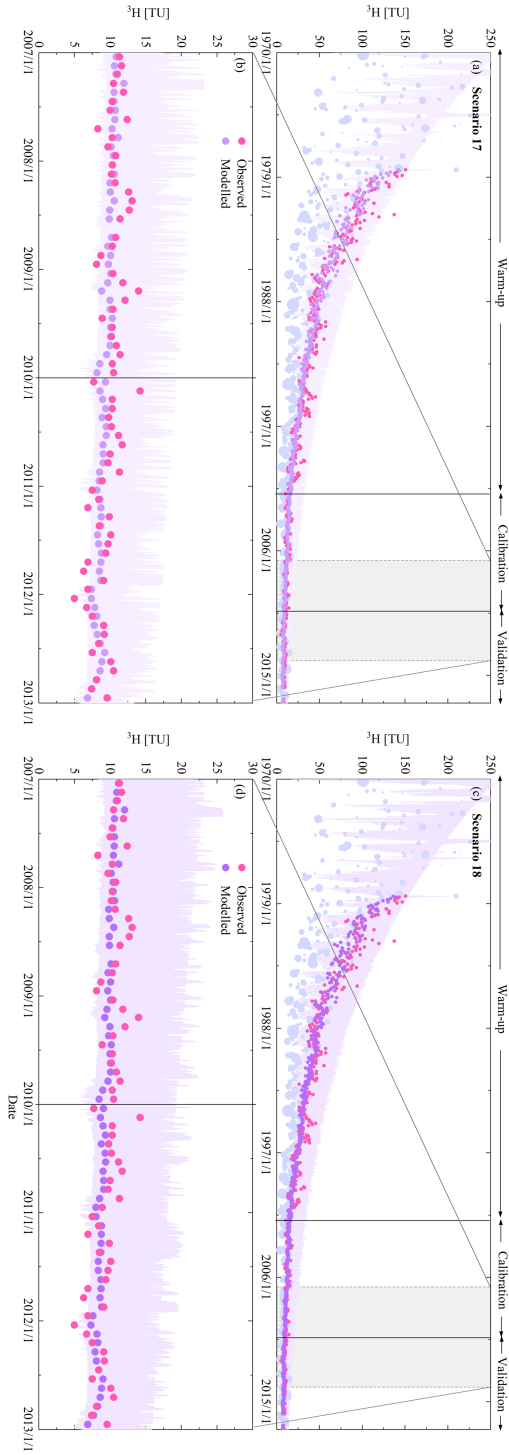


Figure 4.12: Time series of stream ^3H reproduced by model IM-SAS-L based on simultaneous calibration to tracer and the streamflow signatures, i.e. calibration strategy $C_{^3\text{H},Q}$ (scenario 17) and $C_{\delta^{18}\text{O},^3\text{H},Q}$ (scenario 18), for the model calibration and evaluation periods. (a) Observed ^3H signals in precipitation (light blue-purple dots; size of dots indicates associated precipitation volume) and in streamflow (pink dots) as well as the modelled ^3H stream signal based on the most balanced solution, i.e. lowest DE (light purple dots), and the 5th/95th inter-quantile range of all retained pareto optimal solutions obtained from calibration strategy $C_{^3\text{H},Q}$ (light purple shaded area) for scenario 17, (b) zoom-in of observed and modelled ^3H signals for the 01/01/2007 – 31/12/2012 period for scenario 17, (c) Observed ^3H signals in precipitation and in stream same as (a), and the modelled stream ^3H signals (relatively darker purple dots) and the 5th/95th percentile of all retained pareto optimal solutions obtained from calibration strategy $C_{\delta^{18}\text{O},^3\text{H},Q}$ (light purple shaded area) for scenarios 18, (d) zoom-in of observed and modelled ^3H signals in the stream for the 01/01/2007 – 31/12/2012 period for scenarios 18.

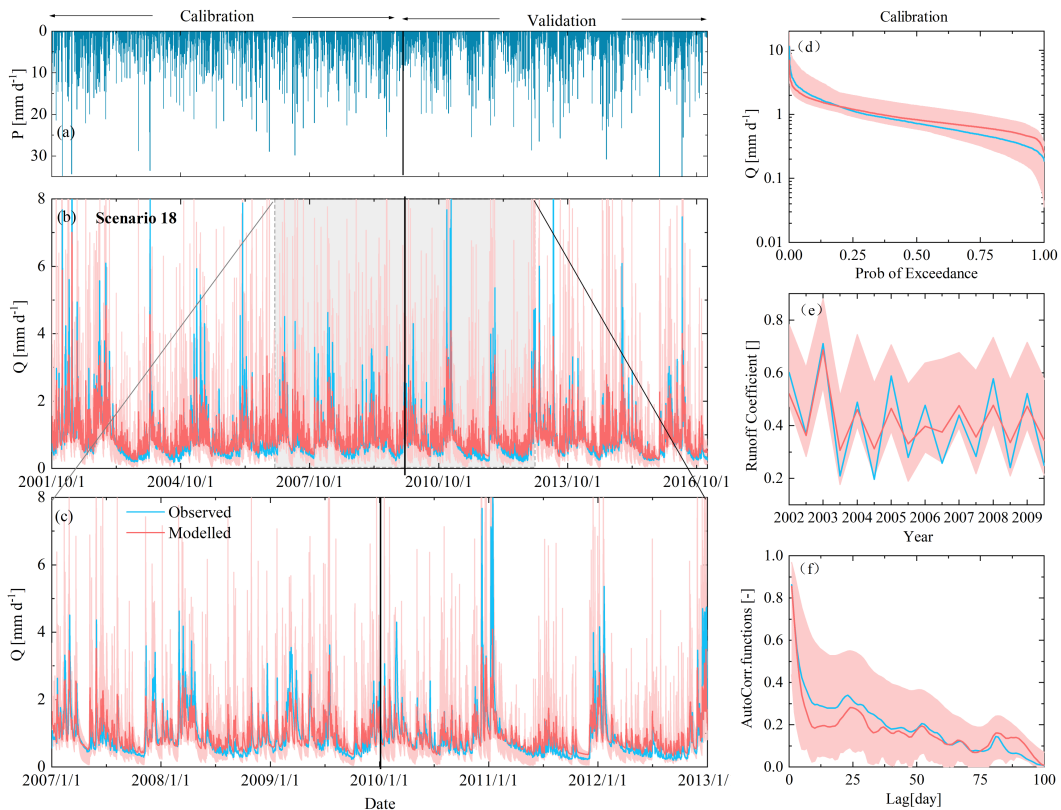


Figure 4.13: Hydrograph and selected hydrological signatures reproduced by IM-SAS-L, following a simultaneous calibration to the hydrological response, $\delta^{18}\text{O}$ and ^3H ($\text{C}_{\delta^{18}\text{O}, ^3\text{H}, \text{Q}}$; scenario 18). (a) Time series of observed daily precipitation; (b) observed and modelled daily stream flow (Q); (c) stream flow zoomed-in to the 01/01/2007 – 31/12/2012 period; (d) flow duration curves (FDC_Q); (e) seasonal runoff coefficients (RC_Q) and (f) autocorrelation functions of stream flow (AC_Q) for the calibration period. Blue lines indicate values based on observed streamflow (Q_o), light red lines are values based on modelled stream flow Q_m representing the most balanced solutions, i.e., lowest D_E and the red shaded areas show the 5th/95th inter-quantile ranges obtained from all pareto optimal solutions.

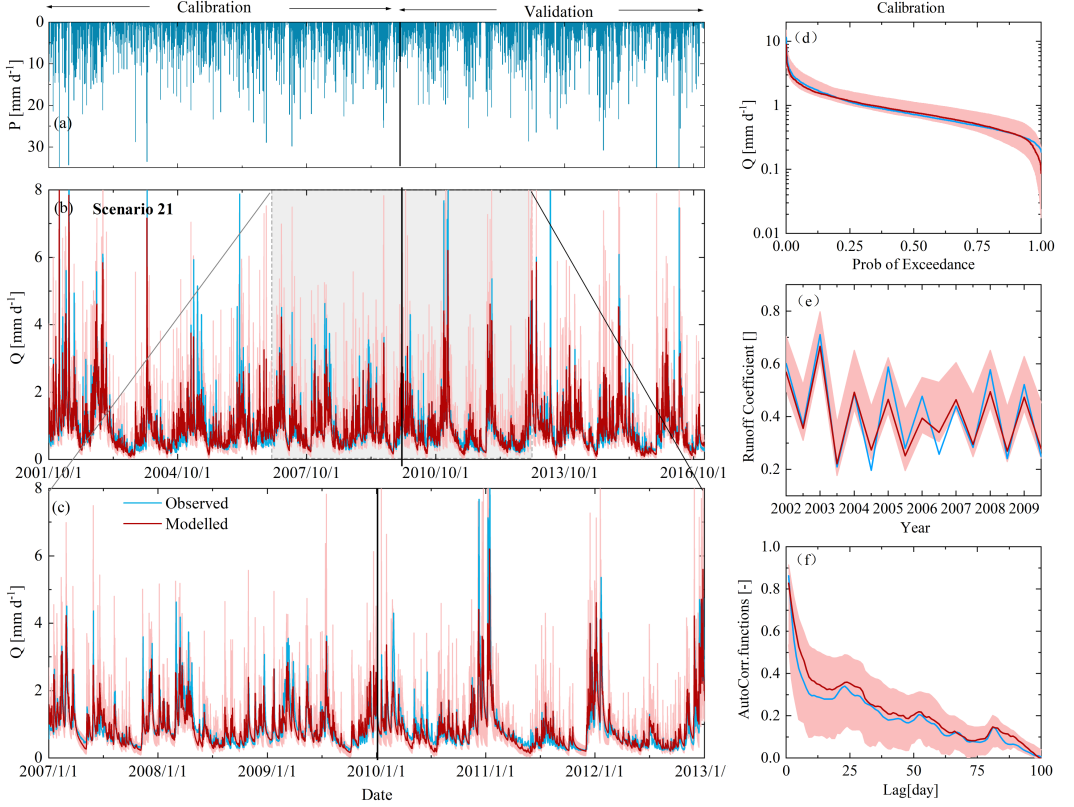


Figure 4.14: Hydrograph and selected hydrological signatures reproduced by IM-SAS-D, following a simultaneous calibration to the hydrological response, $\delta^{18}\text{O}$ and ^3H ($C_{\delta^{18}\text{O}, ^3\text{H}, Q}$; scenario 21). (a) Time series of observed daily precipitation; (b) observed and modelled daily stream flow (Q); (c) stream flow zoomed-in to the 01/01/2007 – 31/12/2012 period; (d) flow duration curves (FDC $_Q$); (e) seasonal runoff coefficients (RC_Q) and (f) autocorrelation functions of stream flow (AC_Q) for the calibration period. Blue lines indicate values based on observed streamflow (Q_o), red lines are values based on modelled stream flow Q_m representing the most balanced solutions, i.e., lowest D_E and the red shaded areas show the 5th/95th inter-quantile ranges obtained from all pareto optimal solutions.

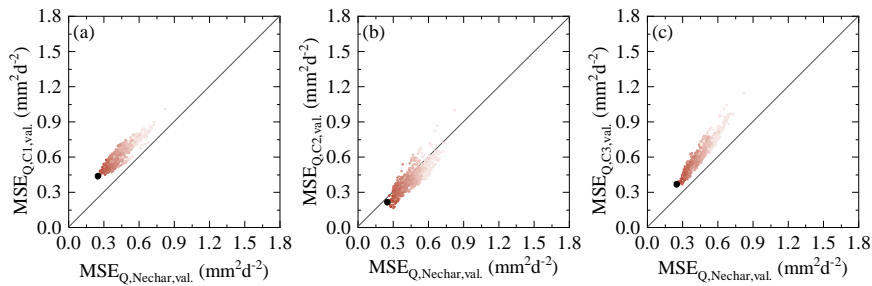


Figure 4.15: Selected model performances in the 01/01/2010 – 31/12/2016 validation period of the overall Neckar basins against the model performance in uncalibrated sub-catchment (a) Kirchentellinsfurt (C1), (b) Calw (C2) and (c) Untergriesheim (C3) based on Scenario 19. The dots indicate all Pareto-optimal solutions in the multi-objective model performance space. The shades from dark to light indicate the overall model performance based on the Euclidean Distance D_E , with the black solutions representing the overall better solutions (i.e. smaller D_E)

4.4.2 MODEL PARAMETERS

Parameters of the SW/CO baseline models (scenarios 1 – 12) directly define the shapes of parametric TTDs and thus the associated metrics of water age, such as MTT following Eqs. (4.6 – 4.10). The CO models representing ^3H signals (scenarios 4, 6, 8, 10, 12) are characterized by values of parameters γ_1 , γ_2 and γ_3 that are by a factor of up to ~ 10 higher than the same parameters of models calibrated to $\delta^{18}\text{O}$ signals (Table 4.3). For example, $\gamma_1 = 513$ d for the CO-EM in scenario 3 and 3795 d in scenario 4.

The individual parameters of the P-SAS and IM-SAS model implementations (scenarios 13 – 21), in contrast, do not directly define parametric TTDs nor can they be readily and directly be linked to water ages. However, it has been previously shown that the sizes of water storage volumes is an important control on water ages (e.g. Harman, 2015) and that in particular total storage volumes, represented by parameter S_{tot} in P-SAS, and the hydrologically passive storage volumes, represented by parameter $S_{s,p}$ in IM-SAS models, are key to regulate in particular older water ages in many systems (e.g. Hrachowitz et al., 2016). Calibration of P-SAS to $\delta^{18}\text{O}$ in scenario 13 suggested $S_{\text{tot}} \sim 15595$ mm while calibration of the lumped IM-SAS-L to $\delta^{18}\text{O}$ and stream flow ($C_{\delta^{18}\text{O},\text{Q}}$) in scenario 16 led to a moderately well identifiable range of this parameter $S_{s,p} \sim 4107 - 10029$ mm across all pareto optimal solutions and in the same order of magnitude as P-SAS (Fig. 4.16a, Table 4.4). Reflecting the water storage capacity in the unsaturated root zone, which is an important control on younger water ages (Hrachowitz et al., 2021), the parameter S_{umaxF} was found to range between $\sim 314 - 415$ mm (Fig. 4.16b, Table 4.4) for the same IM-SAS-L scenario. The calibration of the same models to ^3H (scenarios 14, 17) resulted in a similar parameter ranges for $S_{\text{tot}} \sim 16638$ mm, $S_{s,p} \sim 3924 - 9339$ mm (Fig. 4.16a) as well as, albeit slightly lower, $S_{\text{umaxF}} \sim 236 - 355$ mm (Fig. 4.16b). The similarities between these two scenarios are also reflected in the parameter ranges obtained from the simultaneous calibration to $\delta^{18}\text{O}$ and ^3H ($C_{\delta^{18}\text{O},^3\text{H},\text{Q}}$) in scenarios 15 and 18. The calibration of the distributed IM-SAS-D model following all the three calibration strategies in scenarios 19 – 21, resulted in values for $S_{s,p} \sim 3270 - 9011$ mm (Fig. 4.16c) that are broadly in the similar ranges as for IM-SAS-L ($S_{s,p} \sim 3924 - 13676$ mm). In contrast, the distinction into the individual HRUs led to clear differences between S_{umaxF} , S_{umaxG} and S_{umaxW} (Fig. 4.16d-f), reflective of the different hydrological functioning of these HRUs. Nevertheless, the area-weighted average of these parameters comes close to the equivalent parameter from the lumped model implementation (S_{umaxF}). The general consistency of these parameters obtained from the different calibration strategies is exacerbated by the limited differences in the most balanced solutions (smallest D_E) between the different scenarios. For example the most balanced solutions of $S_{s,p}$ fall between $\sim 4000 - 5000$ mm for all IM-SAS scenarios 16 – 21 (Fig. 4.16a, c). All other parameters, which are less clearly related to water ages, exhibit different levels of variation across the individual scenarios yet not following any clear and systematic pattern (Table 4.4).

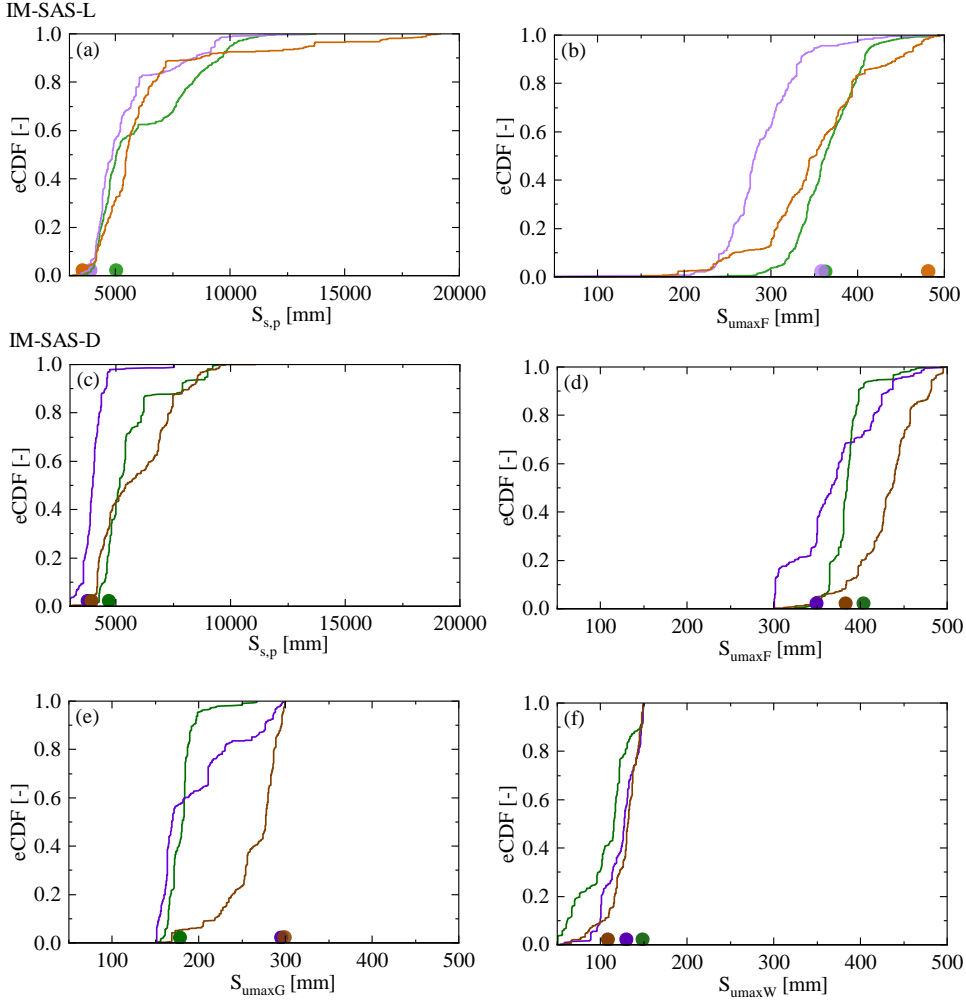


Figure 4.16: Pareto-optimal distributions of selected parameters of the IM-SAS models (i.e., IM-SAS-L, IM-SAS-D) shown as the associated empirical cumulative distribution functions (lines). Light green shades indicate scenario 16, light purple shades indicate scenario 17 and light brown shades indicate scenario 18 in (a) and (b); relatively darker green shades indicate scenario 19, relatively darker purple shades indicate scenario 20 and relatively darker brown shades indicate scenario 21 in (c) - (f). The dots indicate the parameter values associated with the most balanced solution, i.e. lowest D_E .

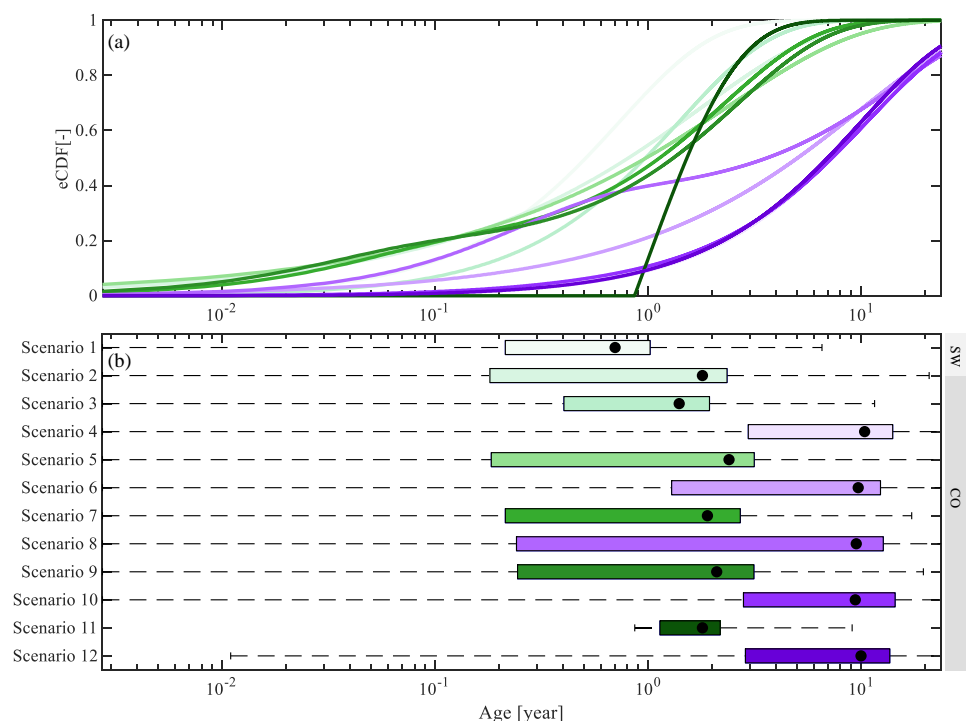


Figure 4.17: Stream flow TTDs derived from the 12 SW/CO model scenarios with the different associated calibration strategies based on different lumped, time-invariant models. The TTDs represent the best fits of the respective time-invariant TTD. Green shades represent the TTDs inferred from $\delta^{18}\text{O}$ (from lighter to darker for scenarios 1, 2, 3, 5, 7, 9, 11) in (a) and (b); the purple shades represent TTDs inferred from ^3H (from lighter to darker for scenario 4, 6, 8, 10 and 12); the black dots in (b) indicate the mean transit time for each model scenario.

4.4.3 WATER AGE DISTRIBUTIONS

Based on a $\delta^{18}\text{O}$ amplitude ratio $A_s/A_p = 0.21$ (Table 4.4), the results of the SW models (scenarios 1, 2) suggest a system that is characterized by rather young stream water with MTT $\sim 0.7 - 1.8$ yr, depending on the choice of TTD (Table 4.8; Fig. 4.17). The TTDs obtained from the CO models calibrated to $\delta^{18}\text{O}$ (scenarios 3, 5, 7, 9, 11) are broadly consistent with that, suggesting MTT $\sim 1.4 - 2.4$ yr. These TTDs suggest mean water ages that are up to ~ 9 yr lower than estimates from CO models calibrated to ^3H (scenarios 4, 6, 8, 10, 12) with MTT $\sim 9.4 - 10.4$ yr (Table 4.8; Fig. 4.17). For higher percentiles the differences in water ages can even reach more than 20 years (Table 4.8). Correspondingly, the fractions of water younger than 3 months, $F(T < 3m)$, exhibit considerable differences of $-2 - 22\%$ points between $\delta^{18}\text{O}$ and ^3H inferred estimates, which further increase to differences of $30 - 64\%$ for $F(T < 3yr)$.

Table 4.8: Metrics of stream flow TTDs derived from the 12 SW/CO model scenarios with the different associated calibration strategies based on different, where $C_{\delta^{18}\text{O}}$ indicates calibration to $\delta^{18}\text{O}$, $C^3\text{H}$ calibration to ^3H . The TTD metrics represent the best fits of the respective time-invariant TTD. The water fractions are shown as the fractions of below a specific age T , i.e. $F(T < \text{age})$. The columns with absolute difference Δ summarize the differences in TTDs from the same models calibrated to $\delta^{18}\text{O}$ and ^3H , respectively. The subscripts indicate the scenarios that are compared (e.g., $\Delta_{3,4}$ compares scenarios 3 and 4). *Note that the fraction of water younger than 3 months $F(T < 3\text{m})$ is comparable to the fraction of young water as suggested by Kirchner (2016).

Scenario	1	2	3	4	5	6	7	8	9	10	11	12	$\Delta_{3,4}$	$\Delta_{5,6}$	$\Delta_{7,8}$	$\Delta_{9,10}$	$\Delta_{11,12}$
Model	SW-EM SW_GM																
Calibration strategy →	C _x																
TTD metric ↓	C _x	C _x	C $_{\delta^{18}\text{O}}$	C ^3H	C $_{\delta^{18}\text{O}}$	C ^3H	C $_{\delta^{18}\text{O}}$	C ^3H	C $_{\delta^{18}\text{O}}$	C ^3H	C $_{\delta^{18}\text{O}}$	C ^3H	CO-EPM	CO-3EM	CO-2EM	CO-GM	CO-EM
Percentiles	Mean (yr)	0.7	1.8	1.4	10.4	2.4	9.7	1.9	9.5	2.1	9.4	1.8	10	9.4	1.8	10	9.4
	10 th	0.1	< 0.1	0.1	1.1	<0.1	0.3	<0.1	<0.1	<0.1	0.9	1.0	1.1	<0.1	<0.1	0.9	1.0
	25 th	0.2	0.2	0.4	3.0	0.2	1.3	0.2	0.3	0.2	2.8	1.1	2.9	0.2	0.3	2.8	1.1
	50 th (median)	0.5	0.8	1.0	7.2	1.0	5.0	1.1	3.6	1.3	7.3	1.5	7	1.3	3.6	7.3	1.5
	75 th	1.0	2.3	1.9	14.4	3.2	13.1	2.7	13.8	3.1	15.0	2.2	13.9	2.7	13.8	15.0	2.2
Water fractions	90 th	1.7	4.8	3.2	26.3	6.8	25.4	4.8	27.3	5.6	25.6	3.0	23.1	5.6	27.3	25.6	3.0
	$F(T < 3\text{m})^*$	29	29	16	2	28	10	26	25	25	3	0	2	14	18	1	22
	$F(T < 6\text{ m})$	49	41	30	5	38	14	34	34	32	6	0	5	25	24	0	26
	$F(T < 1\text{ yr})$	74	55	51	9	50	21	47	40	44	10	13	9	42	29	7	34
	$F(T < 3\text{ yr})$	98	81	88	25	74	39	78	48	74	26	63	35	63	35	30	48
Water fractions (%)	$F(T < 5\text{ yr})$	100	91	97	38	85	50	91	55	88	38	99	39	59	35	36	50
	$F(T < 10\text{ yr})$	100	98	100	62	95	68	99	68	98	60	100	63	38	27	31	38
	$F(T < 20\text{ yr})$	100	100	100	85	100	85	100	84	100	84	100	86	15	15	16	16
	Absolute difference	$\Delta F(T < X)_{\delta^{18}\text{O}-^3\text{H}}$															
	$\Delta T T_{\delta^{18}\text{O}-^3\text{H}}$	$\Delta F(T < X)_{\delta^{18}\text{O}-^3\text{H}}$															

In contrast, from the implementations of the P-SAS and IM-SAS models in scenarios 13 – 21, it can be clearly seen that the stream water ages inferred from $\delta^{18}\text{O}$ are across most percentiles by a factor of around 10 higher than those from SW and CO models, resulting in volume-weighted average MTT $\sim 11 - 17$ yr over the modelling period (Table 4.9; Fig. 4.18). Similarly, all water fractions below 20 years are substantially lower for the P-SAS and IM-SAS models than for SW and CO models. The most pronounced difference is observed at $F(T < 5\text{yr})$ that reaches 38 – 57% for SAS-functions models and 91 – 100% for SW and CO, which equals to a difference of more than 50%. As such, these water age estimates from $\delta^{18}\text{O}$ in SAS-function models (scenarios 13, 16, 19) are not only very similar to the estimates from ^3H in these models (scenarios 14, 17, 20) but $\delta^{18}\text{O}$ suggests, against the expectations, even slightly older water than ^3H does. More specifically, while $\delta^{18}\text{O}$ results in stream water MTT 11–17 yr (scenarios 13, 16, 19), the ^3H -based estimates reach MTT $\sim 11 - 13$ yr (scenarios 14, 17, 20) and thus up to five years younger (Table 4.9; Fig. 4.18). The differences between $\delta^{18}\text{O}$ and ^3H water ages from individual P-SAS and IM-SAS model implementations (scenarios 13 – 21) are similar over all percentiles with $\Delta T T \delta^{18}\text{O}-^3\text{H}$, on average, ~ 1.4 yr and not exceeding ~ 5.5 yr. Accordingly, the fractions of water of any given age up to $T < 20$ years is $\sim 1 - 8$ % higher for ^3H than for $\delta^{18}\text{O}$, suggesting higher fractions of old water modelled with $\delta^{18}\text{O}$ (Table 4.9). Equivalent pattern and comparable magnitudes are found for the combined use of $\delta^{18}\text{O}$ and ^3H in scenarios 15, 18 and 21.

An explicit comparison between the lumped IM-SAS-L (scenarios 16 – 18) and the distributed IM-SAS-D (scenarios 19 – 21) also suggests a good correspondence between the respective inferred water ages for both tracers. While IM-SAS-L generates MTT $\sim 11.2 - 17.4$ years, the MTT obtained from IM-SAS-D reach $\sim 12.8 - 15.6$ years (Table 4.9; Fig. 4.18). Besides the MTT, also the differences in water ages across all percentiles is minor and reaches a maximum of 4.6 years at the 75th percentile. Accordingly, the fractions of water with ages $T < 20$ yr exhibit only marginal differences between the lumped (IM-SAS-L) and distributed model (IM-SAS-D) implementations. It is noted that these overall water ages from IM-SAS-D for the entire Neckar basin emerge from the aggregation of TTDs of the four individual precipitation zones P1 – P4 (Table 4.10; Fig. 4.19), which are characterized by pronounced differences with MTT ranging from $\sim 8 - 10$ years in P4 and $\sim 18 - 22$ years in P2, depending on the scenario.

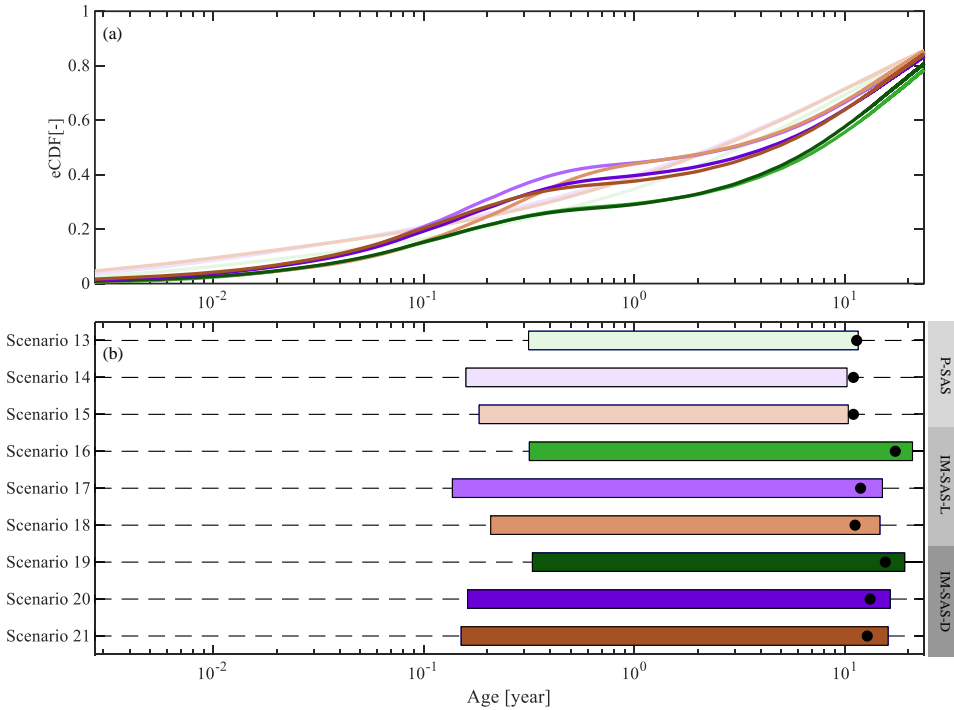


Figure 4.18: Stream flow TTDs derived from the 9 model scenarios with the different associated calibration strategies of P-SAS (scenarios 13 – 15), IM-SAS-L scenarios 16 – 18) and IM-SAS-D model implementations (scenarios 19 – 21). The TTDs represent the volume weighted average daily TTDs for the modelling period 01/10/2001 – 31/12/2016. Green shades represent the TTDs inferred from $\delta^{18}\text{O}$ (from lighter to darker for scenario 13, 16, 19), the purple shades represent TTDs inferred from ^3H (from lighter to darker for scenario 14, 17, 20), the brown lines represent TTDs inferred from combined $\delta^{18}\text{O}$ and ^3H (brown shades from lighter to darker for scenario 15, 18, 21); the black dots in (b) indicate the mean transit time for each model scenario. Note that the mean transit time was estimated by fitting Gamma distributions to the volume-weighted mean TTDs of each individual scenario.

Table 4.9: Metrics of stream flow TTDs derived from the 9 P-SAS and IM-SAS model scenarios with the different associated calibration strategies, where $C_{\delta^{18}\text{O}}$ indicates calibration to $\delta^{18}\text{O}$, $C_{^3\text{H}}$ calibration to ^3H , while $C_{\delta^{18}\text{O},\text{Q}}$, $C_{^3\text{H},\text{Q}}$ and $C_{\delta^{18}\text{O},^3\text{H}}$ indicate multi-objective, i.e. simultaneous calibration to combinations of $\delta^{18}\text{O}$, ^3H and stream flow. The TTD metrics represent the mean of all volume-weighted daily streamflow TTDs for the modelling period 01/10/2001 – 31/12/2016 from the most balanced solutions (i.e. lowest D_E). The values in brackets indicate the 5th/95th percentiles of TTDs representing the pareto optimal solutions. The mean TT was estimated by fitting Gamma distributions to the volume-weighted mean TTDs of each scenario. The water fractions are shown as the fractions of below a specific age T, i.e. $F(T < \text{age})$. The columns with absolute difference δ summarize the differences in TTDs from the most balanced solutions of the same models calibrated to $\delta^{18}\text{O}$ and ^3H , respectively. The subscripts indicate the scenarios that are compared (e.g., $\delta_{13,14}$ compares scenarios 13 and 14). *Note that the fraction of water younger than 3 months $F(T < 3\text{m})$ is comparable to the fraction of young water suggested by Kirchner (2010).

Scenario	13	14	15	16	17	18	19	20	21	$\Delta_{13,14}$	$\Delta_{6,17}$	$\Delta_{9,20}$	
Model	P-SAS			IM-SAS-L							IM-SAS-D		
Calibration strategy → TTD metrics ↓	$C_{\delta^{18}\text{O}}$	$C_{^3\text{H}}$	$C_{\delta^{18}\text{O},^3\text{H}}$	$C_{\delta^{18}\text{O},\text{Q}}$	$C_{^3\text{H},\text{Q}}$	$C_{\delta^{18}\text{O},^3\text{H},\text{Q}}$	$C_{\delta^{18}\text{O},\text{Q}}$	$C_{^3\text{H},\text{Q}}$	$C_{\delta^{18}\text{O},^3\text{H},\text{Q}}$	Absolute difference $\Delta T T_{\delta^{18}\text{O}-^3\text{H}}$ $\Delta F(T < x)_{\delta^{18}\text{O}-^3\text{H}}$			
Percentiles (yr)	Mean (yr)	11.4	11.0	11.0	17.4 (16.9/21.1)	11.9 (11.5/21.3)	11.2 (9.9/16.8)	15.6 (12.0/19.9)	13.2 (13.2/21.1)	12.8 (11.1/18.6)	0.4	5.5	2.4
	1 st 0	0.0	0.0	0.0	0.5 (0.0/0.1)	0.5 (0.0/0.1)	0.4 (0.0/0.1)	0.3 (0.0/0.0)	0.3 (0.0/0.0)	0.3 (0.0/0.1)	0.0	0.0	0.0
	25 th	0.4	0.2	0.2	2.1 (0.1/0.4)	1.9 (0.1/1.2)	1.5 (0.1/1.7)	2.1 (0.1/0.2)	1.5 (0.1/0.2)	1.4 (0.2/0.4)	0.2	0.2	0.6
	50 th (me- dian)	3.2	2.4	2.5	9.0 (9.8/15.9)	6.5 (3.6/11.7)	5.7 (4.8/11.6)	8.6 (4.7/10.9)	6.7 (1.6/5.8)	6.6 (5.4/12.3)	0.7	2.5	1.9
	75 th	13.7	12.5	12.5	22.2 (25.1/28.3)	17.6 (17.1/27.7)	16.3 (14.7/25.0)	20.8 (18.0/26.9)	18.8 (14.3/18.0)	17.8 (16.4/26.7)	1.2	4.6	2.0
95 th	33.4	33.4	32.7	31.3 (32.0/34.0)	29.2 (27.3/33.8)	28.6 (25.2/31.8)	31.1 (28.2/33.1)	30.4 (26.3/28.9)	29.9 (27.1/32.9)	0.0	2.1	0.7	
Water fractions (%)	$F(T < 6\text{m})$ *	22	26	26	18 (23/29)	23 (19/38)	21 (15/33)	16 (28/36)	22 (26/43)	23 (20/29)	-5	-5	-6
	$F(T < 6\text{m})$	27	32	32	21 (25/31)	29 (22/43)	30 (18/36)	20 (30/38)	27 (30/47)	27 (23/32)	-5	-8	-7
	$F(T < 1\text{yr})$	34	39	39	24 (26/33)	32 (24/44)	35 (19/37)	22 (31/39)	30 (33/49)	29 (25/35)	-5	-8	-8
	$F(T < 3\text{yr})$	49	53	52	31 (31/37)	39 (31/49)	42 (22/43)	30 (34/45)	37 (40/53)	37 (31/42)	-4	-8	-7
	$F(T < 5\text{yr})$	57	60	60	38 (33/41)	46 (35/53)	49 (24/51)	38 (38/51)	44 (47/58)	44 (36/48)	-3	-8	-6
	$F(T < 10\text{yr})$	69	71	71	52 (41/50)	59 (41/62)	62 (46/64)	53 (46/62)	58 (60/68)	58 (46/62)	-2	-7	-5
$F(T < 20\text{yr})$	82	83	83	71 (55/65)	77 (52/78)	79 (65/78)	74 (59/78)	76 (75/81)	77 (61/79)	-1	-6	-2	

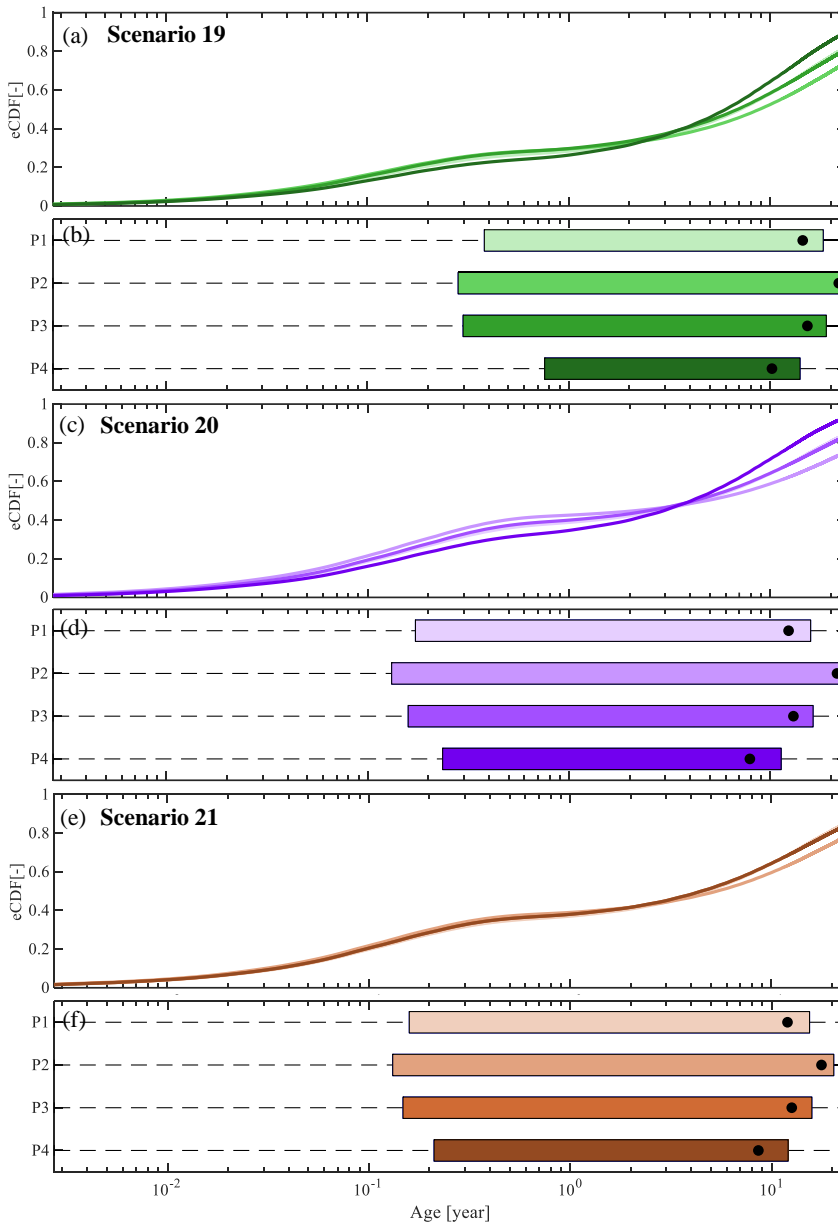


Figure 4.19: Stream flow weighted-TTDs of four precipitation zones (P1-P4) derived from the IM-SAS-D model with the different associated calibration strategies (scenarios 19 – 21). The TTDs represent the volume weighted average daily TTDs for the modelling period 01/10/2001 – 31/12/2016. Green shades from light to dark represent the TTDs inferred from scenario 19 for P1 to P4 in (a) and (b); purple shades from light to dark represent the TTDs inferred from scenario 20 for P1 to P4 in (c) and (d); brown shades from light to dark represent the TTDs inferred from scenario 21 for P1 to P4 in (e) and (f); the black dots in (b), (d) and (f) indicate the mean transit time for each precipitation zone derived from the corresponding scenario. Note that the mean transit time was estimated by fitting Gamma distributions to the volume-weighted mean TTDs of each individual precipitation zone and the long term-mean precipitation for four precipitation zones P1-P4: $P2 < P3 < P1 < P4$.

is comparable to the fraction of young water as suggested by Kirchner (2016) and the long term-mean precipitation for P1-P4: $P2 < P3 < P1 < P4$.

Scenario	19				20				21			
Calibration strategy	$C_{\delta^{18}O_Q}$				C_{δ^3H}				$C_{\delta^{18}O_3H_Q}$			
Precipitation zone → TTD metrics ↓	P1	P2	P3	P4	P1	P2	P3	P4	P1	P2	P3	P4
Mean (yr)	14.5	21.9	15.3	10.2	12.3	21.4	13.0	7.9	12.0	17.7	12.6	8.6
10 th	0.3±0.5	0.4±0.6	0.3±0.5	0.4±0.5	0.3±0.5	0.4±0.7	0.3±0.5	0.3±0.4	0.3±0.4	0.3±0.5	0.3±0.4	0.3±0.4
25 th	2.1±1.6	2.5±2.2	2.1±1.6	2.2±1.2	1.5±1.7	2.0±2.6	1.5±1.7	1.4±1.2	1.5±1.5	1.7±2.0	1.5±1.5	1.6±1.3
50 th (median)	8.4±2.4	10.5±3.7	8.5±2.6	7.2±1.7	6.7±3.6	9.3±6.1	6.7±3.7	5.4±2.1	6.5±3.4	8.1±4.7	6.5±3.4	5.7±2.5
75 th	19.6±2.5	25.8±3.7	20.6±2.8	15.1±1.7	17.1±4.0	25.4±6.8	18.6±4.5	12.4±2.2	17.0±3.8	22.3±5.7	17.6±4.2	13.2±2.6
90 th	30.6±3.8	31.4±4.4	31.0±4.2	25.0±1.9	29.7±4.0	31.3±4.4	30.6±4.2	21.3±2.2	29.0±3.8	31.1±4.4	29.7±4.1	22.6±2.6
Water fractions (%)	F(T<3 m)*	15±9	17±11	16±10	12±8	20±12	22±15	20±13	16±11	21±14	23±15	17±13
	F(T<6 m)	19±11	21±12	20±11	15±9	26±15	29±18	27±16	22±13	26±16	28±17	27±16
	F(T<1 yr)	22±11	23±12	22±11	19±9	30±16	32±18	30±16	26±13	29±15	30±17	29±16
	F(T<3 yr)	30±10	29±11	31±10	30±8	37±14	36±17	37±14	37±11	37±14	36±15	36±12
	F(T<5 yr)	38±9	35±10	38±9	40±7	44±12	41±15	44±13	48±10	44±12	42±14	45±12
	F(T<10 yr)	54±7	48±8	54±7	60±6	59±9	51±13	58±10	67±7	60±9	54±11	59±9
	F(T<20 yr)	75±3	66±5	74±4	84±2	78±5	66±9	76±5	88±2	79±5	71±7	78±5

The consistency between water ages inferred from $\delta^{18}\text{O}$ and ^3H , respectively, in all SAS-function model scenarios is further illustrated by the direction and magnitude of change in water age distributions as a consequence of changing wetness conditions. In particular during wet-up and wet periods, a marked variability of daily TTDs can be observed, with young water fractions $F(T < 3 \text{ m})$ ranging between $\sim 20 - 65\%$ for $\delta^{18}\text{O}$ -based estimates and $\sim 25 - 70\%$ for ^3H (Fig. 4.20a, b, e, f). Less variability in daily TTDs is found under drying and dry conditions with generally $F(T < 3 \text{ m})$ in the range of $\sim 1 - 20\%$, with only very few outliers $> 30\%$. Overall, the volume-weighted average TTDs for wet conditions suggest slightly older water inferred from $\delta^{18}\text{O}$ with a median water age of ~ 3 year and $F(T < 3 \text{ m}) \sim 30\%$, for wet conditions than from ^3H , for which a median age of ~ 1 year and $F(T < 3 \text{ m}) \sim 40\%$ were found (Fig. 4.20d, h). This is in opposite to dry conditions for which the differences between $\delta^{18}\text{O}$ and ^3H -derived water age estimates become mostly negligible (Fig. 4.20d, h).

With P-SAS and IM-SAS models, not only MTT/TTD in streams can be derived but also in any fluxes/storages (i.e., transpiration flux E_a , ground water storage). An even more pronounced young water variability in daily TTDs was found for the transpiration flux E_a leaving the unsaturated root zone storage S_u in the IM-SAS models (scenarios 16 – 21). As shown in Figure 21a, the transpiration TTDs inferred from $\delta^{18}\text{O}$ suggest a median transpiration age during wet conditions of $\sim 2 - 40$ days and $F(T < 3 \text{ m}) \sim 60 - 100\%$. This variability shifts to median ages between $\sim 30 - 100$ days and $F(T < 3 \text{ m}) \sim 30 - 95\%$ for dry conditions. This pattern of variability in daily TTDs in wet and dry periods is very closely matched by the estimates based on ^3H (Fig. 4.21b). Overall, the volume-weighted average TTDs of transpiration suggest median ages of around 14 days for wet conditions and between 35 days (^3H) and 70 days ($\delta^{18}\text{O}$) for dry conditions (Fig. 4.21d).

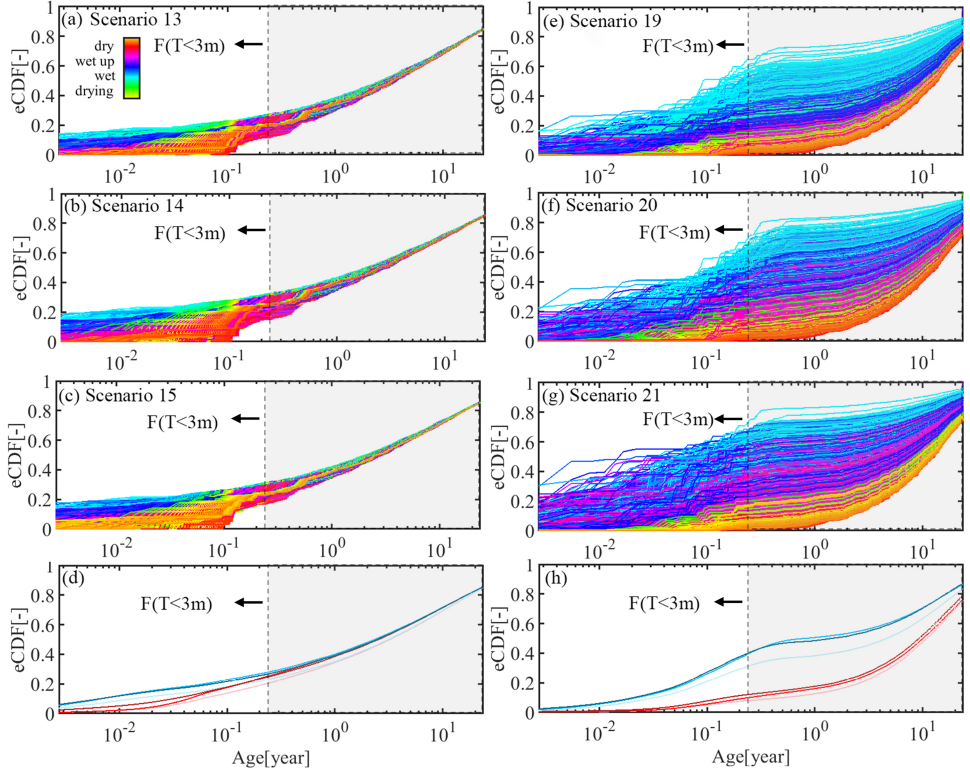


Figure 4.20: Daily streamflow (Q) TTDs extracted from the most balanced model solutions of P-SAS (scenarios 13 – 15) based on (a) calibration strategy $C_{\delta^{18}O}$ (scenario 13), (b) calibration strategy C_{3H} (scenario 14) and (c) calibration strategy $C_{\delta^{18}O, 3H}$ (scenario 15), and IM-SAS-D implementations (scenarios 19 – 21), based on (e) calibration strategy $C_{\delta^{18}O, Q}$ (scenario 19), (f) calibration strategy $C_{3H, Q}$ (scenario 20) and (g) calibration strategy $C_{\delta^{18}O, 3H, Q}$ (scenario 21). The line colors represent the transition between dry and wet periods. Panel (d) shows the volume weighted average TTDs for the wet and dry periods respectively for P-SAS model, the light shades represent calibration strategy $C_{\delta^{18}O}$ (scenario 13), the intermediate shades indicate calibration strategy C_{3H} (scenario 14) and the dark shades are calibration strategy $C_{\delta^{18}O, 3H}$ (scenario 15). Panel (h) shows the volume weighted average TTDs for the wet and dry periods respectively for IM-SAS-D model, the light shades represent calibration strategy $C_{\delta^{18}O, Q}$ (scenario 19), the intermediate shades indicate calibration strategy $C_{3H, Q}$ (scenario 20) and the dark shades are calibration strategy $C_{\delta^{18}O, 3H, Q}$ (scenario 21). For illustrative purposes, also the fraction of water younger than 3 months $F(T < 3m)$ is indicated.

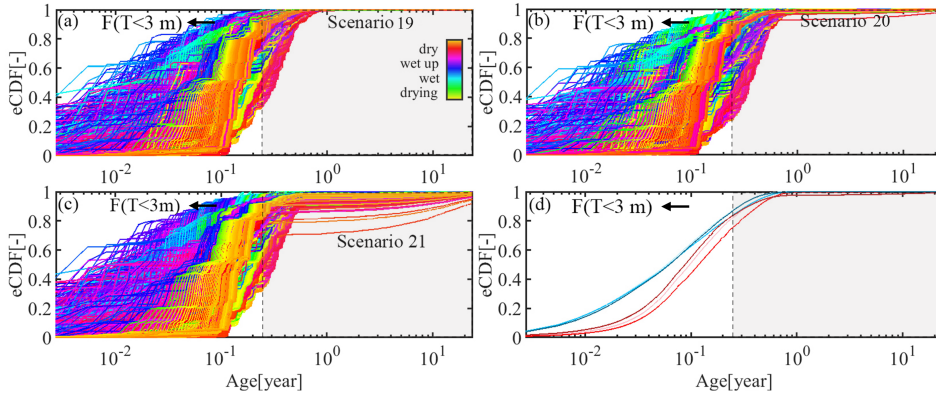


Figure 4.21: Daily transpiration (E_a) TTDs extracted from the most balanced model solutions of the IM-SAS-D implementations (scenarios 19 – 21), based on (a) calibration strategy $C_{\delta^{18}\text{O},\text{Q}}$ (scenario 19), (b) calibration strategy $C_{\text{H},\text{Q}}$ (scenario 20) and (c) calibration strategy $C_{\delta^{18}\text{O},\text{H},\text{Q}}$ (scenario 21). The line colors represent the transition between dry and wet periods. Panel (d) shows the volume weighted average TTDs for the wet and dry periods, respectively. The light shades represent calibration strategy $C_{\delta^{18}\text{O},\text{Q}}$ (scenario 19), the intermediate shades indicate calibration strategy $C_{\text{H},\text{Q}}$ (scenario 20) and the dark shades are calibration strategy $C_{\delta^{18}\text{O},\text{H},\text{Q}}$ (scenario 21). For illustrative purposes, also the fraction of water younger than 3 months $F(T < 3 \text{ m})$ is indicated.

The modelled groundwater, in comparison, was found to be characterized by substantially less temporal variability in TTDs and older water ages (Fig. 4.22). The TTDs inferred from both, $\delta^{18}\text{O}$ and ^3H , are similar and characterized by a median age of ~ 10 years under both, wet and dry conditions. While $F(T < 3 \text{ m})$ of the groundwater largely remains $< 1\%$, around 20 – 25% of the groundwater is older than 20 years.

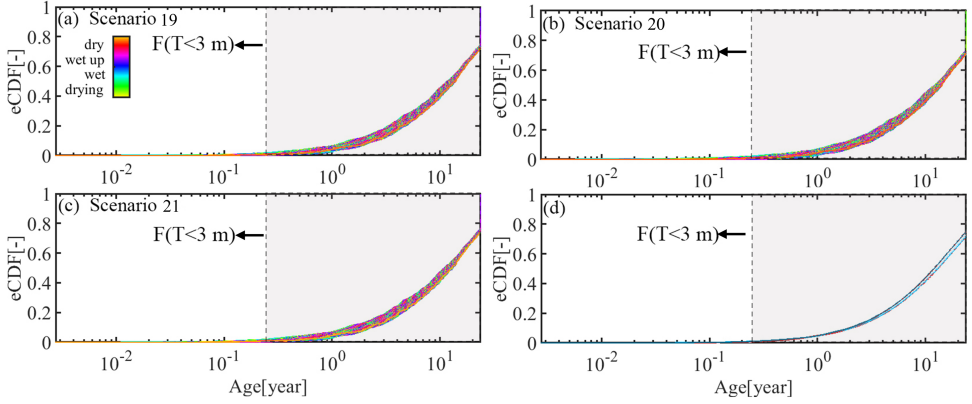


Figure 4.22: Daily groundwater (S_s) RTDs extracted from the most balanced model solutions of the IM-SAS-D implementations (scenarios 19 – 21), based on (a) calibration strategy $C_{\delta^{18}\text{O},Q}$ (scenario 19), (b) calibration strategy $C_{3\text{H},Q}$ (scenario 20) and (c) calibration strategy $C_{\delta^{18}\text{O},3\text{H},Q}$ (scenario 21). The line colors represent the transition between dry and wet periods. Panel (d) shows the volume weighted average RTDs for the wet and dry periods, respectively. The light shades represent calibration strategy $C_{\delta^{18}\text{O},Q}$ (scenario 19), the intermediate shades indicate calibration strategy $C_{3\text{H},Q}$ (scenario 20) and the dark shades are calibration strategy $C_{\delta^{18}\text{O},3\text{H},Q}$ (scenario 21). For illustrative purposes, also the fraction of water younger than 3 months $F(T < 3 \text{ m})$ is indicated.

4.5 IMPLICATIONS, LIMITATIONS AND UNRESOLVED QUESTIONS

What can we learn from the above? We believe the results obtained in this study have several implications for the utility of different tracer and model types, as described in detail below.

4.5.1 THE INDIVIDUAL ROLES OF THE CHOICES OF TRACERS AND MODELS FOR UNDERESTIMATION OF WATER AGES

The overall magnitude of water ages here estimated from time-invariant, lumped SW and CO models in combination with $\delta^{18}\text{O}$ reach MTTs of ~ 2 years (Table 4.8; Fig. 4.17). These values fall within the age ranges reported for comparable model experiments with seasonally variable tracers in many other catchments world-wide (see McGuire and McDonnell, 2006; Godsey et al., 2009; Hrachowitz et al., 2009b; Stewart et al., 2010 and references therein). Similarly, the water ages estimated with the same CO models in combination with ^3H are with MTTs ~ 10 yrs by a factor of ~ 5 higher (Table 4.8; Fig. 4.17), and also well reflect the findings of previous studies, many of which suggest ^3H -inferred catchment MTTs of $\sim 10 - 15$ yr (Stewart et al., 2010 and references therein). This suggests that the Neckar basin does not exhibit unusual or unexpected water age characteristics. By themselves, these results would therefore lend further supporting evidence for the interpretation provided by Stewart et al. (2010) and, crucially, lead us to the same conclusion, that the use of $\delta^{18}\text{O}$ and comparable seasonally variable tracers truncate stream water ages.

However, and in stark contrast, the estimates of water age obtained from all P-SAS and IM-SAS model implementations in this study, i.e., scenarios 13 – 21, are similar to each other irrespective of the tracer used. Water ages estimated from $\delta^{18}\text{O}$ are, with $\text{MTT} > 11.4$ yr, not only substantially older than those inferred from the SW and CO models (scenarios 1 – 3, 5, 7, 9, 11), but, most importantly, similar to those inferred from ^3H in P-SAS and IM-SAS models, which reach $\text{MTT} \sim 11 - 13$ yr (Table 4.9; Fig. 4.18). These water ages highlight the importance of old water in the Neckar basin, similar to what is suggested by the use of ^3H in CO models (scenarios 4, 6, 8, 10, 12).

It is important to note that the IM-SAS and, to a lesser degree, P-SAS models can simultaneously reproduce several signatures of the hydrological response together with the $\delta^{18}\text{O}$ and ^3H stream water signals. They therefore provide a more holistic description of physical transport processes in the system (Table 4.7; Fig. 4.9 – 4.14) than the SW and CO models (Table 4.6 Fig. 4.6 – 4.8), which mimic one single tracer signal and thus one isolated variable at a time. In addition, the P-SAS and IM-SAS model parameters that are most linked to tracer circulation, e.g. S_{tot} , $S_{s,p}$ and S_{umax} (Fig. 4.15), exhibit little difference when obtained from calibration to $\delta^{18}\text{O}$ or ^3H , respectively. This implies that both, $\delta^{18}\text{O}$ and ^3H , provide similar information about how tracers are routed through the model and how water is stored in and released from the system. As a consequence, also the simultaneous representation of all three types of variables under consideration, i.e., the hydrological response as well as the $\delta^{18}\text{O}$ and ^3H stream signals, in these models is consistent with the observed data (scenarios 18, 21).

The above is further corroborated by how water ages in the Neckar basin respond to changing wetness conditions. Although not identical, $\delta^{18}\text{O}$ and ^3H -inferred daily TTDs exhibit nevertheless broad agreement in the directions and magnitudes of change

in response to changing wetness conditions (Fig. 4.20). Changes in stream flow TTDs in IM-SAS are not primarily caused by changes of water ages within individual storage components. In particular, the modelled water age distributions in the groundwater S_s show limited sensitivity to changing wetness conditions, with MTT varying between ~ 18 years in dry periods and ~ 17 years in wet periods (Fig. 4.22). The TTDs in the transpiration flux E_a , which are reflective of the water ages in the unsaturated root zone S_u , exhibit with MTTs between ~ 0.20 and 0.12 years in dry and wet periods (Fig. 4.21), respectively, magnitudes and fluctuations over time that are similar to what has been previously reported in other studies (e.g., Hrachowitz et al., 2015; Soulsby et al., 2016; Visser et al., 2019; Birkel et al., 2020; Kuppel et al., 2020). However, the level of these age fluctuations alone is insufficient to explain the magnitude of change in stream flow TTDs, which can vary by several years. Instead, the temporal variability of stream flow TTDs is largely controlled by switches in the relative contributions of individual storage components to stream flow under different wetness conditions. Under increasingly wet conditions, considerably increasing proportions of comparably young water from S_u contribute over shallow preferential flow pathways (S_f) to stream flow, while the relative proportion of groundwater contributing to stream flow under such conditions is reduced (Hrachowitz et al., 2013). Both tracers, $\delta^{18}\text{O}$ and ^3H , generate these patterns in a corresponding way.

Altogether, this suggests that the P-SAS and IM-SAS models and the resulting estimates of water ages inferred from both, $\delta^{18}\text{O}$ and ^3H , provide plausible descriptions of transport processes and thus water ages in the Neckar basin. Clearly, with current observation technology, it is impossible to know the real water age distribution at river basin scale. However, the water ages and their temporal variability inferred from both, $\delta^{18}\text{O}$ and ^3H using P-SAS and IM-SAS models are widely consistent. This is suggestive that it is not the use of $\delta^{18}\text{O}$ per se that leads to truncation of TTDs, but rather that time-invariant, lumped convolution integral models are incapable of extracting sufficient information from $\delta^{18}\text{O}$ signals. These results mirror anecdotal evidence from several previous studies (e.g., Hrachowitz et al., 2015; Hrachowitz et al., 2021; Ala-Aho et al., 2017; Buzacott et al., 2020; Yang et al., 2021). Although no direct comparison with ^3H data is provided in these studies, they demonstrated the potential of $\delta^{18}\text{O}$ in SAS-based model approaches to estimate water age distributions with considerable fractions of water older than 5 – 10 years and Birkel et al. (2020) explicitly estimated MTTs of up to 18 years. Our results also strongly support the findings and general conclusions of Rodriguez et al., 2021, who undertook a direct comparison of water ages inferred from $\delta^{18}\text{O}$ and ^3H . In their study for a small catchment and based on shorter tracer time series, i.e., 2 years, and a system that is characterized by rather low MTT of ~ 3 years, they found that although ^3H led to higher MTTs than $\delta^{18}\text{O}$, the absolute difference between these ages estimates was with 0.2 years limited and even decreasing for higher percentiles of the water age distributions.

It is therefore argued that the evidence emerging from our results and the above considerations is strong enough to reject the hypothesis that $\delta^{18}\text{O}$ as a tracer generally and systematically “cannot see water older than about 4 years” (Stewart et al., 2010, Stewart, 2012) and the corresponding tails in water age distributions, leading to underestimations of water ages. We further argue that previous underestimations of

water ages are rather a consequence of the use of time-invariant, lumped parameter convolution integral model techniques that cannot resolve the information contained $\delta^{18}\text{O}$ signals in a meaningful way for catchments with transient flow conditions. In contrast, the combined information using hydrological and tracer data and thus the consideration of transient flow conditions results in similar MTTs, independent of the used tracer. Note, that for this reason, time-variant implementations of convolution integral models that can describe transient conditions may hold the potential to similarly generate water age estimates from $\delta^{18}\text{O}$ signals that reflect the results of the P-SAS and IM-SAS models tested here.

However, and notwithstanding the rejection of the above hypothesis it is important to note that overall and in spite of the similarity between $\delta^{18}\text{O}$ and ^3H inferred water ages in the study basin on the basis of P-SAS and IM-SAS models, there may be no general equivalence between $\delta^{18}\text{O}$ and ^3H tracers. Instead, it is plausible to assume that differences will gradually increase with higher water ages. In systems characterized by water older than the water in the Neckar study basin, and where the amplitudes of the $\delta^{18}\text{O}$ stream signal are attenuated to below the analytical precision, the water age estimates from $\delta^{18}\text{O}$ will indeed become subject to increasing uncertainty up to the point where further attenuation and thus older water ages cannot be discerned anymore independent of modelling approaches. The specific magnitude of such a water age threshold remains difficult to quantify with the available data. However, given the results in the Neckar study basin, the question raised by Stewart et al. (2021), if $\delta^{18}\text{O}$ allows to see “the full range of travel times”, can to some extent be answered: it can be assumed that, when used with a suitable model, $\delta^{18}\text{O}$ contains sufficient information for a meaningful characterization of water ages in systems characterized by MTTs of at least $\sim 15 - 20$ years, which encompasses the vast majority of river basins so far analyzed in literature (see Stewart et al., 2010 and references therein). As a step forward, the original hypothesis above can, for future research, be reformulated into: $\delta^{18}\text{O}$ -inferred water age estimates are subject to increasing uncertainty and bias when compared to ^3H -inferred estimates when stream water MTTs of $\sim 15 - 20$ years are exceeded in systems characterized by increasingly old water.

4.5.2 THE ROLE OF SPATIAL AGGREGATION ON UNDERESTIMATION OF WATER AGES

In addition to the above, Kirchner (2016) demonstrated that the use of seasonally variable tracers with time-invariant, lumped parameter model approaches, i.e., SW and CO, has considerable potential to underestimate water ages due to spatial aggregation of heterogeneous MTTs in systems characterized by large spatial contrasts in MTTs. We could here not reproduce that exact experiment, as stream observations were available only at one location for each tracer. However, in the distributed implementation of the IM-SAS-D model (scenarios 19 – 21), we nevertheless explicitly accounted, albeit to a limited degree, for heterogeneity in the system input variables as well as for potential differences in landscape types, as expressed by the three model HRUs. This resulted in different TTDs for the individual precipitation zones (Table 4.10; Fig. 4.19) and elevation zones and HRUs therein. The comparison between the lumped IM-SAS-L (scenarios 16 – 18) and the distributed IM-SAS-D models does not show major differences in their ability

to reproduce the various hydrological signatures nor the $\delta^{18}\text{O}$ and ^3H stream signals (Table 4.7). Against evidence from various previous studies (e.g., Euser et al., 2015; Gao et al., 2016; Nijzink et al., 2016a; Nguyen et al., 2022), this reflects to some degree the conclusion by Loritz et al., 2021, who found in a comparative analysis that distributed model implementations do not necessarily improve a model's ability to reproduce the hydrological response as compared to spatially lumped formulations. In addition, the contrasts in water ages between the discretized model components, with MTTs reaching from ~ 8 to ~ 22 yrs in the individual precipitation zones, may not be sufficient to significantly affect basin overall MTTs. As a consequence, the results of IM-SAS-L and IM-SAS-D also do not show major differences in the associated water age estimates, with MTTs $\sim 11 - 17$ yrs and $12 - 16$ yrs, respectively (Table 4.9; Fig. 4.18).

How can this be interpreted? If significantly older ages were inferred from the distributed IM-SAS-D implementation, this would have provided strong supporting evidence for the role and effect of spatial heterogeneity on water ages as demonstrated by Kirchner (2016). However, the similar water ages inferred from the spatially lumped and distributed implementations, respectively, allow two possible but mutually contradicting interpretations. Either, it could indicate that the aggregation of spatial heterogeneity does not have any discernible effect on water ages inferred from the IM-SAS model in the study basin or, on the contrary, the spatial contrasts in water ages, limited by the spatial resolution of the model and the available data, were not sufficient to detect any significant differences. The evidence found here therefore remains inconclusive and further research is required to describe the role of the aggregation of spatial heterogeneity for estimates of water ages using IM-SAS type of models.

For any estimates of water ages in this study – as in any other study – it is important to bear in mind that they are conditional on the available data and models used. Uncertainties can and do arise from both, data and from decisions taken in the modelling process (e.g., Beven, 2006; Kirchner, 2006). One challenge in this study was that precipitation $\delta^{18}\text{O}$ and ^3H compositions were only available at rather coarse spatial and temporal resolutions. This chapter has used the best available information to spatially extrapolate the tracer precipitation data from the individual sampling stations to estimate their spatial variation across the Neckar basin including stations outside the study basin. The monthly $\delta^{18}\text{O}$ and ^3H distribution in precipitation within South-Germany is generally similar (Stumpp et al., 2014; Schmidt et al., 2020); still, regional correction for $\delta^{18}\text{O}$ might not be sufficient to explain local differences in $\delta^{18}\text{O}$ precipitation data. A similar limitation applies to the temporal resolution of tracer composition in precipitation as only monthly information was available. However, as the available data nevertheless reflect the seasonal variation in $\delta^{18}\text{O}$ and ^3H precipitation input, the uncertainties arising can be assumed to largely affect the short-term dynamics of tracers in the stream and thus rather young water ages, whereas the objective of this analysis was focused on the right tail of the water age distributions and thus on old ages. Notwithstanding these uncertainties, the overall model performances with respect to the hydrological and tracer responses, suggest that the choice of input data and the model formulations led to model results that are largely consistent with the observed responses in the stream. The observation that there is little ambiguity in

the results further suggests that the remaining uncertainties are unlikely to affect the overall interpretation and conclusions of this study.

4.6 CONCLUSIONS

$\delta^{18}\text{O}$ and ^3H are frequently used as tracers in environmental sciences to estimate age distributions of water. However, it has previously been argued that seasonally variable tracers, such as $\delta^{18}\text{O}$, fail to detect the tails of water age distributions and therefore substantially underestimate water ages as compared to radioactive tracers, such as ^3H . In this chapter, based on a >20-year record of hydrological, $\delta^{18}\text{O}$ and ^3H data we systematically scrutinized the above postulate by comparing water age distributions inferred from $\delta^{18}\text{O}$ and ^3H with a total of 21 different model implementations. The main findings of this analysis are the following:

1. Water ages inferred from $\delta^{18}\text{O}$ with commonly used time-invariant, sine wave (SW) and lumped parameter convolution integral models (CO) are with MTTs $\sim 1 - 2$ years substantially lower than those obtained from ^3H with the same models, reaching MTTs ~ 10 years.
2. In contrast, the concept of SAS-functions in combination with hydrological models (P-SAS, IM-SAS) did not only allow simultaneous representations of water storage fluctuations together with $\delta^{18}\text{O}$ and ^3H stream signals, but water ages inferred from $\delta^{18}\text{O}$ were with MTTs $\sim 11 - 17$ years much higher and even higher than inferred from ^3H , which suggested MTTs $\sim 11 - 13$ years.
3. Constraining P-SAS and IM-SAS model implementations individually with $\delta^{18}\text{O}$ and ^3H observations resulted in similar values for parameters that control water ages, such as the total storage Stot (P-SAS) or passive groundwater volumes Ss,p (IM-SAS). In addition, $\delta^{18}\text{O}$ and ^3H -constrained models both exhibited limited differences in the magnitudes of water ages in different parts of the models as well as in the temporal variability of TTDs in response to changing wetness conditions. This suggests that both tracers lead to comparable descriptions of how water is routed through the system.
4. Based on the points above, we reject the hypothesis that $\delta^{18}\text{O}$ as a tracer generally and systematically “cannot see water older than about 4 years” (Stewart et al., 2010; Stewart et al., 2012) and that it truncates the corresponding tails in water age distributions, leading to underestimations of water ages.
5. Instead, these results provide evidence of broad equivalence of $\delta^{18}\text{O}$ and ^3H as age tracers for systems characterized by MTTs of at least 15 – 20 years.
6. The question to which degree aggregation of spatial heterogeneity can further adversely affect estimates of water ages remains unresolved as the lumped and distributed implementations of the IM-SAS model provided similar and thus inconclusive results.

Overall, this chapter demonstrates that previously reported underestimations of water ages are most likely not a result of the use of $\delta^{18}\text{O}$ or other seasonally variable

tracers per se. Rather, these underestimations can be largely attributed to the choices of model approaches which rely on assumptions not frequently met in catchment hydrology. Given the vulnerability of lumped, time-invariant parameter convolution integral approaches in combination with $\delta^{18}\text{O}$ to substantially underestimate water ages due to transient flow conditions, spatial aggregation and potentially other, still unknown effects, it is therefore strongly advocated to avoid the use of this model type in combination with seasonally variable tracers and to instead adopt SAS-based or other model formulations that allow for the representation of transient conditions.

5

LONG-TERM TRANSPORT DYNAMICS IN RESPONSE TO CLIMATIC VARIABILITY BASED ON MULTI-TIME SCALE ANALYSIS

5

Water is ancient and yet eternally new. It has been here since the dawn of time and will be here long after we are gone.

Unknown

This chapter is based on:

Wang, S. et al. "Multi-decadal stability of water ages and tracer transport in a temperate-humid river basin". In: *Environmental Research letters* (2024). Under review

SUMMARY

The temporal dynamics of water ages provide crucial insights into hydrological processes and transport mechanisms, yet there remains a significant gap in quantifying water age variability across different temporal scales. This study utilizes a comprehensive dataset spanning 70 years of hydrological observations and tritium records (1953 – 2022) with a semi-distributed hydrological model with integrated tracer routing routine based on StorageAge Selection functions SAS, to explore the temporal evolution of water ages in the 4000 km² Upper Neckar River basin, Germany. Our findings indicate a systematic convergence of the variability of young water fractions and other metrics of water age in riverflow and evaporation towards stable values when averaging over increasing time scales. While at daily scales exhibiting considerable variability with young water fractions in riverflow $F_{wy,Q} \sim 0.01 - 0.91$ and in evaporation $F_{wy,E} \sim 0.02 - 0.75$, the variability of $F_{wy,Q}$ and $F_{wy,E}$ gradually reduces with increasing averaging time scales and converge to 0.45 – 0.47 and 0.96 – 0.97, respectively, between individual decades. Liquid water input (P_L), comprising rainfall and snow melt, emerges as the dominant driver of $F_{wy,Q}$ across all time scales. In contrast, $F_{wy,E}$ shows varying controls with time scale: soil moisture content governs daily fluctuations, whereas P_L dominates at the decadal scale. As a consequence, water ages demonstrate remarkable stability with only minor deviations: a 20% fluctuation in average decadal P_L results in only $\sim 4\%$ variation in $F_{wy,Q}$ and $\sim 1\%$ in $F_{wy,E}$ over the study period. These findings suggest a lack of major long-term dynamics in water ages, driven by either internal processes or external transport variability. Consequently, these results suggest that the physical transport dynamics in the Upper Neckar River basin, and potentially in comparable river basins with similar water age characteristics, can be considered near-stationary over multiple decades.

5.1 INTRODUCTION

As the crucial link between hydrology and water quality at the catchment scale, water ages and distributions thereof (i.e. transit time distributions; TTDs) are a metric of physical transport through a hydrological system (Hrachowitz et al., 2016). As such they are a descriptor of how water and, as a consequence, nutrients and pollutants are stored in and released from catchments via different flow paths (Rinaldo et al., 2015; Sprenger et al., 2018; Benettin et al., 2022). The celerity-driven hydrological response, including riverflow and evaporation, acts at different time scales than the velocity-driven TTDs that underlie the water quality response in catchments (Weiler et al., 2003; McDonnell and Beven, 2014; Hrachowitz et al., 2016). Temporal variability of the hydrological response over a spectrum of time-scales from minutes to multiple decades has been extensively described in literature (Thompson and Katul, 2012; Berghuijs et al., 2014; Sivapalan and Blöschl, 2015; McMillan, 2020; Berghuijs and Slater, 2023). In contrast, the majority of studies that seek to analyze temporal variability of water ages and the underlying drivers have so far focused on daily time scales. These studies demonstrate that water ages in fluxes such as riverflow or evaporation, can fluctuate considerably at this time scale and that the main driver behind this variability is the available water supply and the associated magnitude of precipitation input at that time scale (Benettin et al., 2015a, Benettin et al., 2017b; Harman, 2015; Hrachowitz et al., 2015; Soulsby et al., 2016; Rodriguez et al., 2018; Kuppel et al., 2020; Wilusz et al., 2020). Beyond that, several studies have reported significant, albeit attenuated variability at time scales from monthly (Kaandorp et al., 2018; Knapp et al., 2019; Stockinger et al., 2019) over seasonal (Birkel et al., 2016; Remondi et al., 2018) to yearly (Heidbüchel et al., 2013; Birkel et al., 2015; Von Freyberg et al., 2018; Wilusz et al., 2017; Stockinger and Stumpp, 2024). At these scales, switches between distinct storage compartments, such as the unsaturated root-zone or the groundwater, as dominant source of water can become an additional factor regulating variability of water ages (Hrachowitz et al., 2013).

However, as a result of insufficiently long tracer records in many catchments, there is only a handful of studies that have analyzed water ages over time periods longer than 10 – 20 years (Hrachowitz et al., 2010b; Wang et al., 2023). Thus, little is known about the variability over such longer time scales and the resulting long-term dynamics of water ages, including potentially systematic trends over time arising therefrom. This is in particular concerning as there is evidence that changes in land management and the associated changes to (sub-)surface flow paths and water storage volumes do affect water ages at such time scales (Danesh-Yazdi et al., 2016; Hrachowitz et al., 2021). Similarly, altered precipitation and atmospheric water demand due to climate change can, as “external transport variability” (Kim et al., 2016), directly impact water ages. As a knock-on effect, catchment properties such as vegetation cover may adjust to a changing climate, potentially leading to additional changes in subsurface flow paths and/or water storage volumes (Wang et al., 2024a), as “internal transport variability” (Kim et al., 2016).

This knowledge gap increases uncertainties in our ability to predict removal of legacy solutes such as nitrate (Basu et al., 2010; Howden et al., 2011) or chloride (Hrachowitz et al., 2015) over time-scales of several decades but also the mobilization of solutes at shorter time-scales, such as phosphorus (e.g. Dupas et al., 2018) under

changing environmental conditions. The problem would be further exacerbated if water ages are non-self-averaging. Such a behavior has been widely observed for tracer and solute concentrations in stream water and is related to the fractal scaling of these variables (Kirchner et al., 2000; Hrachowitz et al., 2009b; Godsey et al., 2010; Kirchner and Neal, 2013; Aubert et al., 2014). In non-self-averaging time series, the variability of their daily, monthly, yearly or decadal means remains constant or converges towards stable averages at rates lower than predicted by the central limit theorem. Such non-self-averaging time series can give rise to trends that can be robust but nevertheless unreliable predictors of future solute dynamics, as demonstrated by Kirchner and Neal, 2013.

The objective of this chapter is to quantify the temporal variability in water ages as well as to identify their dominant controls across time-scales from daily to multi-decadal and to analyze the associated temporal evolution of water ages for riverflow and evaporation in the Upper Neckar basin, Germany, which has been used to test the effects of climatic variability on hydrological response in Chapter 3. The analysis is based on long-term hydrological data and tritium records over a 70-year period (1953 – 2022), together with the SAS-function integrated into the hydrological model suggested by Chapter 4, to estimate water age distributions in riverflow and evaporation. More specifically, we test the hypotheses that (1) water ages of riverflow and evaporation are non-self-averaging and thus unpredictable over decadal time-scales, that (2) different drivers control variability of water ages at different time scales and that (3) water ages are subject to significant long-term dynamics on decadal time scales, reflecting hydro-climatic variability and associated changes in catchment (sub-)surface structure.

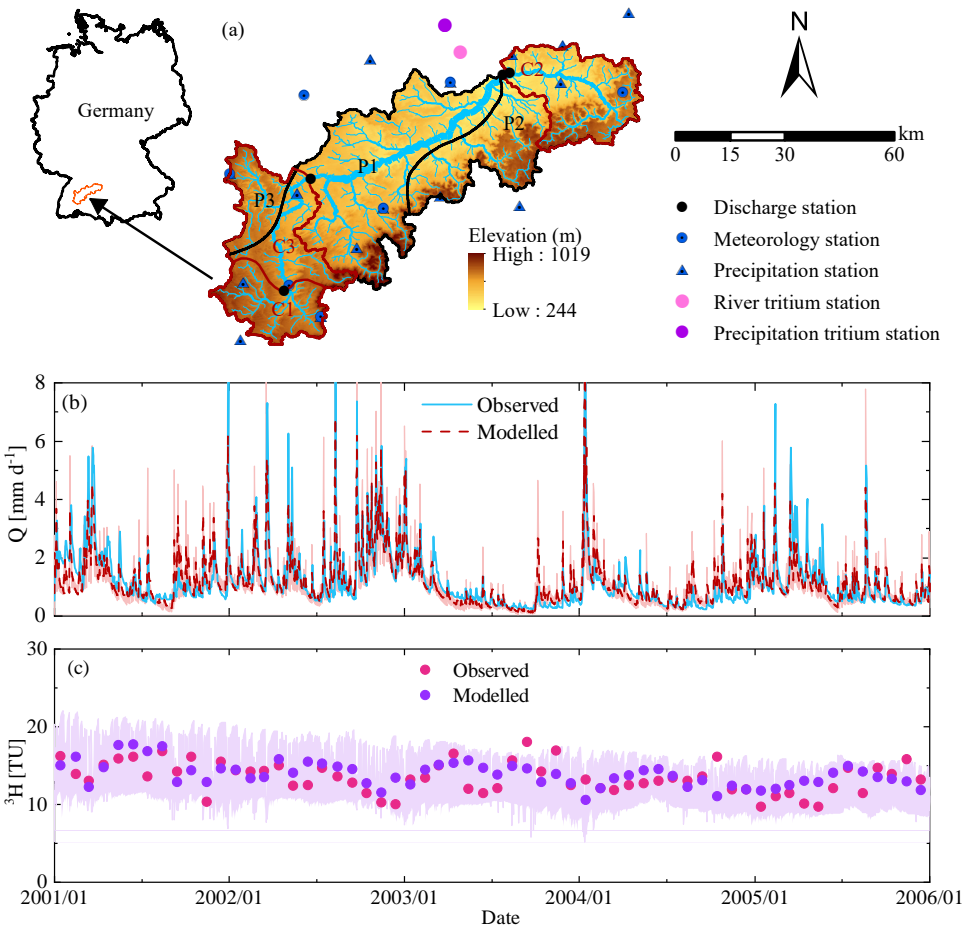


Figure 5.1: (a) Elevation of the Neckar catchment with discharge and hydro-meteorological stations as well as the water sampling locations used in this study, (b) the spatial distribution of long-term mean annual precipitation in the Neckar catchment and the stratification into four distinct precipitation zones P1 – P4 (black line), (c) hydrological response units classified according to their land-cover and topographic characteristics.

5.2 DATA

For the analysis, the same daily hydro-meteorological data records for the time period 01/01/1953 – 31/12/2022 as Chapter 3 are used here (Fig. 5.1a; Fig. 5.2). In addition, the long-term monthly ^3H data (Schmidt et al., 2020) records (Fig. 5.2) are available from the Global Network of Isotopes in Precipitation and the Federal Institute of Hydrology (BfG). Tritium (^3H) data in precipitation and riverflow were available from the stations Stuttgart and Obertürkheim close to the basin outlet for the period 1978 – 2018. Briefly, Long-term monthly ^3H data in precipitation were obtained for the period 01/01/1978 – 31/12/2016 at the Stuttgart station. The tritium record in precipitation (the gray dots in Fig. 5.2d) was reconstructed for the preceding 1953-1977 period by bias correcting data from the sampling stations Ottawa (1953-1960) and Vienna (1961-1977) to establish robust initial conditions for model calibration, available from the Global Network of Isotopes in Precipitation, which is a joint database of the International Atomic Energy Agency (IAEA) and the World Meteorological Organization (WMO). The tritium precipitation samples do not represent instantaneous grab samples but bulk samples from mixed daily samples, which reflect the volume-weighted monthly isotopic composition (Wang et al., 2023). However, tritium stream water samples reflect non-volume-weighted monthly average isotopic compositions based on the used stream water sampling method (Wang et al., 2023).

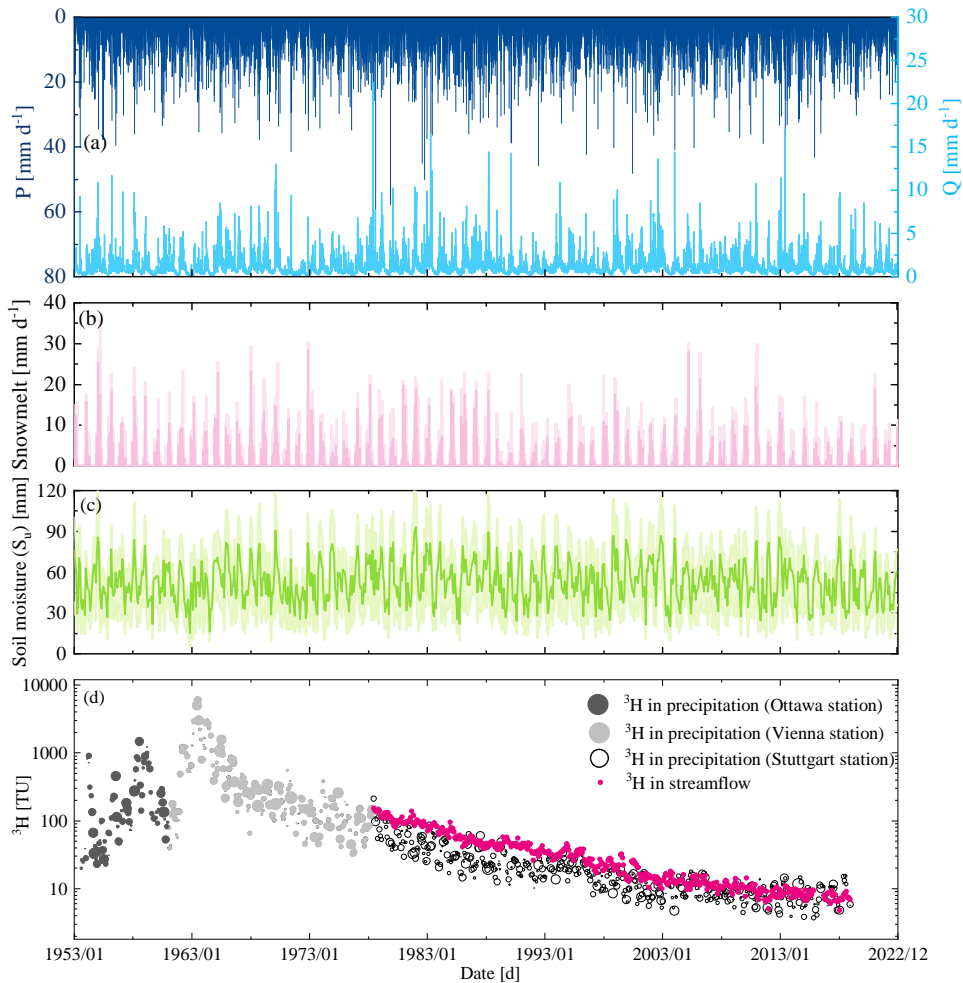


Figure 5.2: (a) The dark blue bars indicate time series of observed daily precipitation P and the blue line indicates time series of daily observed streamflow Q ; (b) daily snowmelt for entire time period (1953–2022), where the relatively dark pink line shows the modelled snowmelt using the best fit parameter sets and the light pink shaded area indicates the associated 5th/95th percentiles of all feasible solutions calibrated based on entire time period; (c) monthly maximum values of estimated soil moisture S_u for 1953–2022, where green line indicates the most balanced solution and light green shade indicates the 5th/95th inter-quantile range obtained from all pareto optimal solutions calibrated based on entire time period; (d) Observed ^3H signals in precipitation (dark gray circles; size of circles indicates the precipitation volume) and observed stream ^3H signals (pink dots). Note that the tritium record in precipitation (the gray dots) was reconstructed for the preceding 1953–1977 period by bias correcting data from the sampling station Ottawa (1953–1960) and Vienna (1961–1977) to establish robust initial conditions for model calibration, available from the Global Network of Isotopes in Precipitation which is a joint database of the International Atomic Energy Agency (IAEA) and the World Meteorological Organization (WMO).

5.3 METHODS

The semi-distributed process-based hydrological model developed in Chapter 2, which has been implemented and tested for Chapter 3. Briefly, this model features three parallel hydrological response units, i.e. forest, grass/cropland and wetland, which are linked through a common storage component representing the groundwater system (Fig. 2.2 in Chapter 2). Overall, the model consists of an elevation-stratified snow storage (S_{snow}) as well as individual interception (S_i), unsaturated root zone (S_u), fast responding (S_f) and slow responding groundwater storage (S_s) components for each hydrological response unit.

The storage-age selection function (SAS) approach (e.g. Rinaldo et al., 2015, see section 4.3.1.3 in Chapter 4) was integrated with the hydrological model to trace ^3H fluxes, which has been tested and suggested by Chapter 4. Briefly, each storage component used a uniform distribution as SAS function. Although this entails that each storage is fully mixed, the different time-scales of the individual storage components, lead to a “combined” SAS functions that does not result in an overall fully mixed system response. The passive water storage $S_{s,p}$ (mm), characterized by $dS_{s,p}/dt = 0$, that physically represents groundwater volumes below the level of the river bed (Zuber, 1986), was added as parameter to the active groundwater storage S_s for a sufficiently large mixing volume (Birkel et al., 2011; Fig. 2.2 in Chapter 2). Note that while the outflow Q_s from the groundwater storage is exclusively regulated by the active storage volume in S_s (Eq. 2.24 in Table 2.2 in Chapter 2), the ^3H of that outflow is sampled from the total groundwater storage volume $S_{s,tot} = S_s + S_{s,p}$.

Following a multi-objective strategy to ensure a plausible representation of model internal processes, the model was calibrated to simultaneously reproduce seven river flow signatures and river water ^3H dynamics (Table 5.1). To reflect the vegetation adapting its active root system to changing climatic conditions during the 70-year study period, we independently estimated the model root-zone storage capacity parameter S_{umax} for each decade, as described by Chapter 3 and accordingly hardcoded the different values of S_{umax} in the model, varying between 95 and 115 mm throughout the study period. Tracking the ^3H signals through the model allowed to estimate the distributions of water ages in riverflow (Q) and actual evaporation, which here is the sum of interception evaporation and transpiration ($E = E_i + E_t$). Hereafter young water fractions (F_{wy}), i.e. water younger than 3 months (Kirchner, 2016) as well as other age metrics, such as F_{w10} , i.e. fraction of water younger than 10 years, are used as robust descriptor to describe water ages in this Chapter. Detailed descriptions of the model implementation and calibration in the study region are provided by Chapter 3 and 4.

Table 5.1: Signatures of stream flow (Q) and tritium concentration (^3H) and the associated performance metrics used for model calibration and evaluation. The performance metrics include the Nash–Sutcliffe efficiency (NSE) and the relative error (RE).

Signature	Symbol	Performance metric
Time series of stream flow	Q	NSE_Q
Time series of $\log(Q)$	$\log(Q)$	$NSE_{\log(Q)}$
Flow duration curve of $\log(Q)$	$FDC_{\log(Q)}$	$NSE_{FDC\log(Q)}$
Seasonal runoff coefficient	C_r	NSE_{C_r}
Autocorrelation function of flow (AC)	AC	NSE_{AC}
Runoff coefficient in summer	$C_{r,\text{summer}}$	$RE_{C_{r,\text{summer}}}$
Runoff coefficient in winter	$C_{r,\text{winter}}$	$RE_{C_{r,\text{winter}}}$
Time series of ^3H in streamflow	^3H	$NSE_{^3\text{H}}$

5.4 RESULTS AND DISCUSSION

The model reproduces the main features of the hydrological response over the entire study period, both at the basin outlet (Fig. 5.1b; Table 5.2 and Fig. 5.3) and, as model test without further re-calibration, in three nested sub-catchments, same as that showed in Figure 3.7 in Chapter 3. It does not only capture the timing of flows (Fig. 5.3a), but also simultaneously reproduces well other observed riverflow signatures including the flow-duration curves (Fig. 5.3d), seasonal runoff coefficients (Fig. 5.3c) and autocorrelation functions (Fig. 5.3e). Similar to a previous implementation in the greater study region by Chapter 4 tested the entire Neckar basin, the model also captures the overall decline of river water ^3H levels with $NSE_{^3\text{H}} > 0.93$. In spite of somewhat underestimating peaks, the magnitude of seasonal ^3H amplitudes and intra-annual fluctuations are represented well (Fig. 5.1c; Fig. 5.4).

Table 5.2: Values of the performance metrics for the most balanced solution and quantiles of all performance metrics for the full set of pareto optimal solutions from the multi-objective calibration.

Performance metric	Balanced (5 th -95 th) quantiles
NSE_Q	0.59 (0.06-0.55)
$NSE_{\log(Q)}$	0.67 (0.34-0.64)
$NSE_{FDC\log(Q)}$	0.96 (0.92-0.99)
NSE_{C_r}	0.99 (0.56-0.97)
NSE_{AC}	0.90 (0.86-0.91)
$RE_{C_{r,\text{summer}}}$	0.83 (0.82-0.89)
$RE_{C_{r,\text{winter}}}$	0.91 (0.89-0.91)
$NSE_{\delta^{18}\text{O}}$	0.93 (0.94-0.97)
D_E	0.80 (0.57-0.78)

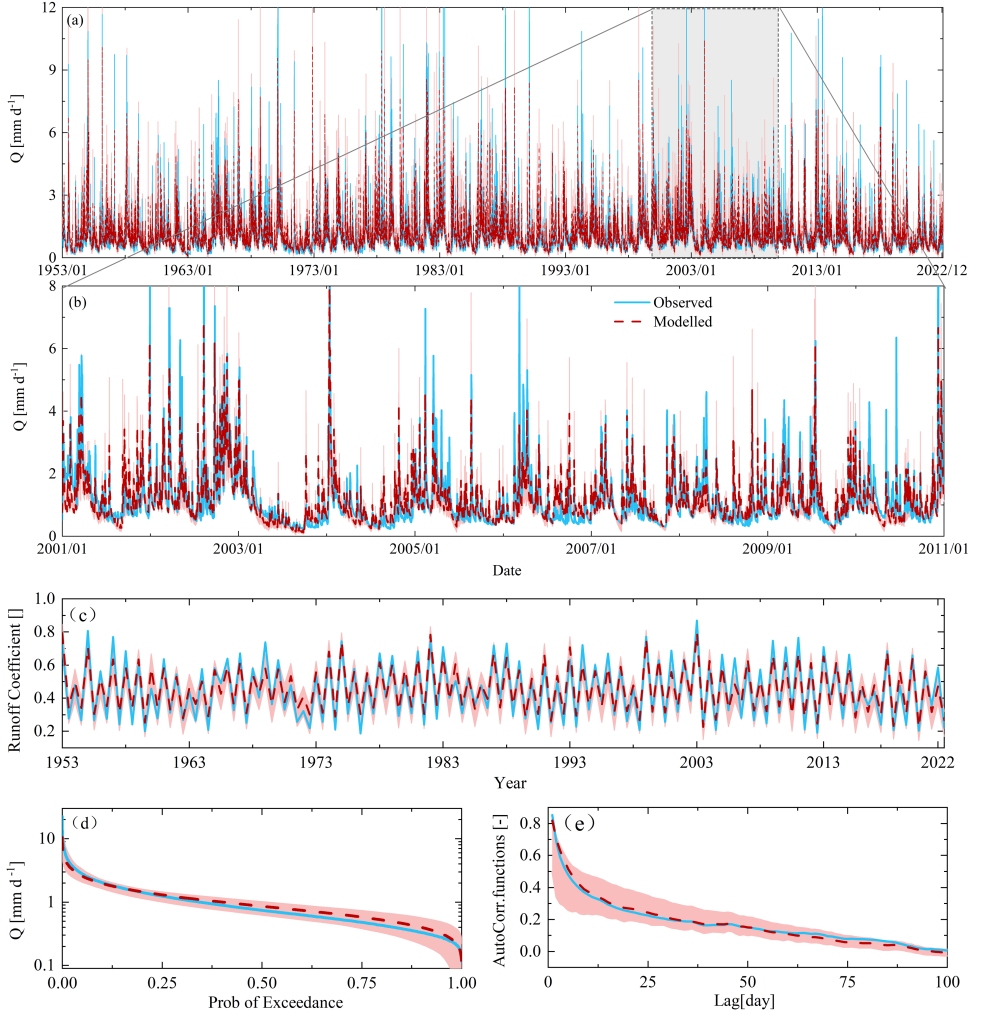


Figure 5.3: Hydrograph and selected hydrological signatures reproduced by the integrated hydrological and tracer transport model, following a simultaneous calibration to Q and ^3H . (a) Time series of observed and modelled daily stream flow (Q), where the red dashed line indicates the most balanced solution, i.e., highest D_E , and the red shaded area the 5th/95th inter-quantile range obtained from all pareto optimal solutions; (b) stream flow zoomed-in to the period 1/1/2001 to 31/12/2010; (c) seasonal runoff coefficients (RC_Q), (d) flow duration curves (FDC_Q), and (e) autocorrelation functions of streamflow (AC_Q) for the entire time period. Blue lines indicate values based on observed streamflow (Q_o), red dashed lines are values based on modelled stream flow (Q_m) representing the most balanced solutions, i.e., highest D_E and the red shaded areas show the 5th/95th inter-quantile ranges obtained from all pareto optimal solutions.

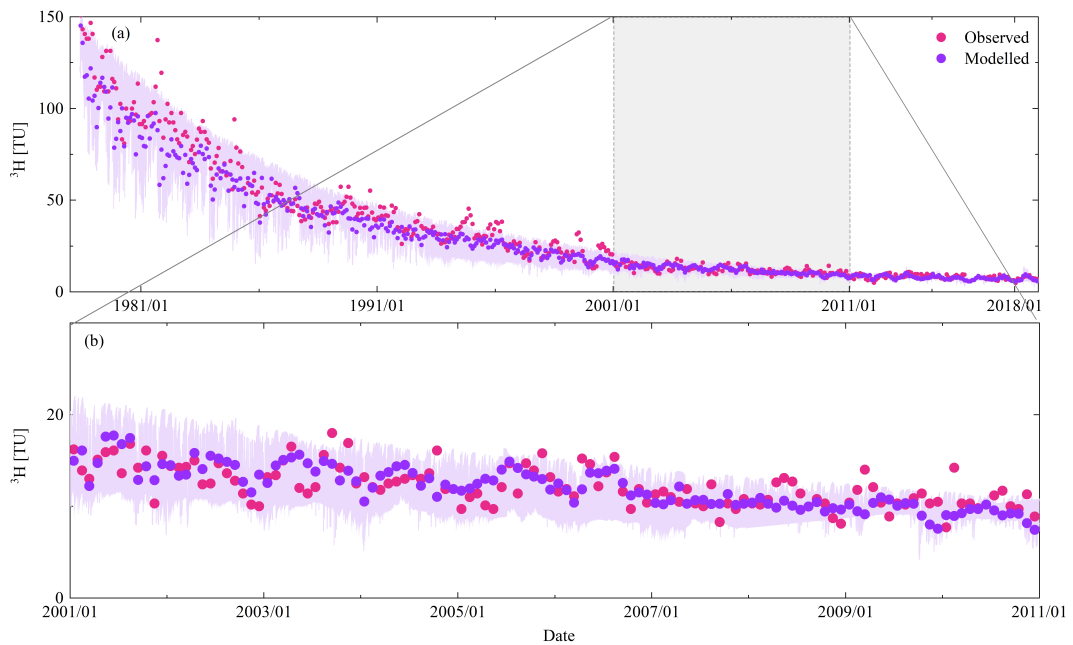


Figure 5.4: The time series of stream ^3H reproduced by the integrated model based on simultaneous calibration to ^3H and the streamflow signatures for the entire time period. (a) Observed stream ^3H signals (pink dots) as well as the most balanced modelled ^3H signal in the stream (purple dots) and the 5th/95th percentile of all retained Pareto optimal solutions (light purple shaded area) (b) zoom-in of observed and modelled ^3H signals in the stream for the period 1/1/2001 to 31/12/2010.

5.4.1 HOW DO WATER AGES VARY OVER DIFFERENT TIME SCALES?

Tracking water fluxes through the model, a median non flow-weighted fraction of young water $F_{wy,Q} \sim 0.34$ emerged for riverflow on a daily time scale. At the same time, a pronounced variability with daily $F_{w10,Q}$ fluctuating between 0.01 and 0.91 (5th/95th percentile) was observed, reflecting differences in daily precipitation and evaporation (Fig. 5.5a,b). Describing older river water, daily $F_{w10,Q}$ varied between 0.41 and 0.95 and thus to a lesser degree in response to changing daily hydroclimatic conditions (Fig. 5.5a,b). To analyse the variability of water ages at different time scales, we computed block averages of F_{wy} , aggregating to weekly, monthly, seasonal, yearly and decadal values. With increasing averaging time scales, a reduction of variability was found. While average monthly $F_{wy,Q}$ oscillates between 0.02 and 0.75, this is eventually reduced to 0.44 – 0.47 for decadal averages with similarly reduced variability for $F_{w10,Q}$ (Fig. 5.5a,b) and other age fractions (Table 5.3). The observed convergence towards increasingly stable water ages is an indicator for a self-averaging process. As robust quantity to further test for self-averaging behaviour in the time series of water ages we plotted the root mean square differences (RMSD) of pairs of adjacent averages against the time interval over which the averages were computed (Fig. 5.5c) as suggested by Kirchner and Neal, 2013. It was found that at averaging time scales of > 1 month, the rates of convergence of both $F_{wy,Q}$ and $F_{w10,Q}$ come close to $n^{-0.5}$, which describes a self-averaging and thus stationary process (e.g. white noise) as dictated by the central limit theorem. Such a process is characterized by weak persistence and thus little long-term fluctuations in water ages at low frequencies over time that here applies to time scales of at least multiple decades.

Evaporation is characterized by a markedly different age structure that is dominated by much younger water as illustrated by median $F_{wy,E} \sim 0.96$ and $F_{w10,E} > 0.99$, respectively. The daily $F_{wy,E}$ ranges from 0.56 to 1, while fractions of older water do not decrease below $F_{w10,E} \sim 0.75$ and thus exhibit less variability (Fig. 5.5d,e). Similar to riverflow, the variability in evaporation ages decreases with increasing averaging time scales (Table 5.4), as illustrated by average monthly $F_{wy,E}$ that ranges from ~ 0.81 to 1 which further decreases to a range of 0.96 to 0.97 for decadal averages (Fig. 5.5d,e). Correspondingly, the traces of RMSD of adjacent means as function of the averaging time scale for both $F_{wy,E}$ and $F_{w10,E}$ show convergence rates close to $n^{-0.5}$ at averaging time scales larger than 6 months (Fig. 5.5f). This suggests that the age structure of evaporation is not subject to major long-term fluctuations and can thus also be assumed stationary at multi-decadal time scales.

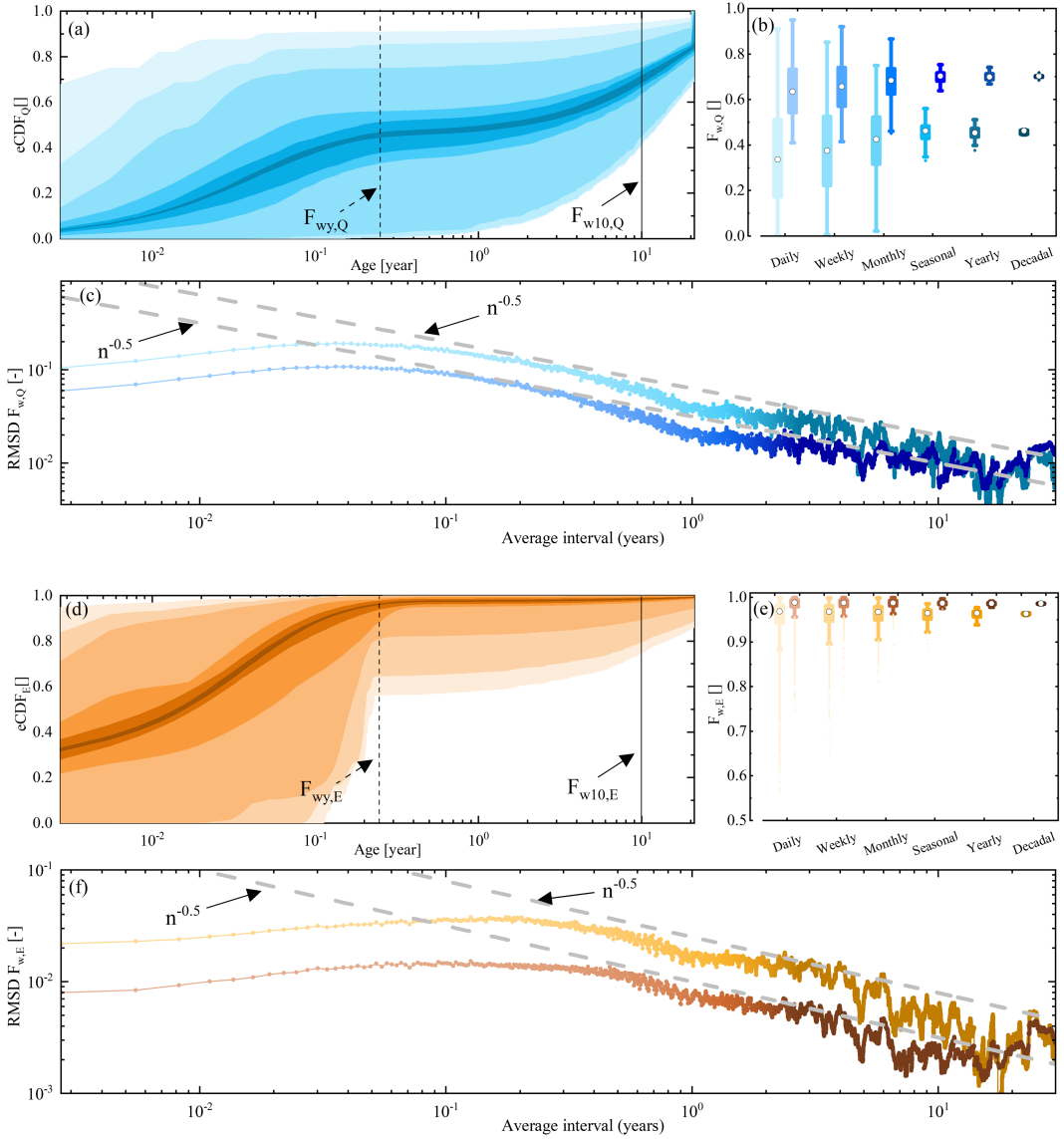


Figure 5.5: The variability of riverflow TTDs ($eCDF_Q$) and evaporation TTDs ($eCDF_E$) from the most balanced model solution over various time scales. (a) The blue shades from lighter to darker indicate the 5th/95th intervals of the $eCDF_Q$ from daily to decadal averaging time-scales, (b) the blue and navy blue box plots (whiskers indicate 5th/95th percentiles) from lighter to darker indicates $F_{wy,Q}$ and $F_{w10,Q}$ from daily to decadal, respectively, (c) Self-averaging behavior in $F_{wy,Q}$ (the gradient blue line) and $F_{w10,Q}$ (the gradient navy blue line) by root mean squared differences between successive average values (RMSD), (d) the orange shades from lighter to darker indicate the $eCDF_E$ from daily to decadal, (e) the yellow and brown boxes from lighter to darker indicates $F_{wy,E}$ and $F_{w10,E}$ from daily to decadal, respectively, (f) Self-averaging behavior in $F_{wy,E}$ (the gradient yellow line) and $F_{w10,E}$ (the gradient brown line) RMSD between successive average values. Note that the dashed grey line is the slope of -0.5 predicted by the central limit theorem for self-averaging time series.

Table 5.3: The water fraction Metrics of stream flow TTDs. The TTD metrics represent the best fits of the respective time-invariant TTD. The water fractions are shown as the fractions of water younger than a specific year n , i.e. $F_{wn,Q}$. *Note that the fraction of water younger than 3 months $F_{wy,Q}$ is comparable to the fraction of young water as suggested by Kirchner (2016).

Time scales → TTD metrics ↓		Daily	Weekly	Monthly	Seasonal	Yearly	Decadal
Water fractions (%)	$F_{wy,Q}^*$	35 (4/71)	38 (6/69)	42 (16/63)	46 (37/52)	45 (45/50)	46 (44/47)
	$F_{w1,Q}$	38 (8/73)	41 (11/71)	45 (20/65)	48 (40/55)	48 (48/53)	49 (47/50)
	$F_{w3,Q}$	45 (19/76)	48 (21/74)	51 (30/69)	54 (47/60)	54 (54/58)	55 (53/56)
	$F_{w5,Q}$	51 (28/79)	54 (30/77)	57 (38/73)	59 (53/65)	59 (59/64)	60 (58/61)
	$F_{w10,Q}$	64 (47/84)	66 (48/83)	68 (54/80)	70 (65/74)	70 (70/73)	70 (68/72)
	$F_{w20,Q}$	80 (71/91)	81 (71/91)	83 (75/89)	83 (81/86)	83 (83/85)	84 (83/84)
	$F_{w40,Q}$	96 (91/100)	96 (91/100)	96 (92/100)	96 (94/100)	96 (95/100)	96 (95/100)

Table 5.4: The water fraction Metrics of evaporation TTDs. The TTD metrics represent the best fits of the respective time-invariant TTD. The water fractions are shown as the fractions of below a specific year n , i.e. $F_{wn,E}$. * Note that the fraction of water younger than 3 months $F_{wy,E}$ is comparable to the fraction of young water as suggested by Kirchner (2016).

Time scales → TTD metrics ↓		Daily	Weekly	Monthly	Seasonal	Yearly	Decadal
Water fractions (%)	$F_{wy,E}$	95 (86/99)	96 (88/99)	96 (90/99)	96 (92/98)	96 (95/98)	96 (96/97)
	$F_{w1,E}$	97 (92/100)	97 (93/100)	98 (94/100)	98 (96/99)	98 (97/98)	98 (97/98)
	$F_{w3,E}$	97 (92/100)	98 (94/100)	98 (95/100)	98 (97/99)	98 (97/99)	98 (98/98)
	$F_{w5,E}$	98 (93/100)	98 (94/100)	98 (95/100)	98 (97/99)	98 (97/99)	98 (98/98)
	$F_{w10,E}$	98 (95/100)	98 (96/100)	99 (96/100)	99 (98/99)	99 (98/99)	99 (98/99)
	$F_{w20,E}$	99 (97/100)	99 (98/100)	99 (98/100)	99 (99/100)	99 (99/99)	99 (99/99)
	$F_{w40,E}$	100 (99/100)	100 (99/100)	100 (99/100)	100 (100/100)	100 (100/100)	100 (100/100)

5.4.2 WHAT ARE THE HYDRO-CLIMATIC DRIVERS OF WATER AGE VARIABILITY AT DIFFERENT TIME SCALES?

To explore which factor can best explain variability in Fwy regression analysis was used. For the entire 70-year study period 1953-2022, the pronounced variability of young water fractions in riverflow $F_{wy,Q}$ at a daily time-scale is to first order controlled by daily liquid water input $P_L = P_{rain} + M_{snow}$ (Fig. 5.6a). This is illustrated by the sensitivity (ψ) of $F_{wy,Q}$ to P_L , approximated by a linear relationship $\psi = \Delta F_{wy,Q} / \Delta P_L \sim 0.03$ ($R^2 = 0.34$). Other potential hydro-climatic drivers, including riverflow Q as aggregate metric of catchment wetness ($R^2 = 0.22$), evaporation E ($R^2 = 0.22$) or root-zone moisture content S_u ($R^2 = 0.20$) exert weaker controls on $F_{wy,Q}$. Across all tested averaging time-scales, P_L remains the strongest driver, reaching $R^2 = 0.89$ with a sensitivity $\psi \sim 0.07$ at the decadal time-scale. P_L also becomes relatively more important compared to the other hydro-climatic variables ($R^2 = 0.25 - 0.82$; Fig. 5.6). At the seasonal time-scale it is notable that $F_{wy,Q}$ is somewhat more sensitive to P_L in winter ($\psi \sim 0.10$) than in summer ($\psi \sim 0.07$). Further analysis revealed that this effect can be attributed to the influence of winter snow melt. Periods of snow cover preceding snow melt, are characterized by low $F_{wy,Q} \sim 0.2$, on average (Fig. 5.7b). Snow melt water is rather young as the presence of snow over periods longer than a few weeks is rare in the study region. As a consequence, snow melt inputs (Fig. 5.7a) increase $F_{wy,Q}$ to ~ 0.7 . In contrast, $F_{wy,Q}$ preceding summer rainfall events (Fig. 5.7e) is, on average, with $F_{wy,Q} \sim 0.4$ considerably higher (Fig. 5.7f). Although summer $F_{wy,Q}$ also reaches ~ 0.7 , the rate of increase from 0.4 to 0.7, and thus its sensitivity, is lower. Overall, controls on fractions of older water $F_{w10,Q}$ correspond to those above with P_L being the strongest control on $F_{w10,Q}$ (Fig. 5.8).

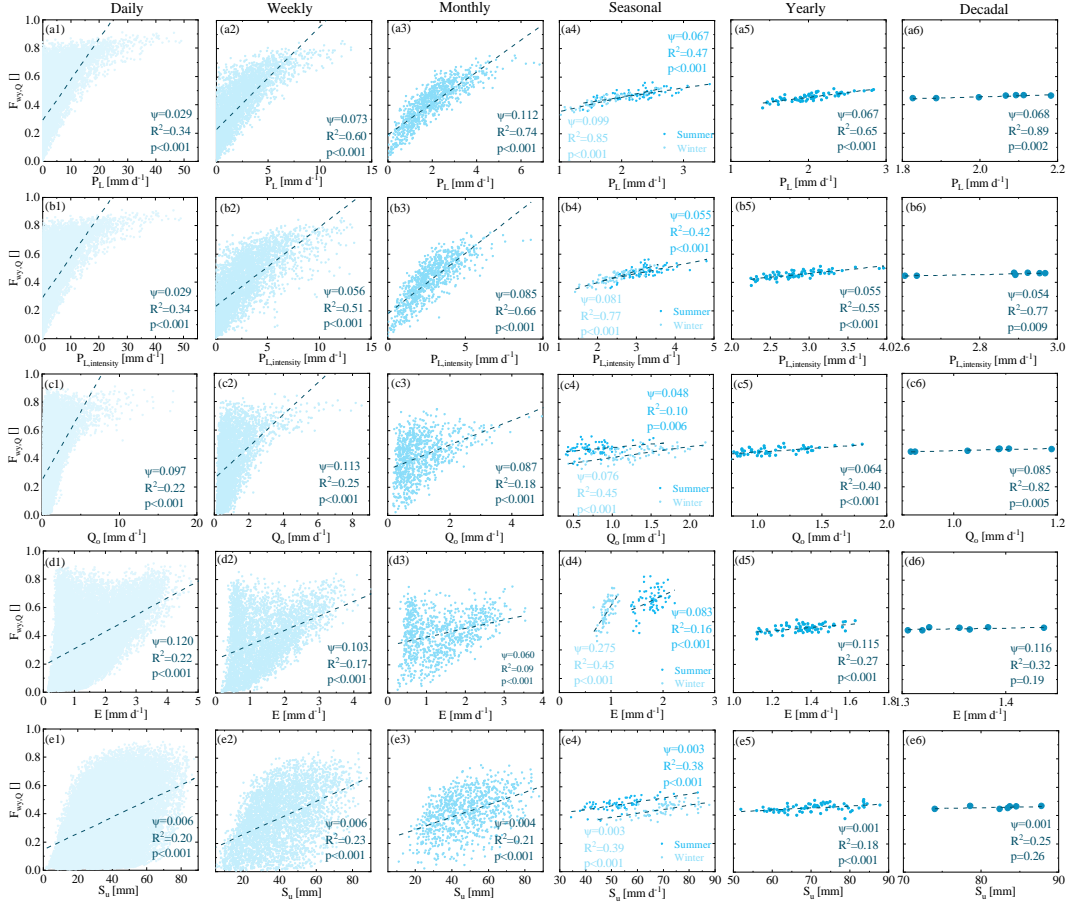


Figure 5.6: Relationship between the young water fraction in riverflow ($F_{wy,Q}$) and hydro-climatic variables over different time scales from daily to decadal including (a) liquid precipitation P_L (rainfall + snowmelt), (b) liquid precipitation intensity $P_{Lintensity}$, (c) riverflow Q_o , (d) evaporation E (e) soil moisture S_u . the dashed lines indicate the linear relationship between the $F_{wy,Q}$ and the various hydro-climatic variables x , used to approximate the sensitivity $\psi = \Delta F_{wy,Q} / \Delta x$.

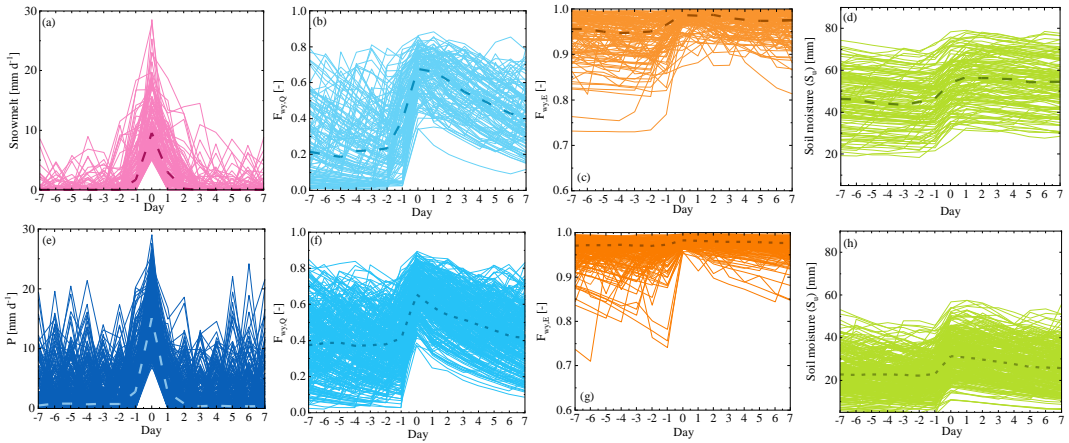


Figure 5.7: Sensitivity analysis of variability of the young water fractions (<3 months) in riverflow ($F_{wy,Q}$) and evaporation ($F_{wy,E}$) as well as soil moisture S_u in response to the selected snowmelt events in winter in (a)-(d) and rainfall events in summer in (e)-(h).

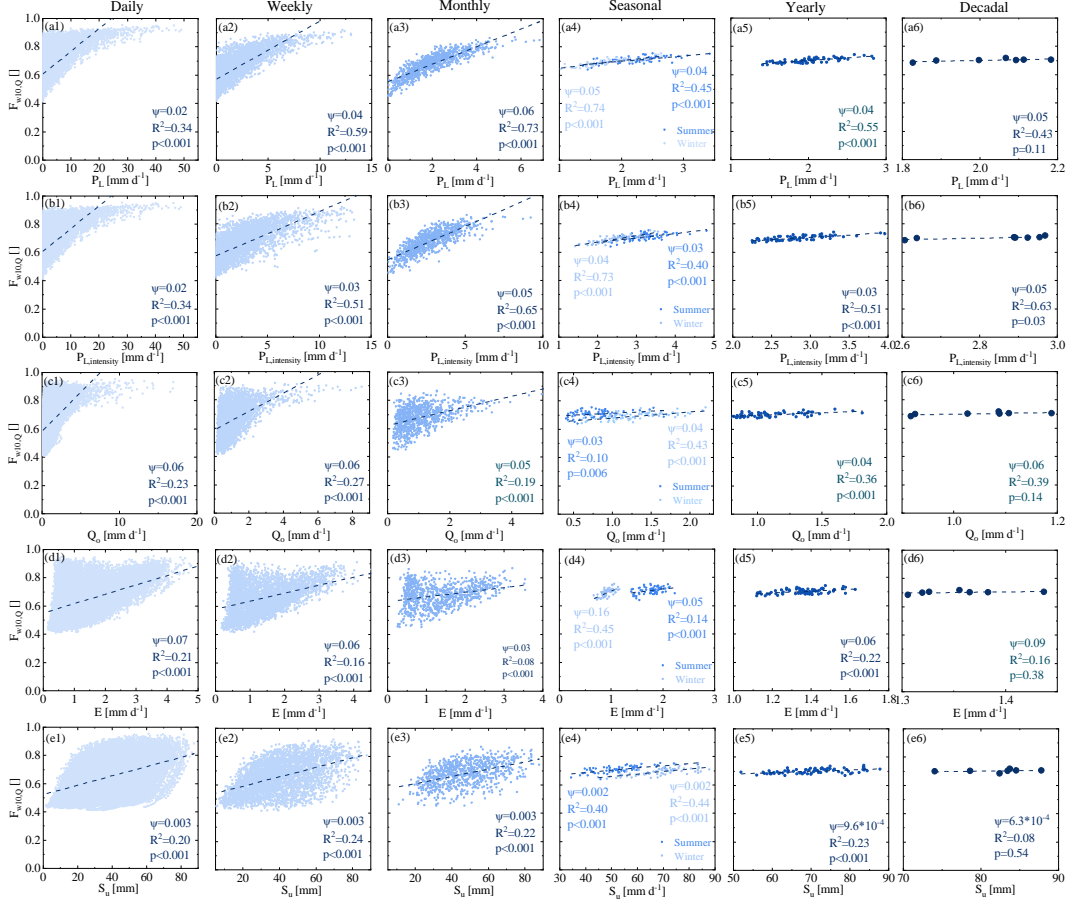


Figure 5.8: Relationship between the young water fraction in riverflow ($F_{w10,Q}$) and hydro-climatic variables over different time scales from daily to decadal including (a) liquid precipitation P_L (rainfall + snowmelt), (b) liquid precipitation intensity $P_{Lintensity}$, (c) riverflow Q_o , (d) evaporation E (e) soil moisture S_u . the dashed lines indicate the linear relationship between the $F_{w10,Q}$ and the various hydro-climatic variables x , used to approximate the sensitivity $\psi = \Delta F_{w10,Q} / \Delta x$.

The variability in daily young water fractions in evaporation $F_{wy,E}$ are driven to a lesser degree by liquid water input P_L ($R^2 = 0.07$; $\psi \sim 3 \cdot 10^{-3}$), but are more dependent on soil moisture S_u ($R^2 = 0.21$, $\psi \sim 10^{-3}$; Fig. 5.9). Aggregating the history of water input and release over the past weeks, S_u captures the interaction between water supply and atmospheric water demand. However, with increasing averaging time-scale the strength of S_u as driver gradually reduces to $R^2 < 0.01$ ($\psi \sim 10^{-5}$). Instead, E exhibits the strongest relation with $F_{wy,E}$ at seasonal scale, with P_L emerging as dominant control on $F_{wy,E}$ at the decadal time-scale ($R^2 = 0.60$; $\psi \sim 0.01$). This switch from S_u over E to P_L as dominant control illustrates that the history of water supply and release interactions in S_u preserves merely the system's memory of the past few weeks. At time-scales longer than that, the water fluxes released from the system become better predictors, while over decadal time-scales variations in water supply, expressed as P_L , control fluctuations in $F_{wy,E}$. It can also be observed that at seasonal time-scale, $F_{wy,E}$ is more sensitive to P_L and E in winter than in summer (Fig. 5.9). For P_L , this difference is explained by the higher sensitivity of $F_{wy,E}$ to winter snow melt (Fig. 5.7c) than to summer rainfall (Fig. 5.7g), similar to $F_{wy,Q}$. Low evaporation due to low temperatures together with little input of new liquid water during periods with snow cover cause water to remain in S_u longer, resulting in older ages during such periods (and thus lower $F_{wy,E}$). With higher temperatures, snow melt and thus input of young water increases, accompanied by higher evaporation rates, that lead to quicker removal of water from S_u . This younger water that is evaporated at higher rates then leads to a faster turnover of water in S_u and thus to a distinct switch ($\psi \sim 0.11$) towards a younger water pool from which evaporation is sourced and the markedly higher $F_{wy,E}$ (Fig. 5.9). Due to the absence of snow, the fluctuation in summer $F_{wy,E}$ is more gradual, as evident by its lower sensitivity to E ($\psi \sim 0.03$). The controls on $F_{w10,E}$ are comparable to those of $F_{wy,E}$ (Fig. 5.10).

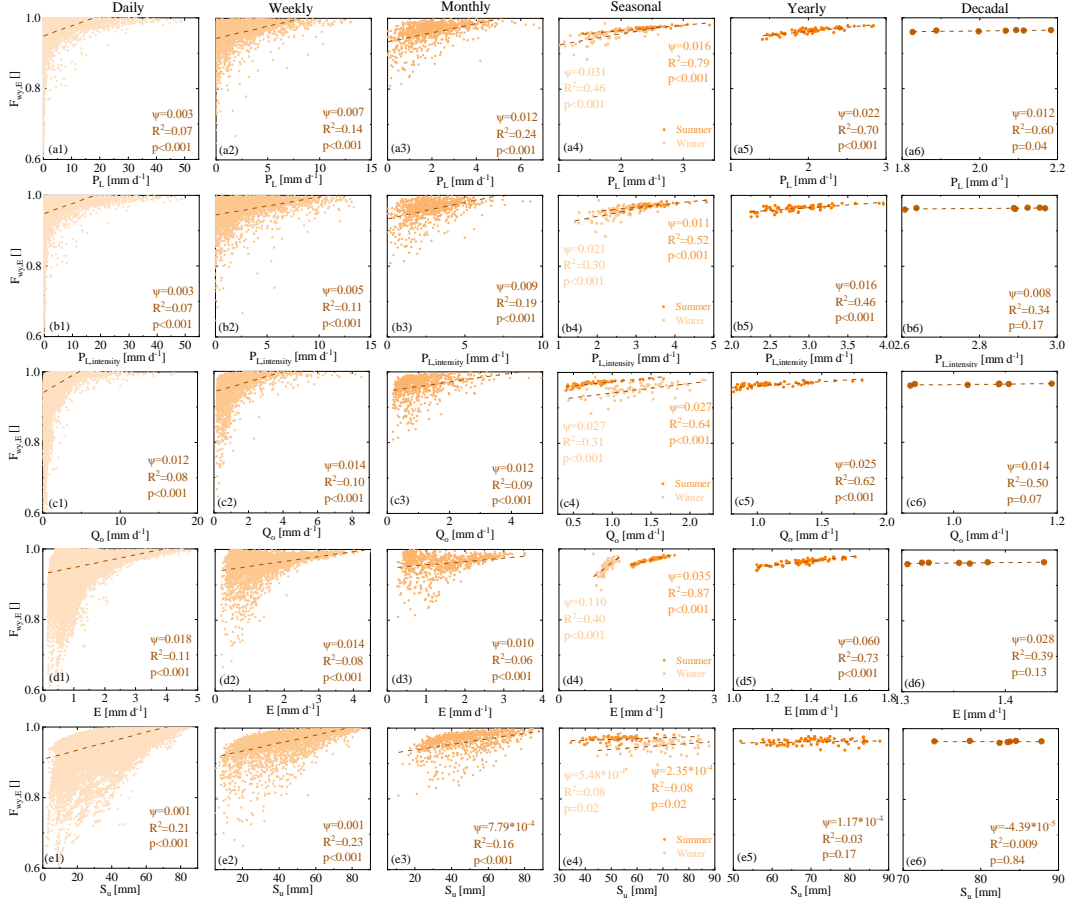


Figure 5.9: Relationship between the young water fraction in evaporation ($FF_{wy,E}$) and hydro-climatic variables over different time scales from daily to decadal including liquid precipitation P_L (rainfall + snowmelt) in (a1)-(a6), liquid precipitation intensity $P_{L,intensity}$ in (b1)-(b6), (c) riverflow Q_o , (d) evaporation E (e) soil moisture S_u . The dashed lines indicate the linear relationship between the $FF_{wy,E}$ and the various hydro-climatic variables x , used to approximate the sensitivity $\psi = \Delta F_{wy,E} / \Delta x$.

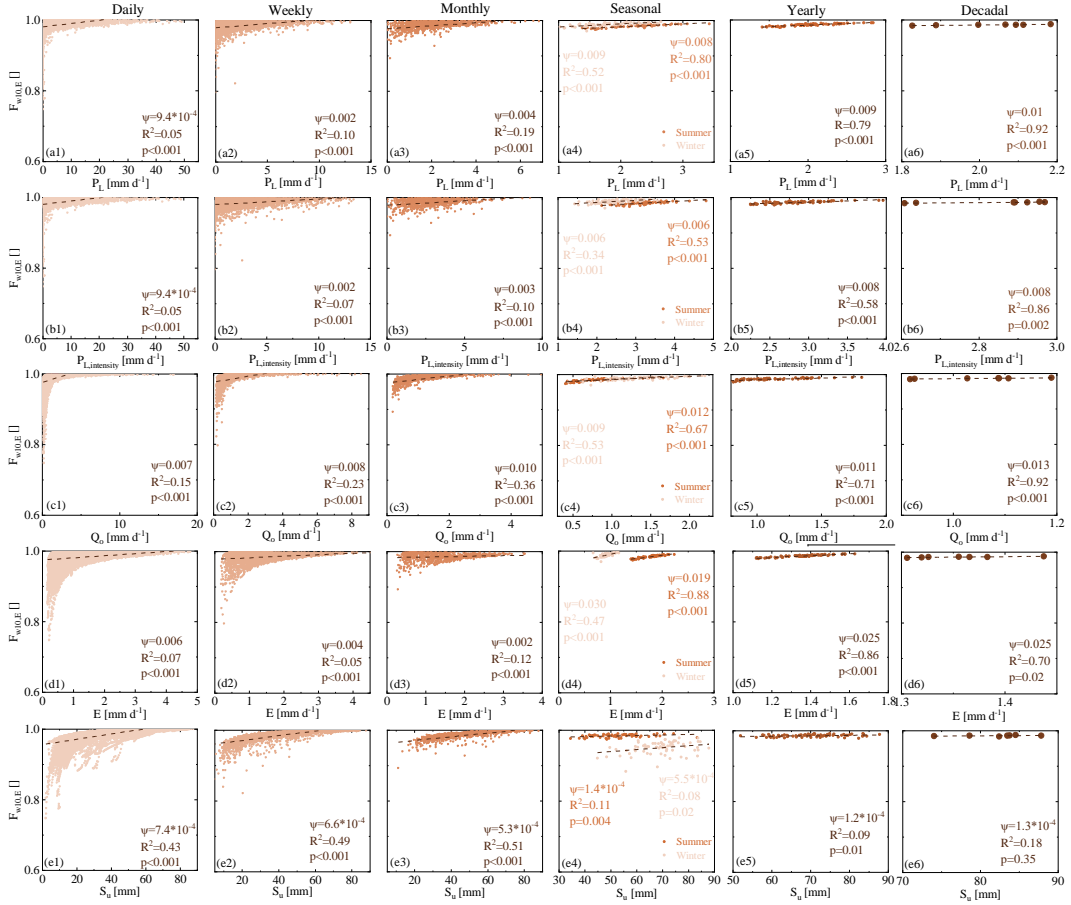


Figure 5.10: Relationship between the young water fraction in evaporation ($FF_{w10,E}$) and hydro-climatic variables over different time scales from daily to decadal including liquid precipitation P_L (rainfall + snowmelt) in (a1)-(a6), liquid precipitation intensity $P_{L,intensity}$ in (b1)-(b6), (c) riverflow Q_o , (d) evaporation E (e) soil moisture S_u . The dashed lines indicate the linear relationship between the $FF_{w10,E}$ and the various hydro-climatic variables x , used to approximate the sensitivity $\psi = \Delta F_{w10,E} / \Delta x$.

5.4.3 TEMPORAL EVOLUTION AND LONG-TERM DYNAMICS OF WATER AGES

Over the seven study decades, remarkably stable water ages can be observed (Fig. 5.11). As a consequence of the above, the fluctuations of average riverflow water ages between the individual decades are very minor. The same is true for the inter-decadal variabilities around these average water ages, for which merely some limited changes in the extremes can be observed (Fig. 5.11c). In spite of higher absolute sensitivities to hydro-climatic variability at decadal ($\psi \sim 0.07$) than at daily time-scales ($\psi \sim 0.03$), the relative sensitivities or elasticities of $F_{wy,Q}$ to P_L , expressed by $\varepsilon = \psi \cdot (P_L/F_{wy,Q})$, were for wide parts of the P_L - $F_{wy,Q}$ space much lower at the decadal time-scale ($\varepsilon \leq \sim 0.32$) than at the daily time-scale ($\varepsilon \leq \sim 1.5$; Fig. 5.12). This implies that while average inter-decadal P_L varied by $\sim 650 - 803 \text{ mm yr}^{-1}$ and thus by $\sim 20\%$, $F_{wy,Q}$ varied between $0.45 - 0.47$ and thus by only $\sim 4\%$. For evaporation $F_{wy,E}$ it was found that $\varepsilon \sim 0.11$, which entails that the 20% fluctuation in P_L as dominant control led to a $F_{wy,E}$ fluctuation of merely $\sim 2\%$, making average $F_{wy,E}$ similarly stable throughout the study period, (Fig. 5.11g-i).

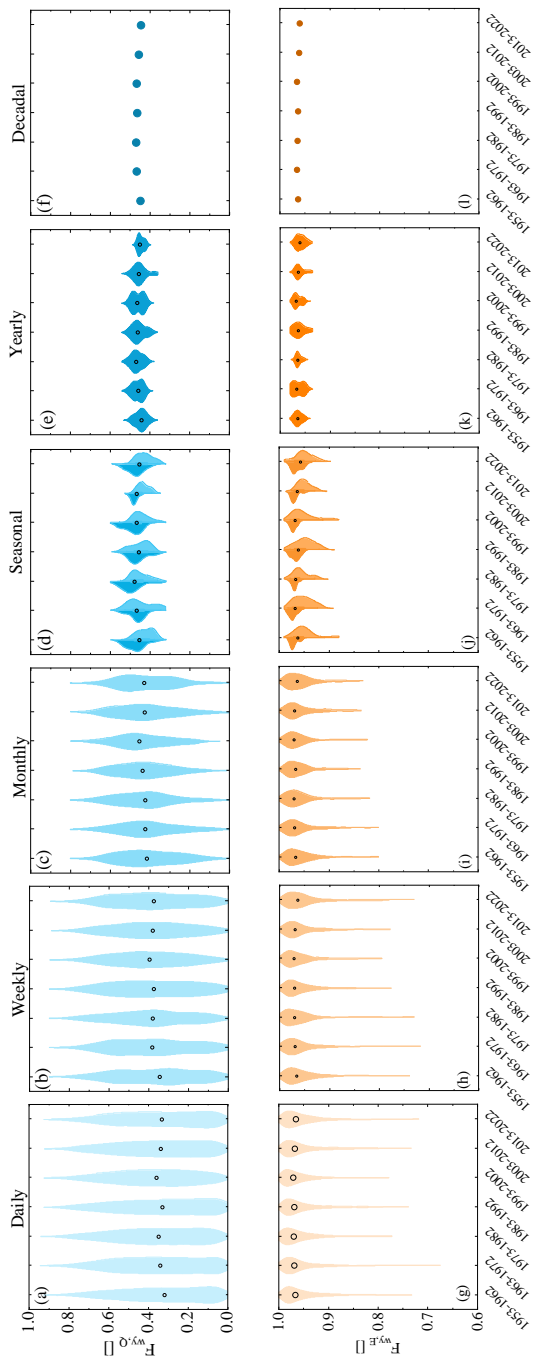


Figure 5.11: The differences of variability of the young water fractions in riverflow ($F_{wy,Q}$, a-f) and evaporation ($F_{wy,E}$, g-l) over multi-decades for each time scale (from lighter to darker for daily to decadal). Note that the relatively darker and lighter color shades in (d) and (j) indicate the F_{wy} in summer months (May–October) and in winter (November–April), respectively.

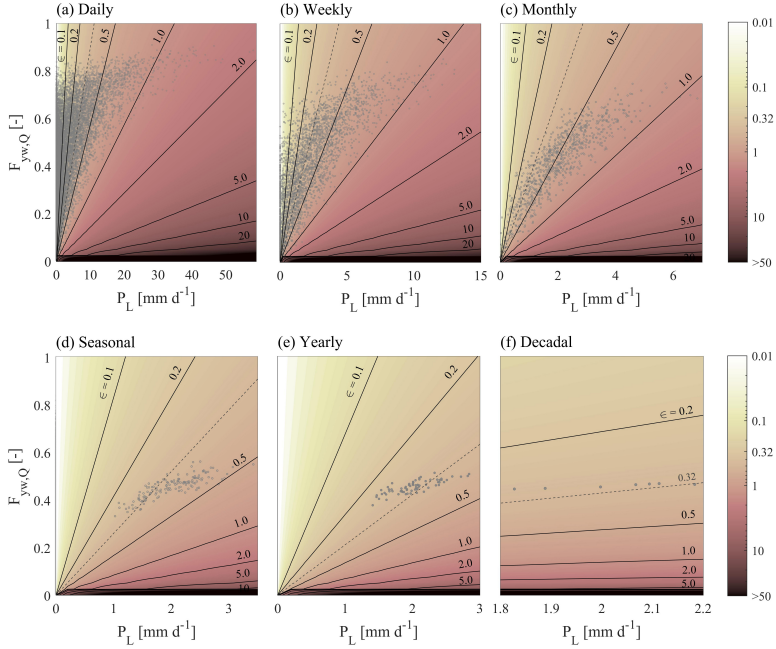


Figure 5.12: Elasticities, expressed as $\varepsilon = \psi \cdot (P_L / F_{wy,Q}) = (\Delta F_{wy,Q} / F_{wy,Q}) / (\Delta P_L / P_L)$ for (a) daily, (b) weekly, (c) monthly, (d) seasonal, (e) yearly and (f) decadal time-scales. Note that here ψ is obtained as least square fit to the data points (see Figure 3a) representing the relationship between P_L and $F_{wy,Q}$ over different time scales from daily to decadal respectively (grey dots). The black lines indicate various elasticity levels, the dashed grey lines indicate the highest elasticity $\varepsilon = 0.32$ at decadal time-scale. Briefly, an elasticity of $\varepsilon = 1$ implies that a 1% increase in $F_{wy,Q}$ (i.e. $\Delta F_{wy,Q} / F_{wy,Q} = 0.01$) follows from a 1% increase in P_L (i.e. $\Delta P_L / P_L = 0.01$). In contrast, for example $\varepsilon = 0.32$ implies a 0.32% increase in $F_{wy,Q}$ (i.e. $\Delta F_{wy,Q} / F_{wy,Q} = 0.0032$) in response to a 1% increase in P_L . At daily ($\varepsilon \leq 1.5$) to seasonal ($\varepsilon \leq 0.5$) time-scales, a considerable proportion of liquid water inputs resulted in higher elasticities ε than at decadal time scales ($\varepsilon \leq 0.32$).

5.4.4 IMPLICATIONS

The general magnitudes of $F_{wy,Q}$ and $F_{wy,E}$ from this analysis are broadly consistent with previous studies (Von Freyberg et al., 2018; Rahimpour Asenjan and Danesh-Yazdi, 2020; Ceperley et al., 2020). The results also qualitatively correspond with previous studies that report reductions in water age variability for timescales from daily to yearly (Wilusz et al., 2017) and up to 8-years (Stockinger and Stumpp, 2024).

As first to analyse water ages over multiple decades, this chapter has found no evidence for pronounced non-self-averaging behaviour. The limited fluctuation of decadal $F_{wy,Q}$ and $F_{wy,E}$ in response to the $\sim 20\%$ variation in P_L and significant 10% increase in EP over the 70-year study period suggests that the study basin buffers water ages against long-term hydro-climatic variability so that water ages and the associated conservative physical transport processes do not exhibit major long-term dynamics and can thus be assumed near-stationary at decadal time-scales with limited “external transport variability” (Kim et al., 2016). Wang et al. (2024a) have shown that vegetation adaptation to inter-decadal hydro-climatic variability in the study basin led to fluctuations in root-zone storage capacities, represented by parameter $S_{u,max}$ in our model. In spite of accounting for the fluctuations of this catchment subsurface property in our analysis $F_{wy,Q}$ and $F_{wy,E}$ remained remarkably insensitive to these changes. This therefore also indicates limited “internal transport variability”, which is consistent with the very minor changes to $F_{wy,Q}$ from 0.12 to 0.13 as a result of deforestation that led to a $> 50\%$ reduction in $S_{u,max}$ in a nearby catchment (Hrachowitz et al., 2021).

The self-averaging and temporally stable water ages contrast with the fractal scaling and non-self-averaging behaviour that is frequently observed in dynamics of river water solute concentrations and that indicates the potential presence of long-term fluctuations or trends in solute circulation dynamics. In spite of several sources of uncertainty in the modelling process (Beven, 2016), our findings that water ages are near-stationary suggest that long-term solute dynamics as manifest by their fractal scaling in many river basins are unlikely to arise from changes in conservative transport processes but may instead largely result from fluctuations in other factors, such as solute supply and/or mobilization. These may include variations in solute input (e.g. fertilizer application, solute concentration in precipitation) but also alterations of (bio-)geochemical transformation processes due to changing ambient conditions, such as temperature or soil water content that regulate for example mineral dissolution kinetics in the subsurface (e.g. Maher, 2011; Li et al., 2017) but also plant nutrient uptake (e.g. Marschner and Rengel, 2023).

It can be expected that water ages may be more sensitive to hydro-climatic variability in catchments which are characterized by younger water, i.e. higher $F_{wy,Q}$, and thus faster physical transport processes. However, it is plausible to assume that physical transport processes in river basins with similar water age structure (Königer et al., 2005; Stewart et al., 2010; Visser et al., 2019; Birkel et al., 2020) may exhibit similarly low elasticity to hydro-climatic variability and thus only limited long-term dynamics.

Overall, there are two wider implications following from the results of this chapter. Firstly, predictions of future solute dynamics in riverflow over long-time scales may be more robust than the frequently observed fractal scaling in river solute concentrations

may suggest if estimated based on water ages instead of on the solute time series themselves. Secondly, the low elasticity of water ages to variability in water supply and the resulting long-term stability of physical transport processes poses practical limits for mitigation and remediation measures of legacy contamination such as nitrate (Basu et al., 2022) that may aim to alter not only reactive processes but also physical transport characteristics by interventions such as wetland restoration or land management.

5.5 CONCLUSIONS

Based on hydro-climatic records and ^3H data we have analyzed the variability of water ages, described by the fraction of young water in riverflow ($F_{wy,Q}$) and evaporation ($F_{wy,E}$), at daily to decadal time-scales in the Upper Neckar Basin, Germany over the 70-year period 1953 – 2022. The main findings of this chapter are the following:

1. Riverflow is with $F_{wy,Q} \sim 0.4$ characterized by considerably older water than evaporation with $F_{wy,E} > 0.95$ across all time-scales.
2. The variabilities of both, $F_{wy,Q}$ and $F_{wy,E}$ systematically decreases with increasing averaging time-scale: average $F_{wy,Q}$ fluctuates merely between 0.45 – 0.47 and $F_{wy,E}$ between 0.96 – 0.97 across individual decades. This indicates that $F_{wy,Q}$ and $F_{wy,E}$ can be considered near-stationary across several decades. These results therefore provide no evidence to support the hypothesis that $F_{wy,Q}$ and $F_{wy,E}$ are non-self-averaging and unpredictable.
3. Liquid water input P_L is the dominant driver of $F_{wy,Q}$ across all time-scales. In contrast, $F_{wy,E}$ is characterized by varying drivers: while soil moisture is the dominant control at daily time-scale, this switches to liquid water input P_L at the decadal time-scale. Thus the hypothesis that the dominant controls on F_{wy} vary across different time-scales can only be rejected for $F_{wy,Q}$.
4. Average water ages were rather stable and subject to minor fluctuations over time. In response to a 20% fluctuation in decadal P_L , $F_{wy,Q}$ varied only by $\sim 4\%$ and $F_{wy,E}$ by $\sim 1\%$ over the study period. The hypothesis that water ages are subject to major long-term dynamics on decadal time scales in the study basin was therefore rejected.

Overall, as first to systematically analyse water ages over multiple decades, it demonstrates that there is no evidence for non-self-averaging and unpredictable in water ages, and long-term average water ages were rather stable and subject to minor fluctuations in the Upper Neckar basin. Consequently, the associated physical transport processes can be assumed to be near-stationary across multiple decades, under either internal or external transport variability.

6

CONCLUSIONS AND OUTLOOKS

行百步者半九十。
The last mile is the longest.
战国策·秦五策

THE goal of this thesis was to obtain more insights of the effects of climatic variability on the hydrological system over multi-decades, with specific focus on the Neckar basin, Germany. Due to the complexity of the hydrological system, not only the water quantity but also the water quality, these effects on the hydrological system are not easy to quantify. Therefore, this thesis also aimed to set-up and use a tracer-aided semi-distributed hydrological model and systematic model experiments to explore the long-term variations of hydrological response and water age distributions in response to climatic variability for the Neckar basin.

6.1 NOVEL CONTRIBUTIONS

LONG-TERM EVOLUTION OF ROOT ZONE STORAGE CAPACITY TO HYDRO-CLIMATIC VARIABILITY

As one of the most important parts of the hydrological system, root zone storage capacity (S_{umax}) not only directly represents the hydrologically relevant information of root-systems at the catchment scale, but also is a critical parameter in hydrological models. This thesis is the first to systematically and explicitly quantify how S_{umax} changes with varying hydro-climatic conditions over multi-decades, based on two methods: water-balance method and hydrological model calibration. As only < 2% land use change over multi-decades is observed, it is concluded that S_{umax} significantly changes over multiple decades reflecting vegetation adaptation to hydro-climatic variability in the Neckar basin. Furthermore, it is found that values of S_{umax} derived from calibration of a hydrological model correspond to that from water-balanced method, with very similar magnitudes and fluctuations. This does provide further evidence that multi-decadal evolution of S_{umax} is a fingerprint of the active root system of vegetation adapting to changing hydro-climatic conditions in temperate, humid climates such as in the Neckar basin.

MINOR EFFECTS OF TIME-VARIANT ROOT ZONE STORAGE CAPACITY ON THE LONG-TERM HYDROLOGICAL DYNAMICS

Knowing that root zone storage capacity (S_{umax}) is a critical factor regulating latent heat fluxes and thus the moisture exchange in hydrological cycle, the influence of time-variant S_{umax} was tested on: precipitation partitioning and hydrological response. It is concluded that time-variant S_{umax} cannot explain the observed deviations from the expected long-term Budyko trajectory in the Neckar basin. This means that the temporal evolution of S_{umax} lacks explanatory power for the long-term variations in precipitation partitioning into streamflow and evaporation. Similarly, this thesis correspondingly suggests that a hydrological model with time-variant S_{umax} cannot better reproduce the hydrological response characteristics compared with a model with stationary S_{umax} . Therefore, using a time-variable parameter S_{umax} does not significantly enhance future predictions and is therefore not essential for at least the next few decades. In other words, this thesis provides process-based evidence for modelers that utilizing time-invariant S_{umax} as model parameter will be also sufficient for predicting meaningful hydrological response in the near future in such a temperate-humid basin.

WATER STABLE ISOTOPES AND TRITIUM TELL THE SAME TALE WITH TIME-VARIANT MODELS

Water age distributions are the physical link between the hydrological response and physical transport processes of conservative solutes in catchments. They are frequently estimated by seasonally variable tracers (i.e., water stable isotopes, $\delta^{18}\text{O}$) and radioactive isotopes, such as tritium (^3H). To scrutinize the notion that seasonally variable tracers are blind to old water compared with ^3H , the influence of potential factors to the underestimation of water ages was tested: tracers, models, limited data records, and spatial aggregation. It is concluded that the previously reported underestimations of water ages can be largely ascribed to models based on assumptions that are seldom met in catchment hydrology, rather than the use of seasonally variable tracers. Due to limited data sets, spatial aggregation and potentially other unknown effects, considering the susceptibility of lumped, time-invariant convolution integral approaches integrated with $\delta^{18}\text{O}$ to significantly underestimate water ages, this thesis strongly recommends avoiding the use of this model type with seasonally variable tracers. Instead, the adoption of SAS-based or alternative time-variant model formulations allowing for the representation of transient conditions are advocated.

MULTI-DECADAL NEAR-STATIONARY PHYSICAL TRANSPORT DYNAMICS

After testing the potential factors for the underestimation of water ages, to ensure reliability for estimating water age distributions, a comprehensive multi-decadal dataset (hydrological and tritium records) with a tritium-aided semi-distributed hydrological model integrated with StorageAge Selection (SAS) functions was used to analyse water age variability across different temporal scales from daily to decadal in the Upper Neckar basin under changing climatic conditions. This thesis suggests that there is no evidence for long-term dynamics in water ages of both riverflow and evaporation. Instead, long-term average water ages were rather stable and subject to minor fluctuations in the Upper Neckar basin. As a consequence, the associated physical transport processes can be assumed to be near-stationary and predictable across multiple decades under either internal (i.e., time-variant root zone storage capacity) or external transport variability (i.e., climatic variability), which contrasts with the frequently reported fractal pattern in stream water solute dynamics.

6.2 IMPLICATIONS

As one of the most important components of the terrestrial hydrological cycle, vegetation controls the long-term precipitation partitioning into two main fluxes (i.e., streamflow and evaporation), which influences the hydrological functioning at catchment scales. For surviving, in response to climatic variability, vegetation needs continuously access to available energy and resources for root systems to satisfy its canopy water demand, which is directly reflected by root zone storage capacity. Therefore, it can be expected that a larger root zone storage capacity is required to bridge dry spells when the climatic conditions change from wetter to drier. However, the fluctuation in root zone storage capacity values in response to a changing environment does not simply follow this generalized expectation. This fluctuation largely depends on the season in

which dry spells mainly occur. If the changing climatic condition is due to reduced precipitation in winter, but unchanged precipitation in summer when evaporative demand is highest, the computation of root zone storage capacity explicitly based on the seasonal water deficit indicates that the value of root zone storage capacity needs to remain stable, which is essential to provide vegetation with sufficient and continuous access to water for sustained transpiration. On the contrary, if the drought occurs in summer, leading to reduced summer precipitation, a larger root zone storage capacity is required to maintain vegetation transpiration.

Furthermore, the magnitude of root zone storage capacity is significantly influenced by the climatic characteristics of the catchment, particularly the seasonal distribution of precipitation. In river basins such as the Neckar basin, characterized as a temperate-humid basin with wet summers, a more evenly distributed annual precipitation pattern results in reduced storage requirements during the summer. This is evidenced by the lower absolute magnitude of root zone storage capacity. Specifically, approximately over half of the annual precipitation occurs during the summer, coinciding with the period when vegetation demand for water is at its peak due to high potential evaporation. This reduces the necessity for a larger root zone storage capacity to act as a water buffer for vegetation survival. Conversely, a lower magnitude of root zone storage capacity means that even relatively small rainstorms can frequently mitigate storage deficits, thus reducing the reliance on stored water. This, in return, constrained fluctuation limits the impact of these changes on the hydrological response, which has broader implications for the application of models in the Neckar basin and potentially other temperate regions with similar hydro-climatic characteristics.

As the maximum volume of water accessible to vegetation within the unsaturated root zone of the subsurface, fluctuations in root zone storage capacity also reflect the variability of this catchment subsurface property. However, water ages spanning multiple decades have remained remarkably insensitive to this internal variability. Moreover, in the face of significant external variability, such as long-term hydro-climatic changes, water ages and the associated conservative physical transport processes can be assumed to exhibit limited transport variability at decadal timescales. The self-averaging and temporally stable water ages, emphasized in this thesis, contrasts with the fractal scaling and non-self-averaging behavior frequently observed in the dynamics of water solute concentrations in rivers, which reflects long-term fluctuations or trends in solute circulation dynamics. As evidenced by the fractal scaling in many river basins and the near-stationary water ages, it is unlikely that long-term solute dynamics result from variability of conservative transport processes. Instead, other factors, like variations in solute input and alterations in (bio-)geochemical transformation processes, may largely explain these dynamics. Consequently, the low sensitivity of water ages to variability in water supply and limited internal and external transport variability, on one hand, provide possibility for the prediction of future solute dynamics in riverflow over long-time scales, on other hand, poses a limitation to mitigation and remediation of legacy pollution such as nitrate.

6.3 OUTLOOK

This thesis highlighted the long-term hydrological response and physical transport dynamics in response to climatic variability, with specific focus on the Neckar basin, Germany. However, there remain some potential opportunities yet to be explored as illustrated in the next sections.

THE ROLE OF CLIMATIC CHARACTERISTICS OF CATCHMENTS

In this thesis, the temporal evolution of root zone storage capacity does not control variation in the partitioning of water fluxes and has no significant effects on fundamental hydrological response characteristics over multi-decades, which is limited in the Upper Neckar basin, a cool-temperature climate with ample summer precipitation. However, this result is different to those reported by (Duethmann et al., 2020) and (Bouaziz et al., 2022), who found more pronounced effects on hydrological response by the changing vegetation dynamics reflected by fluctuations of root zone storage capacity in a somewhat more humid environment. Despite the additional uncertainties introduced by future projections in these previous studies, the significantly less pronounced effects observed in this thesis are likely a result of the smaller magnitude of root zone storage capacity. This lower magnitude is primarily attributed to the climatic characteristics of the basin, particularly the abundant summer precipitation. Therefore, it would be interesting to quantify the magnitude of root zone storage capacity and test if changes of it plays a more prominent role over long time period in more arid basins with less summer precipitation.

TIME-VARIANT CONVOLUTION INTEGRAL MODELS

By comparing water age distributions derived from water stable isotopes (i.e., $\delta^{18}\text{O}$) and tritium (^3H) with several transport model implementations, this thesis provides robust evidence to reject the hypothesis that $\delta^{18}\text{O}$ as a tracer generally and systematically “cannot see water older than about 4 years” (Stewart et al., 2010, Stewart et al., 2012) and the corresponding tails in water age distributions, which lead to underestimations of water ages. Additionally, this thesis argues that previous underestimations of water ages are primarily due to the use of time-invariant, lumped parameter convolution integral models, which are inadequate for resolving the information contained in $\delta^{18}\text{O}$ signals in a meaningful way for catchments with transient flow conditions. This thesis, however, only examines SAS function-based time-variant transport models. It would be beneficial to also examine time-variant implementations of convolution integral models capable of describing transient conditions, as they may possess the potential to generate similar water age estimates by $\delta^{18}\text{O}$ signals that reflect the results obtained from the SAS function-based models tested herein.

THE COMPARISON OF UNCERTAINTY OF OLD WATER ESTIMATION INFERRED FROM $\delta^{18}\text{O}$ AND ^3H

Although the water age distributions inferred by $\delta^{18}\text{O}$ and ^3H are similar in the Neckar basin using SAS function-based models, a general equivalence between $\delta^{18}\text{O}$ and ^3H may not be universally applicable. Indeed, this thesis indicates that $\delta^{18}\text{O}$

provides sufficient information for a robust characterization of water ages in systems with mean water ages of approximately 15 to 20 years in the Neckar basin. This already encompasses the majority of river basins analysed in previous studies (see Stewart et al., 2010, and references therein). However, in river basins containing older water than that in the Neckar basin, where the amplitudes of the $\delta^{18}\text{O}$ stream signal are attenuated below analytical precision, the water age estimations derived from $\delta^{18}\text{O}$ may be increasingly uncertain. This uncertainty escalates as further attenuation occurs, eventually reaching a point where older water ages can no longer be discerned, irrespective of the modelling approaches utilized. The specific magnitude of this water age threshold remains challenging to quantify with the data available in this thesis. Consequently, future research should consider that water ages inferred from $\delta^{18}\text{O}$ are likely to exhibit increasing uncertainty for older water ages compared to those inferred from ^3H in river basins characterized by water ages exceeding approximately 15 to 20 years.

THE EFFECTS OF SPATIAL AGGREGATION ON WATER AGE ESTIMATIONS

Considering that spatial aggregation may be one of the potential reasons for the underestimation of water ages (Kirchner, 2016), this thesis explicitly accounted for the spatial heterogeneity of input variables as well as potential differences in landscape types (i.e., forest, grassland, and wetland) through the implementation of three model HRUs, despite the limitation of available data at only one location for both $\delta^{18}\text{O}$ and ^3H in the Neckar basin. If significantly older ages had been inferred from the spatially distributed implementations, this would strongly support the role and effect of spatial heterogeneity on water ages, as demonstrated by Kirchner (2016). However, the comparison between the spatially lumped and distributed implementations does not show major differences in their ability to reproduce various hydrological signatures, $\delta^{18}\text{O}$ and ^3H stream signals, and water ages. This could indicate either that the aggregation of spatial heterogeneity does not have a discernible effect on water ages inferred from the distributed implementations within the Neckar basin, or that the spatial contrasts in water ages, limited by the spatial resolution of models and available datasets, were insufficient to detect significant differences. Therefore, the evidence presented in this thesis remains inconclusive, and further research is required to explore the role of spatial aggregation in estimating water ages using spatially distributed models with sufficient datasets.

In conclusion, as a key component of the terrestrial hydrological cycle, the active root system of vegetation has to adapt to changing external hydro-climatic conditions for surviving, which directly causes the internal variability of the hydrological system such as subsurface properties. However, under significant external and internal environmental changes, the long-term hydrological response and conservative physical transport dynamics can be assumed to be near-stationary and predictable in temperate-humid climates. This thesis provides us with new information and sufficient analysis with a tracer-aided semi-distributed hydrological model and several model experiments, which help to improve our understanding of the effects of a changing climate in the terrestrial hydrological system. In the future, more research on ecohydrology under climate

changing are expected to be developed and tested in several regions with varying climatic features, with higher quality of spatial and temporal hydrological and tracer datasets, as well as the methods explored in this thesis can be further refined.



APPENDIX

This appendix provides supplementary material for Chapter 3.

Table A.1: The prior parameter ranges and the ranges of the pareto optimal solutions from two calibration cases (Scenarios 1 – 2) are shown here.

Parameter	Unit	Prior range	Posterior distribution				
			Scenario 1	Scenario 2			
			T (1953-2022)	t1 (1953-1972)	t2 (1973-1992)	t3 (1993-2012)	t4 (2013-2022)
T_t	°C	-2.5-2.5	0.40 (-0.80-0.64)	-0.08 (-2.46-0.88)	-0.08 (-2.19-0.97)	0.19 (-1.31-1.69)	1.18 (-1.42-2.49)
C_{melt}	mm °C ⁻¹ d ⁻¹	1-5	4.46 (3.14-4.87)	2.75 (1.79-4.35)	1.77 (1.29-4.55)	1.97 (1.58-4.30)	3.08 (1.24-3.95)
C_a	-	0.1-0.7	0.66 (0.43-0.68)	0.51 (0.41-0.62)	0.60 (0.49-0.67)	0.61 (0.39-0.67)	0.67 (0.42-0.63)
K_s	d ⁻¹	0.002-0.2	0.03 (0.02-0.07)	0.03 (0.03-0.07)	0.05 (0.03-0.15)	0.04 (0.03-0.18)	0.03 (0.01-0.05)
S_{imaxF}	mm	0.1-5	1.55 (1.55-2.87)	2.54 (2.00-4.82)	2.43 (1.93-4.76)	1.82 (1.79-4.69)	3.03 (1.75-3.82)
S_{umaxF}	mm	50-200	158 (138-167)	148 (114-165)	149 (130-174)	120 (100-159)	125 (122-169)
γ_F	-	0.1-5	3.43 (0.58-4.51)	1.02 (1.02-4.18)	2.02 (1.22-4.46)	0.69 (0.39-4.14)	0.44 (0.54-3.43)
D	-	0-1	0.09 (0.04-0.21)	0.06 (0.01-0.43)	0.33 (0.07-0.77)	0.41 (0.10-0.72)	0.27 (0.25-0.97)
C_{pmaxF}	mm d ⁻¹	0.1-4	2.15 (1.97-2.83)	1.83 (0.53-2.53)	0.21 (0.92-2.95)	0.92 (0.91-3.47)	0.12 (0.35-3.42)
K_{fF}	d ⁻¹	0.2-5	0.41 (1.48-3.19)	0.62 (0.22-4.45)	0.30 (0.30-4.94)	0.25 (0.23-4.63)	0.53 (0.21-3.95)
S_{imaxG}	mm	0.1-5	0.97 (0.70-1.30)	1.06 (0.19-1.25)	1.24 (0.44-1.50)	0.93 (0.09-1.25)	0.41 (0.01-1.02)
S_{umaxG}	mm	50-200	94.6 (71.4-123)	68.0 (66.2-124)	115 (88.5-123)	93.2 (67.9-119)	102 (86.4-141)
γ_G	-	0.1-5	4.61 (.033-4.34)	1.93 (0.77-4.48)	0.87 (0.11-1.89)	2.76 (0.57-4.52)	4.58 (0.62-4.04)
C_{pmaxG}	mm d ⁻¹	0.1-4	0.87 (0.87-3.37)	1.85 (1.76-3.67)	3.14 (2.83-3.78)	3.11 (2.61-3.90)	2.62 (1.66-3.96)
K_{fG}	d ⁻¹	0.2-5	0.22 (0.22-1.53)	0.23 (0.21-2.12)	0.25 (0.23-4.56)	0.23 (0.23-4.98)	0.21 (0.24-4.11)
S_{umaxW}	mm	50-200	60.9 (49.1-68.0)	55.0 (27.2-69.0)	68.6 (38.1-66.7)	51.3 (20.3-58.9)	68.5 (14.5-73.5)
γ_W	-	0.1-5	0.35 (0.14-2.40)	0.50 (0.37-4.46)	3.84 (0.22-4.65)	1.26 (0.17-4.73)	0.63 (0.09-3.66)
C_{rmax}	mm d ⁻¹	0-4	1.05 (0.76-2.17)	0.98 (0.32-2.80)	1.13 (0.41-2.11)	1.33 (0.09-2.51)	0.03 (2.34-3.76)

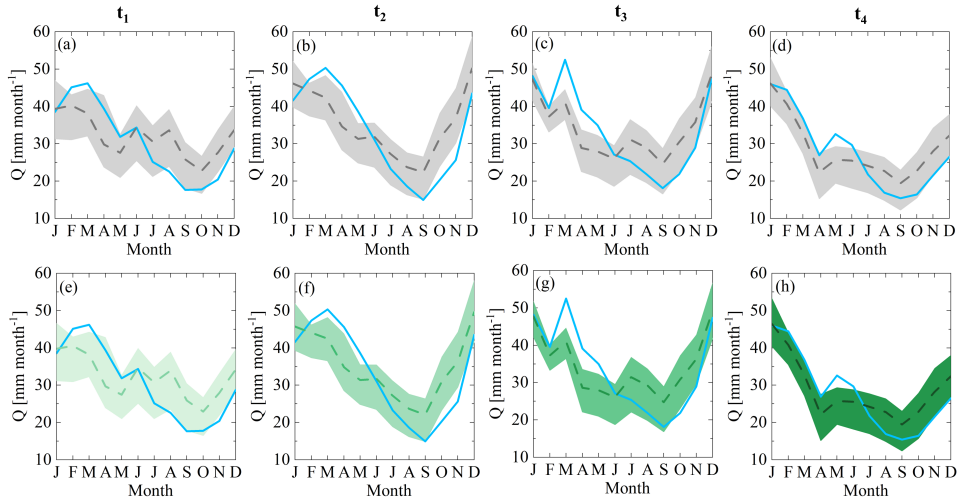


Figure A.1: The mean monthly streamflow for four sub-time periods t_1 - t_4 based on two scenarios ((a)-(d): scenario 1, (e)-(h): scenario 2). The blue lines indicate the observed streamflow. The dashed lines and shaded areas show the most balanced solution and 5th – 95th percentiles based on the Pareto front solutions retained as feasible.

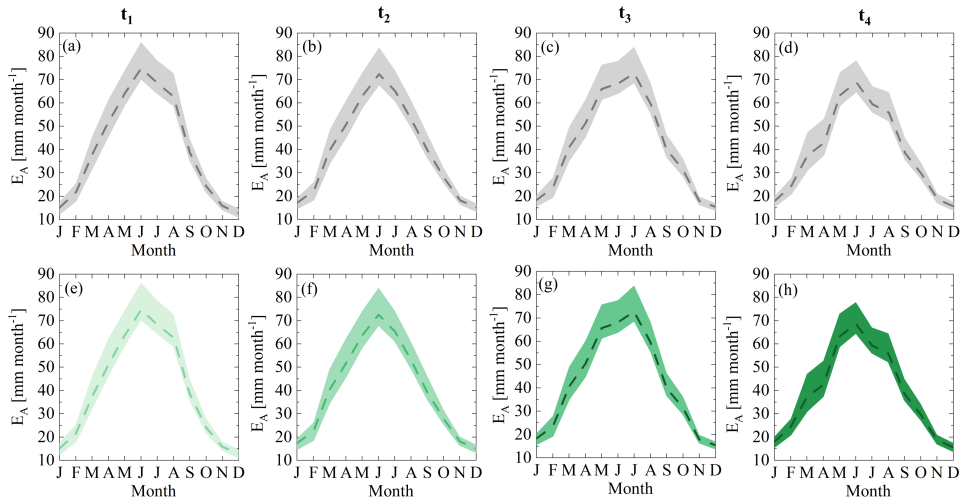


Figure A.2: The mean monthly actual evaporation E_A for four sub-time periods t_1 - t_4 based on two scenarios ((a)-(d): scenario 1, (e)-(h): scenario 2). The dashed lines and shaded areas show the most balanced solution and 5th – 95th percentiles based on the Pareto front solutions retained as feasible.

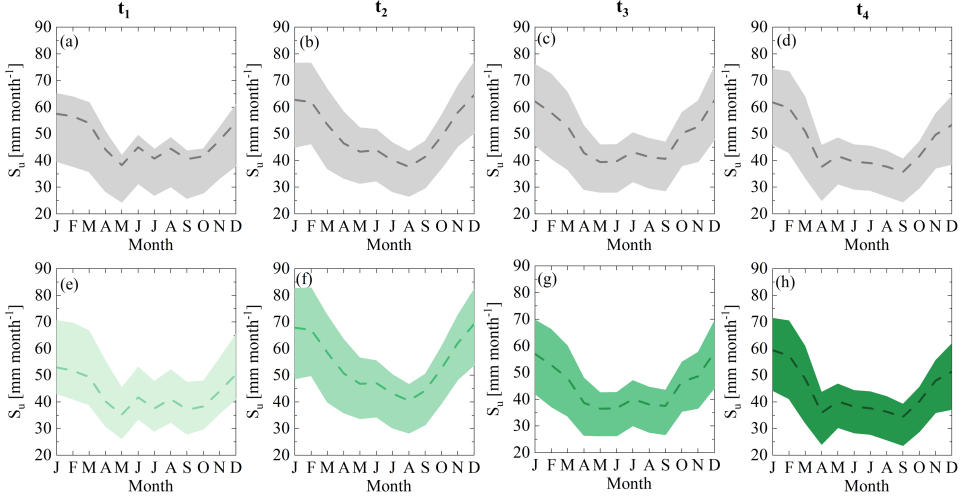


Figure A.3: The mean monthly unsaturated zone storage S_u for four sub-time periods t_1 - t_4 based on two scenarios ((a)-(d): scenario 1, (e)-(h): scenario 2). The dashed lines and shaded areas show the most balanced solution and 5th – 95th percentiles based on the pareto front solutions retained as feasible.

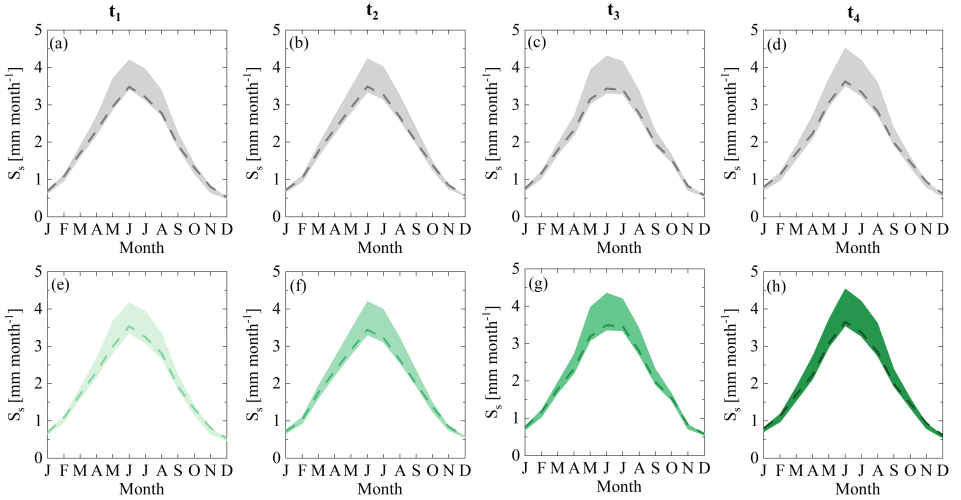


Figure A.4: The mean monthly groundwater storage S_s (active storage) for four sub-time periods t_1 - t_4 based on two scenarios ((a)-(d): scenario 1, (e)-(h): scenario 2). The dashed lines and shaded areas show the most balanced solution and 5th – 95th percentiles based on the pareto front solutions retained as feasible.

B

B

APPENDIX

This appendix provides supplementary material for Chapter 4.

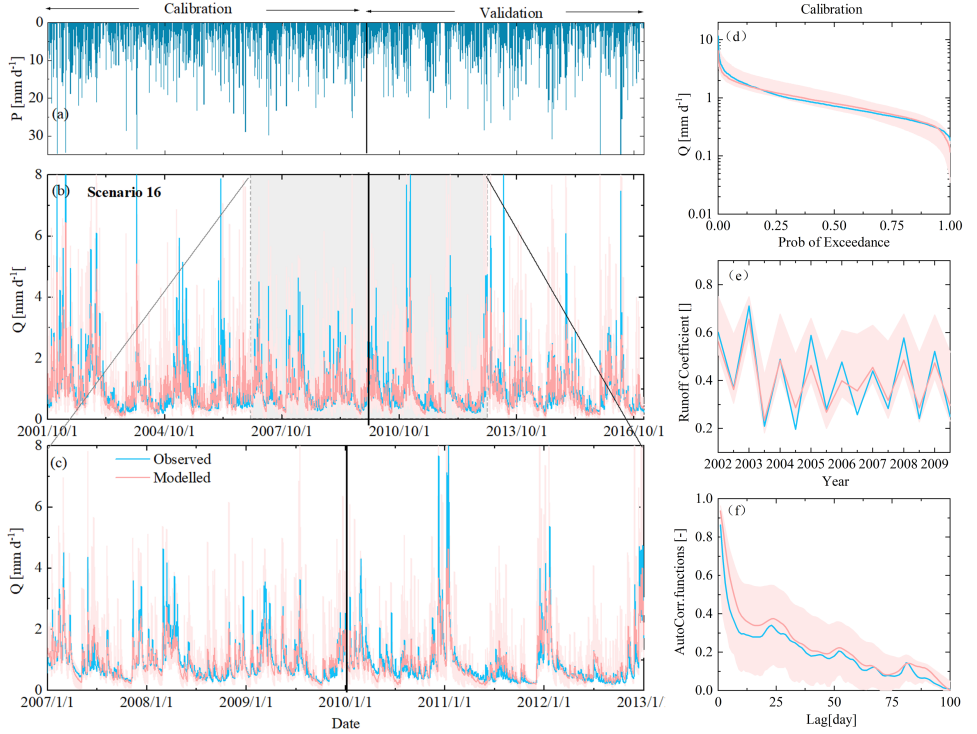


Figure B.1: Hydrograph and selected hydrological signatures reproduced by IM-SAS-L, following a simultaneous calibration to the hydrological response and $\delta^{18}\text{O}$ ($C_{\delta^{18}\text{O},Q}$; scenario 16). (a) Time series of observed daily precipitation; observed and modelled (b) daily stream flow (Q), where the light red line indicates the most balanced solution, i.e., lowest D_E , and the light red shaded area the 5th/95th inter-quantile range obtained from all pareto optimal solutions; (c) stream flow zoomed-in to the 01/01/2007 – 31/12/2012 period; (d) flow duration curves (FDC), (e) seasonal runoff coefficients (RC_Q) and (f) autocorrelation functions of stream flow (AC_Q) for the calibration period. Blue lines indicate values based on observed streamflow (Q_o), light red lines are values based on modelled stream flow (Q_m) representing the most balanced solutions, i.e., lowest D_E and the light red shaded areas show the 5th/95th inter-quantile ranges obtained from all pareto optimal solutions.

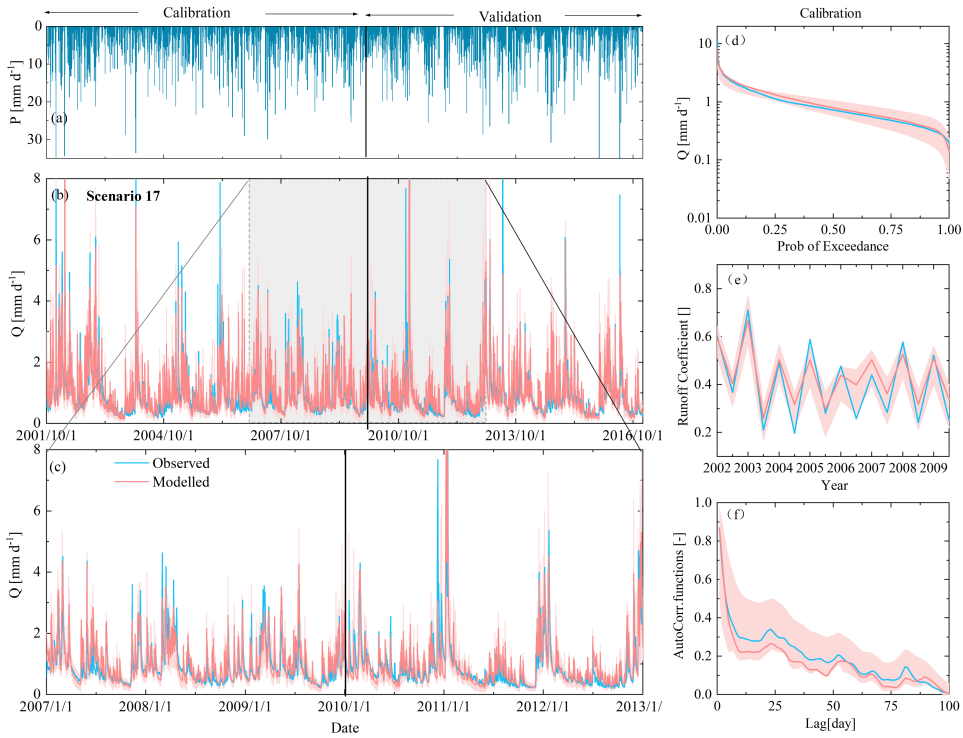


Figure B.2: Hydrograph and selected hydrological signatures reproduced by IM-SAS-L, following a simultaneous calibration to the hydrological response and ^3H ($\text{C}_{3\text{H}_2\text{O}}$; scenario 17). (a) Time series of observed daily precipitation; observed and modelled (b) daily stream flow (Q), where the light red line indicates the most balanced solution, i.e., lowest D_E , and the light red shaded area the 5th/95th inter-quantile range obtained from all pareto optimal solutions; (c) stream flow zoomed-in to the 01/01/2007 – 31/12/2012 period; (d) flow duration curves (FDC), (e) seasonal runoff coefficients (RC_Q) and (f) autocorrelation functions of stream flow (AC_Q) for the calibration period. Blue lines indicate values based on observed streamflow (Q_o), light red lines are values based on modelled stream flow (Q_m) representing the most balanced solutions, i.e., lowest D_E and the light red shaded areas show the 5th/95th inter-quantile ranges obtained from all pareto optimal solutions.

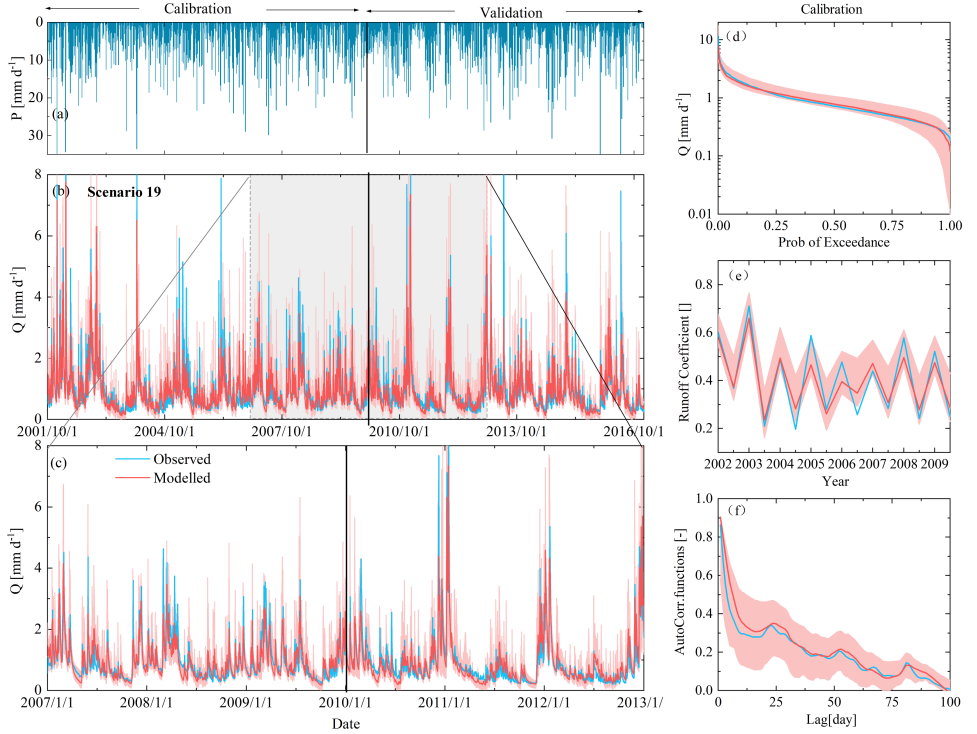


Figure B.3: Hydrograph and selected hydrological signatures reproduced by IM-SAS-D, following a simultaneous calibration to the hydrological response and $\delta^{18}\text{O}$ ($\text{C}\delta^{18}\text{O}_Q$; scenario 19). (a) Time series of observed daily precipitation; observed and modelled (b) daily stream flow (Q), where the light red line indicates the most balanced solution, i.e., lowest D_E , and the light red shaded area the 5th/95th inter-quantile range obtained from all pareto optimal solutions; (c) stream flow zoomed-in to the 01/01/2007 – 31/12/2012 period; (d) flow duration curves (FDC), (e) seasonal runoff coefficients (RCQ) and (f) autocorrelation functions of stream flow (AC_Q) for the calibration period. Blue lines indicate values based on observed streamflow (Q_o), light red lines are values based on modelled stream flow (Q_m) representing the most balanced solutions, i.e., lowest D_E and the light red shaded areas show the 5th/95th inter-quantile ranges obtained from all pareto optimal solutions.

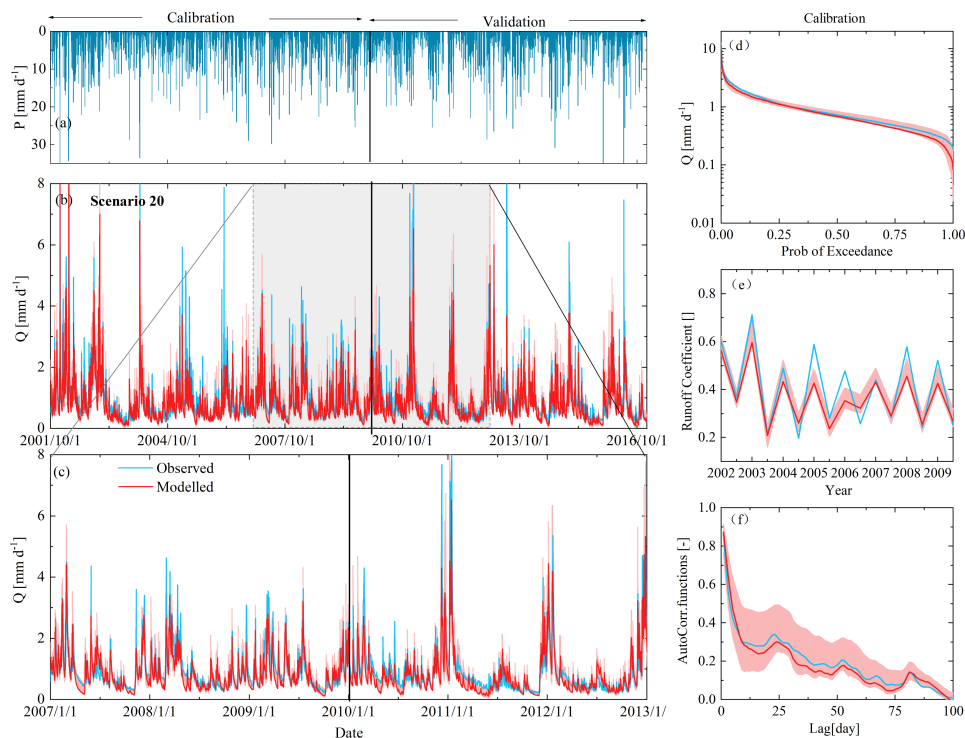


Figure B.4: Hydrograph and selected hydrological signatures reproduced by IM-SAS-D, following a simultaneous calibration to the hydrological response and ^3H ($\text{C}_3\text{H}_3\text{Q}$; scenario 20). (a) Time series of observed daily precipitation; observed and modelled (b) daily stream flow (Q), where the red line indicates the most balanced solution, i.e., lowest D_E , and the light red shaded area the 5th/95th inter-quantile range obtained from all pareto optimal solutions; (c) stream flow zoomed-in to the 01/01/2007 – 31/12/2012 period; (d) flow duration curves (FDC), (e) seasonal runoff coefficients (RCQ) and (f) autocorrelation functions of stream flow (ACQ) for the calibration period. Blue lines indicate values based on observed streamflow (Q_o), red lines are values based on modelled stream flow (Q_m) representing the most balanced solutions, i.e., lowest D_E and the light red shaded areas show the 5th/95th inter-quantile ranges obtained from all pareto optimal solutions.

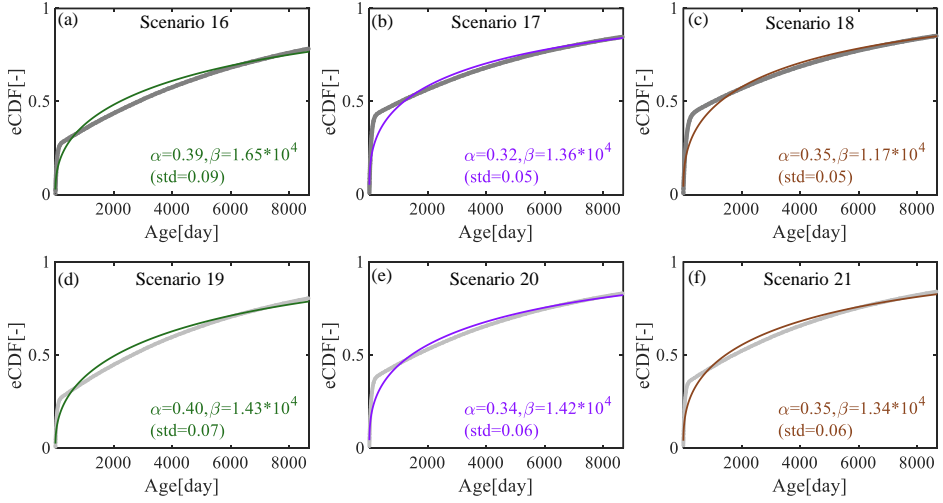


Figure B.5: The Gamma distributions to the volume-weighted mean stream flow TTDs of model IM-SAS (i.e., scenarios 16-21) based on model IM-SAS-L in (a)-(c) and model IM-SAS-D in (d)-(f). Grey shades in (a)-(f) indicate volume-weighted mean TTDs and colored shades indicate the corresponding fitting Gamma distributions, respectively.

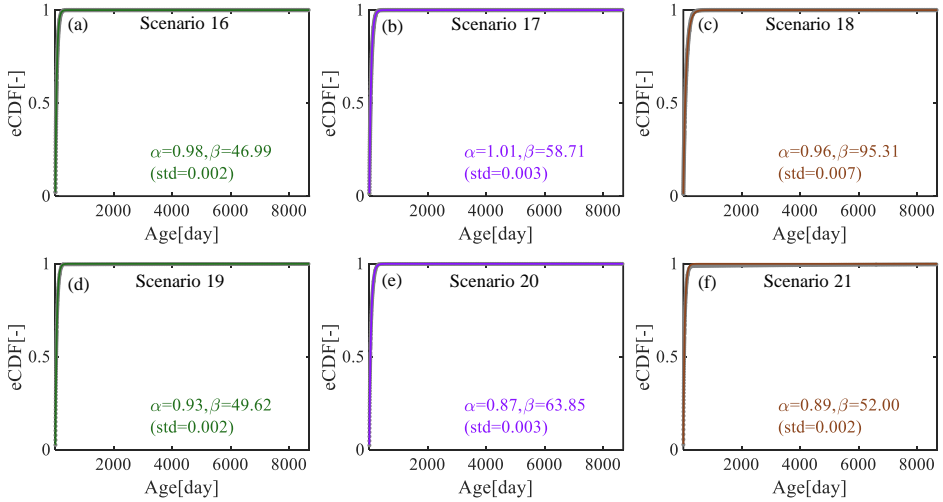


Figure B.6: The Gamma distributions to the volume-weighted mean transpiration (E_a) TTDs of model IM-SAS (i.e., scenarios 16-21) based on model IM-SAS-L in (a)-(c) and model IM-SAS-D in (d)-(f). Grey shades in (a)-(f) indicate volume-weighted mean TTDs and colored shades indicate the corresponding fitting Gamma distributions, respectively.

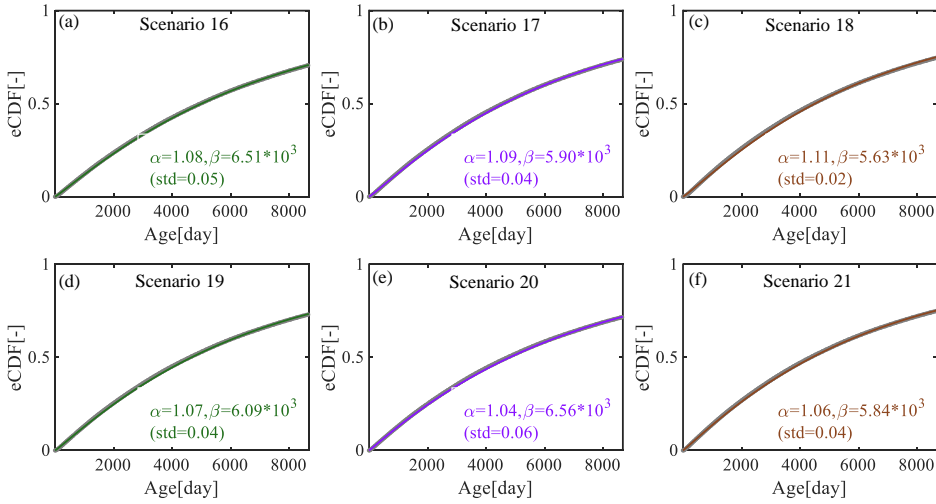


Figure B.7: The Gamma distributions to the volume-weighted mean groundwater (S_s) RTDs of model IM-SAS (i.e., scenarios 16-21) based on model IM-SAS-L in (a)-(c) and model IM-SAS-D in (d)-(f). Grey shades in (a)-(f) indicate volume-weighted mean RTDs and colored shades indicate the corresponding fitting Gamma distributions, respectively.

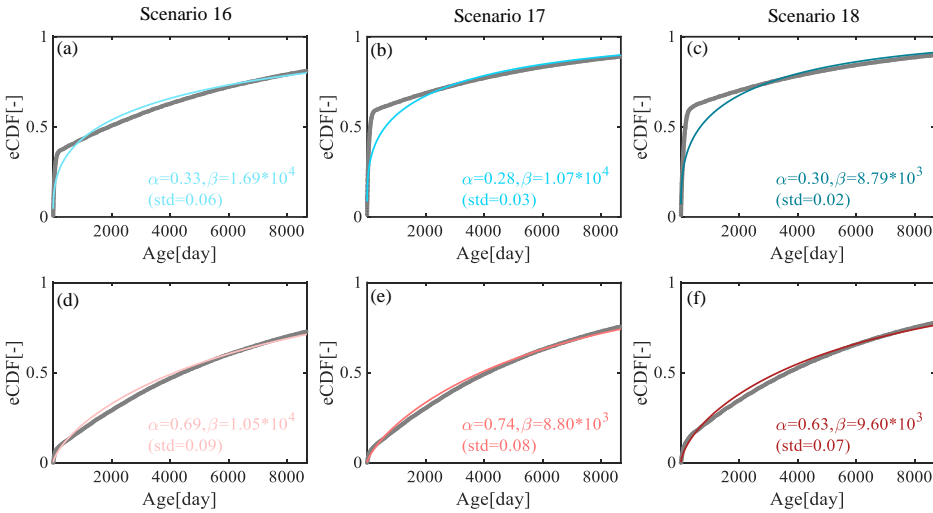


Figure B.8: The Gamma distributions to the volume-weighted mean stream flow TTDs for the wet and dry periods of model IM-SAS-L (i.e., scenarios 16-18) based on wet periods in (a)-(c) and dry periods in (d)-(f). Grey shade and blue shades in (a)-(c) indicate volume-weighted mean TTDs for wet periods and the corresponding fitting Gamma distributions, respectively; grey shade and red shades in (d)-(f) indicate volume-weighted mean TTDs for dry periods and the corresponding fitting Gamma distributions, respectively.

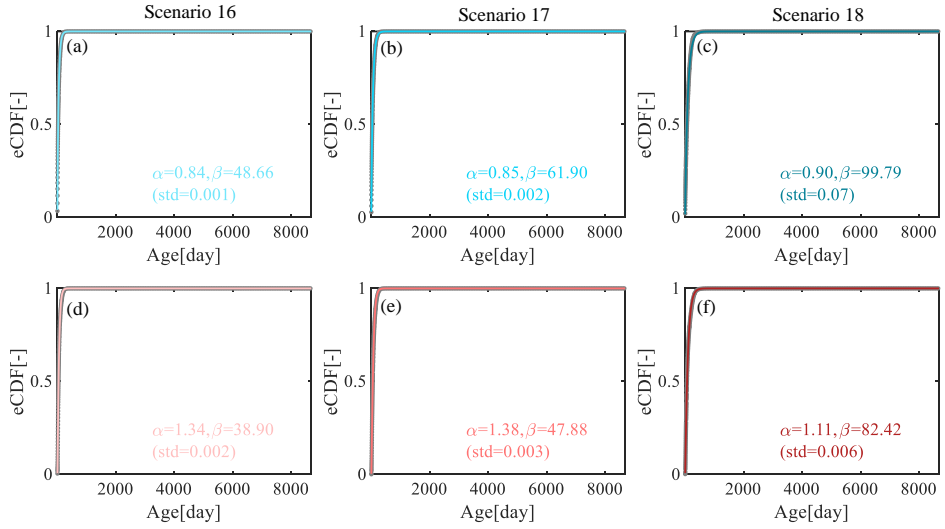


Figure B.9: The Gamma distributions to the volume-weighted mean transpiration (E_a) TTDs for the wet and dry periods of model IM-SAS-L (i.e., scenarios 16-18) based on wet periods in (a)-(c) and dry periods in (d)-(f). Grey shade and blue shades in (a)-(c) indicate volume-weighted mean TTDs for wet periods and the corresponding fitting Gamma distributions, respectively; grey shade and red shades in (d)-(f) indicate volume-weighted mean TTDs for dry periods and the corresponding fitting Gamma distributions, respectively.

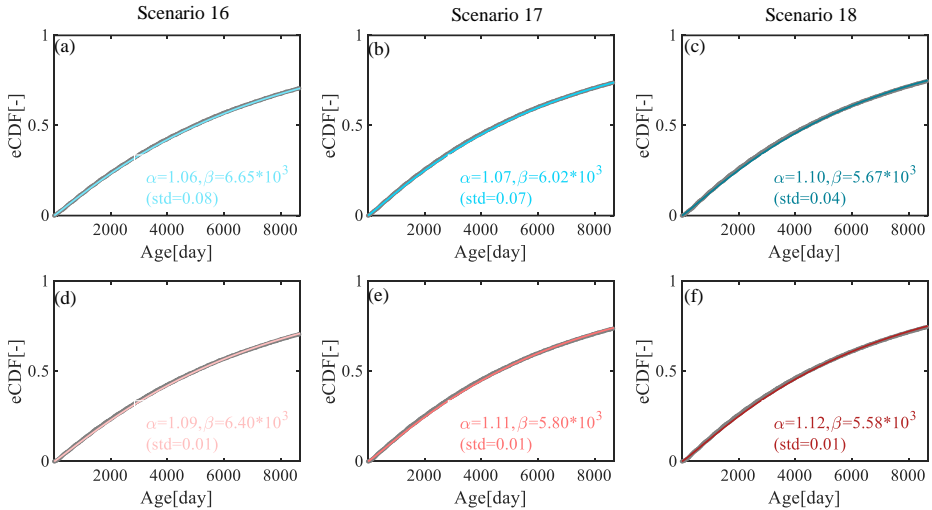


Figure B.10: The Gamma distributions to the volume-weighted mean groundwater (S_s) RTDs for the wet and dry periods of model IM-SAS-L (i.e., scenarios 16-18) based on wet periods in (a)-(c) and dry periods in (d)-(f). Grey shade and blue shades in (a)-(c) indicate volume-weighted mean RTDs for wet periods and the corresponding fitting Gamma distributions, respectively; grey shade and red shades in (d)-(f) indicate volume-weighted mean RTDs for dry periods and the corresponding fitting Gamma distributions, respectively.

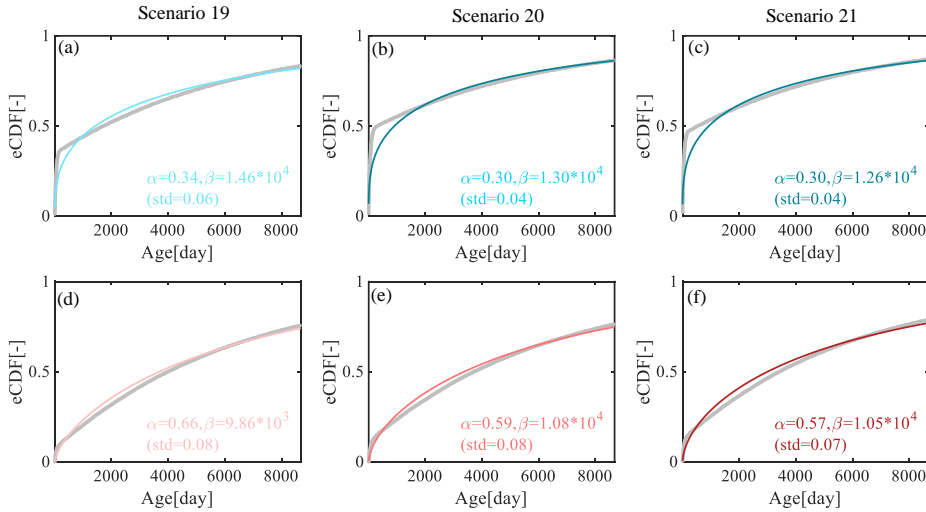


Figure B.11: The Gamma distributions to the volume-weighted mean steam flow TTDs for the wet and dry periods of model IM-SAS-D (i.e., scenarios 19-21) based on wet periods in (a)-(c) and dry periods in (d)-(f). Grey shade and blue shades in (a)-(c) indicate volume-weighted mean TTDs for wet periods and the corresponding fitting Gamma distributions, respectively; grey shade and red shades in (d)-(f) indicate volume-weighted mean TTDs for dry periods and the corresponding fitting Gamma distributions, respectively.

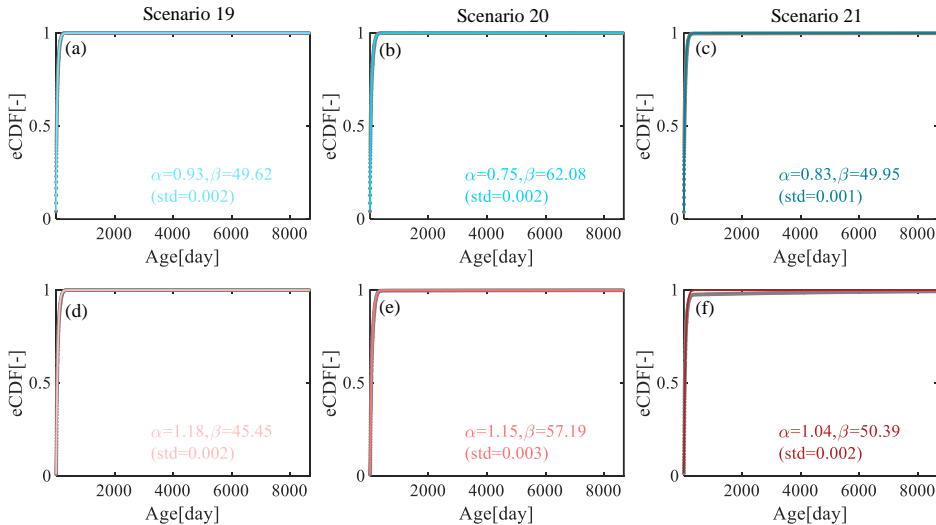


Figure B.12: The Gamma distributions to the volume-weighted mean transpiration (E_a) TTDs for the wet and dry periods of model IM-SAS-D (i.e., scenarios 19-21) based on wet periods in (a)-(c) and dry periods in (d)-(f). Grey shade and blue shades in (a)-(c) indicate volume-weighted mean TTDs for wet periods and the corresponding fitting Gamma distributions, respectively; grey shade and red shades in (d)-(f) indicate volume-weighted mean TTDs for dry periods and the corresponding fitting Gamma distributions, respectively.

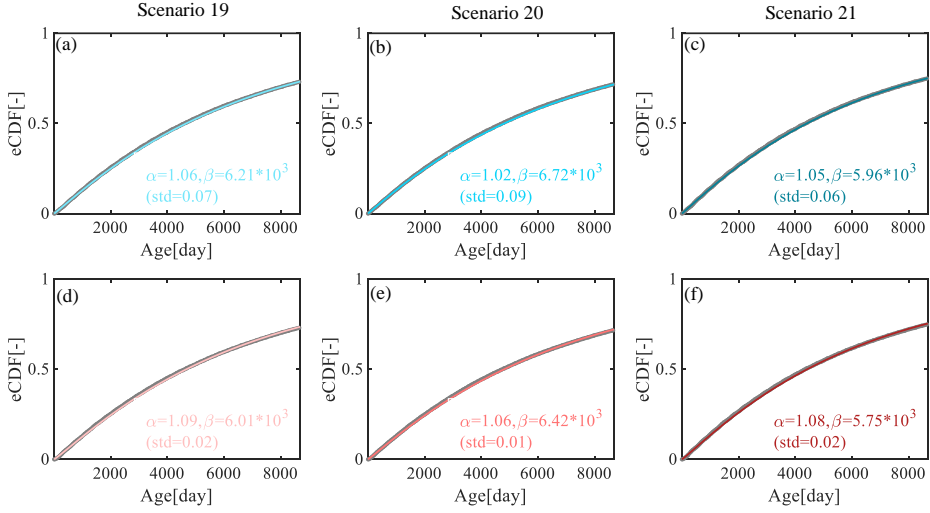


Figure B.13: The Gamma distributions to the volume-weighted mean groundwater (S_s) RTDs for the wet and dry periods of model IM-SAS-D (i.e., scenarios 19-21) based on wet periods in (a)-(c) and dry periods in (d)-(f). Grey shade and blue shades in (a)-(c) indicate volume-weighted mean RTDs for wet periods and the corresponding fitting Gamma distributions, respectively; grey shade and red shades in (d)-(f) indicate volume-weighted mean RTDs for dry periods and the corresponding fitting Gamma distributions, respectively.

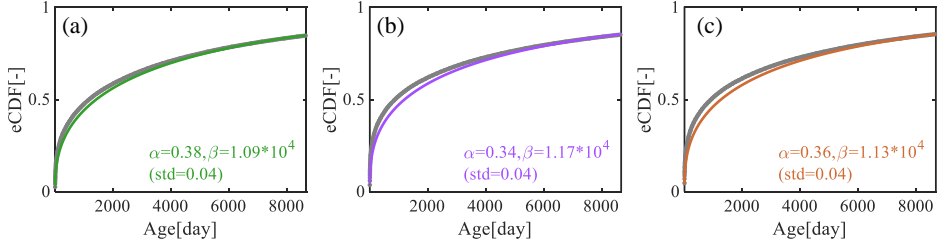


Figure B.14: The Gamma distributions to the volume-weighted mean steam flow TTDs (i.e., scenarios 13-15). Grey shades in (a)-(c) indicate volume-weighted mean TTDs and colored shades indicate the corresponding fitting Gamma distributions (green for Scenario 13, purple for scenario 14 and brown for scenario 15), respectively.

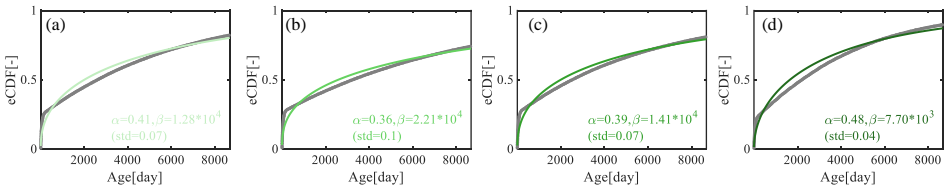


Figure B.15: The Gamma distributions to the volume-weighted mean steam flow TTDs of each precipitation zone based on model IM-SAS-D from scenario 19. Grey shades in (a)-(d) indicate volume-weighted mean TTDs of four precipitation zones (P1-P4) and colored shades indicate the corresponding fitting Gamma distributions, respectively.

Table B.1: Performance metrics of the model implementations and the associated calibration strategies for the 2001 – 2009 calibration period (cal.) and the 2010 – 2016 model evaluation period (val.). The ranges of all performance metrics for the full set of pareto optimal solutions for the multi-objective calibration cases (Scenarios 15 – 21) are shown here.

Scenario		15	16	17	18	19	20	21
Implementation	Model	P-SAS		IM-SAS-L		IM-SAS-D		
	Calibration strategy → Performance metric ↓	Lumped		Distributed		Distributed		
		$C_{\delta^{18}\text{O},^3\text{H}}$	$C_{\delta^{18}\text{O}}$	$C_{\text{tritium},\text{Q}}$	$C_{\delta^{18}\text{O},^3\text{H},\text{Q}}$	$C_{\delta^{18}\text{O},\text{Q}}$	$C_{\text{tritium},\text{Q}}$	$C_{\delta^{18}\text{O},^3\text{H},\text{Q}}$
Performance metrics	$MSE_{\delta^{18}\text{O}}$	cal. 0.069-0.080 val. 0.212-0.216	0.070-0.347 0.134-0.733	- -	0.068-0.756 0.116-1.006	0.068-0.188 0.129-0.648	- -	0.068-0.262 0.141-0.905
	$MSE_{^3\text{H}}$	cal. 2.846-2.869 val. 1.704-1.758	- -	2.972-71.69 1.825-19.97	2.823-130.6 1.908-40.46	- -	2.956-19.75 1.932-4.883	2.975-47.54 1.915-13.29
	MSE_Q	cal. - val. -	0.194-1.287 0.211-1.239	0.193-0.703 0.212-0.706	0.196-2.762 0.215-2.572	0.228-0.817 0.251-0.827	0.232-0.442 0.253-0.454	0.248-1.161 0.273-1.118
	$MSE_{\log(Q)}$	cal. - val. -	0.090-0.584 0.088-0.662	0.091-0.304 0.080-0.362	0.098-0.621 0.083-0.582	0.119-0.334 0.101-0.321	0.101-0.231 0.088-0.310	0.112-0.399 0.105-0.485
	MSE_{FDC_Q}	cal. - val. -	0.003-0.359 0.004-0.369	0.003-0.129 0.002-0.195	0.003-1.042 0.007-0.877	0.002-0.144 0.003-0.141	0.002-0.072 0.012-0.111	0.002-0.212 0.004-0.180
	$MSE_{FDC_{\log(Q)}}$	cal. - val. -	0.001-0.173 0.003-0.229	0.002-0.126 0.002-0.207	0.002-0.377 0.003-0.345	0.002-0.119 0.002-0.093	0.002-0.051 0.004-0.127	0.002-0.167 0.003-0.251
	MSE_{RC}	cal. - val. -	0.003-0.045 0.003-0.040	0.003-0.011 0.002-0.011	0.003-0.070 0.002-0.064	0.003-0.018 0.002-0.016	0.002-0.006 0.002-0.008	0.002-0.026 0.002-0.023
	MSE_{AC_Q}	cal. - val. -	0.000-0.030 0.000-0.034	0.000-0.019 0.000-0.026	0.000-0.034 0.000-0.045	0.000-0.013 0.000-0.027	0.000-0.016 0.000-0.019	0.000-0.019 0.000-0.031

B

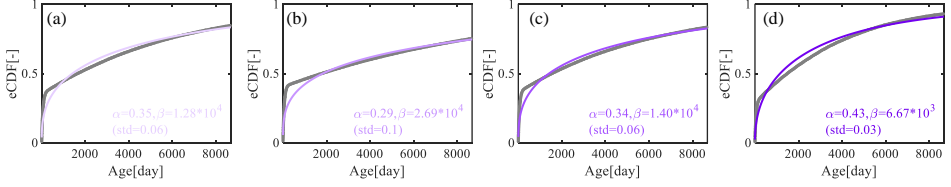


Figure B.16: The Gamma distributions to the volume-weighted mean steam flow TTDs of each precipitation zone based on model IM-SAS-D from scenario 20. Grey shades in (a)-(d) indicate volume-weighted mean TTDs of four precipitation zones (P1-P4) and colored shades indicate the corresponding fitting Gamma distributions, respectively.

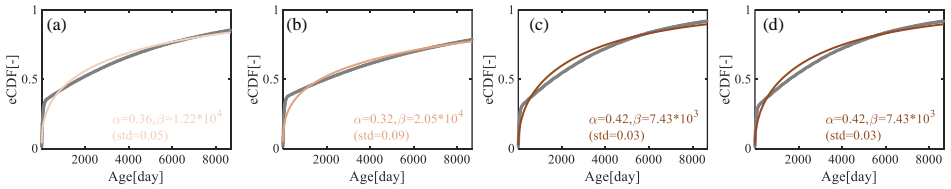


Figure B.17: The Gamma distributions to the volume-weighted mean steam flow TTDs of each precipitation zone based on model IM-SAS-D from scenario 21. Grey shades in (a)-(d) indicate volume-weighted mean TTDs of four precipitation zones (P1-P4) and colored shades indicate the corresponding fitting Gamma distributions, respectively.

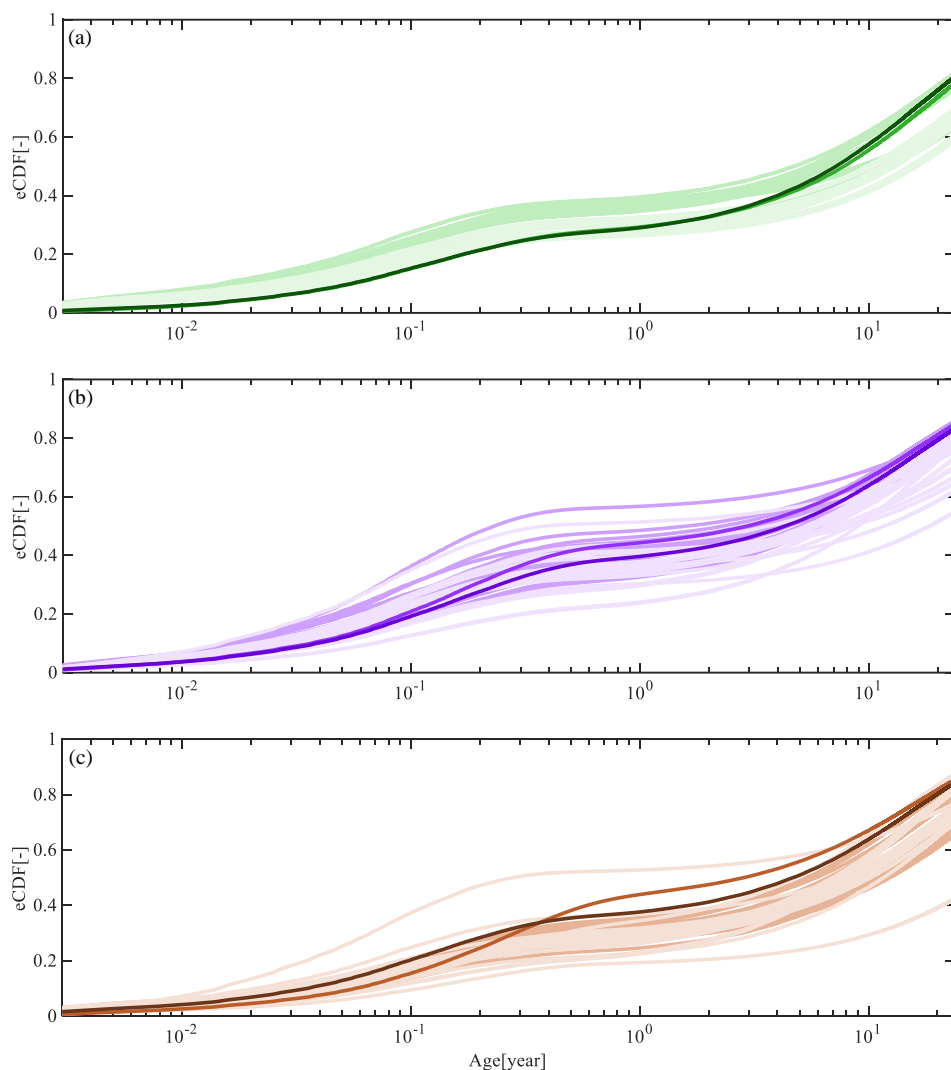


Figure B.18: Stream flow TTDs derived from the 6 model scenarios based on IM-SAS models with the different associated calibration strategies (scenarios 16-21). The selected volume weighted average daily TTDs during the modelling period 01/10/2001 – 31/12/2016 are given. (a) The TTDs inferred from $\delta^{18}\text{O}$; the lightest green lines represent the TTDs based on selected solutions with scenario 16; the relatively lighter green lines represent the TTDs based on selected solutions with scenario 19; the green line represents the TTDs based on best-fit solution with scenario 16; the dark green line represents the TTDs based on best-fit solution with scenario 19; (b) The TTDs inferred from ^3H ; the lightest purple lines represent the TTDs based on selected solutions with scenario 20; the relatively lighter purple lines represent the TTDs based on selected solutions with scenario 17; the purple line represents the TTDs based on best-fit solution with scenario 17; the dark purple line represents the TTDs based on best-fit solution with scenario 20; (c) The TTDs inferred from combined $\delta^{18}\text{O}$ and ^3H ; the lightest brown lines represent the TTDs based on selected solutions with scenario 18; the relatively lighter brown lines represent the TTDs based on selected solutions with scenario 21; the brown line represents the TTDs based on best-fit solution with scenario 18; the dark brown line represents the TTDs based on best-fit solution with scenario 21.

C

C

APPENDIX

This appendix provides supplementary material for Chapter 5.

Table C.1: Statistics analysis for the relationships between young water fraction in riverflow ($F_{wy,Q}$) and hydro-climatic variables over different time scales from daily to decadal including (a) liquid precipitation PL (rainfall +snowmelt), (b) liquid precipitation intensity $PL_{intensity}$, (c) riverflow Q_0 , (d) evaporation E (e) soil moisture S_u . The linear relationship between the $F_{wy,Q}$ and the various hydro-climatic variables x , used to approximate the sensitivity $\psi = \Delta F_{wy,Q}/\Delta x$. Note that seasonal time scale include summer (S) and winter (W).

Hydro-climatic variables \rightarrow		P_L		$P_{L_{intensity}}$		Q_0		E		S_u	
Time scales \downarrow											
Daily	ψ	0.03		0.03		0.10		0.12		0.01	
	R2	0.34		0.34		0.22		0.22		0.20	
	p	<0.001		<0.001		<0.001		<0.001		<0.001	
Weekly	ψ	0.07		0.06		0.11		0.10		0.01	
	R2	0.60		0.51		0.25		0.17		0.23	
	p	<0.001		<0.001		<0.001		<0.001		<0.001	
Monthly	ψ	0.11		0.09		0.09		0.06		0.004	
	R2	0.74		0.66		0.18		0.09		0.21	
	p	<0.001		<0.001		<0.001		<0.001		<0.001	
$F_{wy,Q}$											
Seasonal	ψ		S		W		S		W		S
	R2	0.07	0.10	0.06	0.08	0.05	0.08	0.28	0.003	0.003	0.39
	p	<0.001	<0.001	<0.001	<0.001	0.006	<0.001	<0.001	<0.001	<0.001	<0.001
Yearly	ψ	0.07		0.06		0.06		0.12		0.001	
	R2	0.65		0.55		0.40		0.27		0.18	
	p	<0.001		<0.001		<0.001		<0.001		<0.001	
Decadal	ψ	0.068		0.05		0.09		0.12		0.001	
	R2	0.89		0.77		0.82		0.32		0.25	
	p	0.002		0.009		0.005		0.19		0.26	

Table C.2: Statistics analysis for the relationships between the fraction of water younger than 10 years in riverflow ($F_{w10,Q}$) and hydro-climatic variables over different time scales from daily to decadal including (a) liquid precipitation P_L (rainfall +snowmelt), (b) liquid precipitation intensity $P_{L,intensity}$, (c) riverflow Q_0 , (d) evaporation E (e) soil moisture S_u . The linear relationship between the $F_{wy,Q}$ and the various hydro-climatic variables x , used to approximate the sensitivity $\psi = \Delta F_{wy,Q}/\Delta x$. Note that seasonal time scale include summer (S) and winter (W).

Hydro-climatic variables → Time scales ↓		P_L		$P_{L,intensity}$		Q_0		E		S_u	
Daily	ψ	0.02		0.02		0.06		0.07		0.003	
	R2	0.34		0.34		0.23		0.21		0.20	
	p	<0.001		<0.001		<0.001		<0.001		<0.001	
Weekly	ψ	0.04		0.03		0.06		0.06		0.03	
	R2	0.59		0.51		0.27		0.16		0.24	
	p	<0.001		<0.001		<0.001		<0.001		<0.001	
Monthly	ψ	0.06		0.05		0.05		0.03		0.003	
	R2	0.73		0.65		0.19		0.08		0.22	
	p	<0.001		<0.001		<0.001		<0.001		<0.001	
$F_{wy,Q}$		S	W	S	W	S	W	S	W	S	W
	ψ	0.04	0.05	0.03	0.04	0.03	0.04	0.05	0.16	0.002	0.002
	R2	0.45	0.74	0.40	0.73	0.10	0.43	0.14	0.45	0.40	0.44
	p	<0.001	<0.001	<0.001	<0.001	0.006	<0.001	<0.001	<0.001	<0.001	<0.001
	ψ	0.04		0.03		0.04		0.06		$9.6 \cdot 10^{-4}$	
Seasonal	R2	0.55		0.51		0.36		0.22		0.23	
	p	<0.001		<0.001		<0.001		<0.001		<0.001	
Yearly	ψ	0.05		0.05		0.06		0.09		$6.3 \cdot 10^{-4}$	
	R2	0.43		0.63		0.39		0.16		0.08	
	p	0.11		0.03		0.14		0.38		0.54	

REFERENCES

- AghaKouchak, A. et al. "Water and climate: Recognize anthropogenic drought". In: *Nature* 524.7566 (2015), pp. 409–411. ISSN: 0028-0836. DOI: [10.1038/524409a](https://doi.org/10.1038/524409a).
- Ajami, N. K. et al. "Calibration of a semi-distributed hydrologic model for streamflow estimation along a river system". In: *Journal of hydrology* 298.1-4 (2004), pp. 112–135. ISSN: 0022-1694. DOI: [10.1016/j.jhydrol.2004.03.033](https://doi.org/10.1016/j.jhydrol.2004.03.033).
- Ala-Aho, P. et al. "Using isotopes to constrain water flux and age estimates in snow-influenced catchments using the STARR (Spatially distributed Tracer-Aided Rainfall–Runoff) model". In: *Hydrology and Earth System Sciences* 21.10 (2017), pp. 5089–5110. ISSN: 1027-5606. DOI: [10.5194/hess-21-5089-2017](https://doi.org/10.5194/hess-21-5089-2017).
- Alila, Y. et al. "Forests and floods: A new paradigm sheds light on age-old controversies". In: *Water Resources Research* 45.8 (2009). ISSN: 0043-1397. DOI: [10.1029/2008WR007207](https://doi.org/10.1029/2008WR007207).
- Alizadeh, O. and Babaei, M. "Seasonally dependent precipitation changes and their driving mechanisms in Southwest Asia". In: *Climatic Change* 171.3 (2022), p. 20. ISSN: 0165-0009. DOI: [10.1007/s10584-022-03316-z](https://doi.org/10.1007/s10584-022-03316-z).
- Allen, S. T., Kirchner, J. W., and Goldsmith, G. R. "Predicting spatial patterns in precipitation isotope ($\delta^2\text{H}$ and $\delta^{18}\text{O}$) seasonality using sinusoidal isoscapes". In: *Geophysical Research Letters* 45.10 (2018), pp. 4859–4868. ISSN: 0094-8276. DOI: [10.1029/2018GL077458](https://doi.org/10.1029/2018GL077458).
- Allen, S. T. et al. "Global sinusoidal seasonality in precipitation isotopes". In: *Hydrology and Earth System Sciences* 23.8 (2019), pp. 3423–3436. ISSN: 1027-5606. DOI: [10.5194/hess-23-3423-2019](https://doi.org/10.5194/hess-23-3423-2019).
- Arnold, J. G. et al. "Large Area Hydrologic Modeling and Assessment Part I: Model development". In: *JAWRA Journal of the American Water Resources Association* 34.1 (Feb. 1998), pp. 73–89. ISSN: 1752-1688. DOI: [10.1111/j.1752-1688.1998.tb05961.x](https://doi.org/10.1111/j.1752-1688.1998.tb05961.x).
- Asadollahi, M. et al. "Transport and water age dynamics in soils: A comparative study of spatially integrated and spatially explicit models". In: *Water Resources Research* 56.3 (2020), no–no. ISSN: 0043-1397. DOI: [10.1029/2019WR025539](https://doi.org/10.1029/2019WR025539).
- Aubert, A. H. et al. "Fractal water quality fluctuations spanning the periodic table in an intensively farmed watershed". In: *Environmental Science & Technology* 48.2 (2014), pp. 930–937. ISSN: 0013-936X. DOI: [10.1021/es403723r](https://doi.org/10.1021/es403723r).
- Bahremand, A. and Hosseinalizadeh, M. "Development of conceptual hydrological FLEX-Topo model for loess watersheds influenced by piping and tunnel erosion in Golestan Province of Iran". In: *Journal of Water and Soil Conservation* 29.1 (2022), pp. 115–133. ISSN: 2322-2069. DOI: [10.22069/jwsc.2022.20050.3544](https://doi.org/10.22069/jwsc.2022.20050.3544).

- Barnes, C. and Bonell, M. "Application of unit hydrograph techniques to solute transport in catchments". In: *Hydrological Processes* 10.6 (1996), pp. 793–802. ISSN: 0885-6087. DOI: [10.1002/\(sici\)1099-1085\(199606\)10:6<793::aid-hyp372>3.3.co;2-b](https://doi.org/10.1002/(sici)1099-1085(199606)10:6<793::aid-hyp372>3.3.co;2-b).
- Basu, N. B. et al. "Nutrient loads exported from managed catchments reveal emergent biogeochemical stationarity". In: *Geophysical Research Letters* 37.23 (2010). ISSN: 0094-8276. DOI: [10.1029/2010GL045168](https://doi.org/10.1029/2010GL045168).
- Basu, N. B. et al. "Managing nitrogen legacies to accelerate water quality improvement". In: *Nature Geoscience* 15.2 (2022), pp. 97–105. ISSN: 1752-0894. DOI: [10.1038/s41561-021-00889-9](https://doi.org/10.1038/s41561-021-00889-9).
- Begemann, F. and Libby, W. F. "Continental water balance, ground water inventory and storage times, surface ocean mixing rates and world-wide water circulation patterns from cosmic-ray and bomb tritium". In: *Geochimica et Cosmochimica Acta* 12.4 (1957), pp. 277–296. ISSN: 0016-7037. DOI: [10.1016/0016-7037\(57\)90040-6](https://doi.org/10.1016/0016-7037(57)90040-6).
- Benettin, P., Rinaldo, A., and Botter, G. "Tracking residence times in hydrological systems: Forward and backward formulations". In: *Hydrological Processes* 29.25 (2015), pp. 5203–5213. ISSN: 0885-6087. DOI: [10.1002/hyp.10513](https://doi.org/10.1002/hyp.10513).
- Benettin, P. et al. "Linking water age and solute dynamics in streamflow at the Hubbard Brook Experimental Forest, NH, USA". In: *Water Resources Research* 51.11 (2015), pp. 9256–9272. ISSN: 0043-1397. DOI: [10.1002/2015WR017552](https://doi.org/10.1002/2015WR017552).
- Benettin, P. et al. "Modeling chloride transport using travel time distributions at Plynlimon, Wales". In: *Water Resources Research* 51.5 (2015), pp. 3259–3276. ISSN: 0043-1397. DOI: [10.1002/2014WR016600](https://doi.org/10.1002/2014WR016600).
- Benettin, P. et al. "Using SAS functions and high-resolution isotope data to unravel travel time distributions in headwater catchments". In: *Water Resources Research* 53.3 (2017), pp. 1864–1878. ISSN: 0043-1397. DOI: [10.1002/2016WR020117](https://doi.org/10.1002/2016WR020117).
- Benettin, P. et al. "Young runoff fractions control streamwater age and solute concentration dynamics". In: *Hydrological Processes* 31.16 (2017), pp. 2982–2986. ISSN: 0885-6087. DOI: [10.1002/hyp.11243](https://doi.org/10.1002/hyp.11243).
- Benettin, P. et al. "Tracing and closing the water balance in a vegetated lysimeter". In: *Water Resources Research* 57.4 (2021), e2020WR029049. ISSN: 0043-1397. DOI: [10.1029/2020WR029049](https://doi.org/10.1029/2020WR029049).
- Benettin, P. et al. "Transit time estimation in catchments: Recent developments and future directions". In: *Water Resources Research* 58.11 (2022), e2022WR033096. ISSN: 0043-1397. DOI: [10.1029/2022wr033096](https://doi.org/10.1029/2022wr033096).
- Berghuijs, W. R. and Slater, L. J. "Groundwater shapes North American river floods". In: *Environmental Research Letters* 18.3 (2023), p. 034043. ISSN: 1748-9326. DOI: [10.1088/1748-9326/acbecc](https://doi.org/10.1088/1748-9326/acbecc).
- Berghuijs, W. R. et al. "A global assessment of runoff sensitivity to changes in precipitation, potential evaporation, and other factors". In: *Water Resources Research* 53.10 (2017), pp. 8475–8486. ISSN: 0043-1397. DOI: [10.1002/2017WR021593](https://doi.org/10.1002/2017WR021593).

- Berghuijs, W. R. and Woods, R. A. "A simple framework to quantitatively describe monthly precipitation and temperature climatology". In: *International Journal of Climatology* 36.9 (Oct. 2015), pp. 3161–3174. ISSN: 1097-0088. DOI: [10.1002/joc.4544](https://doi.org/10.1002/joc.4544).
- Berghuijs, W., Woods, R., and Hrachowitz, M. "A precipitation shift from snow towards rain leads to a decrease in streamflow". In: *Nature climate change* 4.7 (2014), pp. 583–586. ISSN: 1758-678X. DOI: [10.1038/nclimate2246](https://doi.org/10.1038/nclimate2246).
- Bergström, S. et al. "Integrated modelling of runoff, alkalinity, and pH on a daily basis". In: *Hydrology Research* 16.2 (1985), pp. 89–104. ISSN: 0029-1277. DOI: [10.2166/nh.1985.0008](https://doi.org/10.2166/nh.1985.0008).
- Beven, K. "Searching for the Holy Grail of scientific hydrology: $Q_t = f(S, R, \Delta t)$ as closure". In: *Hydrology and earth system sciences* 10.5 (2006), pp. 609–618. ISSN: 1027-5606. DOI: [10.5194/hess-10-609-2006](https://doi.org/10.5194/hess-10-609-2006).
- Beven, K. "Facets of uncertainty: epistemic uncertainty, non-stationarity, likelihood, hypothesis testing, and communication". In: *Hydrological Sciences Journal* 61.9 (2016), pp. 1652–1665. ISSN: 0262-6667. DOI: [10.1080/02626667.2015.1031761](https://doi.org/10.1080/02626667.2015.1031761).
- Birkel, C. et al. "Assessing the value of high-resolution isotope tracer data in the stepwise development of a lumped conceptual rainfall–runoff model". In: *Hydrological Processes* 24.16 (2010), pp. 2335–2348. ISSN: 0885-6087. DOI: [10.1002/hyp.7763](https://doi.org/10.1002/hyp.7763).
- Birkel, C. and Soulsby, C. "Advancing tracer-aided rainfall–runoff modelling: A review of progress, problems and unrealised potential". In: *Hydrological Processes* 29.25 (2015), pp. 5227–5240. ISSN: 0885-6087. DOI: [10.1002/2017WR021593](https://doi.org/10.1002/2017WR021593).
- Birkel, C., Soulsby, C., and Tetzlaff, D. "Modelling catchment-scale water storage dynamics: Reconciling dynamic storage with tracer-inferred passive storage". In: *Hydrological Processes* 25.25 (2011), pp. 3924–3936. ISSN: 0885-6087. DOI: [10.1002/hyp.8201](https://doi.org/10.1002/hyp.8201).
- Birkel, C., Soulsby, C., and Tetzlaff, D. "Conceptual modelling to assess how the interplay of hydrological connectivity, catchment storage and tracer dynamics controls nonstationary water age estimates". In: *Hydrological Processes* 29.13 (2015), pp. 2956–2969. ISSN: 0885-6087. DOI: [10.1002/hyp.10414](https://doi.org/10.1002/hyp.10414).
- Birkel, C. et al. "Hydroclimatic controls on non-stationary stream water ages in humid tropical catchments". In: *Journal of Hydrology* 542 (2016), pp. 231–240. ISSN: 0022-1694. DOI: [10.1016/j.jhydrol.2016.09.006](https://doi.org/10.1016/j.jhydrol.2016.09.006).
- Birkel, C. et al. "Tracer-aided modeling in the low-relief, wet-dry tropics suggests water ages and DOC export are driven by seasonal wetlands and deep groundwater". In: *Water Resources Research* 56.4 (2020), e2019WR026175. ISSN: 0043-1397. DOI: [10.1029/2019WR026175](https://doi.org/10.1029/2019WR026175).
- Bolin, B. and Rodhe, H. "A note on the concepts of age distribution and transit time in natural reservoirs". In: *Tellus* 25.1 (1973), pp. 58–62. ISSN: 0040-2826. DOI: [10.1111/j.2153-3490.1973.tb01594.x](https://doi.org/10.1111/j.2153-3490.1973.tb01594.x).
- Bonan, G. B. "Forests and climate change: forcings, feedbacks, and the climate benefits of forests". In: *science* 320.5882 (2008), pp. 1444–1449. ISSN: 0036-8075. DOI: [10.1126/science.1155121](https://doi.org/10.1126/science.1155121).

- Botter, G., Bertuzzo, E., and Rinaldo, A. "Catchment residence and travel time distributions: The master equation". In: *Geophysical Research Letters* 38.11 (2011). ISSN: 0094-8276. DOI: [10.1029/2011GL047666](https://doi.org/10.1029/2011GL047666).
- Bouaziz, L. et al. "Redressing the balance: quantifying net intercatchment groundwater flows". In: *Hydrology and Earth System Sciences* 22.12 (2018), pp. 6415–6434. ISSN: 1027-5606. DOI: [10.5194/hess-22-6415-2018](https://doi.org/10.5194/hess-22-6415-2018).
- Bouaziz, L. J. et al. "Improved understanding of the link between catchment-scale vegetation accessible storage and satellite-derived Soil Water Index". In: *Water Resources Research* 56.3 (2020), e2019WR026365. ISSN: 0043-1397. DOI: [10.1029/2019wr026365](https://doi.org/10.1029/2019wr026365).
- Bouaziz, L. J. et al. "Behind the scenes of streamflow model performance". In: *Hydrology and Earth System Sciences* 25.2 (2021), pp. 1069–1095. ISSN: 1027-5606. DOI: [10.5194/hess-25-1069-2021](https://doi.org/10.5194/hess-25-1069-2021).
- Bouaziz, L. J. et al. "Ecosystem adaptation to climate change: the sensitivity of hydrological predictions to time-dynamic model parameters". In: *Hydrology and Earth System Sciences* 26.5 (2022), pp. 1295–1318. ISSN: 1027-5606. DOI: [10.5194/hess-26-1295-2022](https://doi.org/10.5194/hess-26-1295-2022).
- Braga, A. and Laurini, M. "Spatial heterogeneity in climate change effects across Brazilian biomes". In: *Scientific Reports* 14.1 (2024), p. 16414. ISSN: 2045-2322. DOI: [10.1038/s41598-024-67244-x](https://doi.org/10.1038/s41598-024-67244-x).
- Brath, A., Montanari, A., and Moretti, G. "Assessing the effect on flood frequency of land use change via hydrological simulation (with uncertainty)". In: *Journal of hydrology* 324.1-4 (2006), pp. 141–153. ISSN: 0022-1694. DOI: [10.1016/j.jhydrol.2005.10.001](https://doi.org/10.1016/j.jhydrol.2005.10.001).
- Brown, D. G. et al. "Rural land-use trends in the conterminous United States, 1950–2000". In: *Ecological applications* 15.6 (2005), pp. 1851–1863. ISSN: 1939-5582. DOI: [10.1890/03-5220](https://doi.org/10.1890/03-5220).
- Budyko, M. I. *Climate and life*. Ed. by D. Miller. New York, N.Y. (USA) Academic Press, 1974.
- Buzacott, A. J. et al. "Constraining water age dynamics in a south-eastern Australian catchment using an age-ranked storage and stable isotope approach". In: *Hydrological Processes* 34.23 (2020), pp. 4384–4403. ISSN: 0885-6087. DOI: [10.1002/hyp.13880](https://doi.org/10.1002/hyp.13880).
- Cai, W. et al. "Changing El Niño–Southern oscillation in a warming climate". In: *Nature Reviews Earth & Environment* 2.9 (2021), pp. 628–644. ISSN: 2662-138X. DOI: [10.1038/s43017-021-00199-z](https://doi.org/10.1038/s43017-021-00199-z).
- Ceperley, N. et al. "Seasonal snow cover decreases young water fractions in high Alpine catchments". In: *Hydrological Processes* 34.25 (2020), pp. 4794–4813. ISSN: 0885-6087. DOI: [10.1002/hyp.13937](https://doi.org/10.1002/hyp.13937).
- Cheng, J. et al. "Extreme weather conditions and dengue outbreak in Guangdong, China: Spatial heterogeneity based on climate variability". In: *Environmental research* 196 (2021), p. 110900. ISSN: 0013-9351. DOI: [10.1016/j.envres.2021.110900](https://doi.org/10.1016/j.envres.2021.110900).
- Christian Refsgaard, J., Storm, B., and Clausen, T. "Système Hydrologique Européen (SHE): review and perspectives after 30 years development in distributed physically-based hydrological modelling". In: *Hydrology Research* 41.5 (June 2010), pp. 355–377. ISSN: 2224-7955. DOI: [10.2166/nh.2010.009](https://doi.org/10.2166/nh.2010.009).

- Christophersen, N., Seip, H. M., and Wright, R. F. "A model for streamwater chemistry at Birkenes, Norway". In: *Water Resources Research* 18.4 (1982), pp. 977–996. ISSN: 0043-1397. DOI: [10.1029/wr018i004p00977](https://doi.org/10.1029/wr018i004p00977).
- Christophersen, N. and Wright, R. F. "Sulfate budget and a model for sulfate concentrations in stream water at Birkenes, a small forested catchment in southernmost Norway". In: *Water Resources Research* 17.2 (1981), pp. 377–389. ISSN: 0043-1397. DOI: [10.1029/wr017i002p00377](https://doi.org/10.1029/wr017i002p00377).
- Clark, M. P. et al. "Framework for Understanding Structural Errors (FUSE): A modular framework to diagnose differences between hydrological models". In: *Water Resources Research* 44.12 (2008). ISSN: 0043-1397. DOI: [10.1029/2007WR006735](https://doi.org/10.1029/2007WR006735).
- Coenders-Gerrits, A. M. J. et al. "Uncertainties in transpiration estimates". In: *Nature* 506.7487 (Feb. 2014), E1–E2. ISSN: 1476-4687. DOI: [10.1038/nature12925](https://doi.org/10.1038/nature12925).
- Cook, B. I. et al. "Global warming and 21st century drying". In: *Climate dynamics* 43 (2014), pp. 2607–2627. ISSN: 0930-7575. DOI: [10.1007/s00382-014-2075-y](https://doi.org/10.1007/s00382-014-2075-y).
- Dai, A. "Drought under global warming: a review". In: *Wiley Interdisciplinary Reviews: Climate Change* 2.1 (2011), pp. 45–65. ISSN: 1757-7780. DOI: [10.1002/wcc.81](https://doi.org/10.1002/wcc.81).
- Danesh-Yazdi, M. et al. "Inferring changes in water cycle dynamics of intensively managed landscapes via the theory of time-variant travel time distributions". In: *Water Resources Research* 52.10 (2016), pp. 7593–7614. ISSN: 0043-1397. DOI: [10.1002/2016WR019091](https://doi.org/10.1002/2016WR019091).
- De Boer-Euser, T. et al. "Influence of soil and climate on root zone storage capacity". In: *Water Resources Research* 52.3 (2016), pp. 2009–2024. ISSN: 0043-1397. DOI: [10.1002/2015wr018115](https://doi.org/10.1002/2015wr018115).
- De Grosbois, E., Hooper, R. P., and Christophersen, N. "A multisignal automatic calibration methodology for hydrochemical models: A case study of the Birkenes Model". In: *Water Resources Research* 24.8 (Aug. 1988), pp. 1299–1307. ISSN: 1944-7973. DOI: [10.1029/WR024i008p01299](https://doi.org/10.1029/WR024i008p01299).
- De Grosbois, E., Hooper, R. P., and Christophersen, N. "A multisignal automatic calibration methodology for hydrochemical models: a case study of the Birkenes model". In: *Water Resources Research* 24.8 (1988), pp. 1299–1307. ISSN: 0043-1397. DOI: [10.1029/wr024i008p01299](https://doi.org/10.1029/wr024i008p01299).
- DeWalle, D. et al. "Seasonal isotope hydrology of three Appalachian forest catchments". In: *Hydrological Processes* 11.15 (1997), pp. 1895–1906. ISSN: 0885-6087. DOI: [10.1002/\(SICI\)1099-1085\(199712\)11:15<1895::AID-HYP538>3.0.CO;2-%23](https://doi.org/10.1002/(SICI)1099-1085(199712)11:15<1895::AID-HYP538>3.0.CO;2-%23).
- Di Cecco, G. J. and Gouhier, T. C. "Increased spatial and temporal autocorrelation of temperature under climate change". In: *Scientific reports* 8.1 (2018), p. 14850. ISSN: 2045-2322. DOI: [10.1038/s41598-018-33217-0](https://doi.org/10.1038/s41598-018-33217-0).
- Dinçer, T. et al. "Snowmelt runoff from measurements of tritium and oxygen-18". In: *Water Resources Research* 6.1 (1970), pp. 110–124. ISSN: 0043-1397. DOI: [10.1029/WR006i001p00110](https://doi.org/10.1029/WR006i001p00110).

- Donohue, R. J., Roderick, M. L., and McVicar, T. R. "Roots, storms and soil pores: Incorporating key ecohydrological processes into Budyko's hydrological model". In: *Journal of Hydrology* 436 (2012), pp. 35–50. ISSN: 0022-1694. DOI: [10.1016/j.jhydrol.2012.02.033](https://doi.org/10.1016/j.jhydrol.2012.02.033).
- Donohue, R., Roderick, M., and McVicar, T. R. "On the importance of including vegetation dynamics in Budyko's hydrological model". In: *Hydrology and Earth System Sciences* 11.2 (2007), pp. 983–995. ISSN: 1607-7938. DOI: [10.5194/hess-11-983-2007](https://doi.org/10.5194/hess-11-983-2007).
- Dore, M. H. "Climate change and changes in global precipitation patterns: what do we know?" In: *Environment international* 31.8 (2005), pp. 1167–1181. ISSN: 0160-4120. DOI: [10.1016/j.envint.2005.03.004](https://doi.org/10.1016/j.envint.2005.03.004).
- Dralle, D. N. et al. "Accounting for snow in the estimation of root zone water storage capacity from precipitation and evapotranspiration fluxes". In: *Hydrology and Earth System Sciences* 25.5 (2021), pp. 2861–2867. ISSN: 1027-5606. DOI: [10.5194/hess-25-2861-2021](https://doi.org/10.5194/hess-25-2861-2021).
- Duethmann, D., Blöschl, G., and Parajka, J. "Why does a conceptual hydrological model fail to correctly predict discharge changes in response to climate change?" In: *Hydrology and Earth System Sciences* 24.7 (July 2020), pp. 3493–3511. ISSN: 1607-7938. DOI: [10.5194/hess-24-3493-2020](https://doi.org/10.5194/hess-24-3493-2020).
- Dupas, R. et al. "Multidecadal trajectory of riverine nitrogen and phosphorus dynamics in rural catchments". In: *Water Resources Research* 54.8 (2018), pp. 5327–5340. ISSN: 0043-1397. DOI: [10.1029/2018WR022905](https://doi.org/10.1029/2018WR022905).
- Duvert, C. et al. "Time series of tritium, stable isotopes and chloride reveal short-term variations in groundwater contribution to a stream". In: *Hydrology and Earth System Sciences* 20.1 (2016), pp. 257–277. ISSN: 1027-5606. DOI: [10.5194/hess-20-257-2016](https://doi.org/10.5194/hess-20-257-2016).
- Efstratiadis, A. and Koutsoyiannis, D. "One decade of multi-objective calibration approaches in hydrological modelling: a review". In: *Hydrological Sciences Journal–Journal Des Sciences Hydrologiques* 55.1 (2010), pp. 58–78. ISSN: 0262-6667. DOI: [10.1080/02626660903526292](https://doi.org/10.1080/02626660903526292).
- Ellison, D., Pokorný, J., and Wild, M. "Even cooler insights: On the power of forests to (water the Earth and) cool the planet". In: *Global Change Biology* 30.2 (Feb. 2024). ISSN: 1365-2486. DOI: [10.1111/gcb.17195](https://doi.org/10.1111/gcb.17195).
- Elmendorf, S. C. et al. "Plot-scale evidence of tundra vegetation change and links to recent summer warming". In: *Nature Climate Change* 2.6 (Apr. 2012), pp. 453–457. ISSN: 1758-6798. DOI: [10.1038/nclimate1465](https://doi.org/10.1038/nclimate1465).
- Eriksson, E. "The possible use of tritium for estimating groundwater storage". In: *Tellus* 10.4 (1958), pp. 472–478. ISSN: 0040-2826. DOI: [10.3402/tellusa.v10i4.9265](https://doi.org/10.3402/tellusa.v10i4.9265).
- Euser, T. et al. "The effect of forcing and landscape distribution on performance and consistency of model structures". In: *Hydrological Processes* 29.17 (2015), pp. 3727–3743. ISSN: 0885-6087. DOI: [10.1002/hyp.10445](https://doi.org/10.1002/hyp.10445).
- Fan, Y. et al. "Hydrologic regulation of plant rooting depth". In: *Proceedings of the National Academy of Sciences* 114.40 (2017), pp. 10572–10577. ISSN: 0027-8424. DOI: [10.1073/pnas.1712381114](https://doi.org/10.1073/pnas.1712381114).

- Fenicia, F., Savenije, H., and Avdeeva, Y. "Anomaly in the rainfall-runoff behaviour of the Meuse catchment. Climate, land-use, or land-use management?" In: *Hydrology and Earth System Sciences* 13.9 (2009), pp. 1727–1737. ISSN: 1027-5606. DOI: [10.5194/hess-13-1727-2009](https://doi.org/10.5194/hess-13-1727-2009).
- Fenicia, F. et al. "Is the groundwater reservoir linear? Learning from data in hydrological modelling". In: *Hydrology and Earth System Sciences* 10.1 (2006), pp. 139–150. ISSN: 1027-5606. DOI: [10.5194/hess-10-139-2006](https://doi.org/10.5194/hess-10-139-2006).
- Fenicia, F., Kavetski, D., and Savenije, H. H. G. "Elements of a flexible approach for conceptual hydrological modeling: 1. Motivation and theoretical development". In: *Water Resources Research* 47.11 (Nov. 2011). ISSN: 1944-7973. DOI: [10.1029/2010WR010174](https://doi.org/10.1029/2010WR010174).
- Fenicia, F. et al. "Assessing the impact of mixing assumptions on the estimation of streamwater mean residence time". In: *Hydrological Processes* 24.12 (2010), pp. 1730–1741. ISSN: 0885-6087. DOI: [10.1002/hyp.7595](https://doi.org/10.1002/hyp.7595).
- Fovet, O. et al. "Hydrological hysteresis and its value for assessing process consistency in catchment conceptual models". In: *Hydrology and Earth System Sciences* 19.1 (2015), pp. 105–123. ISSN: 1027-5606. DOI: [10.5194/hess-19-105-2015](https://doi.org/10.5194/hess-19-105-2015).
- Fu, B. "On the calculation of the evaporation from land surface". In: *Scientia Atmospherica Sinica* 5.1 (1981), p. 23.
- Gallart, F. et al. "A GLUE-based uncertainty assessment framework for tritium-inferred transit time estimations under baseflow conditions". In: *Hydrological Processes* 30.25 (2016), pp. 4741–4760. ISSN: 0885-6087. DOI: [10.1002/hyp.10991](https://doi.org/10.1002/hyp.10991).
- Gao, H. et al. "Testing the realism of a topography-driven model (FLEX-Topo) in the nested catchments of the Upper Heihe, China". In: *Hydrology and Earth System Sciences* 18.5 (2014), pp. 1895–1915. ISSN: 1027-5606. DOI: [10.5194/hess-18-1895-2014](https://doi.org/10.5194/hess-18-1895-2014).
- Gao, H., Fenicia, F., and Savenije, H. H. "HESS Opinions: Are soils overrated in hydrology?" In: *Hydrology and Earth System Sciences* 27.14 (2023), pp. 2607–2620. ISSN: 1607-7938. DOI: [10.5194/hess-27-2607-2023](https://doi.org/10.5194/hess-27-2607-2023).
- Gao, H. et al. "Climate controls how ecosystems size the root zone storage capacity at catchment scale". In: *Geophysical Research Letters* 41.22 (2014), pp. 7916–7923. ISSN: 0094-8276. DOI: [10.1002/2014gl061668](https://doi.org/10.1002/2014gl061668).
- Gao, H. et al. "Independent determination of the maximum root zone storage (SuMax) in conceptual models". In: *EGU General Assembly Conference Abstracts*. 2014, p. 5305.
- Gao, H. et al. "Accounting for the influence of vegetation and landscape improves model transferability in a tropical savannah region". In: *Water Resources Research* 52.10 (2016), pp. 7999–8022. ISSN: 0043-1397. DOI: [10.1002/2016WR019574](https://doi.org/10.1002/2016WR019574).
- Gao, H. et al. "The importance of aspect for modelling the hydrological response in a glacier catchment in Central Asia". In: *Hydrological processes* 31.16 (2017), pp. 2842–2859. ISSN: 0885-6087. DOI: [10.1002/hyp.11224](https://doi.org/10.1002/hyp.11224).
- Gao, H. et al. "Root zone in the Earth system". In: *EGUsphere [preprint]* (2024). DOI: [10.5194/egusphere-2024-332](https://doi.org/10.5194/egusphere-2024-332).

- Gentine, P. et al. "Interdependence of climate, soil, and vegetation as constrained by the Budyko curve". In: *Geophysical Research Letters* 39.19 (2012). ISSN: 0094-8276. DOI: [10.1029/2012gl053492](https://doi.org/10.1029/2012gl053492).
- Gharari, S. et al. "An approach to identify time consistent model parameters: sub-period calibration". In: *Hydrology and Earth System Sciences* 17.1 (2013), pp. 149–161. ISSN: 1607-7938. DOI: [10.5194/hess-17-149-2013](https://doi.org/10.5194/hess-17-149-2013).
- Gharari, S. et al. "Using expert knowledge to increase realism in environmental system models can dramatically reduce the need for calibration". In: *Hydrology and Earth System Sciences* 18.12 (2014), pp. 4839–4859. ISSN: 1027-5606. DOI: [10.5194/hess-18-4839-2014](https://doi.org/10.5194/hess-18-4839-2014).
- Gharari, S. et al. "Hydrological landscape classification: investigating the performance of HAND based landscape classifications in a central European meso-scale catchment". In: *Hydrology and Earth System Sciences* 15.11 (2011), pp. 3275–3291. ISSN: 1027-5606. DOI: [10.5194/hess-15-3275-2011](https://doi.org/10.5194/hess-15-3275-2011).
- Ghil, M. and Lucarini, V. "The physics of climate variability and climate change". In: *Reviews of Modern Physics* 92.3 (2020), p. 035002. ISSN: 0034-6861. DOI: [10.1103/RevModPhys.92.035002](https://doi.org/10.1103/RevModPhys.92.035002).
- Girons Lopez, M. et al. "Assessing the degree of detail of temperature-based snow routines for runoff modelling in mountainous areas in central Europe". In: *Hydrology and Earth System Sciences* 24.9 (2020), pp. 4441–4461. ISSN: 1027-5606. DOI: [10.5194/hess-24-4441-2020](https://doi.org/10.5194/hess-24-4441-2020).
- Godsey, S. E., Kirchner, J. W., and Clow, D. W. "Concentration–discharge relationships reflect chemostatic characteristics of US catchments". In: *Hydrological Processes: An International Journal* 23.13 (2009), pp. 1844–1864. ISSN: 0885-6087. DOI: [10.1002/hyp.7315](https://doi.org/10.1002/hyp.7315).
- Godsey, S. E. et al. "Generality of fractal 1/f scaling in catchment tracer time series, and its implications for catchment travel time distributions". In: *Hydrological Processes* 24.12 (2010), pp. 1660–1671. ISSN: 0885-6087. DOI: [10.1002/hyp.7677](https://doi.org/10.1002/hyp.7677).
- Goovaerts, P. "Geostatistical approaches for incorporating elevation into the spatial interpolation of rainfall". In: *Journal of hydrology* 228.1-2 (2000), pp. 113–129. ISSN: 0022-1694. DOI: [10.1016/S0022-1694\(00\)00144-X](https://doi.org/10.1016/S0022-1694(00)00144-X).
- Gornall, J. et al. "Implications of climate change for agricultural productivity in the early twenty-first century". In: *Philosophical Transactions of the Royal Society B: Biological Sciences* 365.1554 (2010), pp. 2973–2989. ISSN: 0962-8436. DOI: [10.1098/rstb.2010.0158](https://doi.org/10.1098/rstb.2010.0158).
- Gumbel, E. J. "The return period of flood flows". In: *The annals of mathematical statistics* 12.2 (1941), pp. 163–190. ISSN: 0003-4851. URL: <https://www.jstor.org/stable/2235766>.
- Guswa, A. J. "The influence of climate on root depth: A carbon cost-benefit analysis". In: *Water Resources Research* 44.2 (2008). ISSN: 0043-1397. DOI: [10.1029/2007wr006384](https://doi.org/10.1029/2007wr006384).
- Hadka, D. and Reed, P. "Borg: An auto-adaptive many-objective evolutionary computing framework". In: *Evolutionary computation* 21.2 (2013), pp. 231–259. ISSN: 1063-6560. DOI: [10.1162/EVCO_a_00075](https://doi.org/10.1162/EVCO_a_00075).
- Han, J. et al. "Assessing the Steady-State Assumption in Water Balance Calculation Across Global Catchments". In: *Water Resources Research* 56.7 (July 2020). ISSN: 1944-7973. DOI: [10.1029/2020WR027392](https://doi.org/10.1029/2020WR027392).

- Hanus, S. et al. "Future changes in annual, seasonal and monthly runoff signatures in contrasting Alpine catchments in Austria". In: *Hydrology and Earth System Sciences* 25.6 (2021), pp. 3429–3453. ISSN: 1027-5606. DOI: [10.5194/hess-25-3429-2021](https://doi.org/10.5194/hess-25-3429-2021).
- Harman, C. J. "Time-variable transit time distributions and transport: Theory and application to storage-dependent transport of chloride in a watershed". In: *Water Resources Research* 51.1 (2015), pp. 1–30. ISSN: 0043-1397. DOI: [10.1002/2014WR015707](https://doi.org/10.1002/2014WR015707).
- Harms, P. A. et al. "Distribution of tritium in precipitation and surface water in California". In: *Journal of Hydrology* 534 (2016), pp. 63–72. ISSN: 0022-1694. DOI: [10.1016/j.jhydrol.2015.12.046](https://doi.org/10.1016/j.jhydrol.2015.12.046).
- Heidbüchel, I., Troch, P. A., and Lyon, S. W. "Separating physical and meteorological controls of variable transit times in zero-order catchments". In: *Water Resources Research* 49.11 (2013), pp. 7644–7657. ISSN: 0043-1397. DOI: [10.1002/2012WR013149](https://doi.org/10.1002/2012WR013149).
- Heidbüchel, I. et al. "The master transit time distribution of variable flow systems". In: *Water Resources Research* 48.6 (2012). ISSN: 0043-1397. DOI: [10.1029/2011WR011293](https://doi.org/10.1029/2011WR011293).
- Hoek van Dijke, A. J. et al. "Shifts in regional water availability due to global tree restoration". In: *Nature Geoscience* 15.5 (2022), pp. 363–368. ISSN: 1752-0894. DOI: [10.1038/s41561-022-00935-0](https://doi.org/10.1038/s41561-022-00935-0).
- Hooper, R. P. et al. "Assessing the Birkenes model of stream acidification using a multisignal calibration methodology". In: *Water Resources Research* 24.8 (1988), pp. 1308–1316. ISSN: 0043-1397. DOI: [10.1029/wr024i008p01308](https://doi.org/10.1029/wr024i008p01308).
- Howden, N. et al. "Modelling long-term diffuse nitrate pollution at the catchment-scale: data, parameter and epistemic uncertainty". In: *Journal of hydrology* 403.3-4 (2011), pp. 337–351. ISSN: 0022-1694. DOI: [10.1016/j.jhydrol.2011.04.012](https://doi.org/10.1016/j.jhydrol.2011.04.012).
- Hrachowitz, M. et al. "Gamma distribution models for transit time estimation in catchments: Physical interpretation of parameters and implications for time-variant transit time assessment". In: *Water Resources Research* 46.10 (2010). ISSN: 0043-1397. DOI: [10.1029/2010WR009148](https://doi.org/10.1029/2010WR009148).
- Hrachowitz, M. et al. "Regionalization of transit time estimates in montane catchments by integrating landscape controls". In: *Water Resources Research* 45.5 (2009). ISSN: 0043-1397. DOI: [10.1029/2008WR007496](https://doi.org/10.1029/2008WR007496).
- Hrachowitz, M. et al. "Using long-term data sets to understand transit times in contrasting headwater catchments". In: *Journal of Hydrology* 367.3-4 (2009), pp. 237–248. ISSN: 0022-1694. DOI: [10.1016/j.jhydrol.2009.01.001](https://doi.org/10.1016/j.jhydrol.2009.01.001).
- Hrachowitz, M. et al. "Catchment transit times and landscape controls—does scale matter?" In: *Hydrological Processes: An International Journal* 24.1 (2010), pp. 117–125. ISSN: 0885-6087. DOI: [10.1002/hyp.7510](https://doi.org/10.1002/hyp.7510).
- Hrachowitz, M. et al. "What can flux tracking teach us about water age distribution patterns and their temporal dynamics?" In: *Hydrology and Earth System Sciences* 17.2 (2013), pp. 533–564. ISSN: 1027-5606. DOI: [10.5194/hess-17-533-2013](https://doi.org/10.5194/hess-17-533-2013).
- Hrachowitz, M. et al. "Process consistency in models: The importance of system signatures, expert knowledge, and process complexity". In: *Water resources research* 50.9 (2014), pp. 7445–7469. ISSN: 0043-1397. DOI: [10.1002/2014WR015484](https://doi.org/10.1002/2014WR015484).

- Hrachowitz, M. et al. "Transit time distributions, legacy contamination and variability in biogeochemical $1/f\alpha$ scaling: how are hydrological response dynamics linked to water quality at the catchment scale?" In: *Hydrological Processes* 29.25 (2015), pp. 5241–5256. ISSN: 0885-6087. DOI: [10.1002/hyp.10546](https://doi.org/10.1002/hyp.10546).
- Hrachowitz, M. et al. "Transit times—The link between hydrology and water quality at the catchment scale". In: *Wiley Interdisciplinary Reviews: Water* 3.5 (2016), pp. 629–657. ISSN: 2049-1948. DOI: [10.1002/wat2.1155](https://doi.org/10.1002/wat2.1155).
- Hrachowitz, M. et al. "Reduction of vegetation-accessible water storage capacity after deforestation affects catchment travel time distributions and increases young water fractions in a headwater catchment". In: *Hydrology and Earth System Sciences* 25.9 (Sept. 2021), pp. 4887–4915. ISSN: 1607-7938. DOI: [10.5194/hess-25-4887-2021](https://doi.org/10.5194/hess-25-4887-2021).
- Huang, J., Guan, X., and Yu, H. *Semi-arid Climate Change*. World Scientific, 2023. ISBN: 9811276196.
- Hulsman, P., Hrachowitz, M., and Savenije, H. H. "Improving the representation of long-term storage variations with conceptual hydrological models in data-scarce regions". In: *Water Resources Research* 57.4 (2021), e2020WR028837. ISSN: 0043-1397. DOI: [10.1029/2020WR028837](https://doi.org/10.1029/2020WR028837).
- Hulsman, P., Savenije, H. H., and Hrachowitz, M. "Learning from satellite observations: increased understanding of catchment processes through stepwise model improvement". In: *Hydrology and Earth System Sciences* 25.2 (2021), pp. 957–982. ISSN: 1027-5606. DOI: [10.5194/hess-25-957-2021](https://doi.org/10.5194/hess-25-957-2021).
- Hulsman, P., Savenije, H. H., and Hrachowitz, M. "Satellite-based drought analysis in the Zambezi River Basin: Was the 2019 drought the most extreme in several decades as locally perceived?" In: *Journal of Hydrology: Regional Studies* 34 (2021), p. 100789. ISSN: 2214-5818. DOI: [10.1016/j.ejrh.2021.100789](https://doi.org/10.1016/j.ejrh.2021.100789).
- Huntington, T. G. "Evidence for intensification of the global water cycle: Review and synthesis". In: *Journal of Hydrology* 319.1-4 (2006), pp. 83–95. ISSN: 0022-1694. DOI: [10.1016/j.jhydrol.2005.07.003](https://doi.org/10.1016/j.jhydrol.2005.07.003).
- Ibrahim, M. et al. "Catchments do not strictly follow Budyko curves over multiple decades but deviations are minor and predictable". In: (Apr. 2024). DOI: [10.5194/hess-2024-120](https://doi.org/10.5194/hess-2024-120).
- Jaramillo, F. and Destouni, G. "Developing water change spectra and distinguishing change drivers worldwide". In: *Geophysical Research Letters* 41.23 (2014), pp. 8377–8386. ISSN: 0094-8276. DOI: [10.1002/2014gl061848](https://doi.org/10.1002/2014gl061848).
- Jaramillo, F. et al. "Dominant effect of increasing forest biomass on evapotranspiration: interpretations of movement in Budyko space". In: *Hydrology and Earth System Sciences* 22.1 (2018), pp. 567–580. ISSN: 1027-5606. DOI: [10.5194/hess-22-567-2018](https://doi.org/10.5194/hess-22-567-2018).
- Jasechko, S. "Plants turn on the tap". In: *Nature Climate Change* 8.7 (2018), pp. 562–563. ISSN: 1758-678X. DOI: [10.1038/s41558-018-0212-z](https://doi.org/10.1038/s41558-018-0212-z).
- Jia, S. et al. "Heterogeneous impact of land-use on climate change: study from a spatial perspective". In: *Frontiers in Environmental Science* 10 (2022), p. 840603. ISSN: 2296-665X. DOI: [10.3389/fenvs.2022.840603](https://doi.org/10.3389/fenvs.2022.840603).

- Jones, R. N. and Ricketts, J. H. "Climate as a complex, self-regulating system". In: *Earth System Dynamics Discussions* 2021 (2021), pp. 1–47. ISSN: 2190-4995. DOI: [10.5194/esd-2021-62](https://doi.org/10.5194/esd-2021-62).
- Kaandorp, V. P. et al. "A conceptual model for the analysis of multi-stressors in linked groundwater–surface water systems". In: *Science of the Total Environment* 627 (2018), pp. 880–895. ISSN: 0048-9697. DOI: [10.1016/j.scitotenv.2018.01.259](https://doi.org/10.1016/j.scitotenv.2018.01.259).
- Kendall, C. and McDonnell, J. J. *Isotope tracers in catchment hydrology*. Elsevier, 2012. ISBN: 008092915X.
- Khan, S. J. et al. "Extreme weather events: Should drinking water quality management systems adapt to changing risk profiles?" In: *Water research* 85 (2015), pp. 124–136. ISSN: 0043-1354. DOI: [10.1016/j.watres.2015.08.018](https://doi.org/10.1016/j.watres.2015.08.018).
- Kim, J. P. et al. "Hydrological utility and uncertainty of multi-satellite precipitation products in the mountainous region of South Korea". In: *Remote Sensing* 8.7 (2016), p. 608. ISSN: 2072-4292. DOI: [10.3390/rs8070608](https://doi.org/10.3390/rs8070608).
- Kim, M. et al. "Direct Observation of Hillslope Scale StorAge Selection Functions in Experimental Hydrologic Systems: Geomorphologic Structure and Preferential Discharge of Old Water". In: *Water Resources Research* 58.3 (2022), e2020WR028959. ISSN: 0043-1397. DOI: [10.1029/2020WR028959](https://doi.org/10.1029/2020WR028959).
- Kirchner, J. W. "Getting the right answers for the right reasons: Linking measurements, analyses, and models to advance the science of hydrology". In: *Water Resources Research* 42.3 (2006). ISSN: 0043-1397. DOI: [10.1029/2005WR004362](https://doi.org/10.1029/2005WR004362).
- Kirchner, J. W. "Aggregation in environmental systems–Part 1: Seasonal tracer cycles quantify young water fractions, but not mean transit times, in spatially heterogeneous catchments". In: *Hydrology and Earth System Sciences* 20.1 (2016), pp. 279–297. ISSN: 1027-5606. DOI: [10.5194/hess-20-279-2016](https://doi.org/10.5194/hess-20-279-2016).
- Kirchner, J. W., Feng, X., and Neal, C. "Fractal stream chemistry and its implications for contaminant transport in catchments". In: *Nature* 403.6769 (2000), pp. 524–527. ISSN: 0028-0836. DOI: [10.1038/35000537](https://doi.org/10.1038/35000537).
- Kirchner, J. W., Feng, X., and Neal, C. "Catchment-scale advection and dispersion as a mechanism for fractal scaling in stream tracer concentrations". In: *Journal of hydrology* 254.1-4 (2001), pp. 82–101. ISSN: 0022-1694. DOI: [10.1016/S0022-1694\(01\)00487-5](https://doi.org/10.1016/S0022-1694(01)00487-5).
- Kirchner, J. W. and Neal, C. "Universal fractal scaling in stream chemistry and its implications for solute transport and water quality trend detection". In: *Proceedings of the National Academy of Sciences* 110.30 (2013), pp. 12213–12218. ISSN: 0027-8424. DOI: [10.1073/pnas.1304328110](https://doi.org/10.1073/pnas.1304328110).
- Kirchner, J. W., Tetzlaff, D., and Soulsby, C. "Comparing chloride and water isotopes as hydrological tracers in two Scottish catchments". In: *Hydrological Processes* 24.12 (2010), pp. 1631–1645. ISSN: 0885-6087. DOI: [10.1002/hyp.7676](https://doi.org/10.1002/hyp.7676).
- Kleidon, A. and Lorenz, R. D. *Non-equilibrium thermodynamics and the production of entropy: life, earth, and beyond*. Springer Science & Business Media, 2004. ISBN: 3540224955.

- Knapp, J. L. et al. "New water fractions and transit time distributions at Plynlimon, Wales, estimated from stable water isotopes in precipitation and streamflow". In: *Hydrology and Earth System Sciences* 23.10 (2019), pp. 4367–4388. ISSN: 1607-7938. DOI: [10.5194/hess-23-4367-2019](https://doi.org/10.5194/hess-23-4367-2019).
- Königer, P. et al. "Tritium balance modelling in a macroscale catchment". In: *Hydrological Processes: An International Journal* 19.17 (2005), pp. 3313–3320. ISSN: 0885-6087. DOI: [10.1002/hyp.5972](https://doi.org/10.1002/hyp.5972).
- Königer, P., Stumpp, C., and Schmidt, A. "Stable isotope patterns of German rivers with aspects on scales, continuity and network status". In: *Isotopes in Environmental and Health Studies* (2022), pp. 1–17. ISSN: 1025-6016. DOI: [10.1080/10256016.2022.2127702](https://doi.org/10.1080/10256016.2022.2127702).
- Kreft, A. and Zuber, A. "On the physical meaning of the dispersion equation and its solutions for different initial and boundary conditions". In: *Chemical Engineering Science* 33.11 (1978), pp. 1471–1480. ISSN: 0009-2509. DOI: [10.1016/0009-2509\(78\)85196-3](https://doi.org/10.1016/0009-2509(78)85196-3).
- Kuppel, S. et al. "EcH₂O-iso 1.0: Water isotopes and age tracking in a process-based, distributed ecohydrological model". In: *Geoscientific Model Development* 11.7 (2018), pp. 3045–3069. ISSN: 1991-959X. DOI: [10.5194/gmd-11-3045-2018](https://doi.org/10.5194/gmd-11-3045-2018).
- Kuppel, S. et al. "Critical zone storage controls on the water ages of ecohydrological outputs". In: *Geophysical Research Letters* 47.16 (2020), e2020GL088897. ISSN: 0094-8276. DOI: [10.1029/2020GL088897](https://doi.org/10.1029/2020GL088897).
- Laio, F. et al. "Plants in water-controlled ecosystems: active role in hydrologic processes and response to water stress: II. Probabilistic soil moisture dynamics". In: *Advances in water resources* 24.7 (2001), pp. 707–723. ISSN: 0309-1708. DOI: [10.1016/S0309-1708\(01\)00005-7](https://doi.org/10.1016/S0309-1708(01)00005-7).
- Lee, H. and Romero, J. *Climate Change 2023: Synthesis Report*. Research rep. IPCC, 2023. URL: https://www.ipcc.ch/report/ar6/syr/downloads/report/IPCC_AR6_SYR_LongerReport.pdf.
- Leigh, C. et al. "Ecological effects of extreme climatic events on riverine ecosystems: Insights from Australia". In: *Freshwater Biology* 60.12 (2015), pp. 2620–2638. ISSN: 0046-5070. DOI: [10.1111/fwb.12515](https://doi.org/10.1111/fwb.12515).
- Li, L. et al. "Expanding the role of reactive transport models in critical zone processes". In: *Earth-science reviews* 165 (2017), pp. 280–301. ISSN: 0012-8252. DOI: [10.1016/j.earscirev.2016.09.001](https://doi.org/10.1016/j.earscirev.2016.09.001).
- Li, W. et al. "Intensification of Northern Hemisphere subtropical highs in a warming climate". In: *Nature Geoscience* 5.11 (2012), pp. 830–834. ISSN: 1752-0894. DOI: [10.1038/ngeo1590](https://doi.org/10.1038/ngeo1590).
- Liancourt, P. et al. "Temporal and spatial variation in how vegetation alters the soil moisture response to climate manipulation". In: *Plant and Soil* 351 (2012), pp. 249–261. ISSN: 0032-079X. DOI: [10.1007/s11104-011-0956-y](https://doi.org/10.1007/s11104-011-0956-y).
- Liang, X. et al. "A simple hydrologically based model of land surface water and energy fluxes for general circulation models". In: *Journal of Geophysical Research: Atmospheres* 99.D7 (July 1994), pp. 14415–14428. ISSN: 0148-0227. DOI: [10.1029/94JD00483](https://doi.org/10.1029/94JD00483).

- Lloyd, C. "Assessing the effect of integrating elevation data into the estimation of monthly precipitation in Great Britain". In: *Journal of Hydrology* 308.1-4 (2005), pp. 128–150. ISSN: 0022-1694. DOI: [10.1016/j.jhydrol.2004.10.026](https://doi.org/10.1016/j.jhydrol.2004.10.026).
- Loaiciga, H. A. et al. "Global warming and the hydrologic cycle". In: *Journal of hydrology* 174.1-2 (1996), pp. 83–127. ISSN: 0022-1694. DOI: [10.1016/0022-1694\(95\)02753-X](https://doi.org/10.1016/0022-1694(95)02753-X).
- Loritz, R. et al. "The role and value of distributed precipitation data in hydrological models". In: *Hydrology and Earth System Sciences* 25.1 (2021), pp. 147–167. ISSN: 1027-5606. DOI: [10.5194/hess-25-147-2021](https://doi.org/10.5194/hess-25-147-2021).
- Lundquist, D. "Hydrochemical modelling of drainage basins. SNSF-project". In: *Norwegian Institute for Water Research, Oslo, Rep. IR 31.77* (1977), p. 27.
- Maher, K. "The role of fluid residence time and topographic scales in determining chemical fluxes from landscapes". In: *Earth and Planetary Science Letters* 312.1-2 (2011), pp. 48–58. ISSN: 0012-821X. DOI: [10.1016/j.epsl.2011.09.040](https://doi.org/10.1016/j.epsl.2011.09.040).
- Małoszewski, P. and Zuber, A. "Determining the turnover time of groundwater systems with the aid of environmental tracers: 1. Models and their applicability". In: *Journal of hydrology* 57.3-4 (1982), pp. 207–231. ISSN: 0022-1694. DOI: [10.1016/0022-1694\(82\)90147-0](https://doi.org/10.1016/0022-1694(82)90147-0).
- Małoszewski, P. et al. "Application of flow models in an alpine catchment area using tritium and deuterium data". In: *Journal of Hydrology* 66.1-4 (1983), pp. 319–330. ISSN: 0022-1694. DOI: [10.1016/0022-1694\(83\)90193-2](https://doi.org/10.1016/0022-1694(83)90193-2).
- Marschner, P. and Rengel, Z. "Nutrient availability in soils". In: *Marschner's Mineral Nutrition of Plants*. Elsevier, 2023, pp. 499–522. DOI: [10.1016/B978-0-12-819773-8.00003-4](https://doi.org/10.1016/B978-0-12-819773-8.00003-4).
- McCormick, E. L. et al. "Widespread woody plant use of water stored in bedrock". In: *Nature* 597.7875 (2021), pp. 225–229. ISSN: 0028-0836. DOI: [10.1038/s41586-021-03761-3](https://doi.org/10.1038/s41586-021-03761-3).
- McDonnell, J. J. and Beven, K. "Debates-The future of hydrological sciences: A (common) path forward? A call to action aimed at understanding velocities, celerities and residence time distributions of the headwater hydrograph". In: *Water Resources Research* 50.6 (2014), pp. 5342–5350. ISSN: 0043-1397. DOI: [10.1002/2013WR015141](https://doi.org/10.1002/2013WR015141).
- McGuire, K. J. and McDonnell, J. J. "A review and evaluation of catchment transit time modeling". In: *Journal of Hydrology* 330.3-4 (2006), pp. 543–563. ISSN: 0022-1694. DOI: [10.1016/j.jhydrol.2006.04.020](https://doi.org/10.1016/j.jhydrol.2006.04.020).
- McMillan, H. "Linking hydrologic signatures to hydrologic processes: A review". In: *Hydrological Processes* 34.6 (2020), pp. 1393–1409. ISSN: 0885-6087. DOI: [10.1002/hyp.13632](https://doi.org/10.1002/hyp.13632).
- McMurtrie, R. E. et al. "Plant root distributions and nitrogen uptake predicted by a hypothesis of optimal root foraging". In: *Ecology and Evolution* 2.6 (2012), pp. 1235–1250. ISSN: 2045-7758. DOI: [10.1002/ece3.266](https://doi.org/10.1002/ece3.266).
- Merz, R., Parajka, J., and Blöschl, G. "Time stability of catchment model parameters: Implications for climate impact analyses". In: *Water resources research* 47.2 (2011). ISSN: 0043-1397. DOI: [10.1029/2010WR009505](https://doi.org/10.1029/2010WR009505).
- Mianabadi, A. et al. "A global Budyko model to partition evaporation into interception and transpiration". In: *Hydrology and Earth System Sciences* 23.12 (2019), pp. 4983–5000. ISSN: 1607-7938. DOI: [10.5194/hess-23-4983-2019](https://doi.org/10.5194/hess-23-4983-2019).

- Michel, R. L. et al. "A simplified approach to analysing historical and recent tritium data in surface waters". In: *Hydrological processes* 29.4 (2015), pp. 572–578. ISSN: 0885-6087. DOI: [10.1002/hyp.10174](https://doi.org/10.1002/hyp.10174).
- Miralles, D. G. et al. "On the Use of the Term "Evapotranspiration"". In: *Water Resources Research* 56.11 (Oct. 2020). ISSN: 1944-7973. DOI: [10.1029/2020WR028055](https://doi.org/10.1029/2020WR028055).
- Mora, C. et al. "The projected timing of climate departure from recent variability". In: *Nature* 502.7470 (2013), pp. 183–187. ISSN: 0028-0836. DOI: [10.1038/nature12540](https://doi.org/10.1038/nature12540).
- Morgenstern, U., Stewart, M. K., and Stenger, R. "Dating of streamwater using tritium in a post nuclear bomb pulse world: continuous variation of mean transit time with streamflow". In: *Hydrology and Earth System Sciences* 14.11 (2010), pp. 2289–2301. ISSN: 1027-5606. DOI: [10.5194/hess-14-2289-2010](https://doi.org/10.5194/hess-14-2289-2010).
- Mostbauer, K. et al. "The temporally varying roles of rainfall, snowmelt and soil moisture for debris flow initiation in a snow-dominated system". In: *Hydrology and Earth System Sciences* 22.6 (2018), pp. 3493–3513. ISSN: 1027-5606. DOI: [10.5194/hess-22-3493-2018](https://doi.org/10.5194/hess-22-3493-2018).
- Nguyen, T. V. et al. "Disparate Seasonal Nitrate Export From Nested Heterogeneous Subcatchments Revealed With StorAge Selection Functions". In: *Water Resources Research* 58.3 (Mar. 2022). ISSN: 1944-7973. DOI: [10.1029/2021WR030797](https://doi.org/10.1029/2021WR030797).
- Nicholson, S. E. "The nature of rainfall variability over Africa on time scales of decades to millenia". In: *Global and planetary change* 26.1-3 (2000), pp. 137–158. ISSN: 0921-8181. DOI: [10.1016/S0921-8181\(00\)00040-0](https://doi.org/10.1016/S0921-8181(00)00040-0).
- Niemi, A. J. "Residence time distributions of variable flow processes". In: *The International Journal of Applied Radiation and Isotopes* 28.10-11 (1977), pp. 855–860. ISSN: 0020-708X. DOI: [10.1016/0020-708x\(77\)90026-6](https://doi.org/10.1016/0020-708x(77)90026-6).
- Nijzink, R. et al. "Constraining conceptual hydrological models with multiple information sources". In: *Water Resources Research* 54.10 (2018), pp. 8332–8362. ISSN: 0043-1397. DOI: [10.1029/2017wr021895](https://doi.org/10.1029/2017wr021895).
- Nijzink, R. et al. "The evolution of root-zone moisture capacities after deforestation: a step towards hydrological predictions under change?" In: *Hydrology and Earth System Sciences* 20.12 (2016), pp. 4775–4799. ISSN: 1027-5606. DOI: [10.5194/hess-20-4775-2016](https://doi.org/10.5194/hess-20-4775-2016).
- Nijzink, R. C. et al. "The importance of topography-controlled sub-grid process heterogeneity and semi-quantitative prior constraints in distributed hydrological models". In: *Hydrology and Earth System Sciences* 20.3 (2016), pp. 1151–1176. ISSN: 1027-5606. DOI: [10.5194/hess-20-1151-2016](https://doi.org/10.5194/hess-20-1151-2016).
- Nir, A. "Tracer relations in mixed lakes in non-steady state". In: *Journal of Hydrology* 19.1 (1973), pp. 33–41. ISSN: 0022-1694. DOI: [10.1016/0022-1694\(73\)90091-7](https://doi.org/10.1016/0022-1694(73)90091-7).
- Ol'Dekop, E. "On evaporation from the surface of river basins". In: *Transactions on meteorological observations* 4 (1911), p. 200.
- Oudin, L. et al. "Which potential evapotranspiration input for a lumped rainfall–runoff model?: Part 2—Towards a simple and efficient potential evapotranspiration model for rainfall–runoff modelling". In: *Journal of hydrology* 303.1-4 (2005), pp. 290–306. ISSN: 0022-1694. DOI: [10.1016/j.jhydrol.2004.08.026](https://doi.org/10.1016/j.jhydrol.2004.08.026).

- Oudin, L. et al. "Has land cover a significant impact on mean annual streamflow? An international assessment using 1508 catchments". In: *Journal of hydrology* 357.3-4 (2008), pp. 303–316. ISSN: 0022-1694. DOI: [10.1016/j.jhydrol.2008.05.021](https://doi.org/10.1016/j.jhydrol.2008.05.021).
- Pfister, L. et al. "Bedrock geology controls on catchment storage, mixing, and release: A comparative analysis of 16 nested catchments". In: *Hydrological Processes* 31.10 (2017), pp. 1828–1845. ISSN: 0885-6087. DOI: [10.1002/hyp.11134](https://doi.org/10.1002/hyp.11134).
- Polley, H. W. "Implications of atmospheric and climatic change for crop yield and water use efficiency". In: *Crop science* 42.1 (2002), pp. 131–140. ISSN: 0011-183X. DOI: [10.2135/cropsci2002.1310](https://doi.org/10.2135/cropsci2002.1310).
- Prenner, D. et al. "The value of using multiple hydrometeorological variables to predict temporal debris flow susceptibility in an alpine environment". In: *Water Resources Research* 54.9 (2018), pp. 6822–6843. ISSN: 0043-1397. DOI: [10.1029/2018WR022985](https://doi.org/10.1029/2018WR022985).
- Pugnaire, F. I. et al. "Climate change effects on plant-soil feedbacks and consequences for biodiversity and functioning of terrestrial ecosystems". In: *Science advances* 5.11 (2019), eaaz1834. ISSN: 2375-2548. DOI: [10.1126/sciadv.aaz1834](https://doi.org/10.1126/sciadv.aaz1834).
- Rahimpour Asenjan, M. and Danesh-Yazdi, M. "The effect of seasonal variation in precipitation and evapotranspiration on the transient travel time distributions". In: *Advances in Water Resources* 142 (Aug. 2020), p. 103618. ISSN: 0309-1708. DOI: [10.1016/j.advwatres.2020.103618](https://doi.org/10.1016/j.advwatres.2020.103618).
- Rank, D. et al. "Temporal and spatial distribution of isotopes in river water in Central Europe: 50 years experience with the Austrian network of isotopes in rivers". In: *Isotopes in Environmental and Health Studies* 54.2 (2018), pp. 115–136. ISSN: 1025-6016. DOI: [10.1080/10256016.2017.1383906](https://doi.org/10.1080/10256016.2017.1383906).
- Reaver, N. G. et al. "Theoretical and empirical evidence against the Budyko catchment trajectory conjecture". In: *Hydrology and Earth System Sciences* 26.5 (2022), pp. 1507–1525. ISSN: 1027-5606. DOI: [10.5194/hess-26-1507-2022](https://doi.org/10.5194/hess-26-1507-2022).
- Reckerth, A., Stichler, W., and Schmidt, A. "Long-term data set analysis of stable isotopic composition in German rivers". In: *J Hydrol* 552.null (2017), p. 718. ISSN: null. DOI: [10.1016/j.jhydrol.2017.07.022](https://doi.org/10.1016/j.jhydrol.2017.07.022).
- Remondi, F. et al. "Water flux tracking with a distributed hydrological model to quantify controls on the spatio-temporal variability of transit time distributions". In: *Water Resources Research* 54.4 (2018), pp. 3081–3099. ISSN: 0043-1397. DOI: [10.1002/2017WR021689](https://doi.org/10.1002/2017WR021689).
- Rinaldo, A. et al. "Catchment travel time distributions and water flow in soils". In: *Water resources research* 47.7 (2011). ISSN: 0043-1397. DOI: [10.1029/2011WR010478](https://doi.org/10.1029/2011WR010478).
- Rinaldo, A. et al. "Storage selection functions: A coherent framework for quantifying how catchments store and release water and solutes". In: *Water Resources Research* 51.6 (2015), pp. 4840–4847. ISSN: 0043-1397. DOI: [10.1002/2015WR017273](https://doi.org/10.1002/2015WR017273).
- Roberts, K. J. et al. "Dynamic load balancing for predictions of storm surge and coastal flooding". In: *Environmental Modelling & Software* 140 (2021), p. 105045. ISSN: 1364-8152. DOI: [10.1016/j.envsoft.2021.105045](https://doi.org/10.1016/j.envsoft.2021.105045).

- Roderick, M. L. and Farquhar, G. D. "A simple framework for relating variations in runoff to variations in climatic conditions and catchment properties". In: *Water Resources Research* 47.12 (2011). ISSN: 0043-1397. DOI: [10.1029/2010WR009826](https://doi.org/10.1029/2010WR009826).
- Rodriguez, N. B. and Klaus, J. "Catchment travel times from composite StorAge Selection functions representing the superposition of streamflow generation processes". In: *Water Resources Research* 55.11 (2019), pp. 9292–9314. ISSN: 0043-1397. DOI: [10.1029/2019wr024973](https://doi.org/10.1029/2019wr024973).
- Rodriguez, N. B., McGuire, K. J., and Klaus, J. "Time-varying storage–water age relationships in a catchment with a Mediterranean climate". In: *Water Resources Research* 54.6 (2018), pp. 3988–4008. ISSN: 0043-1397. DOI: [10.1029/2017WR021964](https://doi.org/10.1029/2017WR021964).
- Rodriguez, N. B. et al. "A comparison of catchment travel times and storage deduced from deuterium and tritium tracers using StorAge Selection functions". In: *Hydrology and Earth System Sciences* 25.1 (2021), pp. 401–428. ISSN: 1027-5606. DOI: [10.5194/hess-25-401-2021](https://doi.org/10.5194/hess-25-401-2021).
- Rodríguez-Iturbe, I. and Porporato, A. *Ecohydrology of water-controlled ecosystems: soil moisture and plant dynamics*. Cambridge University Press, 2007. ISBN: 1139441957.
- Roodari, A. et al. "Signatures of human intervention—or not? Downstream intensification of hydrological drought along a large Central Asian river: the individual roles of climate variability and land use change". In: *Hydrology and Earth System Sciences* 25.4 (2021), pp. 1943–1967. ISSN: 1027-5606. DOI: [10.5194/hess-25-1943-2021](https://doi.org/10.5194/hess-25-1943-2021).
- Rozanski, K., Gonfiantini, R., and Araguas-Araguas, L. "Tritium in the global atmosphere: Distribution patterns and recent trends". In: *Journal of Physics G: Nuclear and Particle Physics* 17.S (1991), S523. ISSN: 0954-3899. DOI: [10.1088/0954-3899/17/s/053](https://doi.org/10.1088/0954-3899/17/s/053).
- Sadayappan, K. et al. "Drier streams despite a wetter climate in woody-encroached grasslands". In: *Journal of Hydrology* 627 (2023), p. 130388. ISSN: 0022-1694. DOI: [10.1016/j.jhydrol.2023.130388](https://doi.org/10.1016/j.jhydrol.2023.130388).
- Salinger, M. J. "Climate variability and change: past, present and future—an overview". In: *Climatic change* 70.1 (2005), pp. 9–29. ISSN: 0165-0009. DOI: [10.1007/s10584-005-5936-x](https://doi.org/10.1007/s10584-005-5936-x).
- Savenije, H. H. "The importance of interception and why we should delete the term evapotranspiration from our vocabulary". In: *Hydrological Processes* 18.8 (2004), pp. 1507–1511. ISSN: 1099-1085. DOI: [10.1002/hyp.5563](https://doi.org/10.1002/hyp.5563).
- Savenije, H. H. and Hrachowitz, M. "HESS Opinions Catchments as meta-organisms—a new blueprint for hydrological modelling". In: *Hydrology and Earth System Sciences* 21.2 (2017), pp. 1107–1116. ISSN: 1027-5606. DOI: [10.5194/hess-21-1107-2017](https://doi.org/10.5194/hess-21-1107-2017).
- Schenk, H. J. and Jackson, R. B. "Rooting depths, lateral root spreads and below-ground/above-ground allometries of plants in water-limited ecosystems". In: *Journal of Ecology* (2002), pp. 480–494. ISSN: 0022-0477. URL: [/](https://doi.org/10.1002/hyp.13691).
- Schmidt, A. et al. "Overview of tritium records from precipitation and surface waters in Germany". In: *Hydrological Processes* 34.6 (2020), pp. 1489–1493. ISSN: 0885-6087. DOI: [10.1002/hyp.13691](https://doi.org/10.1002/hyp.13691).
- Schreiber, P. "Über die Beziehungen zwischen dem Niederschlag und der Wasserführung der Flüsse in Mitteleuropa". In: *Z. Meteorol* 21.10 (1904), pp. 441–452.

- Scrivner, C. and Ruppert, D. *Thickness of soil solum as a parameter of plant-available water storage capacity in soils underlain by carbonate rocks*. Report. 1970.
- Seeger, S. and Weiler, M. "Reevaluation of transit time distributions, mean transit times and their relation to catchment topography". In: *Hydrology and Earth System Sciences* 18.12 (2014), pp. 4751–4771. ISSN: 1027-5606. DOI: [10.5194/hess-18-4751-2014](https://doi.org/10.5194/hess-18-4751-2014).
- Seibert, J., McDonnell, J. J., and Woodsmith, R. D. "Effects of wildfire on catchment runoff response: a modelling approach to detect changes in snow-dominated forested catchments". In: *Hydrology research* 41.5 (2010), pp. 378–390. ISSN: 0029-1277. DOI: [10.2166/nh.2010.036](https://doi.org/10.2166/nh.2010.036).
- Seip, H. M. et al. "Model of sulphate concentration in a small stream in the Harp Lake catchment, Ontario". In: *Canadian Journal of Fisheries and Aquatic Sciences* 42.5 (1985), pp. 927–937. ISSN: 0706-652X. DOI: [10.1139/f85-117](https://doi.org/10.1139/f85-117).
- Shaw, S. B. et al. "Investigating a high resolution, stream chloride time series from the Biscuit Brook catchment, Catskills, NY". In: *Journal of Hydrology* 348.3-4 (2008), pp. 245–256. ISSN: 0022-1694. DOI: [10.1016/j.jhydrol.2007.10.009](https://doi.org/10.1016/j.jhydrol.2007.10.009).
- Shrestha, R. R. et al. "Modelling spatial and temporal variability of hydrologic impacts of climate change in the Fraser River basin, British Columbia, Canada". In: *Hydrological Processes* 26.12 (2012), pp. 1840–1860. ISSN: 0885-6087. DOI: [10.1002/hyp.9283](https://doi.org/10.1002/hyp.9283).
- Singh, C. et al. "Rootzone storage capacity reveals drought coping strategies along rainforest-savanna transitions". In: *Environmental Research Letters* 15.12 (2020), p. 124021. ISSN: 1748-9326. DOI: [10.1088/1748-9326/abc377](https://doi.org/10.1088/1748-9326/abc377).
- Sivandran, G. and Bras, R. L. "Identifying the optimal spatially and temporally invariant root distribution for a semiarid environment". In: *Water Resources Research* 48.12 (2012). ISSN: 0043-1397. DOI: [10.1029/2012wr012055](https://doi.org/10.1029/2012wr012055).
- Sivapalan, M. and Blöschl, G. "Time scale interactions and the coevolution of humans and water". In: *Water Resources Research* 51.9 (2015), pp. 6988–7022. ISSN: 0043-1397. DOI: [10.1002/2015WR017896](https://doi.org/10.1002/2015WR017896).
- Soulsby, C., Birkel, C., and Tetzlaff, D. "Characterizing the age distribution of catchment evaporative losses". In: *Hydrological Processes* 30.8 (2016), pp. 1308–1312. ISSN: 0885-6087. DOI: [10.1002/hyp.10751](https://doi.org/10.1002/hyp.10751).
- Speich, M. J., Lischke, H., and Zappa, M. "Testing an optimality-based model of rooting zone water storage capacity in temperate forests". In: *Hydrology and Earth System Sciences* 22.7 (2018), pp. 4097–4124. ISSN: 1607-7938. DOI: [10.5194/hess-22-4097-2018](https://doi.org/10.5194/hess-22-4097-2018).
- Sprenger, M. et al. "Water ages in the critical zone of long-term experimental sites in northern latitudes". In: *Hydrology and Earth System Sciences* 22.7 (2018), pp. 3965–3981. ISSN: 1027-5606. DOI: [10.5194/hess-22-3965-2018](https://doi.org/10.5194/hess-22-3965-2018).
- Sprenger, M. et al. "The demographics of water: A review of water ages in the critical zone". In: *Reviews of Geophysics* 57.3 (2019), pp. 800–834. ISSN: 8755-1209. DOI: [10.1029/2018RG000633](https://doi.org/10.1029/2018RG000633).

- Sriwongsitanon, N. et al. "Using normalised difference infrared index patterns to constrain semi-distributed rainfall-runoff models in tropical nested catchments". In: *Hydrology and Earth System Sciences* 27.11 (2023), pp. 2149–2171. issn: 1607-7938. doi: [10.5194/hess-27-2149-2023](https://doi.org/10.5194/hess-27-2149-2023).
- Stephens, C. M. et al. "Landscape changes and their hydrologic effects: Interactions and feedbacks across scales". In: *Earth-Science Reviews* 212 (2021), p. 103466. issn: 0012-8252. doi: [10.1016/j.earscirev.2020.103466](https://doi.org/10.1016/j.earscirev.2020.103466).
- Stevenson, J. L., Birkel, C., and Neill, A. J. "Effects of streamflow isotope sampling strategies on the calibration of a tracer-aided rainfall-runoff model". In: *Hydrol Process* 35.6 (2021), e14223. issn: null. doi: [10.1002/hyp.14223](https://doi.org/10.1002/hyp.14223).
- Stewart, M. K., Mehlhorn, J., and Elliott, S. "Hydrometric and natural tracer (oxygen-18, silica, tritium and sulphur hexafluoride) evidence for a dominant groundwater contribution to Pukemanga Stream, New Zealand". In: *Hydrological Processes: An International Journal* 21.24 (2007), pp. 3340–3356. issn: 0885-6087. doi: [10.1002/hyp.6557](https://doi.org/10.1002/hyp.6557).
- Stewart, M. K. and Morgenstern, U. "Importance of tritium-based transit times in hydrological systems". In: *Wiley Interdisciplinary Reviews: Water* 3.2 (2016), pp. 145–154. issn: 2049-1948. doi: [10.1002/wat2.1134](https://doi.org/10.1002/wat2.1134).
- Stewart, M. K., Morgenstern, U., and McDonnell, J. J. "Truncation of stream residence time: how the use of stable isotopes has skewed our concept of streamwater age and origin". In: *Hydrological Processes* 24.12 (2010), pp. 1646–1659. issn: 0885-6087. doi: [10.1002/hyp.7576](https://doi.org/10.1002/hyp.7576).
- Stewart, M. K. "A 40-year record of carbon-14 and tritium in the Christchurch groundwater system, New Zealand: Dating of young samples with carbon-14". In: *Journal of Hydrology* 430–431 (Apr. 2012), pp. 50–68. issn: 0022-1694. doi: [10.1016/j.jhydrol.2012.01.046](https://doi.org/10.1016/j.jhydrol.2012.01.046).
- Stewart, M. K., Morgenstern, U., and Cartwright, I. "Comment on "A comparison of catchment travel times and storage deduced from deuterium and tritium tracers using StorAge Selection functions" by Rodriguez et al.(2021)". In: *Hydrology and Earth System Sciences* 25.12 (2021), pp. 6333–6338. issn: 1027-5606. doi: [10.5194/hess-25-6333-2021](https://doi.org/10.5194/hess-25-6333-2021).
- Stewart, M. and Thomas, J. "A conceptual model of flow to the Waikoropupu Springs, NW Nelson, New Zealand, based on hydrometric and tracer (^{18}O , Cl, ^3H and CFC) evidence". In: *Hydrology and Earth System Sciences* 12.1 (2008), pp. 1–19. issn: 1027-5606. doi: [10.5194/hess-12-1-2008](https://doi.org/10.5194/hess-12-1-2008).
- Stewart, M. et al. "The 'hidden streamflow' challenge in catchment hydrology: a call to action for stream water transit time analysis". In: *Hydrological Processes* 26.13 (2012), pp. 2061–2066. issn: 0885-6087. doi: [10.1002/hyp.9262](https://doi.org/10.1002/hyp.9262).
- Stocker, B. D. et al. "Global patterns of water storage in the rooting zones of vegetation". In: *Nature geoscience* 16.3 (2023), pp. 250–256. issn: 1752-0894. doi: [10.1038/s41561-023-01125-2](https://doi.org/10.1038/s41561-023-01125-2).

- Stockinger, M. P. and Stumpp, C. “Lessons learned from the spatiotemporal analysis of long-term and time-variable young water fractions of large central European river basins”. In: *Hydrological Processes* 38.2 (2024), e15038. ISSN: 0885-6087. DOI: [10.1002/hyp.15038](https://doi.org/10.1002/hyp.15038).
- Stockinger, M. P. et al. “Time variability and uncertainty in the fraction of young water in a small headwater catchment”. In: *Hydrology and Earth System Sciences* 23.10 (2019), pp. 4333–4347. ISSN: 1607-7938. DOI: [10.5194/hess-23-4333-2019](https://doi.org/10.5194/hess-23-4333-2019).
- Stumpp, C., Klaus, J., and Stichler, W. “Analysis of long-term stable isotopic composition in German precipitation”. In: *Journal of Hydrology* 517 (2014), pp. 351–361. ISSN: 0022-1694. DOI: [10.1016/j.jhydrol.2014.05.034](https://doi.org/10.1016/j.jhydrol.2014.05.034).
- Tadros, C. V. et al. “Tritium in Australian precipitation: A 50 year record”. In: *Journal of hydrology* 513 (2014), pp. 262–273. ISSN: 0022-1694. DOI: [10.1016/j.jhydrol.2014.03.031](https://doi.org/10.1016/j.jhydrol.2014.03.031).
- Tempel, N. T. et al. “Vegetation Response to Climatic Variability: Implications for Root Zone Storage and Streamflow Predictions”. In: (Feb. 2024). DOI: [10.5194/egusphere-2024-115](https://doi.org/10.5194/egusphere-2024-115).
- Teuling, A. J. and Hoek van Dijke, A. J. “Forest age and water yield”. In: *Nature* 578.7794 (2020), E16–E18. ISSN: 0028-0836. DOI: [10.1038/s41586-020-1941-5](https://doi.org/10.1038/s41586-020-1941-5).
- Teuling, A. J. et al. “Climate change, reforestation/afforestation, and urbanization impacts on evapotranspiration and streamflow in Europe”. In: *Hydrology and Earth System Sciences* 23.9 (2019), pp. 3631–3652. ISSN: 1607-7938. DOI: [10.5194/hess-23-3631-2019](https://doi.org/10.5194/hess-23-3631-2019).
- Thirumalai, K. et al. “Extreme temperatures in Southeast Asia caused by El Niño and worsened by global warming”. In: *Nature communications* 8.1 (2017), p. 15531. ISSN: 2041-1723. DOI: [10.1038/ncomms15531](https://doi.org/10.1038/ncomms15531).
- Thompson, S. E. and Katul, G. G. “Multiple mechanisms generate Lorentzian and $1/f\alpha$ power spectra in daily stream-flow time series”. In: *Advances in Water Resources* 37 (2012), pp. 94–103. ISSN: 0309-1708. DOI: [10.1016/j.advwatres.2011.10.010](https://doi.org/10.1016/j.advwatres.2011.10.010).
- Thornton, P. K. et al. “Climate variability and vulnerability to climate change: a review”. In: *Global change biology* 20.11 (2014), pp. 3313–3328. ISSN: 1354-1013. DOI: [10.1111/gcb.12581](https://doi.org/10.1111/gcb.12581).
- Timmermann, A. et al. “El Niño–southern oscillation complexity”. In: *Nature* 559.7715 (2018), pp. 535–545. ISSN: 0028-0836. DOI: [10.1038/s41586-018-0252-6](https://doi.org/10.1038/s41586-018-0252-6).
- Tixeront, J. “Prévision des apports des cours d’eau”. In: *Publication de l’Association internationale d’hydrologie scientifique* 63 (1964), pp. 118–126.
- Tong, R. et al. “The value of satellite soil moisture and snow cover data for the transfer of hydrological model parameters to ungauged sites”. In: *Hydrology and Earth System Sciences* 26.7 (2022), pp. 1779–1799. ISSN: 1027-5606. DOI: [10.5194/hess-26-1779-2022](https://doi.org/10.5194/hess-26-1779-2022).
- Trenberth, K. E. *Climate system modeling*. Cambridge University Press, 1992. ISBN: 0521432316.
- Uhlenbrook, S. et al. “Hydrograph separations in a mesoscale mountainous basin at event and seasonal timescales”. In: *Water Resources Research* 38.6 (2002), pp. 31-1-31–14. ISSN: 0043-1397. DOI: [10.1029/2001wr000938](https://doi.org/10.1029/2001wr000938).

- Van der Velde, Y. et al. "Quantifying catchment-scale mixing and its effect on time-varying travel time distributions". In: *Water Resources Research* 48.6 (2012). ISSN: 0043-1397. DOI: [10.1029/2011WR011310](https://doi.org/10.1029/2011WR011310).
- Van der Velde, Y. et al. "Exploring hydroclimatic change disparity via the Budyko framework". In: *Hydrological Processes* 28.13 (2014), pp. 4110–4118. ISSN: 0885-6087. DOI: [10.1002/hyp.9949](https://doi.org/10.1002/hyp.9949).
- Van der Velde, Y. et al. "Consequences of mixing assumptions for time-variable travel time distributions". In: *Hydrological Processes* 29.16 (2015), pp. 3460–3474. ISSN: 0885-6087. DOI: [10.1002/hyp.10372](https://doi.org/10.1002/hyp.10372).
- Van Loon, A. F. et al. "Drought in a human-modified world: reframing drought definitions, understanding, and analysis approaches". In: *Hydrology and Earth System Sciences* 20.9 (2016), pp. 3631–3650. ISSN: 1027-5606. DOI: [10.5194/hess-20-3631-2016](https://doi.org/10.5194/hess-20-3631-2016).
- Van Oorschot, F. et al. "Climate-controlled root zone parameters show potential to improve water flux simulations by land surface models". In: *Earth System Dynamics* 12.2 (2021), pp. 725–743. ISSN: 2190-4979. DOI: [10.5194/esd-12-725-2021](https://doi.org/10.5194/esd-12-725-2021).
- Van Oorschot, F. et al. "Influence of irrigation on root zone storage capacity estimation". In: *Hydrology and Earth System Sciences* 28.10 (May 2024), pp. 2313–2328. ISSN: 1607-7938. DOI: [10.5194/hess-28-2313-2024](https://doi.org/10.5194/hess-28-2313-2024).
- Verdin, K. L. "Hydrologic Derivatives for Modeling and Applications (HDMA) Data". In: (2017). DOI: [10.5066/F7S180ZP](https://doi.org/10.5066/F7S180ZP).
- Visser, A. et al. "Cosmogenic isotopes unravel the hydrochronology and water storage dynamics of the Southern Sierra Critical Zone". In: *Water Resources Research* 55.2 (2019), pp. 1429–1450. ISSN: 0043-1397. DOI: [10.1029/2018WR023665](https://doi.org/10.1029/2018WR023665).
- Vitvar, T. and Balderer, W. "Estimation of mean water residence times and runoff generation by 180 measurements in a Pre-Alpine catchment (Rietholzbach, Eastern Switzerland)". In: *Applied Geochemistry* 12.6 (1997), pp. 787–796. ISSN: 0883-2927. DOI: [10.1016/S0883-2927\(97\)00045-0](https://doi.org/10.1016/S0883-2927(97)00045-0).
- Von Freyberg, J. et al. "Sensitivity of young water fractions to hydro-climatic forcing and landscape properties across 22 Swiss catchments". In: *Hydrology and Earth System Sciences* 22.7 (2018), pp. 3841–3861. ISSN: 1607-7938. DOI: [10.5194/hess-22-3841-2018](https://doi.org/10.5194/hess-22-3841-2018).
- Wagener, T. et al. "Towards reduced uncertainty in conceptual rainfall-runoff modelling: Dynamic identifiability analysis". In: *Hydrological processes* 17.2 (2003), pp. 455–476. ISSN: 0885-6087. DOI: [10.1002/hyp.1135](https://doi.org/10.1002/hyp.1135).
- Wagener, T. et al. "The future of hydrology: An evolving science for a changing world". In: *Water Resources Research* 46.5 (2010). ISSN: 0043-1397. DOI: [10.1029/2009WR008906](https://doi.org/10.1029/2009WR008906).
- Wang, S., Hrachowitz, M., and Schoups, G. "Multi-decadal fluctuations in root zone storage capacity through vegetation adaptation to hydro-climatic variability has minor effects on the hydrological response in the Neckar basin, Germany". In: *Hydrology and Earth System Sciences* 28.17 (2024), pp. 4011–4033. ISSN: 1812-2116. DOI: [10.5194/hess-28-4011-2024](https://doi.org/10.5194/hess-28-4011-2024).

- Wang, S. et al. "Effects of industry structures on water quality in different urbanized regions using an improved entropy-weighted matter-element methodology". In: *Environmental Science and Pollution Research* 27.7 (Dec. 2019), pp. 7549–7558. ISSN: 1614-7499. DOI: [10.1007/s11356-019-07400-3](https://doi.org/10.1007/s11356-019-07400-3).
- Wang, S. et al. "Stable water isotopes and tritium tracers tell the same tale: no evidence for underestimation of catchment transit times inferred by stable isotopes in StorAge Selection (SAS)-function models". In: *Hydrology and Earth System Sciences* 27.16 (2023), pp. 3083–3114. ISSN: 1607-7938. DOI: [10.5194/hess-27-3083-2023](https://doi.org/10.5194/hess-27-3083-2023).
- Wang, S. et al. "Multi-decadal stability of water ages and tracer transport in a temperate-humid river basin". In: *Environmental Research letters* (2024). Under review.
- Wang-Erlandsson, L. et al. "Global root zone storage capacity from satellite-based evaporation". In: *Hydrology and Earth System Sciences* 20.4 (2016), pp. 1459–1481. ISSN: 1027-5606. DOI: [10.5194/hess-20-1459-2016](https://doi.org/10.5194/hess-20-1459-2016).
- Weiler, M. et al. "How does rainfall become runoff? A combined tracer and runoff transfer function approach". In: *Water Resources Research* 39.11 (2003). ISSN: 0043-1397. DOI: [10.1029/2003WR002331](https://doi.org/10.1029/2003WR002331).
- Wetz, M. S. and Yoskowitz, D. W. "An 'extreme' future for estuaries? Effects of extreme climatic events on estuarine water quality and ecology". In: *Marine Pollution Bulletin* 69.1-2 (2013), pp. 7–18. ISSN: 0025-326X. DOI: [10.1016/j.marpolbul.2013.01.020](https://doi.org/10.1016/j.marpolbul.2013.01.020).
- Whitehead, P. G. et al. "A review of the potential impacts of climate change on surface water quality". In: *Hydrological sciences journal* 54.1 (2009), pp. 101–123. ISSN: 0262-6667. DOI: [10.1623/hysj.54.1.101](https://doi.org/10.1623/hysj.54.1.101).
- Wilusz, D. C., Harman, C. J., and Ball, W. P. "Sensitivity of catchment transit times to rainfall variability under present and future climates". In: *Water Resources Research* 53.12 (2017), pp. 10231–10256. ISSN: 0043-1397. DOI: [10.1002/2017WR020894](https://doi.org/10.1002/2017WR020894).
- Wilusz, D. et al. "Using particle tracking to understand flow paths, age distributions, and the paradoxical origins of the inverse storage effect in an experimental catchment". In: *Water Resources Research* 56.4 (2020), e2019WR025140. ISSN: 0043-1397. DOI: [10.1029/2019WR025140](https://doi.org/10.1029/2019WR025140).
- Wu, L., Xu, Y., and Wang, S. "Comparison of TMPA-3B42RT Legacy Product and the Equivalent IMERG Products over Mainland China". In: *Remote Sensing* 10.11 (Nov. 2018), p. 1778. ISSN: 2072-4292. DOI: [10.3390/rs10111778](https://doi.org/10.3390/rs10111778).
- Wu, L. et al. "Enhanced warming over the global subtropical western boundary currents". In: *Nature Climate Change* 2.3 (2012), pp. 161–166. ISSN: 1758-678X. DOI: [10.1038/nclimate1353](https://doi.org/10.1038/nclimate1353).
- Yang, D., Yang, Y., and Xia, J. "Hydrological cycle and water resources in a changing world: A review". In: *Geography and Sustainability* 2.2 (2021), pp. 115–122. ISSN: 2666-6839. DOI: [10.1016/j.geosus.2021.05.003](https://doi.org/10.1016/j.geosus.2021.05.003).
- Yang, K. et al. "Recent climate changes over the Tibetan Plateau and their impacts on energy and water cycle: A review". In: *Global and Planetary Change* 112 (2014), pp. 79–91. ISSN: 0921-8181. DOI: [10.1016/j.gloplacha.2013.12.001](https://doi.org/10.1016/j.gloplacha.2013.12.001).

- Yang, Y. et al. "A novel approach for modelling vegetation distributions and analysing vegetation sensitivity through trait-climate relationships in China". In: *Scientific Reports* 6.1 (2016), p. 24110. ISSN: 2045-2322. DOI: [10.1038/srep24110](https://doi.org/10.1038/srep24110).
- Zhang, L. et al. "A rational function approach for estimating mean annual evapotranspiration". In: *Water Resources Research* 40.2 (Feb. 2004). ISSN: 1944-7973. DOI: [10.1029/2003WR002710](https://doi.org/10.1029/2003WR002710).
- Zhang, L., Dawes, W., and Walker, G. "Response of mean annual evapotranspiration to vegetation changes at catchment scale". In: *Water resources research* 37.3 (2001), pp. 701–708. ISSN: 0043-1397. DOI: [10.1029/2000wr900325](https://doi.org/10.1029/2000wr900325).
- Zhang, Y. et al. "Effect of soil water deficit on evapotranspiration, crop yield, and water use efficiency in the North China Plain". In: *Agricultural Water Management* 64.2 (2004), pp. 107–122. ISSN: 0378-3774. DOI: [10.1016/S0378-3774\(03\)00201-4](https://doi.org/10.1016/S0378-3774(03)00201-4).
- Zhou, J. et al. "Exploring the water storage changes in the largest lake (Selin Co) over the Tibetan Plateau during 2003–2012 from a basin-wide hydrological modeling". In: *Water Resources Research* 51.10 (2015), pp. 8060–8086. ISSN: 0043-1397. DOI: [10.1002/2014WR015846](https://doi.org/10.1002/2014WR015846).
- Zhou, S. et al. "Soil moisture–atmosphere feedbacks mitigate declining water availability in drylands". In: *Nature Climate Change* 11.1 (2021), pp. 38–44. ISSN: 1758-678X. DOI: [10.1038/s41558-020-00945-z](https://doi.org/10.1038/s41558-020-00945-z).
- Zuber, A. "On the interpretation of tracer data in variable flow systems". In: *Journal of Hydrology* 86.1-2 (1986), pp. 45–57. ISSN: 0022-1694. DOI: [10.1016/0022-1694\(86\)90005-3](https://doi.org/10.1016/0022-1694(86)90005-3).

ACKNOWLEDGEMENTS

Four years have passed in the blink of an eye. Though these years might seem ordinary, filled with the bittersweet experiences of life, they are uniquely special to me as they allowed me to meet a group of respectable, lovable, and kind-hearted individuals. Whether in my studies or personal life, these people have consistently provided support when I needed it most, and offered guidance when I was lost and confused, helping me see the way forward. As graduation approaches, please allow me to sincerely thank everyone who has helped and cared for me.

I would like to thank Prof. Thom A. Bogaard for recommending me to Dr. Markus Hrachowitz at the beginning which give me the potential opportunity to do my PhD studies in this world-renown University.

My deepest gratitude goes to my promoter, Dr. Markus Hrachowitz, for granting me the opportunity to study and work within his esteemed hydrology group. His unwavering enthusiasm for hydrological sciences has been a constant source of inspiration for me. Dr. Hrachowitz's prompt responses to my queries and draft manuscripts have been invaluable, enabling me to complete my thesis on time. His extensive knowledge of hydrological modeling and water ages has significantly enhanced our manuscripts. Over these four years, I have received exceptional training not only in hydrology but also in developing clear and logical academic thinking. I am immensely grateful for his patience with my less-than-perfect English and occasionally illogical ideas. Additionally, I deeply appreciate his efforts in organizing the wonderful hydrology breakfasts.

I would like to thank my co-supervisor Dr. Gerrit schoups. His systematic knowledge on statistics and mathematics helped me to choose the method to classify the precipitation zones and model calibration algorithm. And I appreciate very much that he always can give very useful comments from different perspectives, so that improve our manuscript.

I would like to thank my co-author Prof. Christine Stumpp. For her kind and patience, I appreciate very much that she always can give very useful and professional comments to improve our manuscript.

I would like to thank my best friend Shengnan Zhang. We came to Netherlands together and company with each other for already almost four years. Whenever I need you, you are always there, give me your hand and support. I really appreciate that warmth from you encourage me to rise me up from the dark time. In addition, I also would like to thanks Fransje for giving me the pills when I got corona in Birmingham and HuiHui gives me too much support and company last year. And to sweet and cute Ekaterina, my only roommate during this four year, even just one week in SWISS, but your kind and warm heart is like the sunshine in my last a bit boring time here. And to Felix, my boyfriend, I am lucky to meet you in my dark time. You always be there to support all of my decision, and make me feel freedom and be loved deeply. I really

appreciate your help in my daily life and also my research. And to my friend Wenjin, for the happy time we travel together and take good photos for each other. And to some people, I even don't know their name, for their help and encouragement when I fell down on the street with the ice.

I am grateful for the Chinese Scholarship Council (CSC). Without its financial support, it was impossible for me to do a PhD in the Netherlands.

Finally, thousands thanks go to my parents and my dear sister (also my special unique good friend), for their unconditional supports!

Siyuan Wang

22:33 20/07/2024, Delft, Netherlands

CURRICULUM VITAE

Siyuan WANG

04-03-1993 Born in Henan, China.

EDUCATION

2013 – 2017	BSc Physical Geography and Resource Environment China University of Geosciences, China
2017 – 2020	MSc Physical Geography Nanjing University, China
2020 – 2024	PhD Hydrology Delft University of Technology, the Netherlands

LIST OF PUBLICATIONS

First author:

4. Wang, S. et al. "Multi-decadal stability of water ages and tracer transport in a temperate-humid river basin". In: *Environmental Research letters* (2024). Under review
3. Wang, S. et al. "Multi-decadal fluctuations in root zone storage capacity through vegetation adaptation to hydro-climatic variability has minor effects on the hydrological response in the Neckar basin, Germany". In: *Hydrology and Earth System Sciences* 28.17 (2024), pp. 4011–4033. ISSN: 1812-2116. DOI: [10.5194/hess-28-4011-2024](https://doi.org/10.5194/hess-28-4011-2024)
2. Wang, S. et al. "Stable water isotopes and tritium tracers tell the same tale: no evidence for underestimation of catchment transit times inferred by stable isotopes in StorAge Selection (SAS)-function models". In: *Hydrology and Earth System Sciences* 27.16 (2023), pp. 3083–3114. ISSN: 1607-7938. DOI: [10.5194/hess-27-3083-2023](https://doi.org/10.5194/hess-27-3083-2023)
1. Wang, S. et al. "Effects of industry structures on water quality in different urbanized regions using an improved entropy-weighted matter-element methodology". In: *Environmental Science and Pollution Research* 27.7 (Dec. 2019), pp. 7549–7558. ISSN: 1614-7499. DOI: [10.1007/s11356-019-07400-3](https://doi.org/10.1007/s11356-019-07400-3)

Co-author:

1. Wu, L. et al. "Comparison of TMPA-3B42RT Legacy Product and the Equivalent IMERG Products over Mainland China". In: *Remote Sensing* 10.11 (Nov. 2018), p. 1778. ISSN: 2072-4292. DOI: [10.3390/rs10111778](https://doi.org/10.3390/rs10111778)

Propositions

accompanying the dissertation

**LONG-TERM HYDROLOGICAL RESPONSE AND PHYSICAL TRANSPORT
DYNAMICS IN RESPONSE TO CLIMATIC VARIABILITY
INSIGHTS FROM THE NECKAR BASIN**

by

Siyuan WANG

1. The root zone storage capacity is not always as important as frequently considered in hydrological models, especially for temperate-humid climates with ample summer precipitation. [*this thesis*]
2. The long-term stability of physical transport processes, despite external and internal changes in the system, can limit the options available for water quality management. [*this thesis*]
3. The age of streamwater depends on the model used for estimation, not the tracer employed. [*this thesis*]
4. How ecosystem adapt to a changing climate is not the same for all catchments. [*this thesis*]
5. Each water particle serves as both a component of outflows and a carrier of information about the duration of water's journey..
6. Any model should strike a balance between accurately representing underlying processes and minimizing uncertainty.
7. Water neither stops for anyone or changes for anyone, yet it can adapt to any form.
8. All things are both small and magnificent.
9. In science flowers and thorns coexist, much like success and failure are intertwined.
10. Large floods can arise from small streams.

These propositions are regarded as opposable and defensible, and have been approved as such by the promotor Dr. M. Hrachowitz and copromotor Dr.ir G.H.W. Schoups.